
Mémoire présenté pour l'obtention de
l'Habilitation à Diriger des Recherches

par

Jonathan Gula

Université de Bretagne Occidentale

Mesoscale and submesoscale turbulence in the presence of topography

Soutenue le 16 janvier 2020, devant le jury composé de :

M.	Xavier CAPET
M.	Hervé GIORDANI
M.	Pierrick PENVEN
Mme.	Anne PETRENKO
M.	Guillaume ROULLET
M.	Achim WIRTH

Contents

1	In a nutshell	1
	A brief history	1
	A few highlights	2
2	Ocean turbulence at the meso and submesoscale	5
2.1	Introduction	5
2.1.1	Different spatial scales of the ocean	5
2.1.2	Different time scales of the ocean	10
2.1.3	Interactions between scales	11
2.2	Methods	17
2.2.1	Realistic modeling of the ocean	17
2.2.2	Dynamical budgets	20
2.2.3	Pyticles	22
2.3	Effects of topography and eddies on the large scale circulation	24
2.3.1	From the idealized gyre to the real ocean	24
2.3.2	Barotropic vorticity balance in the North-Atlantic subtropical gyre	27
2.3.3	Eddy effects on the mean Gulf Stream	30
2.3.4	Barotropic vorticity balance in the North-Atlantic subpolar gyre	31
2.4	Instabilities and formation of mesoscale eddies	36
2.4.1	Baroclinic and barotropic instabilities	36
2.4.2	The impact of the topography	39
2.5	Submesoscale processes in the surface layer	49
2.5.1	Frontogenesis	49
2.5.2	Barotropic Shear instability	58
2.5.3	Mixed-layer baroclinic instability	65
2.5.4	Interpreting the energy cascade	74
2.6	Surface signature of submesoscale processes and internal waves	77
2.6.1	Separation between balanced and unbalanced motions	77
2.6.2	The signature of internal waves at the surface	78
2.6.3	Lee waves signature at the surface	80
2.7	Submesoscale processes in the bottom layer	83
2.7.1	The topographic drag	83
2.7.2	Centrifugal instability and dissipation	84
2.7.3	Generation of Submesoscale Coherent Vortices	89
2.7.4	SCVs feeding the Rockall Trough anticyclone	90
2.8	Impacts of submesoscale and internal waves in the deep ocean	95
2.8.1	Submesoscale and internal waves in the deep ocean	95
2.8.2	Impacts of submesoscale and internal waves on the mean circulation	95
2.8.3	Impact on dispersion of hydrothermal effluents and larvae	97
2.9	Bonus	99
2.9.1	Retroaction of the atmosphere	99

3 Project: Impacts of submesoscale processes on the oceanic circulation	101
3.1 Modeling the Atlantic ocean at submesoscale	102
3.2 Impacts of deep submesoscale turbulence (and internal waves) on the large scale circulation	102
3.2.1 Quantify impacts of submesoscale turbulence on the large scale circulation	104
3.2.2 Characterise processes responsible for water-mass transformations	105
3.2.3 Parameterise impacts of deep submesoscale using machine learning	107
3.3 Impacts of submesoscale coherent vortices	109
3.3.1 Basin scale statistics for SCVs	111
3.3.2 Generation mechanisms and life-cycle of SCVs	111
3.3.3 Impacts on the large scale circulation	111
3.4 Impacts of submesoscale fronts on the vertical fluxes of tracers	111
3.4.1 Impact of submesoscale dynamics on the fate of exported particles in the deep ocean	112
3.4.2 Impact of submesoscale on air-sea exchanges	113
3.5 Resources	113
Bibliography	116
4 Curriculum Vitae	129
Curriculum vitae	129
Publications	133
Communications	137

In a nutshell

Summary

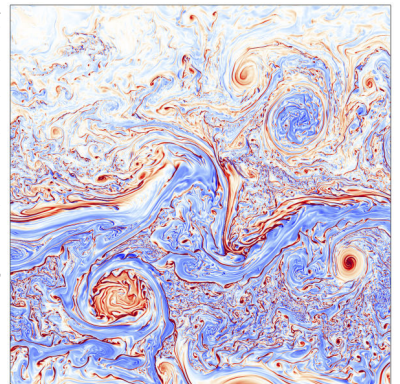
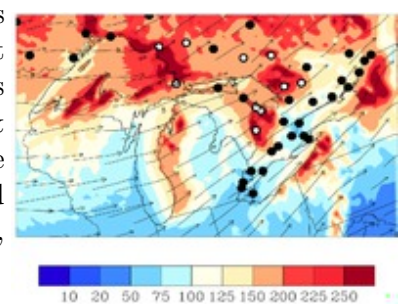
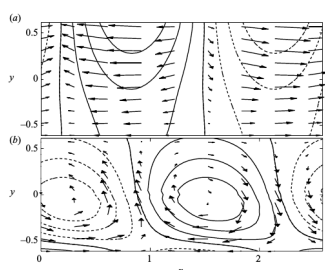
My research centers on better understanding ocean dynamics at mesoscale and submesoscale and how it connects to global ocean circulation and climate. I use numerical models, theory and observations to get dynamical insights on mesoscale and submesoscale processes.

A brief history

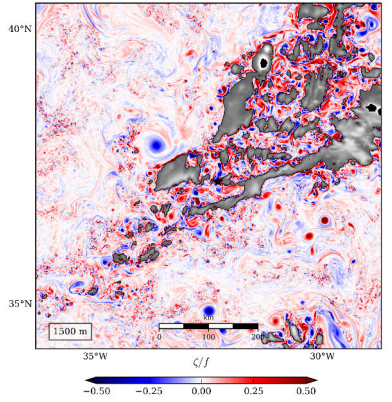
During my thesis I have been working on ageostrophic instabilities of fronts, looking for mechanisms susceptible of inducing small scale energy dissipation and generating gravity waves in the ocean or the atmosphere. I have been using analytical and numerical methods as well as a mesoscale atmospheric model (Gula *et al.*, 2009*a,b*; Flór *et al.*, 2011; Gula & Zeitlin, 2014). This has led me to work on the stability of coastal oceanic currents, the non-linear development of perturbations (Gula & Zeitlin, 2010; Gula *et al.*, 2010), and the formation of coherent structures (Ribstein *et al.*, 2010).

Following my PhD, I have been working at the University of Toronto as a postdoctoral fellow for two years. I studied the impact of the Great Lakes on the regional climate, using a suite of global climate models (NCAR's CCSM3 and CESM1) and the regional model WRF (Gula & Peltier, 2012). I have coupled a freshwater lake model (FLakes) to the WRF model to better represent the modifications of their ice cover and impacts on the atmosphere (d'Orgeville *et al.*, 2014; Mallard *et al.*, 2014, 2015).

I moved to UCLA in 2012 to work on ocean dynamics. My work focused on the dynamics of the Gulf Stream and the understanding of submesoscale (< 10 km) processes in the ocean. I combined state-of-the-art high resolution numerical modelling with theory and idealized simulations to investigate the dynamics of the meso and submesoscale processes and how they contributed to the large scale ocean circulation. My studies spanned a wide range of processes and scales: gyre-scale vorticity balance (Schoonover *et al.*, 2016), mesoscale instabilities (Gula *et al.*, 2015*a*), and submesoscale processes (Gula *et al.*, 2014, 2015*b*, 2016*a*; McWilliams *et al.*, 2015). Model results have been confronted to available observations, in particular in the context of the LatMix ONR program (Klymak *et al.*, 2016; Callies *et al.*, 2015).



I am an assistant professor at the University of Brest since Sep. 2015. My research still centers on ocean dynamics at mesoscale and submesoscale and how it connects to global ocean circulation and climate. One of my focus is the generation of submesoscale turbulence by flow-topography interactions (Vic *et al.*, 2015; Gula *et al.*, 2016b; Krug *et al.*, 2017; Gula *et al.*, 2019; Tedesco *et al.*, 2019; Morvan *et al.*, 2019; Smilena *et al.*, 2019) and the impact for the dispersion of biogeochemical tracers in the deep ocean (Vic *et al.*, 2018). A more recent focus is the impact of internal waves on the ocean dynamics (Lahaye *et al.*, 2019a,b). I still work on the impact of mesoscale on the large scale ocean circulation (Le Corre *et al.*, 2019c). I also follow numerous collaborations on related topics: Gulf Stream dynamics (McWilliams *et al.*, 2019), Potential Vorticity budgets (Morel *et al.*, 2019; Wenegrat *et al.*, 2018b), air-sea interactions at meso and submesoscale (Renault *et al.*, 2016a, 2018), satellite estimation of surface currents (Chelton *et al.*, 2019), currents around Madagascar (Ramanantsoa *et al.*, 2017, 2018), and impacts of submesoscale currents on wind-wave heights (Ardhuin *et al.*, 2017).

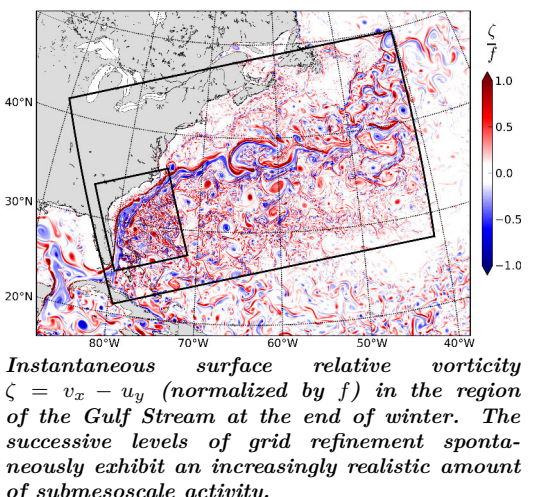


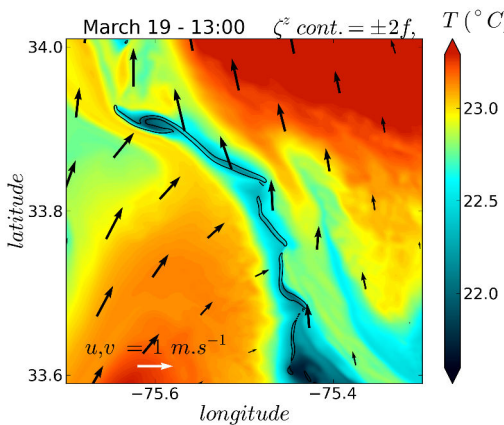
A few highlights

Most of the ocean kinetic energy is contained in the large scale currents and the vigorous geostrophic eddy field, at horizontal scales of order 100 km. To achieve equilibrium the geostrophic currents must viscously dissipate their kinetic energy at much smaller scale. However, geostrophic turbulence is characterized by an inverse cascade of energy towards larger scale, and the pathways of energy toward dissipation are still in question (Müller *et al.*, 2005; Ferrari & Wunsch, 2009). Submesoscale (1 - 30 km) processes can provide a relaxation from the strict geostrophic balance. They can extract energy from geostrophic flows and transfer it to unbalanced motions, from where it may be cascaded to smallest scale where irreversible molecular mixing takes place. Numerical modelling, at very high resolution, has been leading the way in the discovery of new submesoscale processes and the understanding of their impact on the large scale circulation. Recent modelling and observational studies are exposing the ubiquity of submesoscale dynamics in the ocean and transforming the way we view the ocean circulation (McWilliams, 2016).

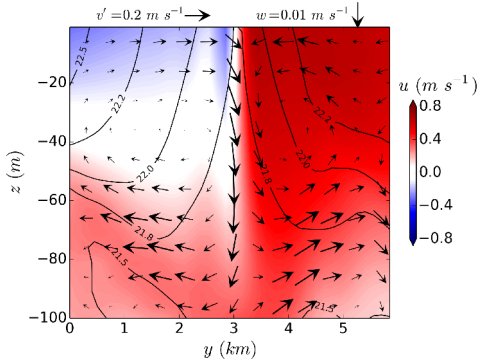
Submesoscale processes in the surface layer

One pathway of energy has been identified in the oceanic surface layer where frontogenesis in the intense fronts (Capet *et al.*, 2008b) and filaments (Gula *et al.*, 2014) is an efficient way to transfer energy from the mesoscale to unbalanced motions. Results from high resolution Gulf Stream simulations clearly highlight the emergence of smaller submesoscale currents full of sharp fronts, filaments, and coherent vortices. They are created by mesoscale strain fields that explosively highly unstable.





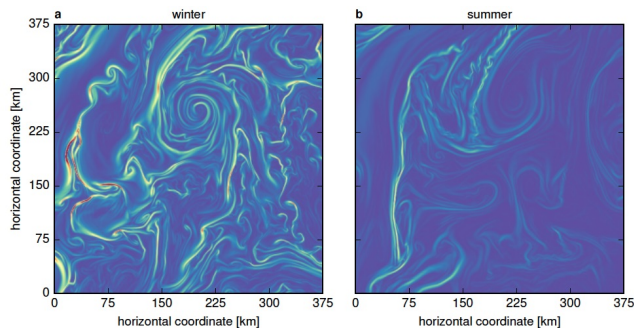
SST showing the instability of a cold filament in the winter time Gulf Stream.



Vertical section of a cold filament.

Surface submesoscale filaments: The life cycle of the intense submesoscale cold filaments that form on the subtropical gyre interior wall of the Gulf Stream has been studied using a set of realistic, very high resolution simulations. The surface buoyancy gradients and ageostrophic secondary circulations intensify in response to the mesoscale strain field as predicted by the theory of frontogenesis. A cold filament has a stronger secondary circulation than a single front due to the amplification at its center. Frontogenesis is disrupted by vigorous submesoscale horizontal shear instabilities; this contrasts with the usual baroclinic instability of submesoscale surface fronts. The life cycle of a filament is typically a few days in duration, from intensification to quasi-stationarity to instability to dissipation. These results are reported in Gula *et al.* (2014).

Turbulent thermal wind: The filament dynamics (and more generally frontal dynamics) in the presence of a mixed layer is not adequately described by the classical thermal wind balance. The effect of vertical mixing of momentum due to turbulence in the surface layer is of the same order of magnitude as the pressure gradient and Coriolis force and contributes equally to a so-called turbulent thermal wind balance (TTW). This has been described in Gula *et al.* (2014), and further investigated using idealized simulations in McWilliams *et al.* (2015). The impacts of such balance on surface fluxes of potential vorticity have been studied in Wenegrat *et al.* (2018b).



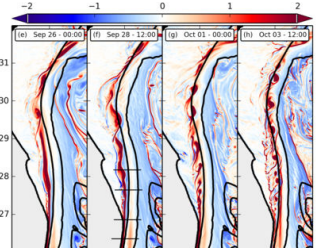
Surface buoyancy gradients in winter (left) and summer (right)

Seasonal cycle of submesoscale turbulence: Submesoscale flows undergo a seasonal cycle in the surface mixed layer: they are much stronger in winter than in summer. Submesoscale flows are energized by baroclinic instabilities that develop around geostrophic eddies in the deep winter mixed layer at a horizontal scale of order 1-10 km. This has been confirmed for the first time by observations in the region of the Gulf Stream in Callies *et al.* (2015). The inverse cascade of energy driven by these structures energize the mesoscale structures, for example in the Agulhas Current as shown in Schubert *et al.* (2019a).

Topographic generation of submesoscale turbulence

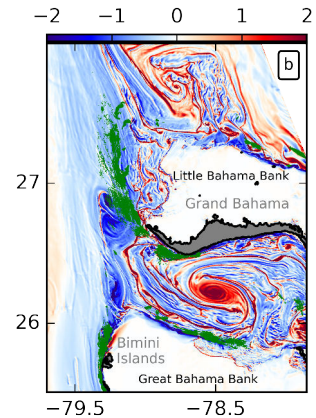
While submesoscale turbulence in the oceanic surface layer has been widely investigated in the past 10 years, the submesoscale turbulence at the bottom of the ocean still remains largely unknown. A mechanism leading to the generation of submesoscale flows by interaction of geostrophic flows with steep topographic slopes has been highlighted recently (Molemaker *et al.*, 2015).

Formation of submesoscale cyclones: The Gulf Stream strongly interacts with topography as it flows through the Florida Straits. On the cyclonic side, flow-topography interactions lead to barotropic shear instability and formation of streets of submesoscale vortices. The topographic drag against the slope amplifies the cyclonic shear by generating large positive vertical vorticity values within the sloped turbulent bottom boundary layer. The flow partially separates from the topography downstream from the Straits, and becomes unstable to submesoscale barotropic instability, rolls up, and forms streets of submesoscale vortices. Submesoscale cyclones will also similarly be created at any place where a current interacts with the topography on its left (in the northern hemisphere). This work is described in Gula *et al.* (2016b). Similar submesoscale cyclones generated in the Agulhas Current have been sampled by gliders (Krug *et al.*, 2017) and analyzed with models (Tedesco *et al.*, 2019).



Surface relative vorticity in the Gulf Stream, showing the formation of submesoscale cyclones along the slope.

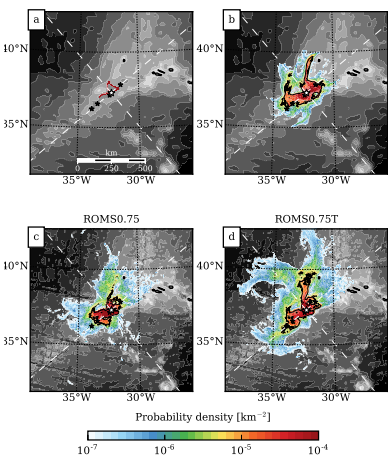
Centrifugal instability and energy dissipation: The interaction of a geostrophic oceanic current with topography can generate unbalanced submesoscale turbulence, and lead to significant energy dissipation and mixing outside the oceanic boundary layers. The sequence of processes comprises the generation of large negative vertical vorticity values in the turbulent bottom boundary layer, and the onset of intense centrifugal instability. This mechanism has been exposed in the context of the Gulf Stream, by means of realistic simulations of the ocean with unprecedented resolution, but it is generic for any current flowing past a topographic slope. These processes lead to large energy dissipation rates that are comparable to the rates observed in highly energetic frontal regions in the surface layer of the ocean, and provide a new and significant route toward small scales and energy dissipation for geostrophic flows. This work is described in Gula *et al.* (2016b).



Relative vorticity (blue and red) and high energy dissipation rates (green) are created by the Gulf Stream flowing along topographic slopes.

Dispersion of larvae by deep submesoscale turbulence

Deep-sea hydrothermal vents effluents and larvae are dispersed and transported long distances by deep ocean currents, but these currents are largely undersampled and little is known about their variability. We have used a series of nested high-resolution regional oceanic numerical simulations over the Mid-Atlantic Ridge to highlight the role of submesoscale currents and tides on the dispersion of the hydrothermal vent effluents and larvae. We have shed light on a submesoscale regime of oceanic turbulence at 1500 m depth. The tidal and submesoscale currents impact larval paths and connectivity between vent communities at biologically-relevant time scales. This is described in Vic *et al.* (2018).



Probability density of particles at 180 days, in a simulation with (a) time mean currents only, (b) mesoscale currents, (c) submesoscale currents and (d) submesoscale currents and tide.

Ocean turbulence at the meso and submesoscale

2.1 Introduction

This manuscript presents some of the different topics I have worked on during the past 10 years. I focus here on **dynamical processes in the ocean**, in particular **flow instabilities**, and the role they play in generating energy fluxes across scales. One important ingredient of my research has been the **bottom topography**, and how dynamical processes may be impacted by its presence.

While I try to provide the important references for the different topics being discussed, this manuscript is by no means an extensive review and focuses exaggeratedly on the works I have contributed to, which are cited in bold in the manuscript.

2.1.1 Different spatial scales of the ocean

At the first order the large scale mean circulation in the upper ocean corresponds to the wind-driven **ocean gyres**. A simplified view of this circulation for the North Atlantic ocean is shown in Fig. 2.1. The understanding of the gyre circulation dates back to the work of Stommel (1948) and Munk (1950). In particular the presence of an intensified western boundary current – the Gulf Stream in the subtropical North Atlantic ocean – is explained by the variation of the Coriolis parameter with latitude (Stommel, 1948). This time-mean circulation is well understood and explained by simplified models, e.g. using the quasi-geostrophic approximation and a flat bottom ocean.

Our vision of the ocean dynamics has evolved over the last few decades by realizing the important role played by the **mesoscale eddies** in the ocean (Fig. 2.2). Mesoscale eddies correspond roughly to motions on the scale of the first Rossby deformation radius and larger. The first Rossby deformation radius has an inverse relationship with latitude and varies between 200 km at the equator, 40 km at mid-latitudes to about 10 km at 60°N (Chelton *et al.*, 1998). Mesoscale motions at mid-latitudes (e.g. the latitude of the Gulf Stream) have scales between 50 - 200 km. Characterization of the mesoscale motions has been made possible by the advances in satellite observations – in particular altimetry (Chelton *et al.*, 2007, 2011). Altimetry made it possible to sample motions down to scales $O(100 \text{ km})$ on a global scale by measuring the Sea Surface Height (SSH). Altimetry has been dubbed *the most successful ocean experiment of all times* by Walter Munk.

The important role played by **submesoscale currents** has been realized over the last decade (McWilliams, 2016). They correspond to currents with lateral scales of 100 m–10 km and temporal scales of hours to weeks. The submesoscale structures catalyze energy dissipation for the large-scale circulation and mesoscale eddies, and are responsible for a large part of the vertical fluxes of mass, buoyancy, and materials in the upper ocean layers. They have intermediate space and time scales between the quasi-geostrophic mesoscale eddies and the fully three-dimensional turbulence, which make direct observations of these processes an open challenge. However, high resolution images of the ocean, such as satellite observations of Sea Surface Temperature (SST) and ocean color images (Fig. 2.3), are exposing the ubiquity of submesoscale motions, visible in the form of density fronts and filaments. A smaller portion of the ocean, south of the Gulf Stream, is shown using infrared imagery in Fig. 2.4.

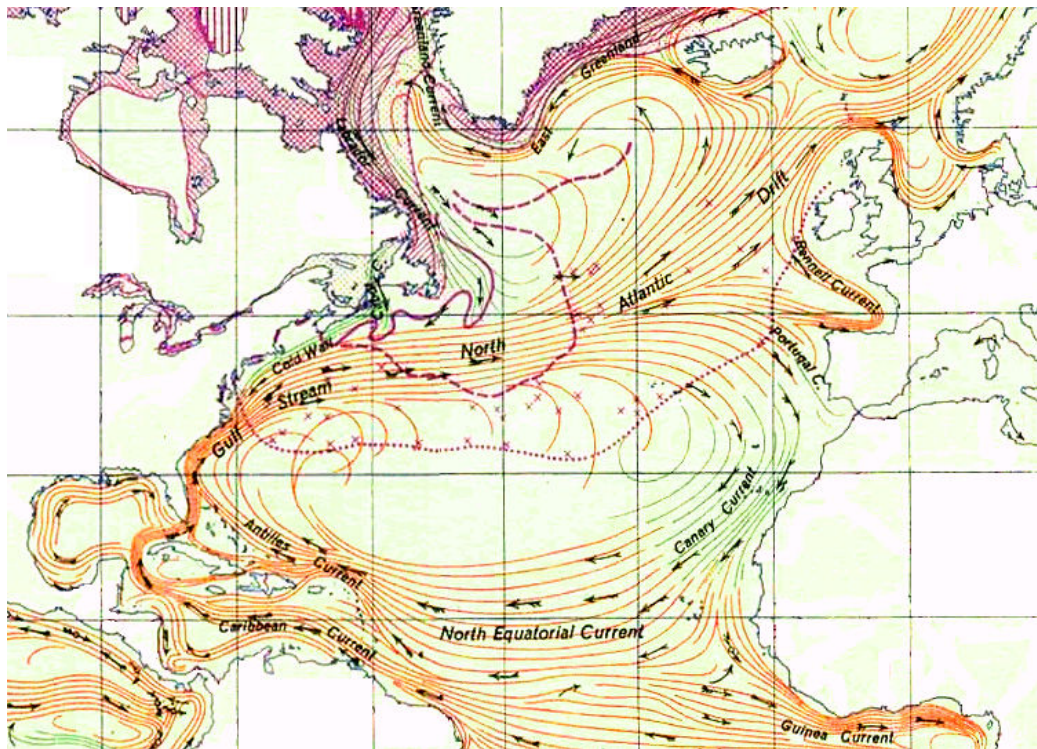


Figure 2.1 – Artistic view of the time-mean surface circulation in the North Atlantic. Image from the Atlas of World Maps, United States Army Service Forces, Army Specialized Training Division. Army Service Forces Manual M-101 (1943).

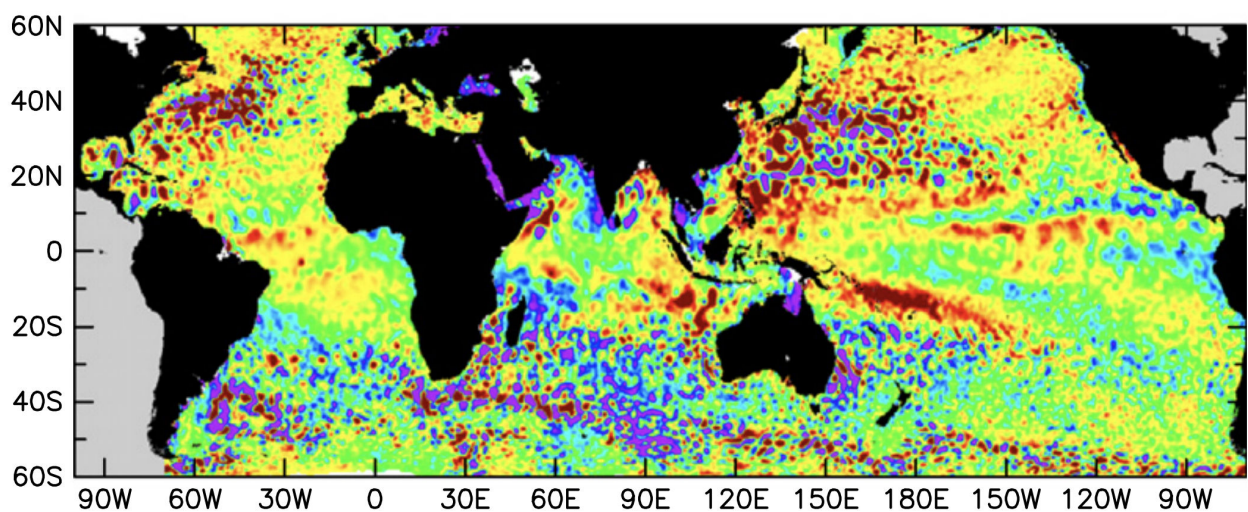


Figure 2.2 – Mesoscale eddies in altimeter observations of Sea Surface Height on 28 August 1996 from the merged T/P and ERS-1 data in the AVISO Reference Series. Image from Chelton *et al.* (2011).

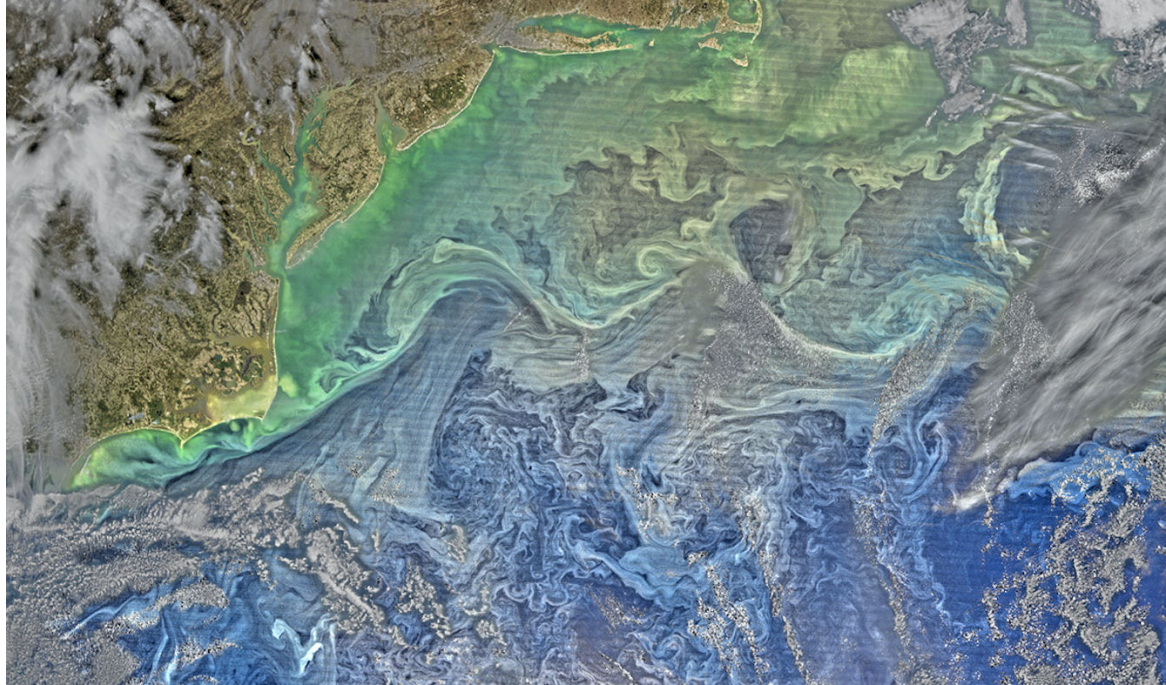


Figure 2.3 – Ocean color image of the Gulf Stream from March 9, 2016, collected by the Visible Infrared Imaging Radiometer Suite on The NASA-NOAA Suomi NPP satellite.

The very sharp fronts appear even more clearly as we zoom in.

It is quite difficult to sample submesoscale features in-situ. Measuring the actual velocities in the upper ocean is still a very complicated task at these scales. Only a few dedicated programs have been able to acquire data with enough spatial and temporal resolution to allow a quantitative characterisation of submesoscale turbulence regimes, *e.g.*, LatMix (Shcherbina *et al.*, 2013), OSMOSIS (Buckingham *et al.*, 2016), CARTHE (D’Asaro *et al.*, 2018). However, measuring vertical velocities at the submesoscale is still a near impossible task.

Numerical models have been instrumental in exposing the ubiquity of meso and submesoscales. An example using the Regional Oceanic Modeling System (ROMS, Shchepetkin & McWilliams 2005) with $\delta x = 500$ m in the region of the Gulf Stream is shown in Fig. 2.5. The surface relative vorticity $\zeta = v_x - u_y$ is a good proxy to highlight the presence of intense velocity gradients and order one Rossby numbers (ζ/f).

The horizontal kinetic energy spectra near the surface in the Gulf Stream (Fig. 2.6) illustrates the repartition of kinetic energy at the different scales. In a region with relatively intense submesoscale motions, there is a convergence with increasing resolution toward a shallow $\sim k^{-2}$ shape, instead of the $\sim k^{-3}$ shape enstrophy inertial range of geostrophic turbulence. This follows results in the California Current shown by Capet *et al.* (2008a). But of course this behavior will be highly dependent on the region chosen and time of the year, which can correspond to different types of dynamical regimes.

Submesoscale currents are not only present in the upper ocean. Energetic submesoscale currents can be found at the bottom of the ocean as well, especially in the presence of steep topography such as seamounts and ridges. An example of the deep circulation from a numerical simulation using ROMS with $\delta x = 750$ m at 1500 m depth over the Mid-Atlantic Ridge (MAR) south of the Azores is shown in Fig. 2.7. A submesoscale regime of oceanic turbulence – with a shallow $\sim k^{-2}$ shape – is visible over the MAR. It contrasts with open-ocean – *i.e.*, far from topographic features – regimes of turbulence,

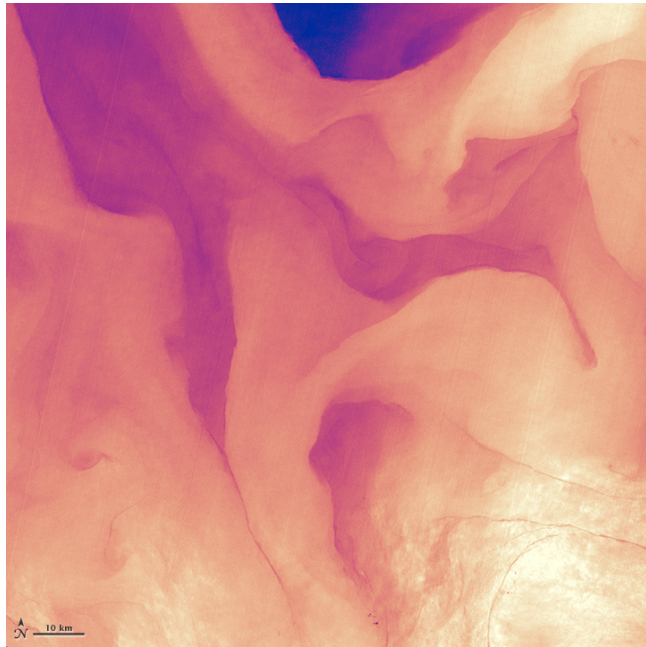


Figure 2.4 – Infrared image south of the Gulf Stream, centered at 33.06N, 73.86W, acquired on April 9, 2013, by the Thermal Infrared Sensor (TIRS) on the Landsat 8 satellite. Water temperatures range from 18° to 21.25°, with cooler temperatures in purple and the warmest nearly white. From <https://landsat.visibleearth.nasa.gov/view.php?id=82649>

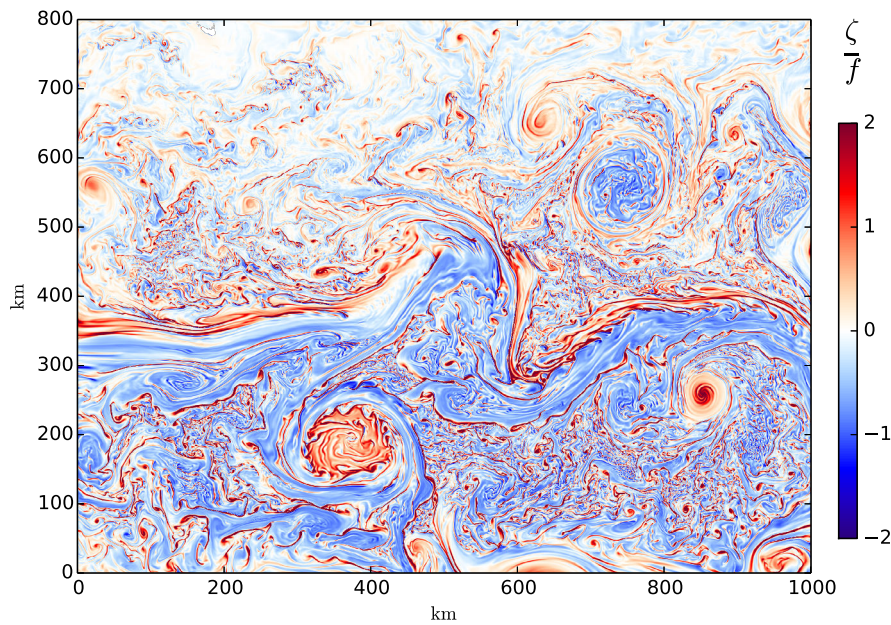


Figure 2.5 – Instantaneous surface relative vorticity $\zeta = v_x - u_y$ normalized by f at the surface in the wintertime Gulf Stream after separation from the western boundary in a nested ROMS simulation with $\delta x = 500$ m horizontal resolution. Notice the meandering Stream in the center, the northern warm anticyclonic and southern cold cyclonic mesoscale Rings, and the nearly ubiquitous submesoscale features of many types: North Wall “comma” instabilities and streamers, Ring interior instabilities, cyclonic coherent vortices, and “submesoscale soup” in-between. Data adapted from **Gula et al. (2015a)**. This picture has been used as a cover for *Proceedings of the Royal Society A: Mathematical, Physical and Engineering Sciences* June 2016; volume 472, issue 2190

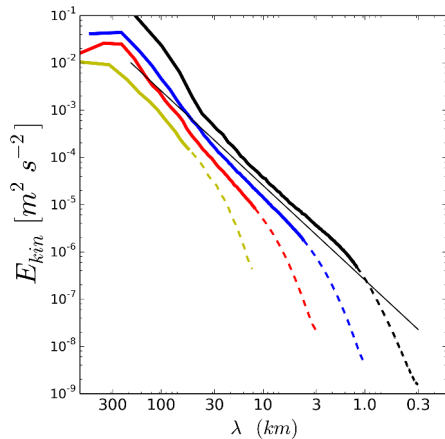


Figure 2.6 – Horizontal wavenumber spectra of surface kinetic energy at the surface in the Gulf Stream (in the region of Fig. 2.5) from models with increasing horizontal resolution: $\delta x = 6 \text{ km}, 1.5 \text{ km}, 500 \text{ m}$, and 150 m . The black line follows a k^{-2} slope.

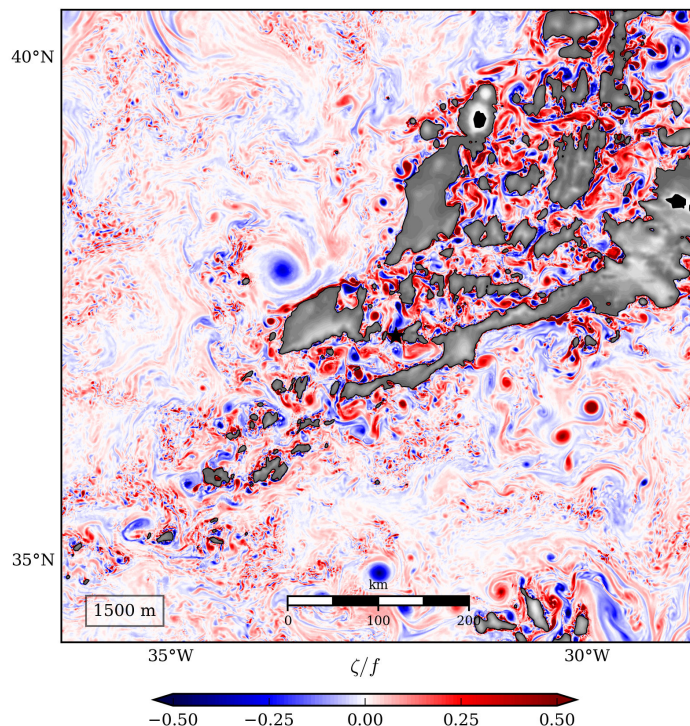


Figure 2.7 – Instantaneous relative vorticity $\zeta = v_x - u_y$ at 1500 m depth over the Mid-Atlantic Ridge. Data from a ROMS simulation with $\delta x = 750 \text{ m}$ horizontal resolution. Image from **Vic et al. (2018)**. This image has been used as a cover for *Deep-Sea Research: Part 1* March 2018; volume 133

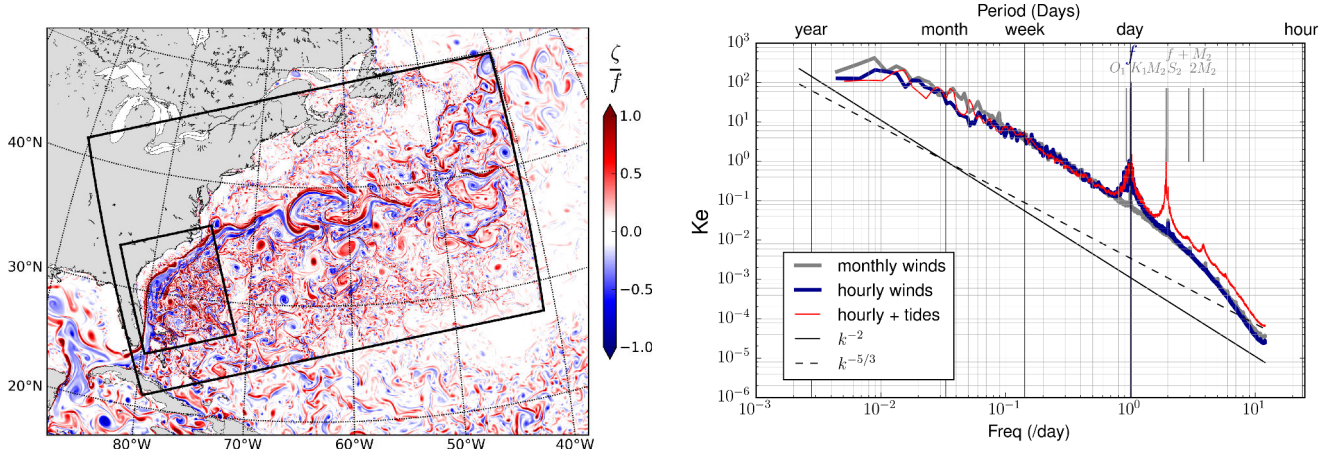


Figure 2.8 – (left) Instantaneous surface relative vorticity $\zeta = v_x - u_y$ in ROMS simulations with increasing resolution (from 6 km to 2.5 km to 750 m). (right) **Frequency spectrum of surface kinetic energy** $\int E(k, \omega) dk$ in the Sargasso Sea from the $\delta x = 750$ m simulations. Simulations are forced with different type of forcings: monthly varying winds, hourly winds, or hourly winds plus tides.

dominated by mesoscales.

2.1.2 Different time scales of the ocean

Mesoscale motions have time scales ranging from weeks to months, and submesoscale motions have time scales ranging from hours to days. We usually classify them as the subinertial motions (slower than f), even if the submesoscale motions can in fact be faster than f (see section 2.6.1). Other fundamental ingredients for the ocean dynamics are the **internal waves**, which constitute the bulk of the super-inertial (faster than f) motions.

The three main types of internal waves are the near-inertial waves, the internal tides, and the lee waves. The **near-inertial waves** (NIW) are generated directly at the surface of the ocean by the wind. They have frequency close to the Coriolis frequency f and large spatial scales. The **internal tides** are generated by the interaction of the barotropic tidal currents with the bottom topography. They have frequencies close to the tidal harmonics (M_1 , M_2 , etc.). Finally the **lee waves** are generated by the interaction of geostrophic currents with the bottom topography. Thus, they have low frequencies corresponding to the time scales of the geostrophic currents generating them.

We can compute a frequency spectrum of kinetic energy to highlight the presence of different time scales in the flow. An example in the region of the Sargasso Sea (Fig. 2.8) shows a continuum of energy extending from years to hours, but also the presence of energy peaks at specific frequencies: f , the tidal components O_1 , K_1 , M_2 , S_2 , and their harmonics $2M_2$, $f + M_2$, etc. The numerical simulations allow to play around with the sources of the internal waves by turning off tides and/or high-frequency wind forcings to see the effect of the forcings on the frequency spectra. Going from monthly to hourly winds makes a strong inertial energy peak appear (Fig. 2.8). Adding different tidal components will make the peaks appear at the corresponding frequencies.

To get an overview of the space and time scales of the flow, we can decompose the kinetic energy in space and time in the form of wavenumber frequency spectra (Fig. 2.9). The different types of motions appear clearly in different parts of the diagram as meso- and submesoscale motions, as well as near-inertial waves and internal tides. However, it is also clear that the different types of motions may overlap in certain regions of the diagram.

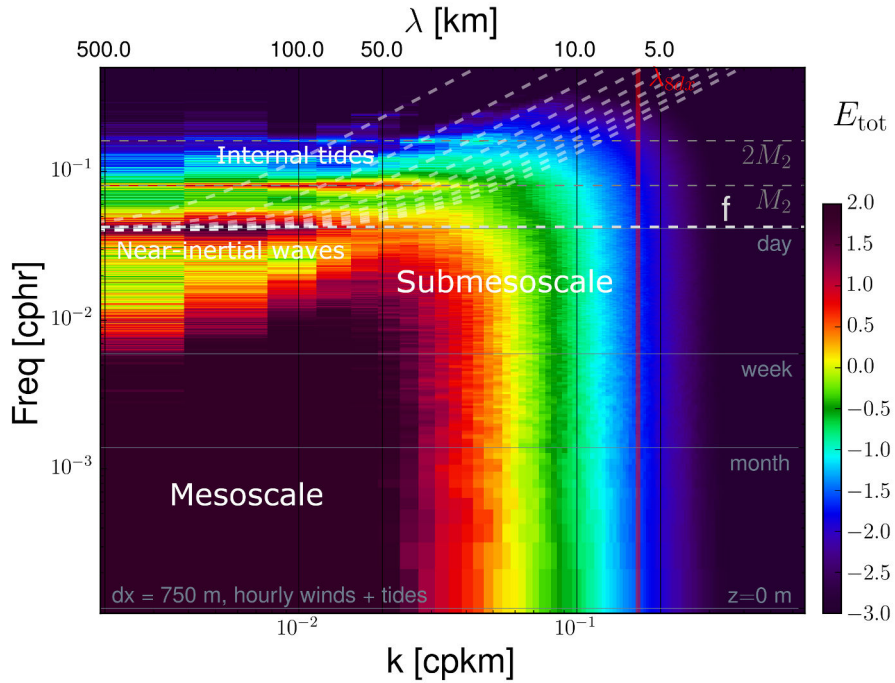


Figure 2.9 – **Wavenumber frequency spectra.** Horizontal wavenumber-frequency spectrum of surface kinetic energy $E(k, \omega)$ for the Sargasso Sea. The simulation has a horizontal resolution of $\delta x = 750$ m and is forced with hourly wind and tidal forcings. White lines in the upper panels show the dispersion relations for inertia-gravity waves from mode 1 through mode 10.

This wavenumber-frequency diagram is slightly different for each region of the world, depending on the relative intensity of the various components (meso/submesoscale, tides, etc.). This can be illustrated by looking at 2 other regions corresponding to different dynamical regimes (Fig. 2.10). The California Current is an eastern boundary with intense submesoscale activity. The Mid-Atlantic Ridge, in the interior of the North Atlantic subtropical gyre, is a region with lower mesoscale eddy activity, but more energetic internal tides (Fig. 2.10).

2.1.3 Interactions between scales

What makes fluid dynamics interesting is that the equations of motions are not linear. They include a non-linear term that allows different time and spatial scales to interact together and energy to be transferred between scales. This is called the **energy cascade**.

Traditionally the balanced dynamics (*e.g.*, the geostrophically balanced motions) and the unbalanced one (*e.g.*, internal waves) are considered separated with very weak interactions. Most of the ocean's kinetic energy is contained in the mesoscale eddy field (Ferrari & Wunsch, 2009), with flows characterized by the hydrostatic and geostrophic balances. Such “balanced” motions tend to aggregate into larger scales, following an inverse cascade of energy and a barotropization of the flow. A significant fraction of the dissipation then occurs through bottom friction (Salmon, 1980; Sen *et al.*, 2008). However, a large part of the energy dissipation needs to happen at much smaller scales. But how energy is transferred from the large scales to the very small scales is still an open question (Müller *et al.*, 2005; Ferrari & Wunsch, 2009).

This is one of the main questions that has driven my research from my PhD until now: *how is energy extracted from the mesoscale balanced dynamics and transferred to unbalanced motions*, where it will be able to cascade toward smaller and smaller scales and ultimately reach the viscous scales

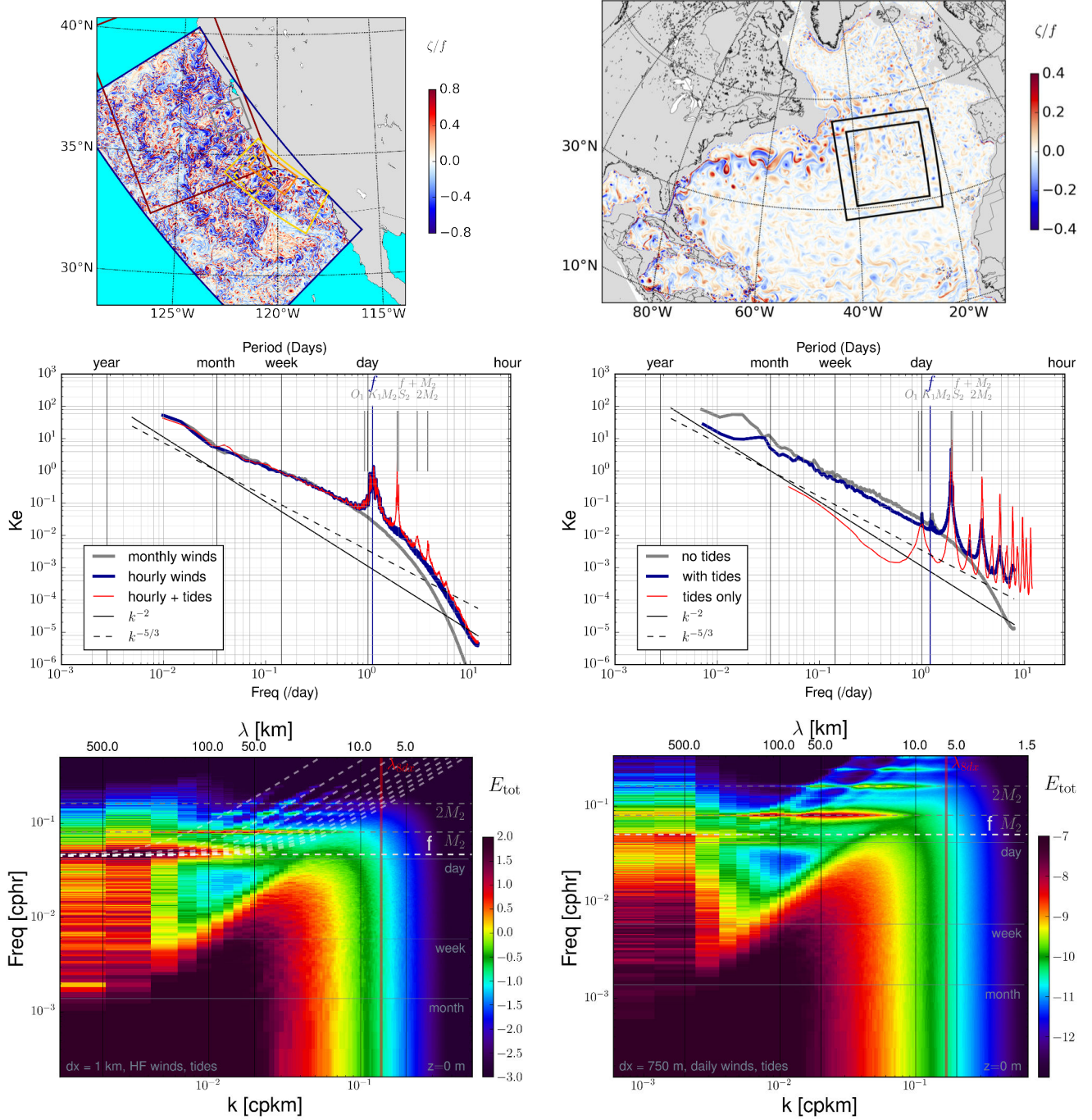


Figure 2.10 – (top) Instantaneous surface relative vorticity $\zeta = v_x - u_y$ in (left) the region of the California Current, and (right) over the Mid-Atlantic ridge. (middle) frequency spectrum of surface kinetic energy $\int E(k, \omega) dk$, and (bottom) Horizontal wavenumber-frequency spectrum of surface kinetic energy $E(k, \omega)$,

where it will be dissipated? To answer this question I have tried to identify the various processes contributing to the generation of smaller scales and quantify their importance in the energy cascade.

Different type of motions and their corresponding scales are summarized in Fig. 2.12. The scheme is of course highly simplified, but distinguishes the main types of motions as: large-scale and mesoscale balanced motions, submesoscale motions (that include both balanced and unbalanced parts), and internal waves. There are possible interactions between all the different categories but their relative importance is still a subject of active research (Ferrari & Wunsch, 2009). I review briefly below some of the known processes driving these interactions, including generation of mesoscale from the large-scale currents, generation of submesoscale currents, and interactions between the meso/submesoscale and the internal wave field.

2.1.3.1 Generation of mesoscale eddies

The generation of mesoscale eddies by large-scale current instabilities is a well documented topic. The main processes are **baroclinic and barotropic instabilities**, which are associated with large-scale vertical and horizontal velocity shear, respectively. Different aspects of my work related to mesoscale dynamics are summarized in section 2.4. Some properties of baroclinic and barotropic instabilities, from highly idealized studies or realistic flows, are recalled in subsection 2.4.1, effects of a coast and of a bottom topography on flow instabilities are discussed in subsection 2.4.2. The feedback of the mesoscale and topography effects on the large-scale circulation is discussed in 2.3.

2.1.3.2 From mesoscale to submesoscale

The cascade of energy from the mesoscale to the submesoscale in the surface ocean involves multiple processes, which have been documented in many papers (see review in McWilliams, 2016). I have worked on several of these processes, as detailed in section 2.5, and briefly recalled below:

- The **stirring induced by mesoscale structures** is a direct way to generate submesoscale density fronts and filaments (McWilliams, 1984). The mesoscale field induces a straining that tends to intensify tracer gradients and form elongated filaments. This is well described in the classical quasi-geostrophic theories where it corresponds to a direct cascade of tracer variance toward smaller scales. An example of an intense filament generated by mesoscale straining and undergoing frontogenesis is analyzed in details in subsection 2.5.1.
- An efficient mechanism to generate submesoscale currents is the **mixed-layer baroclinic instability** (MLI) (Haine & Marshall, 1999; Boccaletti *et al.*, 2007; Fox-Kemper *et al.*, 2008). MLI is essentially geostrophic in nature but has a smaller horizontal scale due to the reduced scale of the Rossby deformation radius in the mixed layer. The MLI is converting eddy potential to kinetic energy by constantly acting toward a restratification of the flow. Results showing the importance of MLI in different regions and demonstrating the seasonality of MLI are presented in subsection 2.5.3.
- Different types of **ageostrophic instabilities** like horizontal shear instabilities, or anticyclonic, ageostrophic instability can provide a direct route from balanced mesoscale dynamics to unbalanced submesoscale behaviours (Molemaker *et al.*, 2005; McWilliams, 2016). Atmospheric forcing at fronts can also make the flow unstable to **symmetric instability** and initiate a forward cascade of energy down to dissipation (Taylor & Ferrari, 2009; Thomas & Taylor, 2010; D'Asaro *et al.*, 2011). Some example of ageostrophic instabilities driving such energy cascades are discussed in subsection 2.5.2.

The submesoscale motions can trigger a forward cascade of energy toward smaller scales, but they can also feedback energy to the mesoscale and enhance the mesoscale turbulent activity. The balanced part of the submesoscale is expected to drive an inverse cascade of energy towards larger scales, similarly to the mesoscale inverse cascade (Capet *et al.*, 2008c; Fox-Kemper & Ferrari, 2008). This has been verified by Sasaki *et al.* (2014) in North Pacific Ocean simulations, who showed an intensification of the mesoscale eddy activity following episodes of intense submesoscale activity (mostly due to the winter intensification of mixed-layer baroclinic instabilities). This is discussed in subsection 2.5.4.

Another ingredient that has been more recently considered is the influence of **topography**. A significant part of my work over the last few years has addressed this influence:

- The **topographic generation of submesoscale flows** is a more recent and much less studied mechanism associated with interactions of geostrophic flows with steep topographic slopes (Molemaker *et al.*, 2015; Dewar *et al.*, 2015; Gula *et al.*, 2015b, 2016b). This can lead to elevated local dissipation and mixing through triggering of centrifugal instability or intense horizontal shear instability and the formation of submesoscale coherent vortices. My works on the topic are detailed in section 2.7

2.1.3.3 Interactions between meso/submesoscale and the internal wave field

The coupling between meso/submesoscale and internal waves is a long-standing question in geophysical fluid dynamics. Traditionally the two were believed to be well separated, with slow balanced motions on one side, and fast unbalanced motions on the other side, that would not be able to interact. However, recent works have shown that the distinction is becoming blurry, and that a “slow manifold” does not exist anymore, when considering energetic unbalanced submesoscale motions with high Rossby numbers. Wavenumber-frequency power spectra in Fig. 2.9 and 2.10 are showing that submesoscale motions extends well into the superinertial frequency band and get superimposed with internal waves for certain time and spatial scales. This highlights the possibility for interactions between the different type of motions, which can happen through different mechanisms:

- Geostrophic flows can **spontaneously emit internal waves** (see review in Vanneste, 2013). This is an important mechanism in the atmosphere (see review in Plougonven & Zhang, 2014). The spontaneous emission of internal gravity waves was an important motivation during my PhD work, following the results of Williams *et al.* (2008), which observed inertia-gravity waves emitted from balanced flows in a rotating two-layer annulus experiment. This is discussed in subsection 2.4.2.1. The emission also depends on the Rossby number such that intense fronts, which can reach very high Rossby numbers ($Ro \sim 10 - 100f$) are likely source for spontaneously emitted internal waves (Shakespeare & Taylor, 2014; Nagai *et al.*, 2015). A snapshot of vertical velocity at 1000 m depth in the Gulf Stream, further decomposed into superinertial ($\omega > f$) and subinertial ($\omega < f$) parts, shows the presence of spontaneously emitted internal waves, which can be quite intense at the North Wall (Fig. 2.11). However, the overall level of energy for the spontaneously generated internal waves is estimated to be several orders of magnitude smaller than the energy of the other types of internal waves in the ocean (Danioux *et al.*, 2012).
- The **near-inertial wave field** excited by the wind can also directly extract significant energy from the large scale flow (Xie & Vanneste, 2015; Wagner & Young, 2016), and from density fronts (Whitt & Thomas, 2013; Grisouard & Thomas, 2016), especially at the frontogenetic fronts (Thomas, 2019). Externally forced waves (in particular near-inertial waves) can stimulate the mesoscale to submesoscale energy transfer (Barkan *et al.*, 2017). This is a process dubbed **stimulated imbalance**, which can catalyze a forward energy cascade from mesoscale down to dissipative processes. These aspects are part of my current work and are mostly described in

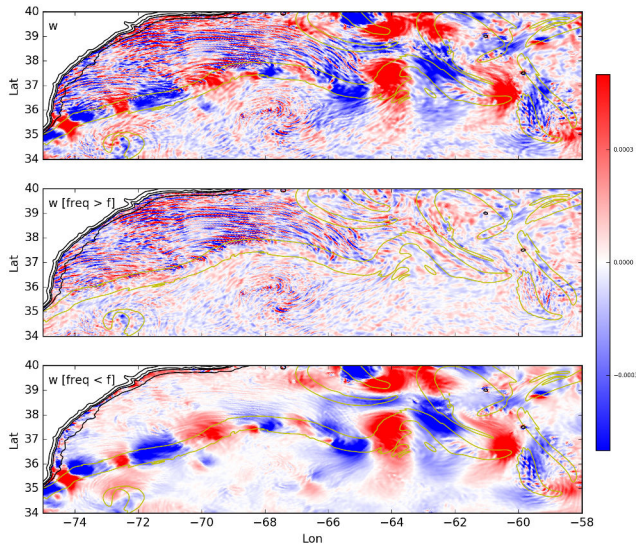


Figure 2.11 – Snapshot of vertical velocity at 1000 m depth in a Gulf Stream ROMS simulation at $\delta x = 2.5$ km. (top) full vertical velocity, (middle) superinertial ($\omega > f$), and (bottom) subinertial ($\omega < f$) part of the vertical velocity.

the project section 3.2.1.2.

- Another pathway lies at the bottom of the ocean where interactions of geostrophic flows with small scale bottom topography generate **lee waves** that can break and dissipate energy at small scales (Nikurashin *et al.*, 2013). Works related to lee wave generation in the Gulf Stream, and their impact on the mean current, are presented in section 2.6.3.

2.1.3.4 Retroaction on the large-scale circulation and other impacts

A following question is: *are the meso- and submesoscale processes important for the large-scale circulation?*

In other words: **why do we care about such processes and about the way the energy is transferred and dissipated?**

The impacts of the mesoscale turbulence on the large-scale circulation and the global budgets of tracers are now well documented. Some aspects are discussed in section 2.3. The impact of submesoscale turbulence is also more and more acknowledged. The intensification of mesoscale eddies due to the inverse cascade driven by balanced submesoscales instabilities in one example (subsection 2.5.4). I also present some results on the impact of deep meso- and submesoscale turbulence and internal waves on the deep circulation and dispersion of tracers in subsection 2.8. More generally, this will be a central question for the research project I present in section 3, and will be discussed more extensively there.

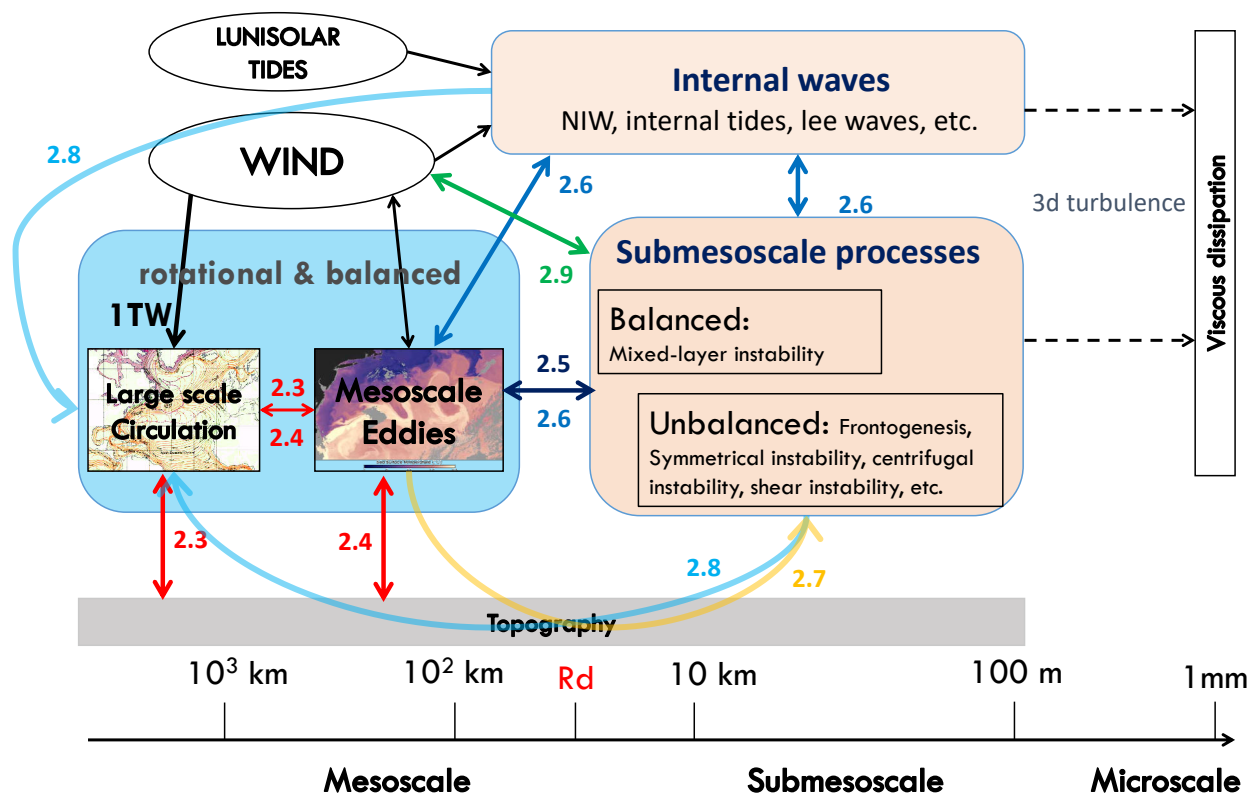


Figure 2.12 – The main energy reservoirs in the ocean and (some of) the known interactions between them. The numbers correspond to subsections in this manuscript in which the processes involved in the interactions between the different type of motions are addressed.

2.2 Methods

2.2.1 Realistic modeling of the ocean

A very useful tool to tackle these questions, besides idealized theory and process modeling, is **realistic modeling** using multiply nested grids in a variety of geographical environments. Most of the simulations I have used have been realized with the Regional Oceanic Modeling System (ROMS, Shchepetkin & McWilliams 2005), which is presented below with the nesting procedure (subsection 2.2.1.1). I also present the main simulations I have designed and used along with a few typical examples of diagnostics used for the validations of such simulations in subsection 2.2.1.2.

2.2.1.1 The ROMS/CROCO model

The ROMS model solves the hydrostatic Primitive Equations for the velocity \vec{u} , potential temperature θ , and salinity S , using a full equation of state for seawater (Shchepetkin & McWilliams, 2008, 2011). Since coming back to France in 2015, I use the model in its Coastal and Regional Ocean COnmunity version (CROCO, <https://www.croc-ocean.org/>), which is very similar to the original UCLA version.

CROCO is discretized in coastline- and terrain-following curvilinear coordinates using high-order numerical methods. The vertical grid system concentrates vertical levels near the surface and bottom following the formula described in Lemarié *et al.* (2012). The depth of the transition between flat z levels and terrain-following σ levels is typically $h_{cline} = 300$ m, and the two parameters controlling the bottom and surface refinement of the grid are typically $\sigma_b = 2$, $\sigma_s = 5$. It is a split-explicit, free-surface ocean model, where short time steps are used to advance the surface elevation and barotropic momentum, with a much larger time step used for temperature, salinity, and baroclinic momentum. The model has a 2-way time-averaging procedure for the barotropic mode, which satisfies the 3D continuity equation. The specially designed 3rd order predictor-corrector time step algorithm allows a substantial increase in the permissible time-step size. The complete time stepping algorithm is described in Shchepetkin & McWilliams (2005). Associated with the 3rd order time-stepping, a 3rd or 5th-order, upstream-biased advection scheme allows the generation of steep gradients, enhancing the effective resolution of the solution for a given grid size. Because of the implicit diffusion in the upstream-biased advection scheme, explicit lateral viscosity is not needed in CROCO, except in sponge layers near the open boundaries where it increases smoothly close to the lateral open boundaries.

The default option for the vertical mixing of tracers and momentum is the K-Profile Parameterization (KPP, Large *et al.* 1994) at the surface and bottom, which I have used for most simulations. New simulations now use a k- ϵ model (GLS, Umlauf & Burchard (2003)), which appears to be more effective in regions of deep convection. The effect of bottom friction is parameterized through a logarithmic law of the wall with a roughness length typically $Z_0 = 0.01$ m.

Bathymetry for all domains is constructed from datasets such as SRTM30-plus (available online at http://topex.ucsd.edu/WWW_html/srtm30_plus.html) based on the 1-minute Smith & Sandwell (1997) global dataset and higher resolution data where available. A Gaussian smoothing kernel with a width of at least 4 times the topographic grid spacing is used to avoid aliasing whenever the topographic data is available at higher resolution than the computational grid. Terrain-following models such as ROMS have computational restrictions with regards to the steepness and roughness of the topography (Beckmann & Haidvogel, 1993). Local smoothing is applied where the steepness of the topography exceeds a factor $r_{max} = 0.2$.

Because the primary target is often submesoscale currents with horizontal scales of <10 km, an aggressive approach to nesting is taken with successively finer resolution in a sequence of steps where

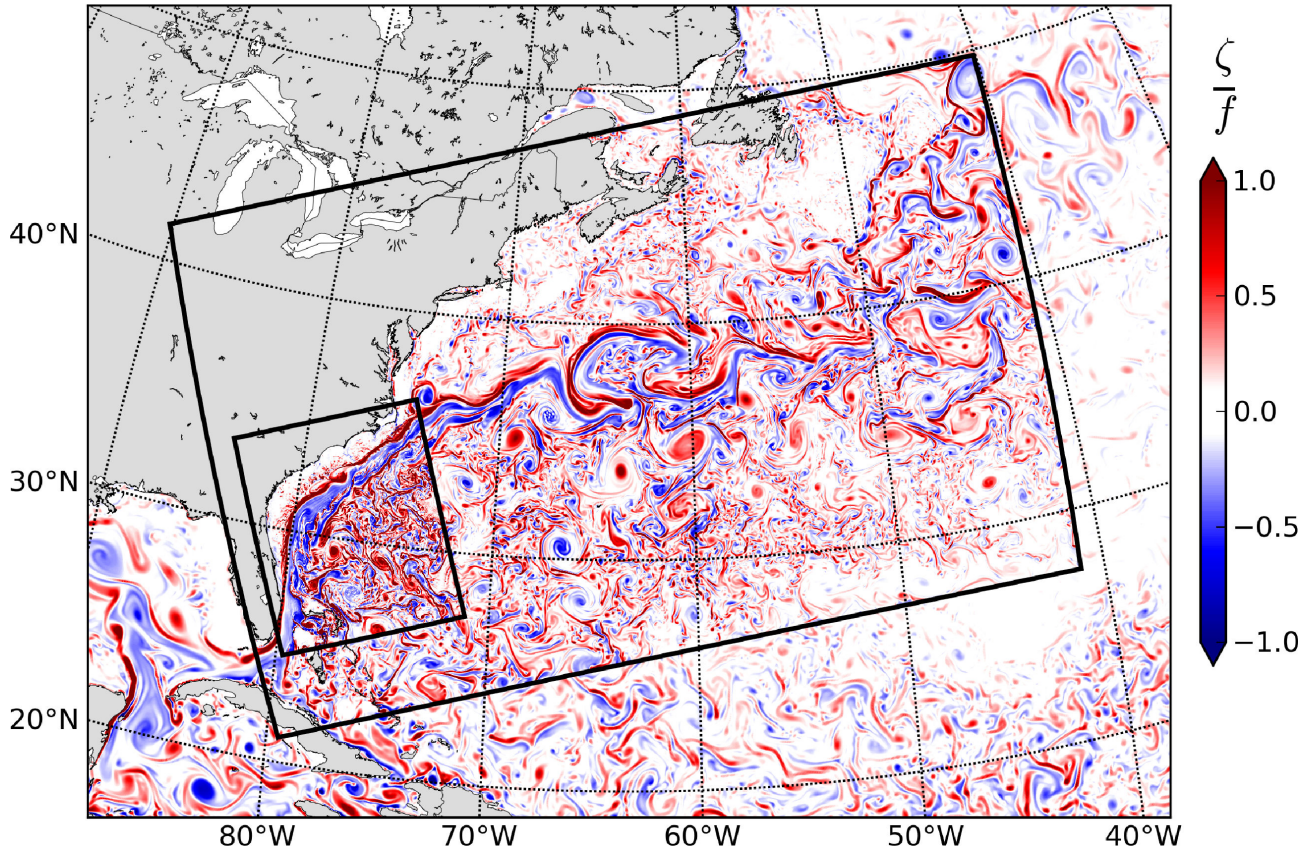


Figure 2.13 – Instantaneous surface relative vorticity $\zeta = v_x - u_y$ in the region of the Gulf Stream at the end of winter as simulated by ROMS. The parent domain ($\Delta x \approx 6$ km) covers most of the Atlantic Ocean. The boundaries of the successive nested domains ($\Delta x = 2.5$ km) and ($\Delta x = 750$ m) are delineated by thick black lines. The relative vorticity plotted inside each of the domains is computed using data at the corresponding resolution. The successive levels of grid refinement spontaneously exhibit an increasingly realistic amount of submesoscale activity. From **Gula et al. (2015a)**.

each “child” grid utilizes “parent” grid data at the open boundaries of the regional domains. A typical sequence of nests is shown in Fig. 2.13. The nesting procedure is one-way, from larger to finer scales without feedback from the child grid solution onto the parent grid (Penven *et al.*, 2006), and offline, grids are run independently and each nest supplies boundary forcing data to the next one. The boundary condition algorithm consists of a modified Flather-type scheme for the barotropic mode (Mason *et al.*, 2010) and an Orlanski-type scheme for the baroclinic mode (including T and S; Marchesiello *et al.* 2001).

2.2.1.2 Presentation of different configurations

Numerous configurations have been designed over the years, with various objectives in mind usually oriented toward process-studies. Most of the simulations I designed were located in the North Atlantic ocean, in particular in the Gulf Stream region (Fig. 2.14), but also the eastern part of the subpolar gyre above the Mid-Atlantic ridge (Fig. 2.7), and in the subpolar gyre (Fig. 2.30). I have also worked in the Agulhas Current (Fig. 2.60), around Madagascar (Fig. 2.16), in the California Current (Fig. 2.10), and in the equatorial Pacific in the context of various collaborations.

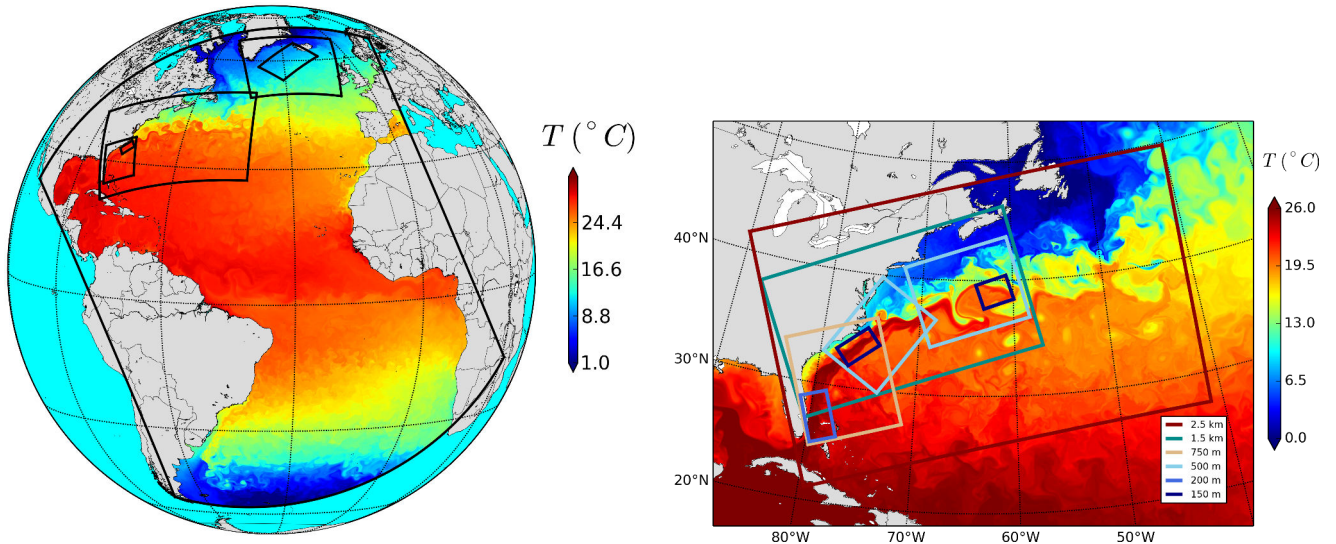


Figure 2.14 – Various Atlantic domains used to run ROMS simulations over the years.

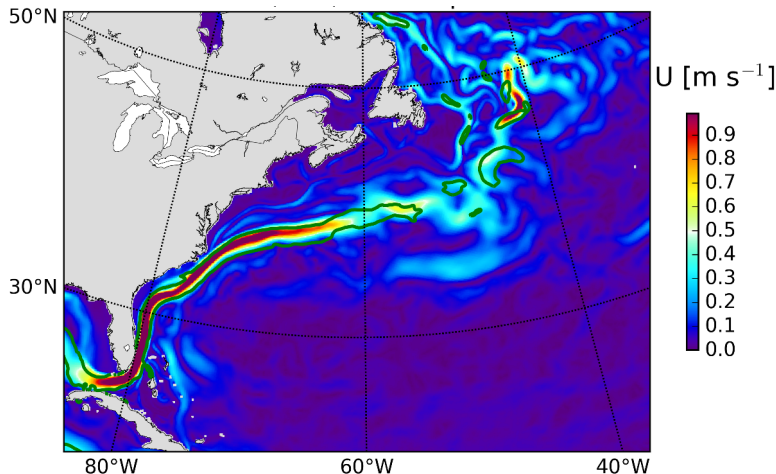


Figure 2.15 – Mean surface geostrophic velocity (colors, in m s^{-1}) from a $\delta x = 6 \text{ km}$ simulation of the North-Atlantic. The green line shows the 0.3 m s^{-1} contour level of climatological surface geostrophic velocity derived from the AVISO altimetry data set.

2.2.1.3 Validation of the simulations

Validation of the different simulations in the context of submesoscale process-studies usually involve a statistical comparison of the large-scale environment (stratification and currents) and the mesoscale activity. Direct comparisons of the properties of the submesoscale dynamics are much more difficult to achieve and possible only in the context of specifically designed observations (*e.g.*, Shcherbina *et al.*, 2013).

The mean currents are usually the first comparison to be performed. The mean surface velocity from an Atlantic simulation is plotted Fig. 2.15 with superimposed contours showing geostrophic velocity derived from the AVISO altimetry data set. The Gulf Stream separation and path are notoriously difficult simulation targets, but it is showing a very nice agreement with observations in this case. However, if it is relatively easy to find accurate observations of the Gulf Stream velocities, it can be much more difficult for weaker and smaller currents, in particular close to the coast where altimetry becomes blind. An example of disagreement between different observations datasets is illustrated in Fig. 2.16, at the location of the South-west Madagascar Coastal Current (Ramanantsoa *et al.*,

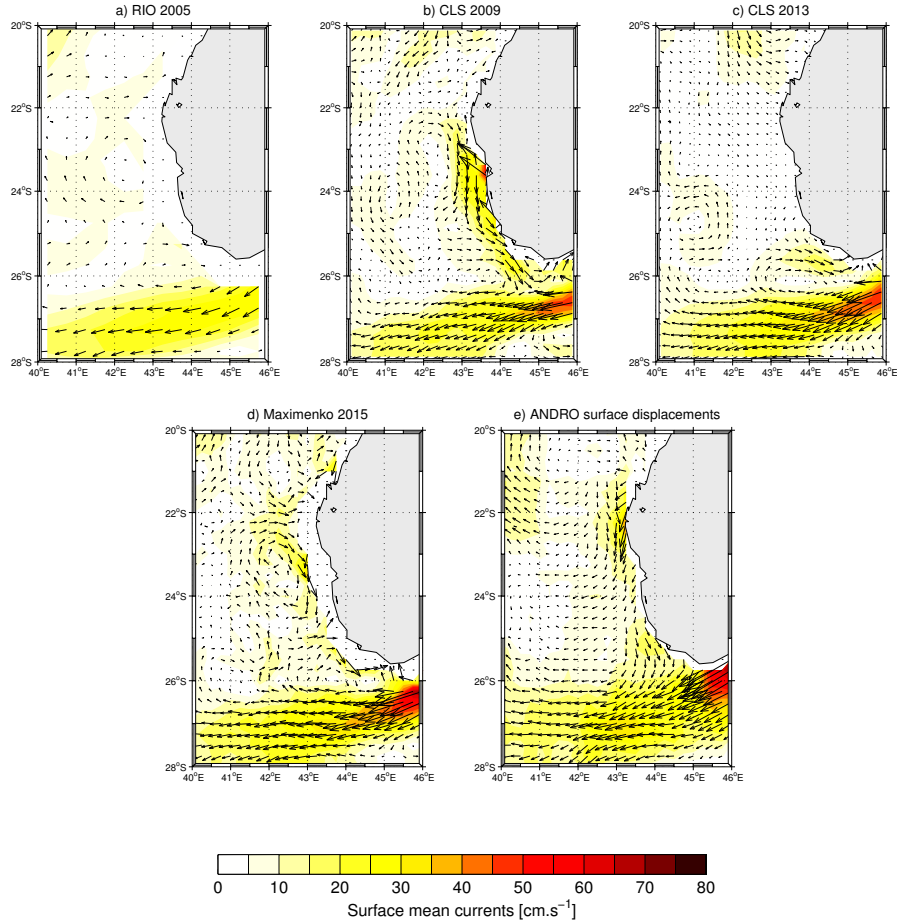


Figure 2.16 – Mean geostrophic currents derived from different mean dynamic topographies: RIO-2005, CLS-2009, CLS-2013, from a global drifter climatology, and from ARGO floats surface displacement. From **Ramanantsoa *et al.* (2018)**.

2018).

The variability of currents can be evaluated by computing the eddy kinetic energy (EKE) or the free surface variability η'^2 . An example is shown in Fig. 2.17 for the Gulf Stream. Observations from AVISO or from surface drifters can be used. The former has the disadvantage of being much smoother in time and space than the model data, such that it is necessary to smooth the model outputs to make for a valid comparison.

The satellite and drifters data are available only at the surface of the ocean and cannot be used to measure the interior turbulence. But another measure can be given by the Eddy Available Potential Energy (EAPE), which measures the available potential energy associated with the turbulent part of the currents (Roullet *et al.*, 2014). Global EAPE maps have been computed from the Argo floats dataset by Roullet *et al.* (2014) to provide ocean modelers with a reference product to assess the energetics of numerical simulations in the ocean's interior. An example of comparison is shown in Fig. 2.18.

2.2.2 Dynamical budgets

A significant part of my work over the last few years has been dedicated to develop tools (in Python/-Fortran) and implement online diagnostics in the ROMS/CROCO code to be able to close offline and

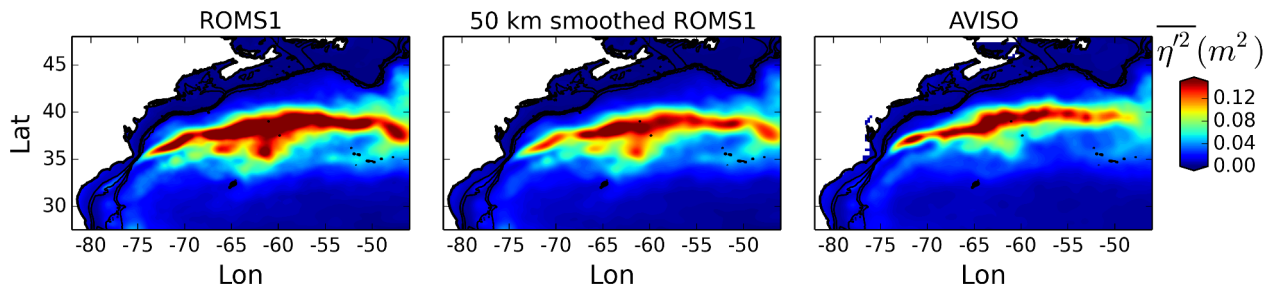


Figure 2.17 – Free surface variability $\overline{\eta^2}$ (in m^2) for (a) ROMS1 ($\Delta x \approx 2.5$ km, averaged over 18 years), (b) ROMS1 smoothed using a 50 km halfwidth gaussian, and (c) observations from AVISO.

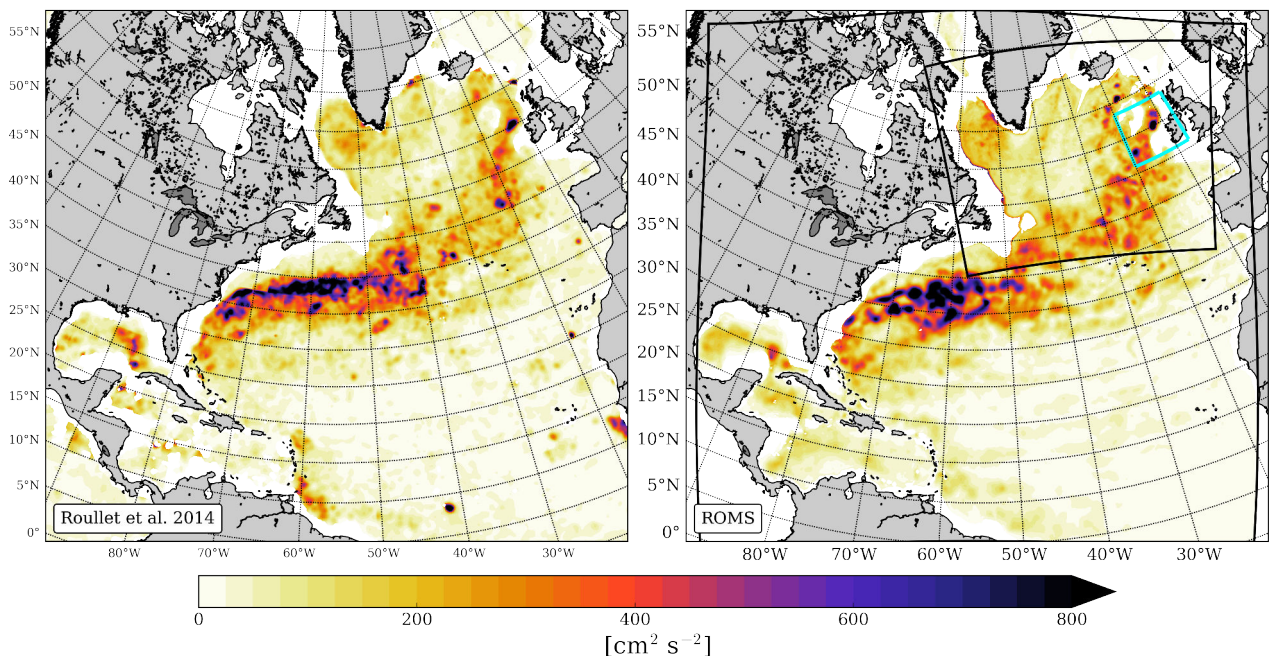


Figure 2.18 – Eady Available Potential Energy (EAPE) at 1000-m computed from Argo data (left) and from the CROCO simulations (right). From **Le Corre et al. (2019b)**.

online budgets of various dynamical quantities. These include momentum, tracers, kinetic energy, barotropic vorticity and potential vorticity (PV).

2.2.2.1 Momentum balance

The horizontal momentum equations in the Boussinesq approximation are:

$$\frac{\partial u}{\partial t} = -u_j \frac{\partial u}{\partial x_j} - w \frac{\partial u}{\partial z} + fv - \frac{P_x}{\rho_0} + \mathcal{V}_u + \mathcal{D}_u + \mathcal{S}_u + \mathcal{B}_u \quad (2.1)$$

$$\underbrace{\frac{\partial v}{\partial t}}_{rate} = \underbrace{-u_j \frac{\partial v}{\partial x_j}}_{hadv} - \underbrace{w \frac{\partial v}{\partial z}}_{vadv} - \underbrace{fu}_{cor} - \underbrace{\frac{P_y}{\rho_0}}_{Prsgrd} + \underbrace{\mathcal{V}_v}_{vmix} + \underbrace{\mathcal{D}_v}_{hmix} + \underbrace{\mathcal{S}_v}_{nudg} + \underbrace{\mathcal{B}_v}_{baro} \quad (2.2)$$

where Cartesian tensor notation with summation convention has been used for $j = 1, 2$; $\vec{u} = (u, v)$ is the horizontal velocity vector, w is the vertical velocity, f is the Coriolis parameter, P is the pressure anomaly, $\vec{\mathcal{V}} = (\mathcal{V}_u, \mathcal{V}_v) = \frac{\partial}{\partial z} (K_M v \frac{\partial \vec{u}}{\partial z})$ is the vertical mixing, $\vec{\mathcal{D}} = (\mathcal{D}_u, \mathcal{D}_v)$ the horizontal diffusion, $\vec{\mathcal{B}} = (\mathcal{B}_u, \mathcal{B}_v)$ the term due to barotropic/baroclinic coupling, and $\vec{\mathcal{S}} = (\mathcal{S}_u, \mathcal{S}_v)$ other sources and sinks (due to restoring, nudging, boundary conditions, etc.). Diagnostics of the momentum tendency terms in ROMS were already implemented and I have contributed to update them to follow the latest code developments in the last few years.

2.2.2.2 Kinetic energy equation

The kinetic energy equation is formed by taking the inner product of the horizontal velocities with the momentum equations:

$$\frac{1}{2} \frac{\partial u_i^2}{\partial t} + u_j \frac{\partial \frac{1}{2} u_i^2}{\partial x_j} + w \frac{\partial \frac{1}{2} u_i^2}{\partial z} = -\frac{u_i}{\rho_0} \frac{\partial P}{\partial x_i} + \mathcal{V}_i u_i + \mathcal{D}_i u_i + \mathcal{S}_i u_i \quad (2.3)$$

where Cartesian tensor notation with summation convention has been used, $i = 1, 2$, $j = 1, 2$; u_i are the horizontal components of the velocity vector u_j ; $u_3 = w$ is the vertical velocity.

I have implemented online diagnostics of kinetic energy tendency terms in ROMS/CROCO which are closed up to machine precision. Examples of kinetic energy budget with ROMS using these diagnostics can be found in **Gula et al. (2016b)**.

2.2.3 Pyticles

Pyticles is a Python/Fortran hybrid parallelized code for 3D advection of Lagrangian particles. It advects particles offline, using high-resolution ocean models data. It has been designed for sigma models (ROMS/CROCO) and optimised for very large grids.

A patch of particles is initialized in the model coordinates system (xu, yv, σ) , where xu and yv are coordinates on u- and v-grid respectively. Each particle is described by its position (xp, yp, zp) at a given time t (Figure 2.19 shows the coordinate system). The 3D velocity field is extracted from simulation outputs with a given frequency (the higher the better) and is linearly interpolated in time between two outputs with a higher frequency.

The default timestepping is a 4th order Runge-Kutta (RK4) scheme. Although more expensive than Adams methods (same family of predictor-corrector algorithms) of comparable order, Runge-

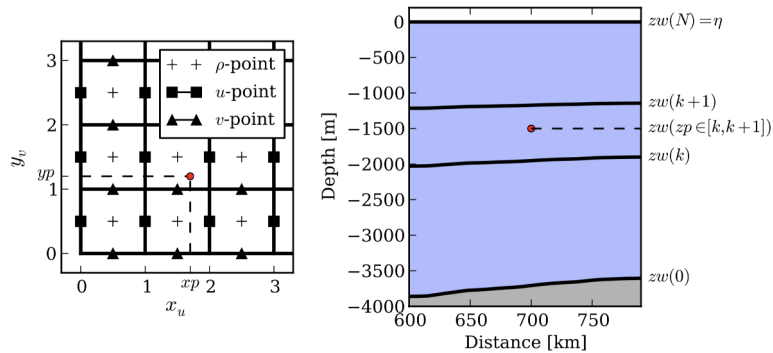


Figure 2.19 – Particle (left) horizontal and (right) vertical coordinates (x_p , y_p , z_p). The red point represents a particle. x_p coordinate is on the u-grid, y_p coordinate is on the v-grid (horizontal C-grid) and z_p coordinate is on the w-levels. Figure from C. Vic.

Kutta methods are more stable and accurate. As advection of particles requires both stability and accuracy (at the expense of higher computational cost), RK4 method is particularly well suited. Several interpolation schemes are implemented (linear, cubic, spline, WENO) for the interpolation of the velocity field at each particle location. The default is linear, as higher order interpolations do not provide significant changes in all tested situations.

The code has been cleaned up and adapted to Python 3 in 2019 by Jeremy Collin. It is available on GitHub: <https://github.com/Mesharou/Pyicles>. The code has been used in **Gula et al. (2014)**; **Vic et al. (2015)**; **Gula et al. (2016a)**; **Klymak et al. (2016)**; **Ramanantsoa et al. (2017, 2018)**; **Vic et al. (2018)**; **Gula et al. (2019)**.

2.3 Effects of topography and eddies on the large scale circulation

2.3.1 From the idealized gyre to the real ocean

The wind-driven circulation in a subtropical gyre has been originally described by Stommel (1948) for a barotropic gyre in a rectangular domain with a flat bottom. In this case, we can write a linear vorticity balance for the flow in a permanent regime as:

$$0 = \beta V + \vec{k} \cdot \vec{\nabla} \times \frac{\vec{\tau}^{wind}}{\rho_0} - \vec{k} \cdot \vec{\nabla} \times \frac{\vec{\tau}^{bot}}{\rho_0} \quad (2.4)$$

with V the meridional velocity, the Coriolis parameter $f = f_0 + \beta y$, $\vec{\tau}^{wind}$ the wind forcing and $\vec{\tau}^{bot}$ the bottom drag (a linear drag $\vec{\tau}^{bot} = -R\vec{u}$ in the case of Stommel (1948)). This leads to the circulations in Fig. 2.20 for an anticyclonic wind forcing corresponding to the subtropical oceanic gyres for cases with or without the β -effect.

The β -effect explains the formation of an intensified western boundary current (WBC). Over most of the gyre, the first order balance is between the wind curl and the βV term, *i.e.*, the anticyclonic wind drives a southward circulation, this is the **Sverdrup balance**. However the gyre circulation needs to be closed at the western boundary. This is possible through the formation of an intense northward current in which the dissipative term becomes strong enough to balance the northward βV .

A finer description of the wind-driven circulation has been derived by Munk (1950), who considered the more general case of a baroclinic ocean with surface intensified currents vanishing at depths. The main balance for the barotropic (depth-integrated) vorticity is similar to equation 2.5, except that the bottom drag disappears due to the absence of bottom currents, and is replaced by a horizontal eddy viscosity acting at the western boundary.

For a vertically stratified ocean, we can define the barotropic vorticity as the vorticity of the vertically integrated velocities:

$$\omega_{\Sigma} = \frac{\partial \bar{v}}{\partial x} - \frac{\partial \bar{u}}{\partial y}$$

where (u, v) are the (x, y) components of the horizontal flow. The overbar denotes a vertically inte-

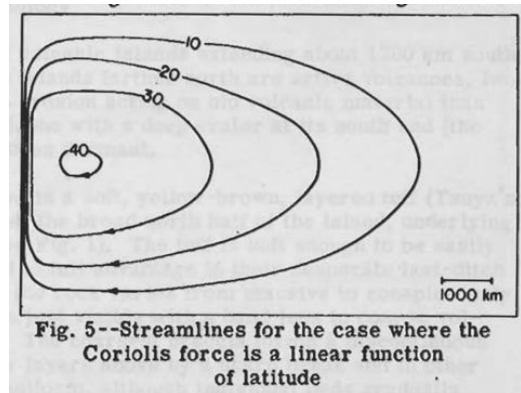
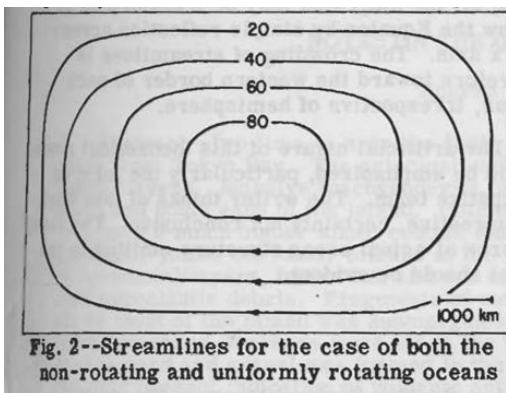


Figure 2.20 – Wind driven circulation in a barotropic rectangular ocean with or without the β -effect. Figures from Stommel (1948).

grated quantity, and is defined as

$$\bar{u} = \int_{-h}^{\zeta} u \, dz$$

where $\zeta(x, y, t)$ is the free-surface height, $h(x, y) > 0$ the depth of the topography and $H(i, j, t) = \int_{-h}^{\zeta} dz = \zeta(i, j, t) + h(i, j)$ is the total depth of the water column. Note that the barotropic vorticity is not exactly identical to the vertically integrated vorticity.

The barotropic vorticity equation can then be derived in general for a primitive equations model by integrating the momentum equations in the vertical and cross differentiating them:

$$\begin{aligned} \underbrace{\frac{\partial \omega_{\Sigma}}{\partial t}}_{\text{rate}} &= - \underbrace{\vec{\nabla} \cdot (f \vec{u})}_{\text{planet. vort.}} + \underbrace{\frac{\mathbf{J}(P_b, h)}{\rho_0}}_{\text{bot. pres. torque}} + \underbrace{\vec{k} \cdot \vec{\nabla} \times \frac{\vec{\tau}^{\text{wind}}}{\rho_0}}_{\text{wind curl}} - \underbrace{\vec{k} \cdot \vec{\nabla} \times \frac{\vec{\tau}^{\text{bot}}}{\rho_0}}_{\text{bot. drag curl}} \\ &+ \underbrace{\mathcal{D}_{\Sigma}}_{\text{horiz. dissip.}} - \underbrace{A_{\Sigma}}_{\text{NL adv terms}}, \end{aligned} \quad (2.5)$$

where \mathcal{D}_{Σ} is the term due to the horizontal diffusion in the model (implicit and/or explicit).

The main additions compared to the balance of Stommel (1948) will be the curl of the **nonlinear advection** terms:

$$A_{\Sigma} = \frac{\partial^2(v\bar{v} - \bar{u}\bar{u})}{\partial xy} + \frac{\partial^2\bar{u}\bar{v}}{\partial xx} - \frac{\partial^2\bar{u}\bar{v}}{\partial yy},$$

and the **bottom pressure torque** $\mathbf{J}(P_b, h)$, which arises from the variation of bottom pressure along isobaths. It derives from the twisting of the force that the bottom topography exerts on the ocean. The bottom pressure torque is closely related to the bottom vortex stretching term (*e.g.*, Zhang & Vallis 2007). It is possible to write the relation $-f\vec{u}_b \cdot \vec{\nabla} h = \frac{\mathbf{J}(P_b, h)}{\rho_0}$ for an idealized linear case of a current in geostrophic balance with a free slip condition at the bottom. Given the kinematic condition at the bottom $\omega_b = -\vec{u}_b \cdot \vec{\nabla} h$, the bottom pressure torque could then be written $\frac{\mathbf{J}(P_b, h)}{\rho_0} = -f\omega_b$, that is the bottom vortex stretching.

The barotropic vorticity balance for a low resolution rectangular gyre with a flat bottom using CROCO (Fig. 2.21) is shown in Fig. 2.22 for the full gyre and the WBC. This highlights a Sverdrup balance in the interior of the gyres and a viscous balance for the WBC as predicted by Stommel (1948) and Munk (1950).

The results are slightly modified for the WBC when the resolution is increased and the viscosity decreased (Fig. 2.23). The viscous term (now implicit) is very high but only over a very narrow region close to the boundary and the nonlinear term is positive over the extent of the WBC to locally balances the northward βV .

This view of the dynamical balance for the gyre, however, does not take into account an important aspect of the ocean. The fact that **the bottom of the ocean is not flat** and that the boundaries are not vertical walls. When the bottom topography is taken into account, the dynamical balance changes drastically over the western boundary (Fig. 2.24) and one term becomes dominant: the **bottom pressure torque**.

The **bottom pressure torque** (BPT) represents the contribution of the topography to the

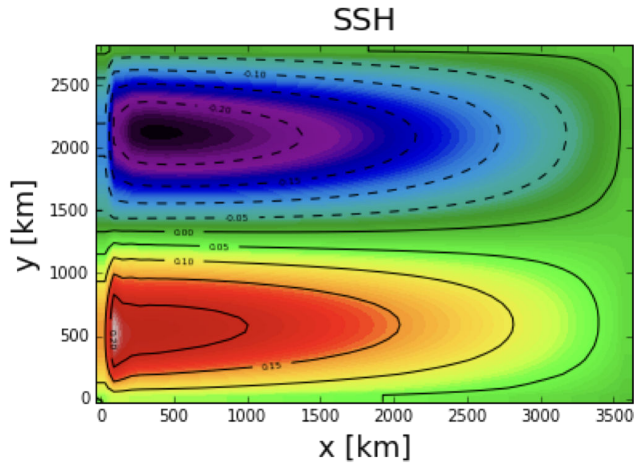


Figure 2.21 – Mean streamfunction for an idealized double gyre model

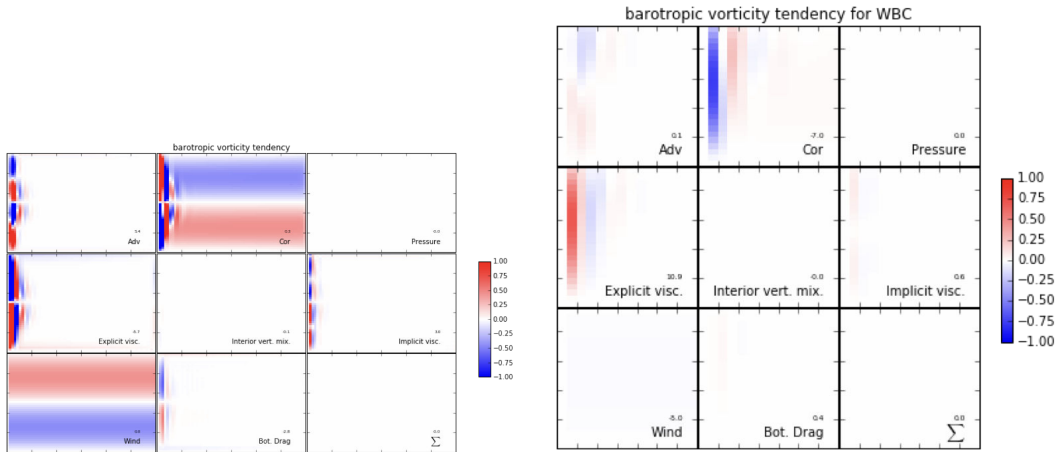


Figure 2.22 – (left) Barotropic vorticity balance for an idealized double gyre model, and (right) zoomed view of the western boundary current.

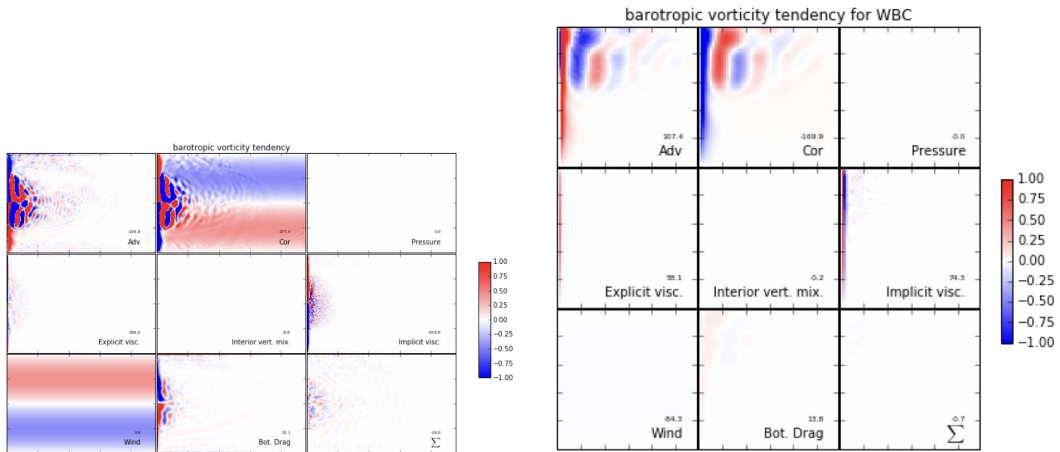


Figure 2.23 – Barotropic vorticity balance for an idealized double gyre model with higher resolution and less viscosity (left) and zoomed view over the western boundary current (right).

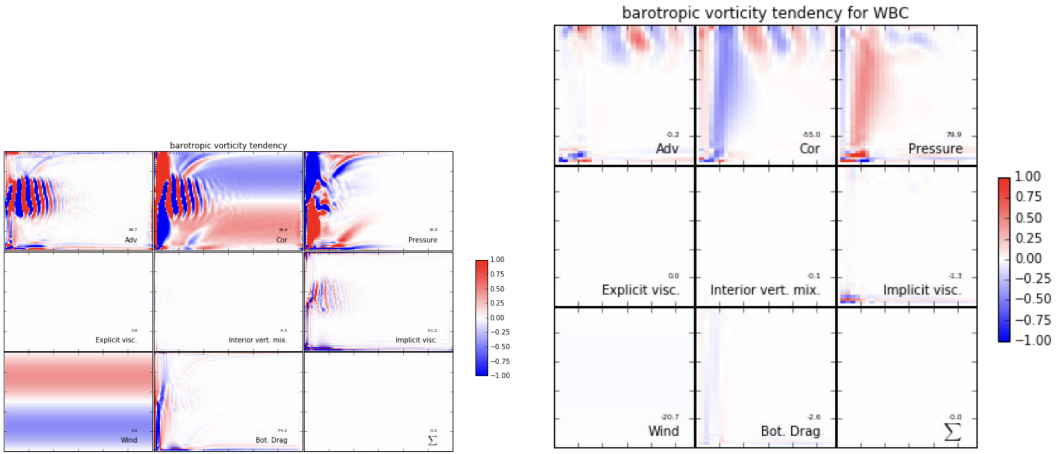


Figure 2.24 – Barotropic vorticity balance for an idealized double gyre model with a large scale zonal topographic slope (left) and zoomed view over the western boundary current (right).

barotropic vorticity evolution of the flow. Hughes (2000), Hughes & De Cuevas (2001) and Jackson *et al.* (2006) have shown by using theoretical arguments, numerical results for an idealized gyre simulation, and realistic simulations from a large scale global model that western boundary currents do not imply a viscous balance against the seaboard, but a nearly inviscid one. The bottom pressure torque is the term locally enabling the return flow of the wind-driven transport in western boundary currents and providing most of the overall positive input of vorticity balancing the negative input by anticyclonic wind curl on the scale of the gyre.

We will see in the next subsections how this holds for realistic subtropical and subpolar gyres.

2.3.2 Barotropic vorticity balance in the North-Atlantic subtropical gyre

Analysis of the mean dynamical balances in the Gulf Stream have been described in Gula et al. (2015a) and Schoonover et al. (2016). We present some aspects showing the impact of topography on the large-scale circulation in this subsection.

Terms of the barotropic vorticity balance for the subpolar gyre in a realistic Atlantic simulation (ROMS with $\delta x = 6$ km) are shown in Fig. 2.25. The wind stress curl $\vec{k} \cdot \vec{\nabla} \times \frac{\tau_{wind}}{\rho_0}$ amplitude is small compared to the other terms over this region (notice the different colorscale). It is however a first-order term when integrated over the whole gyre (Fig. 2.26). We can see that the pattern of the real wind is slightly more complicated (Fig. 2.25) than in the idealized case due to the geometry of the basin. It is however still mostly negative everywhere, except for a positive ribbon following the path of the Gulf Stream.

The BPT and nonlinear terms have the largest amplitudes and strongly reflects the regional topography. But they tend to cancel each other with large positive-negative signals around small-scale topography features, which results from the balance between pressure forces and inertia. The sum of the two terms $J(P_b, h)/\rho_0 - A_\Sigma$ is an order of magnitude smaller with most of the intense small scale structures gone.

Fig. 2.26 shows the integrated balance for the gyre enclosed between the $\Psi = 0$ and $\Psi = 30$ streamlines. If we enclose the whole gyre area we can expect the βV term to vanish as the flow going north on the western boundary is going south on the other side of the gyre. The major term for the area is as expected the negative input from the wind which is driving the anticyclonic gyre. The

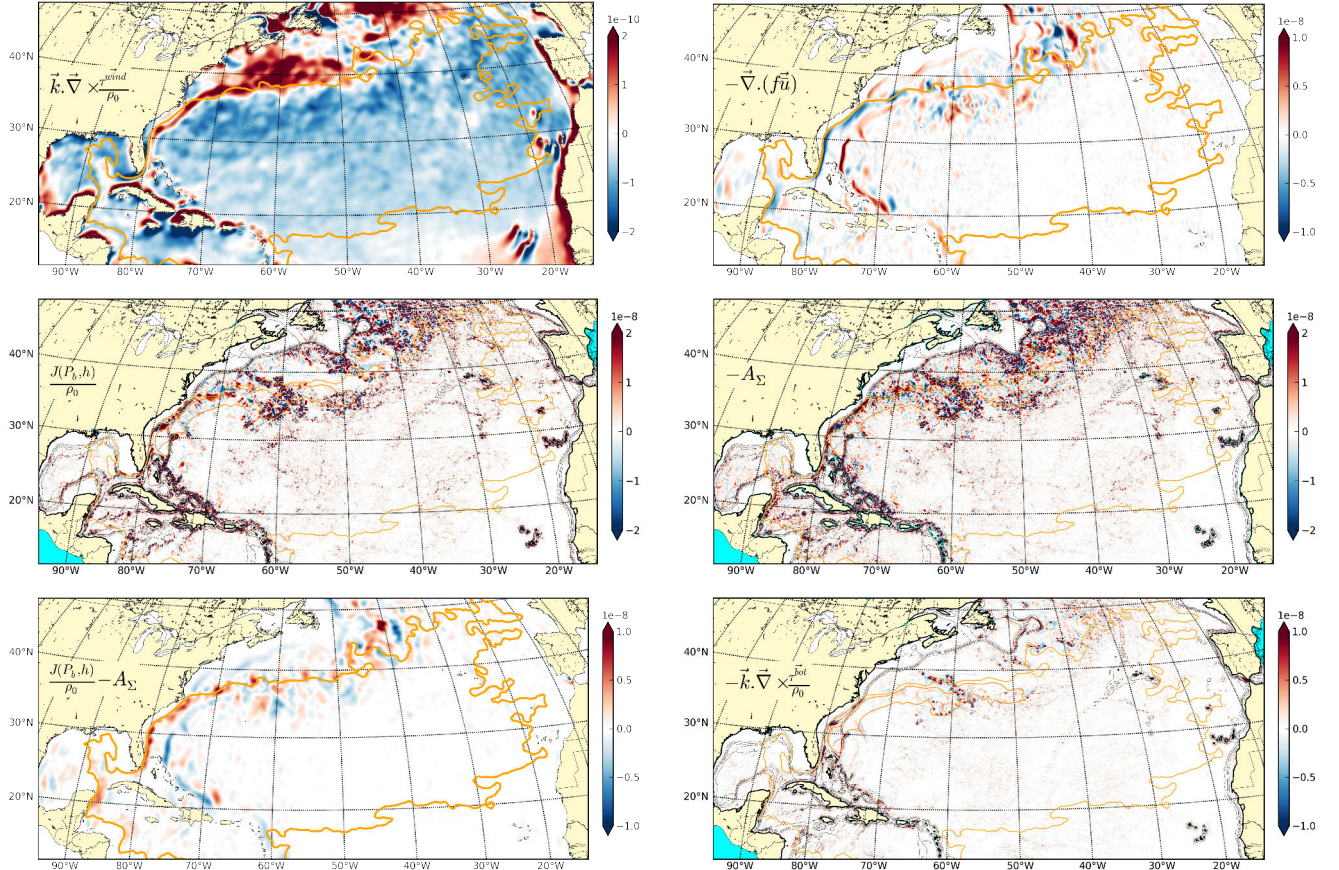


Figure 2.25 – Time-mean of the different terms in the barotropic vorticity balance equation; (a) wind curl $\vec{k} \cdot \vec{\nabla} \times \frac{\vec{r}^{wind}}{\rho_0}$, (b) meridional transport βV , (c) bottom pressure torque $J(P_b, h)/\rho_0$, (d) non-linear advective terms in the barotropic vorticity balance equation $-A_\Sigma$, (e) $J(P_b, h)/\rho_0 - A_\Sigma$, and (f) bottom drag curl $\vec{k} \cdot \vec{\nabla} \times \frac{\vec{r}^{bot}}{\rho_0}$, Units are $m s^{-2}$. Topography is shown in black contours at 0 m, 200 m, 600 m, 1000 m, and 2000 m isobaths. The two orange contours show the barotropic streamfunction at 1 Sv and 30 Sv, which are used to define the gyre and the Gulf Stream.

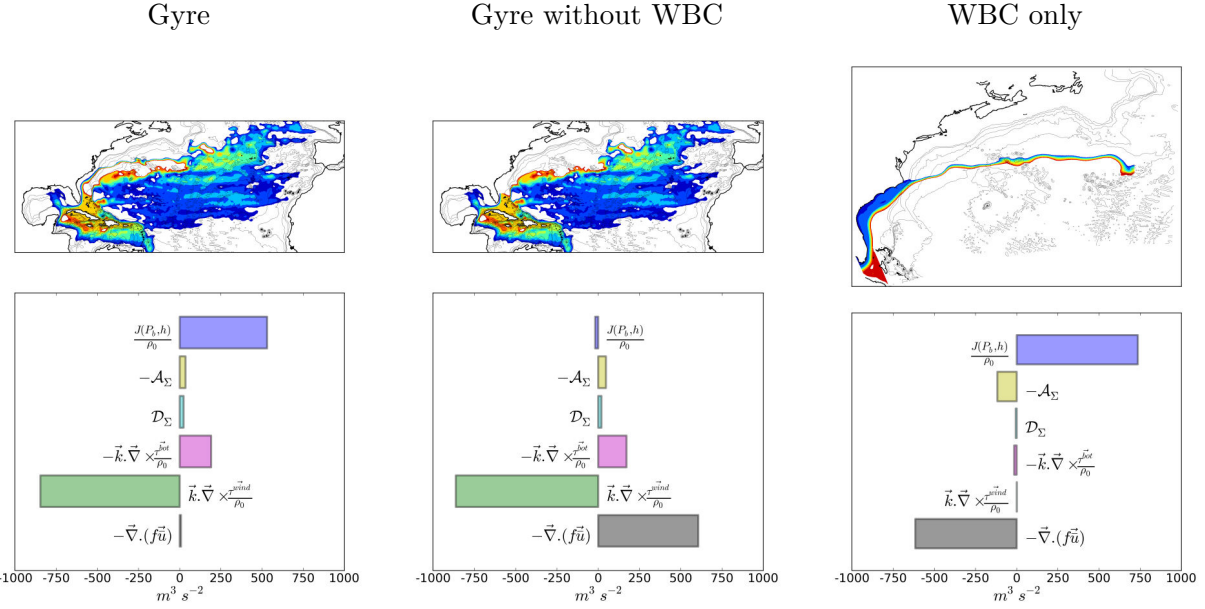


Figure 2.26 – Time mean (3 years) of spatial integral of vorticity balance equation terms over the North Atlantic gyre enclosed between the $\Psi = 0$ and $\Psi = 30$ streamlines (left) and the same area with the Gulf Stream removed (right) for the ATLBIG simulation (6km). Corresponding areas are shaded on the bottom panels. Unit is $m^3 s^{-2}$.

positive contributions from the BPT is the major term balancing the wind input. The bottom drag is also a significant sink of negative vorticity, especially due to the presence of the strong recirculation gyre just south of the Gulf Stream.

We can verify that the balance for the same area with the Gulf Stream path removed, as shown in the middle panel of Fig. 2.26, illustrates the classical Sverdrup balance where the negative input of the wind stress is balanced mainly by the meridional transport of water. Evaluation of the Sverdrup Balance using satellite observations and ARGO floats velocity measurements also shows that it is valid for the gyre interior (Gray & Riser, 2014).

The balance for the Gulf Stream path only is shown in the right panel of Fig. 2.26. The Gulf Stream is defined here as the area enclosed between the $\Psi = 1$ and $\Psi = 30$ streamlines, north of 28°N and west of 74°W. The balance over the Gulf Stream path is almost exclusively between βV and the BPT.

The validity of these results have been tested using numerical simulations conducted across different model platforms (ROMS, MITgcm, and POP) and with different resolutions (from 1.5 km to 2°) in **Schoonover et al. (2016)**. One aim was to try to relate differences in the barotropic vorticity balance across models with the different behaviors observed for the Gulf Stream separation. The barotropic vorticity diagnostics have confirmed that the subtropical gyre is characterized by an inviscid balance primarily between the applied wind stress curl and BPT. In the area-integrated budget over the Gulf Stream, the northward return flow is balanced by BPT in all models (Fig. 2.27). The integrated budgets are consistent across model platforms and resolution, suggesting that these balances are robust. Two of the simulations, at 100- and 10-km resolutions, produce a more northerly separating Gulf Stream but obtain the correct integrated vorticity balances. In these simulations, the viscous effects are nonnegligible on smaller scales, indicating that the separation is linked to the details of the local dynamics. These results are shown to be consistent with a scale analysis argument that suggests

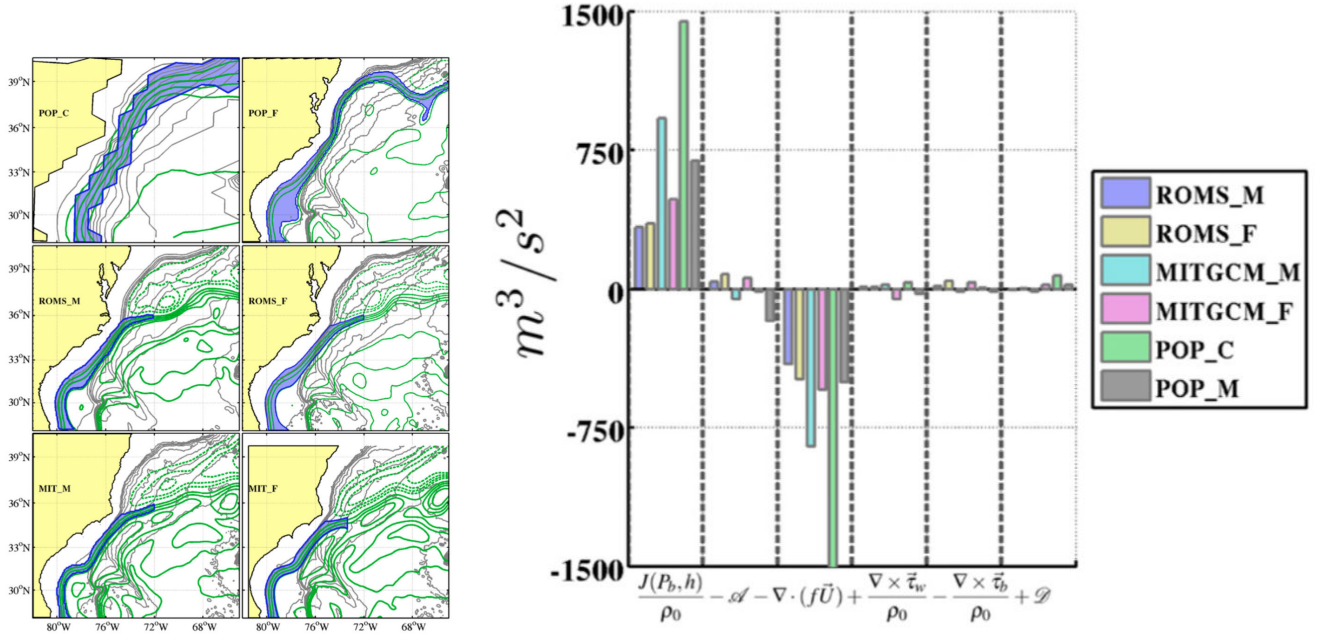


Figure 2.27 – The time-averaged and Gulf Stream-integrated barotropic vorticity budget for each model simulation using the Gulf Stream regions depicted on the left. Although the magnitude of each of the terms varies between simulations, the relative contribution of each term within a given simulation is similar. Figures From **Schoonover et al. (2016)**.

that the biharmonic viscous torque in particular is upsetting the inviscid balance in simulations with a more northerly separation. In addition to providing evidence for locally controlled inviscid separation, these results provide motivation to revisit the formulation of subgrid-scale parameterizations in general circulation models.

2.3.3 Eddy effects on the mean Gulf Stream

We show in Fig 2.28 the barotropic streamfunction for nested simulations with increasing resolution (ROMS0 = 6 km, ROMS1 = 2.5 km and ROMS2 = 1.5 km). The increase in resolution causes an increase in the barotropic transport of the Gulf Stream after separation due to intensified inertial recirculation gyres north and south of the Gulf Stream.

The barotropic vorticity balances for the two recirculation gyres north and south of the Gulf Stream in the 2.5 km simulation is shown in Fig. 2.29. The bottom drag is the main sink of vorticity for both gyres, this term being positive for the anticyclonic gyre and negative for the cyclonic one. The northern cyclonic gyre is driven mostly by advective fluxes, with a smaller contribution from the wind, which has a positive curl locally along the Gulf Stream path (see Fig. 2.25). The southern anticyclonic gyre is also driven by the wind and the advective fluxes, which are both negative. The BPT contribution is more difficult to interpret as it is negative for both gyres, which would make it a sink of vorticity in the northern gyre but surprisingly a source in the southern one. However this negative contribution of the BPT in the southern gyre is due to the presence of the deep return current flowing along topography westward and southward, penetrating the gyre contour at Cape Hatteras and then flowing along the Blake ridge with intense negative BPT.

Note that the positive input from the wind stress curl in the northern gyre may be too strong due to the fact that the Gulf Stream path in the simulation is a little more south than the observed Gulf

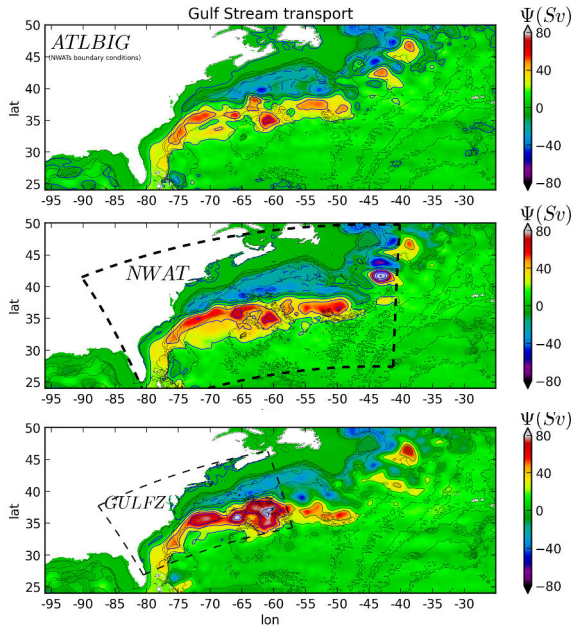


Figure 2.28 – Mean Gulf Stream transport (in Sv) for simulations with increasing resolution (from top to bottom).

Stream path (as seen from the difference between the positive wind curl ribbon in Fig. 2.25 and the streamfunction contours). This effect might even amplify this shift as there is a positive retroaction between a southern displacement of the Gulf Stream path, which will increase the positive input of vorticity in the northern recirculation gyre, reinforce it and act to displace the Gulf Stream path even further south. This defect should be addressed by using surface forcings computed from a bulk formula based on wind and current velocities rather than observed wind stress.

2.3.4 Barotropic vorticity balance in the North-Atlantic subpolar gyre

The analysis of the dynamics of the North-Atlantic subpolar gyre is part of Mathieu Le Corre's PhD, whom I supervise since 2016 with Anne-Marie Treguier, and who will defend his PhD in January 2020. I present below some results showing the impact of topography and eddies on the large-scale circulation which are have been submitted in Le Corre et al. (2019c).

Modeling the circulation of the North Atlantic Subpolar Gyre (SPG) is a challenging task. The currents are strongly influenced by the topography and the eddies. Eddy-permitting resolutions have been shown to improve the characteristics of the boundary currents of the SPG, including a better position of the currents, and narrower lateral extensions and velocity amplitudes closer to observations (Treguier *et al.*, 2005; Marzocchi *et al.*, 2015).

The strong barotropic component of the currents leads to strong interactions with the topography, which in turns have an impact on the structure of the SPG (Aken, 1995; Daniault *et al.*, 2011; Fischer *et al.*, 2004). This idea emerged quite early with Luyten *et al.* (1985); Wunsch & Roemmich (1985), who pointed out a failure of the Sverdrup balance in the SPG and put forward the importance of the bottom topography in driving the SPG dynamics. The prevalence of the BPT in the SPG has also been demonstrated by Hughes & De Cuevas (2001); Spence *et al.* (2012); Yeager (2015). More recently, Sonnewald *et al.* (2019) clustered regions dominated by different barotropic vorticity balances using a global $1^\circ \times 1^\circ$ model. They retrieved the results of a SPG dominated by BPT effects, but also a part of the gyre dominated by Non-Linear (NL) effects, despite the relatively coarse resolution of the model. Wang *et al.* (2017) showed the importance of the NL term in driving the dynamics in the

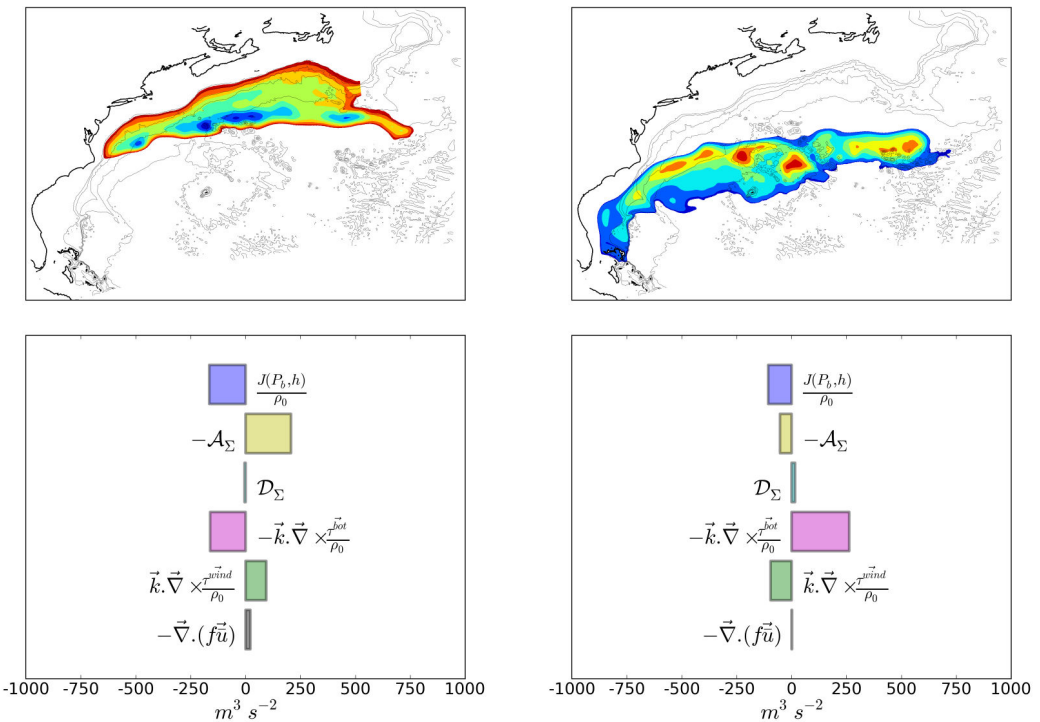


Figure 2.29 – Time mean (18 years) of spatial integral of vorticity balance equation terms over the north cyclonic recirculation gyre (left) and the south anticyclonic recirculation gyre (right) for the NWAT simulation (2.5 km). Both areas are defined using the largest possible closed contour of the barotropic streamfunction. Corresponding areas are shaded on the bottom panels. Unit is $m^3 s^{-2}$.

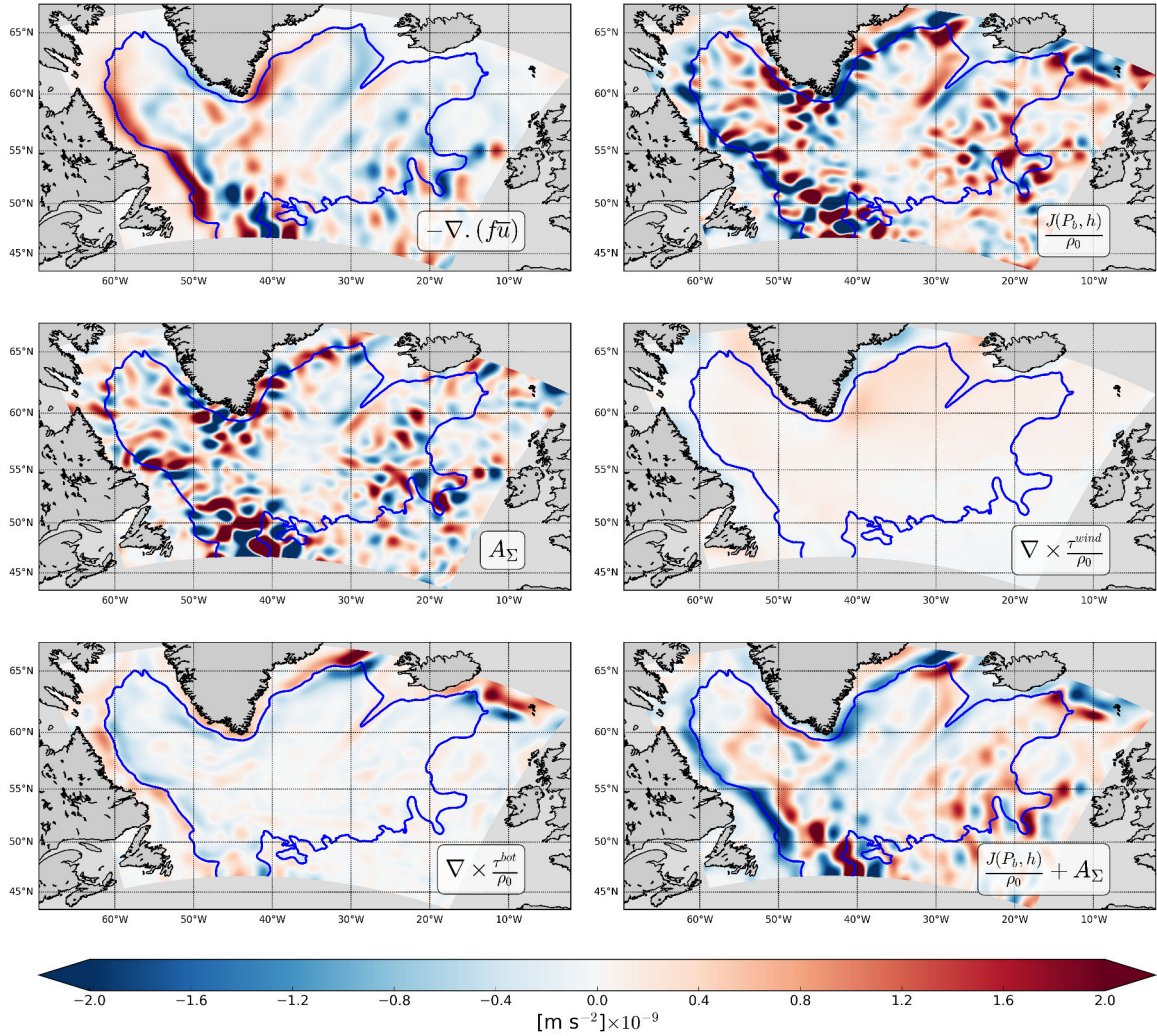


Figure 2.30 – Mean barotropic vorticity terms in the North Atlantic subpolar gyre horizontally smoothed with a kernel of 1° radius. Blue contour represents the limit of our boundary area and is the -3 Sv barotropic streamline. From Le Corre *et al.* (2019c).

North Western Corner (NWC) and around the Labrador Sea.

We recover the importance of BPT and non-linear terms from a ROMS 2-km simulation of the subpolar gyre (Fig. 2.30). We also performed integrations of the terms inside two different contours: one corresponding to the whole SPG and the -3 Sv contours defined by the barotropic streamfunction (fig 2.31). We can check that the term βV integrates to zero as we choose closed contours. The larger contour tends to overlap the upper slope and the shelf (especially along West Greenland and East Canada) while the -3 Sv contour does not include the shelves. The main balance between the integrated terms is quite different depending of the chosen contour.

When integrated inside the -3 Sv contour (which means excluding the shelf area, Fig. 2.31c), the main sources for the cyclonic circulation of the gyre are the wind and the BPT. They are balanced by the bottom drag curl (BDC). The input of the wind does not contribute much locally, but becomes significant when spatially integrated over the gyre. The BPT is the major source of positive vorticity and helps the flow moves cyclonically around the gyre. The major sinks of vorticity are the NLA and the BDC. The BDC is very intense where the flow is close to a steep topography, as in the case of the Western Labrador Sea Current (WLSC) and the Western Greenland Current, but also near the CGFZ.

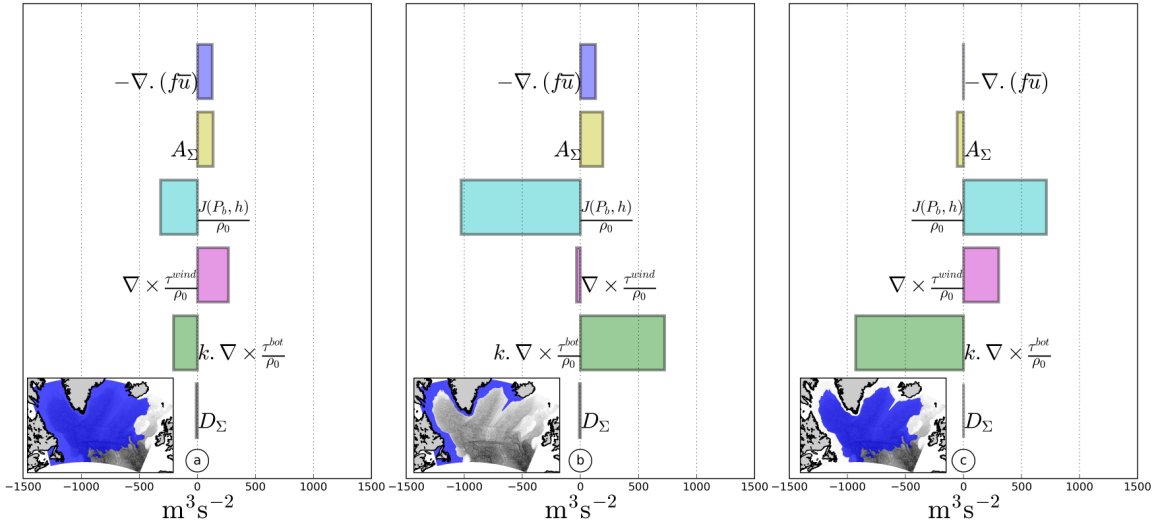


Figure 2.31 – Integration of the barotropic vorticity terms over the full domain (a), the shelf region only (b) and over the gyre interior (right). The limit between the shelf and the gyre is defined as the -3 Sv contour. From **Le Corre et al. (2019c)**.

When integrated on the whole gyre (Fig. 2.31a), the balance is slightly different. The wind is still a major contributor for the cyclonic circulation and the BDC still represents the major sink of vorticity. However, the NL term replaces the BPT as a source of cyclonic vorticity for the gyre. In this interpretation, both the wind and the NL term forces the gyre cyclonically, while the drag balances this input along steep topography.

The difference between the two balances is highlighted by looking at the balance in the region in-between the two contours, which covers the upper slope and the shelf. It corresponds to a balance between BPT, NLA and bottom drag. This balance is close to the one described in Csanady (1997) and evokes a buoyancy driven flow in this area.

It is clear from the patterns of the different terms of the barotropic vorticity balance that the local balances over the boundary currents are very different than what is happening in the interior of the gyre. The classical picture of a gyre interior in a quasi-Sverdrup balance that applies in the subtropical gyre, does not apply here.

To better understand what drives the interior of the subpolar gyre, we further divide the domain into an inner part and a boundary part, as represented in fig. 2.32. The two domains are defined using the -3 Sv line as previously, and the 3000 m isobath. What is between the -3 Sv line and the 3000 m isobath is considered as the boundary zone and the rest is considered as the inner zone. The choice of the 3000 m isobath is purely subjective but the results are not sensitive to the choice of the isobath.

In the boundary zone, the main source of cyclonic vorticity is the BPT. Secondary sources are the curl of the wind and the βV . The negative NL term sign indicates vorticity advection outside of this domain toward the shelf or the inner gyre.

In the inner zone, the NLA term represents the major contribution to the cyclonic circulation. It is balanced by the BDC, the BPT and the βV terms. Contributions from the BDC are of similar magnitude in the inner and boundary zones. The wind input of vorticity is smaller than in the boundary zone, as the major wind source of vorticity is located along the Greenland area (fig 2.30)

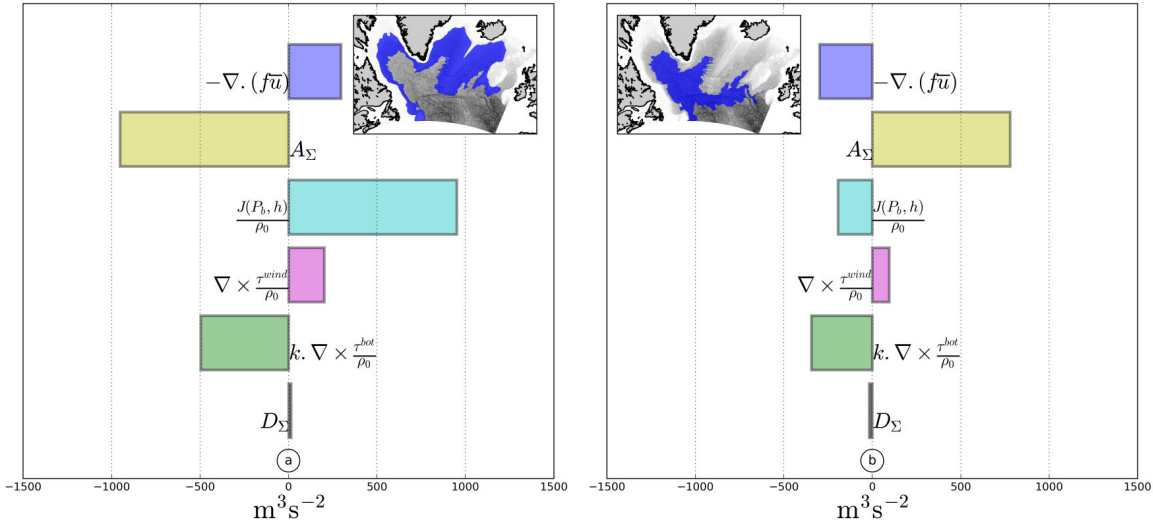


Figure 2.32 – Integration of the barotropic vorticity terms over the gyre separated into a boundary region (left) and a deep inner part (right). The limit between the two regions is defined as the 3000 m isobath. From **Le Corre et al. (2019c)**.

and not uniformly distributed over the gyre. It confirms that the inner part of the gyre is not in Sverdrup balance at the first order, which would imply a dominant balance between a negative βV and a positive input from the curl of the wind stress, but is driven by nonlinear effects.

The nonlinear term is playing a role in providing an input of positive barotropic vorticity from the boundary toward the inside of the gyre (Fig. 2.32). The nonlinear term can be further decomposed into a time-mean and an eddy part, as well as into a barotropic and a baroclinic part. The decompositions show that the major input of barotropic vorticity in the inside of the gyre is due to barotropic eddy activity along the boundary currents around the gyre, preferentially in Eastern Boundary currents. The second source is the North Atlantic Current with a mean baroclinic input of vorticity in the North West Corner.

2.4 Instabilities and formation of mesoscale eddies

2.4.1 Baroclinic and barotropic instabilities

Mesoscale eddies are generated due to instabilities of the large-scale currents (*e.g.*, Drazin & Reid, 1981): **baroclinic and barotropic instabilities**. In this subsection I present some of their basic properties, including the sources of energy for the instabilities, which are a very useful diagnostics that has been used on many occasions in my work (Gula *et al.*, 2009a,b; Gula & Zeitlin, 2010; Gula *et al.*, 2010; Flór *et al.*, 2011; Gula & Zeitlin, 2014; Gula *et al.*, 2014, 2015a, 2016a, 2015b, 2016b; Vic *et al.*, 2015; Krug *et al.*, 2017; Le Corre *et al.*, 2019c; Tedesco *et al.*, 2019; Morvan *et al.*, 2019).

Baroclinic instability is related to a vertical velocity shear in the flow. It has been well studied since the works of Charney (1947) and Eady (1949). An instability criterion is the Charney-Stern criterion, which states that a necessary condition for instability is a change of sign of the potential vorticity horizontal gradient somewhere in the vertical plane.

Baroclinic instability can be interpreted as interactions between Rossby waves (or more generally vortical modes, *i.e.*, modes which exists due to a potential vorticity gradient). The two modes, propagating at different depth are in resonance when they have the same Doppler shifted phase speed and give rise to baroclinic instability, as explained *e.g.* in Hoskins *et al.* (1985). The structure of the unstable mode for baroclinic instability of a two-layer flows in a rotating annulus is shown in figure 2.33 (Gula *et al.*, 2009b; Gula & Zeitlin, 2014).

Barotropic instability is related to a horizontal velocity shear in the flow. The Rayleigh-Kuo criterion for instability (Kuo, 1949), which is a generalisation of the Rayleigh criterion (Rayleigh, 1880) for rotating non-divergent flows, states that the absolute vorticity horizontal gradient must change sign somewhere in the horizontal plane. This condition has then been reinforced by Fjørtoft (1950) to give the Rayleigh-Fjørtoft necessary condition for instability.

Barotropic instability can also be interpreted as interactions between vortical modes, but now in the horizontal plane. Resonance between modes is made possible by the presence of a horizontal velocity shear. An example of barotropic instability for a configuration corresponding to a horizontally sheared coastal current is shown in figure 2.34 (Gula & Zeitlin, 2010).

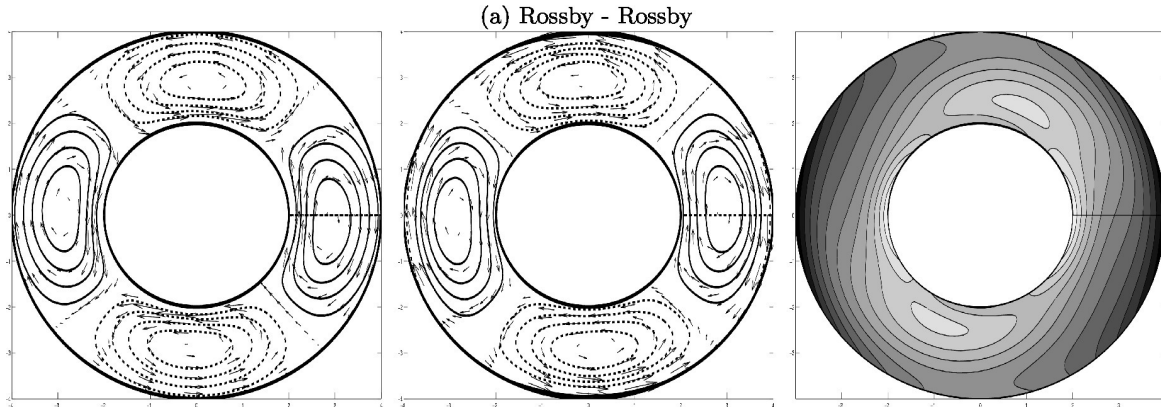


Figure 2.33 – Pressure and velocity fields in the upper (left) and in the lower layer (middle), and interface height (right) of the baroclinically unstable Rossby-Rossby mode at $k = 2$ ($kR_d = 0.9$). From Gula & Zeitlin (2014).

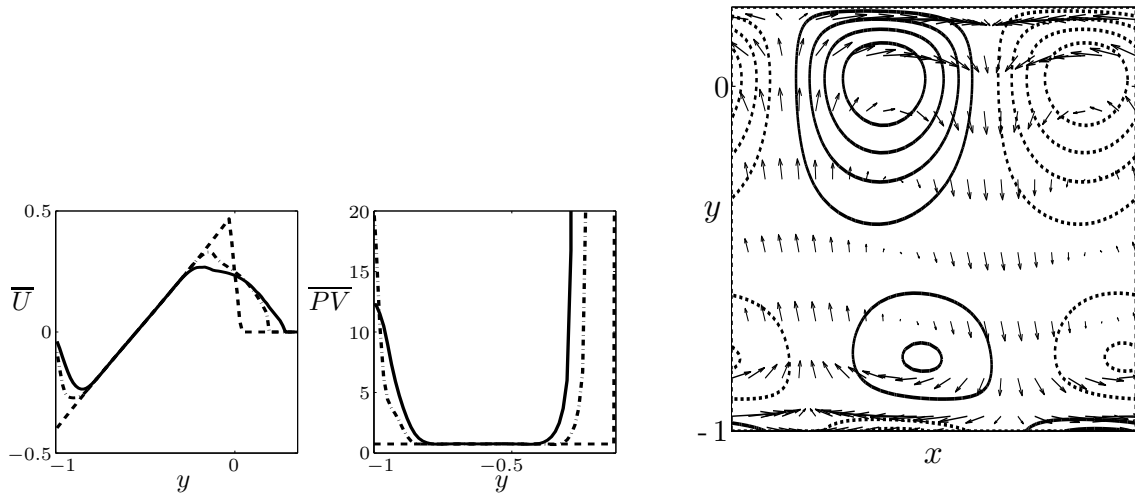


Figure 2.34 – (a) mean zonal velocity and (b) mean zonal PV for a coastal current : Initial state $t = 0$ (dashed line), primary unstable mode saturated at $t = 40$ (dash-dotted line), late stage $t = 300$ (thick line). (bottom) Height and velocity fields of the most unstable mode for the late stage flow. Only one wavelength is plotted. From **Gula & Zeitlin (2010)**.

2.4.1.1 Energy sources for the instabilities

Baroclinic and barotropic instabilities gain their energy from different sources: the barotropic instability from the kinetic energy of the mean flow, and the baroclinic instability from the potential energy of the mean flow. A good way to identify which mechanism is at play in a realistic turbulent flow, where it is usually not possible to perform a simple stability analysis, is to diagnose the energy source for the perturbations (the eddy part).

To quantify their source of energy, we can decompose the kinetic energy equation of the flow into a mean and an eddy part. The mean kinetic energy of the flow $\text{KE} = \frac{1}{2}(\bar{u}^2 + \bar{v}^2)$ is the sum of the kinetic energy of the mean flow, $\text{MKE} = \frac{1}{2}(\bar{u}^2 + \bar{v}^2)$, and the eddy kinetic energy, $\text{EKE} = \frac{1}{2}(u'^2 + v'^2)$, where the overbar denotes a time average, and the prime denotes fluctuations relative to the time average (the eddying motions).

The mean kinetic energy equation (MKE) is formed by taking the inner product of the mean horizontal velocities with the mean terms in the momentum equations,:

$$\bar{u}_i \frac{\partial \bar{u}_i}{\partial t} + \underbrace{\frac{\partial \left(\frac{1}{2} \bar{u}_j \bar{u}_i^2 + \frac{1}{\rho_0} \bar{u}_j \bar{p} \right)}{\partial x_j}}_{\text{Boundary Transport}} = -\bar{u}_i \underbrace{\frac{\partial \bar{u}'_j \bar{u}'_i}{\partial x_j}}_{\text{EKE} \rightarrow \text{MKE}} + \underbrace{\bar{w} \bar{b}}_{\text{MPE} \rightarrow \text{MKE}} + \underbrace{\bar{V}_i \bar{u}_i}_{\text{Vertical mixing}} + \underbrace{\bar{D}_i \bar{u}_i}_{\text{Horizontal diffusion}}, \quad (2.6)$$

where Cartesian tensor notation with summation convention has been used, $i = 1, 2$, $j = 1, 2, 3$; u_i are the horizontal components of the velocity vector u_j ; $u_3 = w$ is the vertical velocity; p is the pressure anomaly; $b = -\frac{g\rho}{\rho_0}$ is the buoyancy anomaly; V_i and D_i are the vertical mixing and horizontal diffusion terms in the horizontal momentum equations.

The eddy kinetic energy equation is formed by subtracting the energy equation of the mean flow

from that of the total flow:

$$\overline{u'_i \frac{\partial u'_i}{\partial t}} + \underbrace{\frac{\partial \left(\frac{1}{2} \overline{u'_j u'_i} + \frac{1}{2} \overline{u'_j u'_i}^2 + \frac{1}{\rho_0} \overline{u'_j p'} \right)}{\partial x_j}}_{\text{Boundary Transport}} = \underbrace{- \overline{u'_j u'_i} \frac{\partial \overline{u_i}}{\partial x_j}}_{\text{MKE} \rightarrow \text{EKE}} + \underbrace{\overline{w' b'}}_{\text{EPE} \rightarrow \text{EKE}} + \underbrace{\overline{V'_i u'_i}}_{\text{Vertical mixing}} + \underbrace{\overline{D'_i u'_i}}_{\text{Horizontal diffusion}} . \quad (2.7)$$

Note in particular the decomposition:

$$\frac{u_i}{\rho_0} \frac{\partial P}{\partial x_i} = \frac{\partial \left(\frac{1}{\rho_0} u_j p \right)}{\partial x_j} + w b$$

with summation convention $i = 1, 2$, $j = 1, 2, 3$; which shows that the contribution of the pressure gradient term can be split into the divergence of an energy flux at the boundaries of the domain volume ($\frac{\partial \left(\frac{1}{\rho_0} u_j p \right)}{\partial x_j}$) and conversion between potential and kinetic energy (wb).

Mechanisms responsible for generation of transient eddies can be identified by looking at the source terms for the eddy kinetic energy (EKE). The conversion between eddy potential and eddy kinetic energy due to a vertical buoyancy flux is $VBF = \overline{w' b'}$. The conversion from mean kinetic energy to eddy kinetic energy can be decomposed into the conversion due to the horizontal Reynolds stress: $HRS = -\overline{u'^2} \frac{\partial \overline{u}}{\partial x} - \overline{u' v'} \frac{\partial \overline{u}}{\partial y} - \overline{v'^2} \frac{\partial \overline{v}}{\partial y} - \overline{u' v'} \frac{\partial \overline{v}}{\partial x}$, and the one due to the vertical Reynolds stress: $VRS = -\overline{u' w'} \frac{\partial \overline{u}}{\partial z} - \overline{v' w'} \frac{\partial \overline{v}}{\partial z}$. Predominance of one of the three source terms indicates that the eddy generation mechanism is primarily: a baroclinic instability ($VBF > 0$), a barotropic instability ($HRS > 0$) or a vertical shear (Kelvin-Helmholtz type) instability ($VRS > 0$).

Note that the mean is usually defined as a time-mean over a period long enough compared to the time scales of the instabilities. However, it is also possible to define the mean state as a spatial average or a mixture of space and time average. To study the instability of a jet over a short period of time, it is possible to define the mean flow using an along-stream average (**Gula et al., 2015b; Tedesco et al., 2019**) instead of the time-mean. Similarly it is possible to define an along-front direction to study the instability of a front or filament (**Gula et al., 2014**), which can be curved or even fully circular to study the instability along the rim of a vortex (**Gula et al., 2016a**). A mixture of time and along-stream average can also be used, as was the case to interpret energy transfers from in-situ gliders data (**Krug et al., 2017**).

2.4.1.2 Application to realistic flows: the Gulf Stream

The energy source terms for baroclinic and baroclinic instability in the Gulf Stream are plotted Fig. 2.35. We see a strong positive signal right after separation of the Stream from the continental slope (east of 76°W), which indicates a region of very strong baroclinic and barotropic conversion. Due to these strong instabilities there is a strong eddy generation which is broadening the flow and weakening the mean cross flow gradients, hence diminishing vorticity on the north side (where vorticity is positive) and increasing vorticity on the south side (where vorticity is negative).

Measurements by Dewar & Bane (1989a) and Dewar & Bane (1989b) also confirm that the effects of the eddy field are significantly different upstream and downstream of Hatteras and that the Gulf Stream is strongly baroclinically unstable downstream of Hatteras while the barotropic shear energy

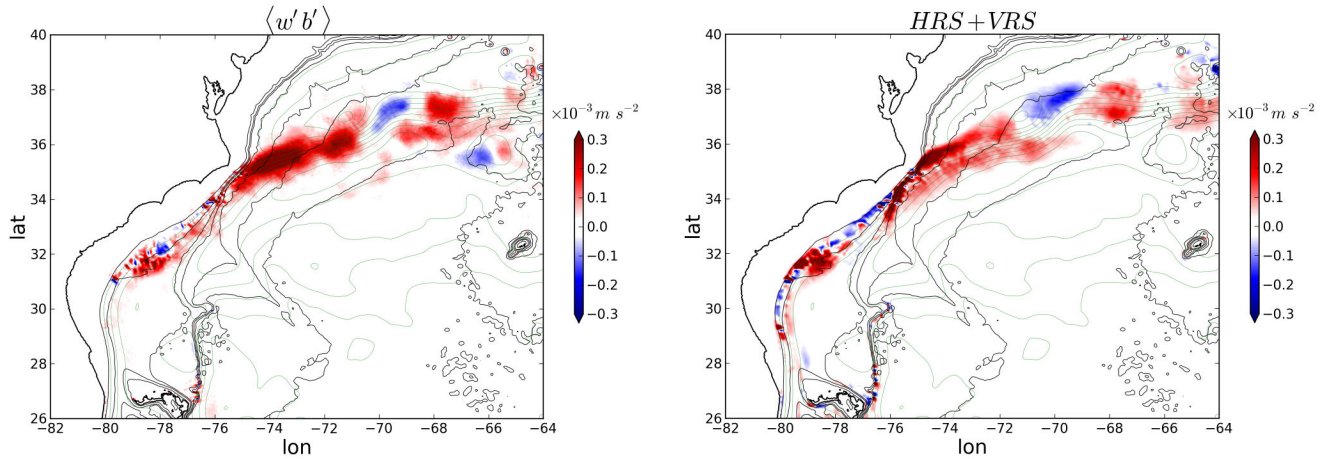


Figure 2.35 – Depth integrated (a) $VBF = \langle w'b' \rangle$, and (b) $HRS + VRS$. Units are $m^2.s^{-3}$.

dominates close to the surface. The strong eddy generation which happens after separation of the Gulf Stream is also intensified by the increased transport and the confluence of the flow which acts to sharpen the cross frontal gradients.

2.4.2 The impact of the topography

In this subsection I present some results related to the role of a coast and a sloping bottom topography on the stability of the flow. The effect can be either to modify the stability properties of the flow for baroclinic and/or barotropic instabilities (subsection 2.4.2.3) or to introduce new possible types of instabilities (subsections 2.4.2.1 and 2.4.2.2). This includes results from (**Gula et al., 2009a,b**; **Gula & Zeitlin, 2010**; **Gula et al., 2010**; **Flór et al., 2011**; **Gula & Zeitlin, 2014**; **Gula et al., 2015a**).

2.4.2.1 A new type of instability: the Rossby-Kelvin instability

Including a coast, in the form of a vertical wall, in a flow stability problem introduces new modes in the system: **the Kelvin and Poincaré waves**. In a two-layer fluid configuration analog to the Philips model, under specific conditions for the vertical shear and stratification, these new modes can interact with the Rossby waves and give rise to a new type of instability: **the Rossby-Kelvin instability**. This type of instability was first studied theoretically by Sakai (1989). Such mechanism is particularly interesting for its potential to couple balanced motions (the Rossby wave) with unbalanced motions (the Kelvin and Poincaré waves).

I have studied the emergence of the RK instability for different type of setups (Fig. 2.36) like a 2-layer fluid in a channel (**Gula et al., 2009a**) or in a rotating annulus (**Gula et al., 2009b**) and use them to interpret experimental results (**Flór et al., 2011**). We have shown that the RK instability would trigger in the parameter regimes predicted by theory in the form of a Rossby wave in one layer interacting with a Kelvin wave in the other layer (Fig. 2.37).

These results have been extended to the continuously stratified case and the non-linear evolution of the mode has been studied using the Weather Research and Forecasting (WRF) Model (**Gula et al., 2009b**). The simulations confirmed the presence of the RK instability with characteristics comparable to those found in the two-layer case. The mode saturates at finite amplitude through the steepening and breaking of the Kelvin wave, which leads to the development of unbalanced small-scale

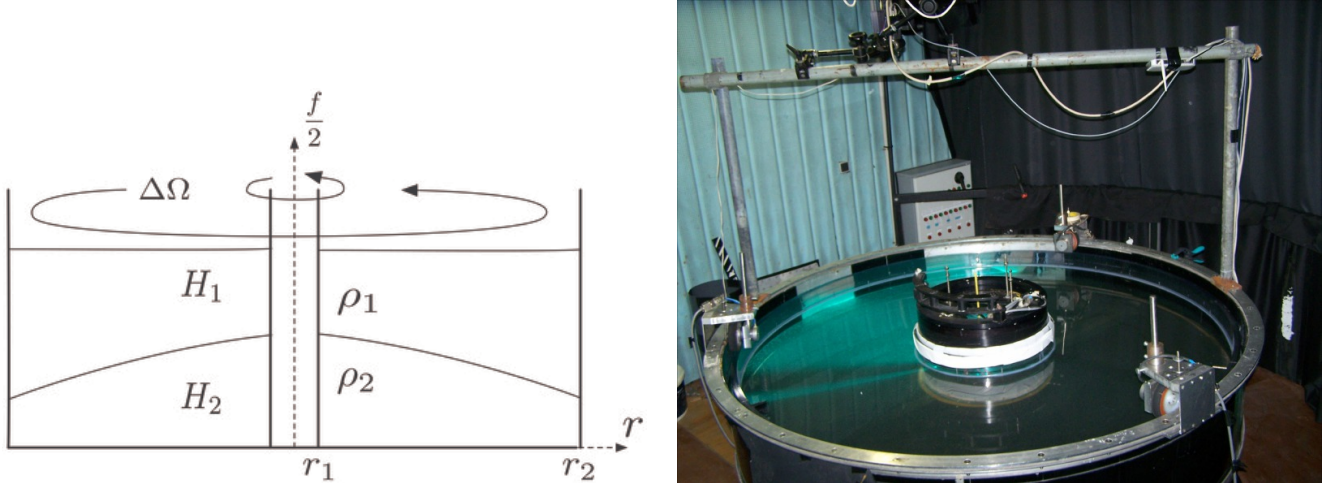


Figure 2.36 – The two-layer model in a rotating annulus (left) and a picture of the experiment realized at LEGI (**Flór et al., 2011**) (right).

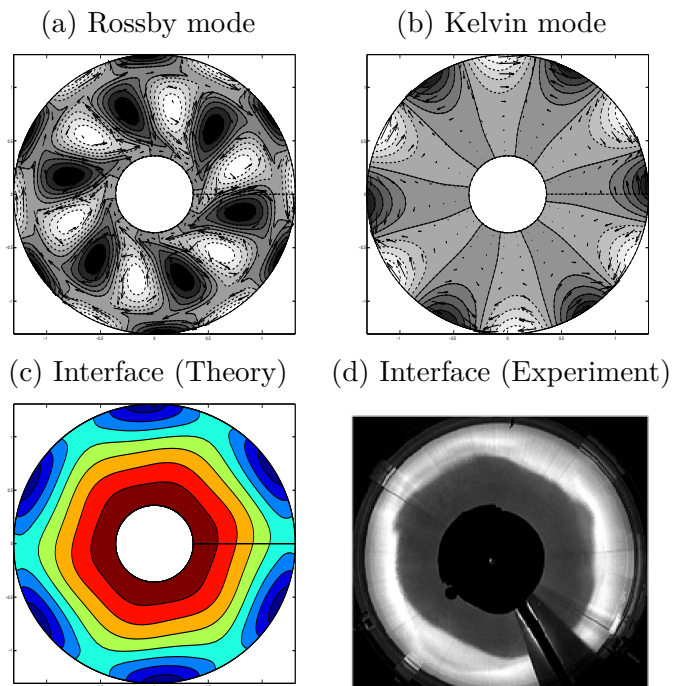


Figure 2.37 – Pressure and velocity fields in the upper (a) and in the lower layer (b), and interface height (c) for the theoretical RK mode and from the experiments (d). From Flór et al. (2011).

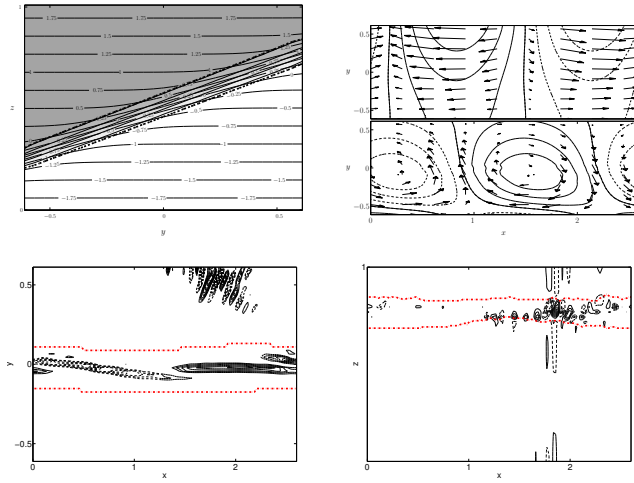


Figure 2.38 – (a) Potential temperature initial distribution (contours) and zonal geostrophic current (grey) in the (y, z) plane. (b) Pressure (contours) and velocity (vectors) in the (x, y) plane vertically averaged above (top) and (below) the front. (c) Horizontal and (d) vertical section of the velocity divergence after the saturation of the RK instability. Notice the apparition of small scale divergent motions where the Kelvin wave steepens and breaks. From **Gula et al. (2009a)**.

instabilities along the front (Fig. 2.38). Remarkably, the developing instability leads to conversion of kinetic energy of the basic flow to potential energy, contrary to classical baroclinic instability.

2.4.2.2 Arrested Kelvin wave in a coastal current

A barotropic equivalent of the previous mechanism is possible in a presence of a coast and a horizontal velocity shear. This is a configuration typical of buoyancy-driven coastal currents (Fig. 2.39), which are bounded by a coast and a surface density front. Such currents are playing an important role in the mesoscale variability of the ocean (*e.g.*, the Leeuwin current on the west coast of Australia Fig. 2.39).

In such configuration, one type of instability is due to the resonance of a frontal mode, which is a vortical mode propagating on the PV gradient of the front, and a Kelvin wave (**Gula & Zeitlin, 2010**), see Fig. 2.40. We have studied the nonlinear evolution of this unstable mode with the help of a high-resolution well-balanced finite-volume numerical scheme for shallow-water equations. At the first stage, the Kelvin component of the unstable mode breaks, forms a Kelvin front, and leads to small scale dissipation and generation of internal gravity wave. It also leads to the reorganization of the mean flow through dissipative and wave-mean flow interaction effects. The mechanism is very similar to the nonlinear saturation of the RK mode seen previously. At the second stage, a new, secondary unstable mode of the Rossby type develops on the background of the reorganized mean flow, and then breaks, forming coherent vortex structures (**Gula et al., 2010**), see Fig. 2.41.

2.4.2.3 Stabilisation of baroclinic instability

A sloped bottom topography can also have an impact on the flow by modifying the growth rate of the baroclinic instability (**Gula & Zeitlin, 2014**). In this section we study the impact of bathymetry, in a form of a constant-slope shelf, on the stability of the flow. Following Pennel *et al.* (2012) we define

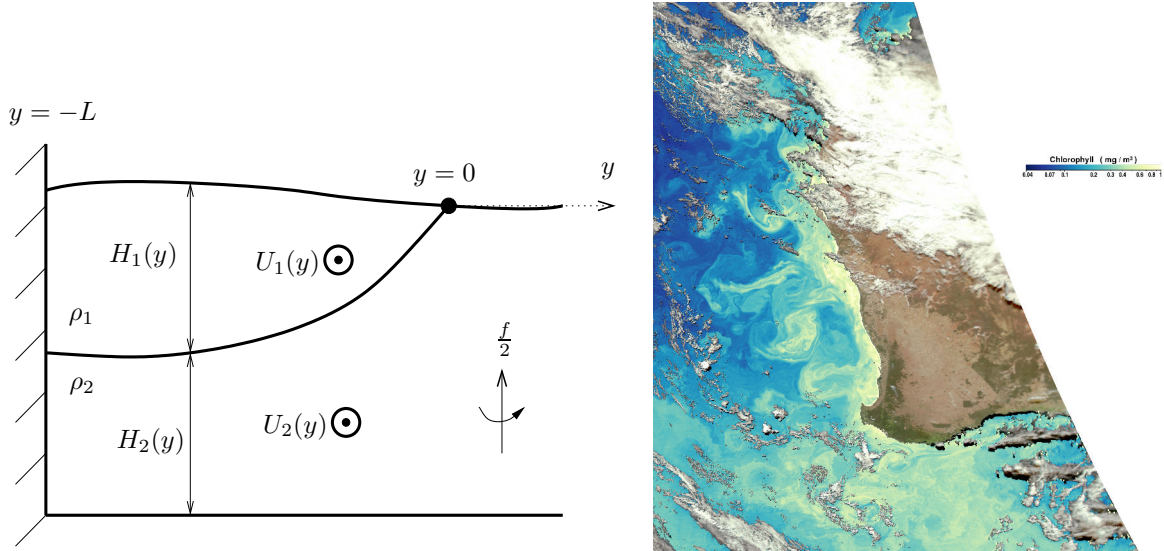


Figure 2.39 – (left) Schematic representation of a coastal current bounded by a density front. (right) Chlorophyll concentration in the Leeuwin Current (NASA/GSFC). From **Gula & Zeitlin (2010)**.

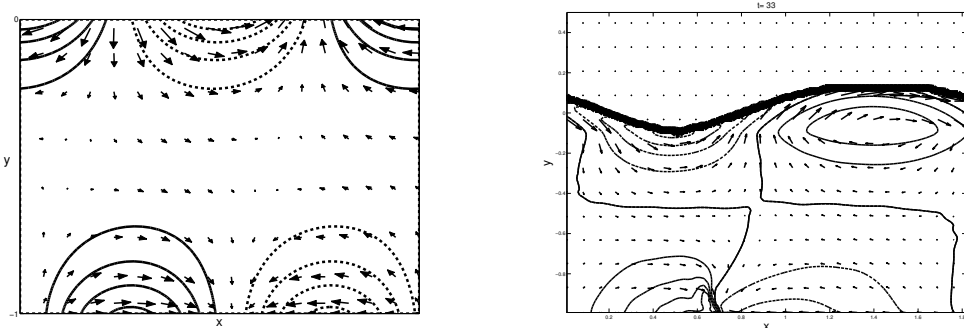


Figure 2.40 – (left) Height and velocity fields of the most unstable mode, corresponding to the resonance between the Kelvin and the frontal mode, from the linear stability analysis. (right) The same mode after nonlinear saturation and formation of a Kelvin front. From **Gula & Zeitlin (2010)**.

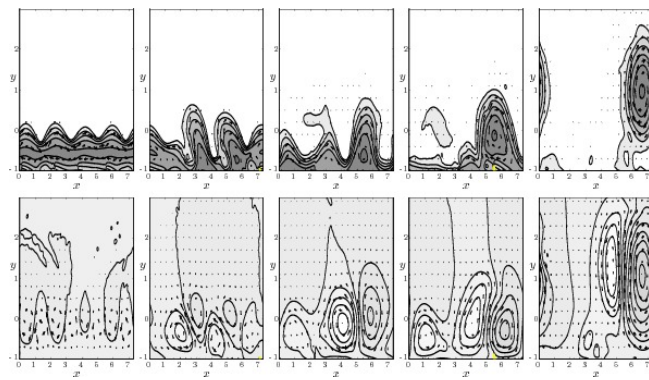


Figure 2.41 – Sea surface height (top) and pressure in the bottom layer (bottom) at $t = 110, 130, 250, 300$ and 500 , from left to right, for the development of the most unstable mode for a basic flow with constant PV and a depth ratio $r = 2$. The calculation domain is periodic in the x -direction and corresponds to 4 wavelengths of the most unstable mode. From **Gula et al. (2010)**.

a topography parameter To as the ratio of the shelf slope γ to the isopycnal slope α :

$$To = \frac{\gamma}{\alpha}, \quad (2.8)$$

where α is defined as the slope of the interface between the layers at the location of the front (Fig. 2.42). The parameter To has been found relevant for quantifying the shelf impact on the surface current (Pennel *et al.* (2012)), as previously suggested by works in the quasi-geostrophic Phillips model. Positive values of To , as in figure 2.42 correspond to isopycnal and shelf slopes in the same direction, which is typical of upwelling events along the coast of western boundary currents. Negative values of To correspond to isopycnal and shelf slopes in the opposite directions and are typical of buoyant coastal currents.

The nontrivial topography allows for specific topographic waves, in addition to Frontal, Kelvin, Rossby and Poincaré waves discussed previously. These waves may resonate with other types of waves and, thus, lead to new instabilities. On the other hand, topography changes the propagation speed of these waves and may, thus, "detune" the resonances, leading to stabilization of the flow. We observe both effects, depending on To . Figure 2.42 shows the growth rates of the most unstable modes as a function of To and non-dimensional wavenumber. In all cases there is a strong stabilization of the flow for a positive To , with growth rates vanishing for To close to 1 (topography almost parallel to the interface). The most unstable modes in such configurations are due to the resonances of a frontal wave or a Rossby wave with topographic waves. It is clear from the expressions for the PV gradient in the lower layer:

$$\partial_r Q_2 = -f \frac{\partial_r H_2}{H_2^2}, \quad (2.9)$$

and for the topography parameter

$$To = \left. \frac{\partial_r H_t}{\partial_r H_2 + \partial_r H_t} \right|_{r_1+L}, \quad (2.10)$$

that $To \rightarrow 1$ will imply $\partial_r Q_2 \rightarrow 0$, which explains the stabilization.

Thus, linear stability analysis shows that a shelf slope always has a stabilizing effect for the baroclinic instability of retrograde current such as the Gulf Stream (**Gula & Zeitlin, 2014**). A coastal flow is retrograde if the topographic Rossby waves propagate in the opposite direction from the current, meaning that the flow has the coast on its left in the Northern Hemisphere. This corresponds to a positive ratio of the bottom slope over the isopycnal slope. There is however no direct and simple effect of the slope on the linear stability for barotropic-type mechanisms of a baroclinic flow (*e.g.*, Poulin *et al.* 2014).

2.4.2.4 Application to a realistic western boundary current: the Gulf Stream

We explain in this section how the previous results will apply in the case of a realistic western boundary current flowing along the continental slope. The Gulf Stream passes through the Strait of Florida, and then flows northward pressed against the confining wall of the southeastern U.S. continental shelf, before leaving the slope at Cape Hatteras (Fig. 2.43). The Gulf Stream is much more stable along the slope than it is after separation. There are only a few large meanders visible on the inshore side of the Gulf Stream, with cyclonic eddies propagating along the shelf.

These eddies are referred to as **frontal eddies** and occur where the Gulf Stream interacts with the slope and shelf. Statistics on the generation and propagation of frontal eddies, as well as a detailed study of the structure and emergent submesoscale interior of a Gulf Stream frontal eddy in a high

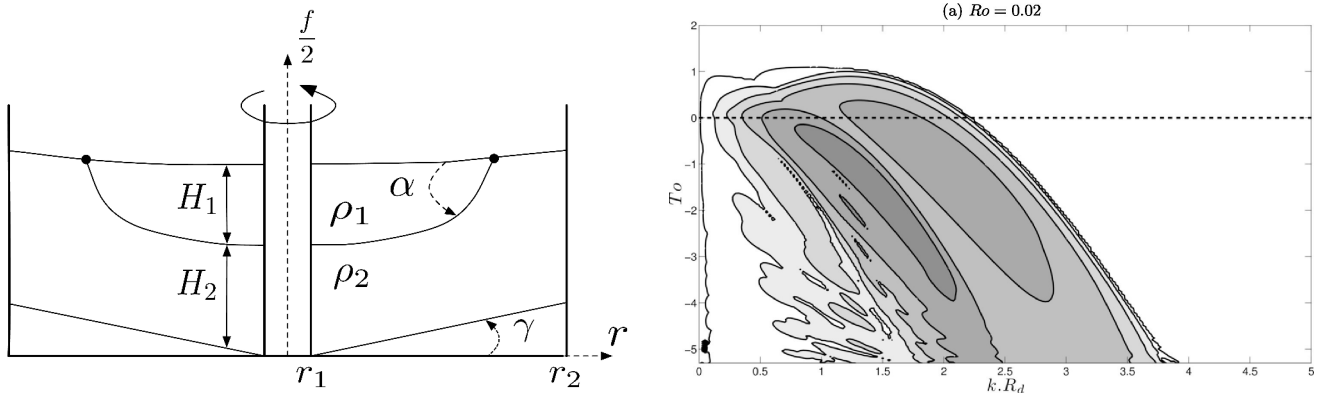


Figure 2.42 – (left) Schematic representation of a two-layer outcropping flow in the annulus with linearly sloping bottom. (right) Growth rate of the most unstable modes as a function of the topography parameter To for $Ro = 0.02$ and $\delta_H = 0.1$. From **Gula & Zeitlin (2014)**.

resolution simulation is given in **Gula et al. (2016a)**. The frontal eddies are formed in the troughs of northward propagating meanders and consist of deeply upwelled cold domes (Fig. 2.44). They have typical wavelengths of 100-250 km and propagate downstream at speeds of 30-70 km/d (*e.g.*, Glenn & Ebbesmeyer (1994) and references therein). Typical cross-stream length scales for frontal eddies are 30-50 km upstream of the Charleston Bump (south of 31°N, see Fig. 2.43) and can reach up to 100 km downstream. They are often associated with shallow warm filaments, known as "shingles" (von Arx *et al.*, 1955), which form at the surface and extend from the leading meander crest along the shoreward side of the cold dome. Similar eddies exist in other western boundary currents (Schaeffer *et al.*, 2017).

2.4.2.4.1 Stability of the Gulf Stream along the continental slope: The energy source terms for baroclinic ($\overline{w'b'}$, Fig. 2.35a) and barotropic instability (HRS, Fig. 2.35b) in the Gulf Stream shows that it is strongly unstable around 32°N (Fig. 2.35), where frontal eddies are generated. This corresponds to the location of a prominent topographic feature called the Charleston Bump, centered at coordinates (79°W, 31.5°N), which rises off the surrounding Blake Plateau from 600 m deep to a depth of about 200 m (Fig. 2.45).

Along-stream variations of eddy kinetic energy $EKE = 0.5(\overline{u'^2} + \overline{v'^2})$ and the two source terms HRS and $\overline{w'b'}$ are shown in Fig. 2.46. These quantities have been integrated vertically over the entire water column and in the cross-stream direction over the full Stream and multiplied by the mean density $\rho_0 = 1027.4 \text{ kg m}^{-3}$ such that the unit of EKE is $\text{kg m s}^{-1} = \text{J m}^{-1}$, and the unit of the eddy conversion terms is $\text{J m}^{-1} \text{s}^{-1}$. The variations of EKE along the Stream show a weak growth of eddy energy upstream of the Bump, a rapid growth at the Charleston Bump, a decay downstream of the Bump, and again a large increase past Cape Lookout. This is consistent with the patterns of the energy conversions terms whose sum is weakly positive upstream of the Bump, strongly positive at the Bump, negative downstream of the Bump and again strongly positive past Cape Lookout. Amplitudes of the baroclinic and barotropic energy conversions and their overall contribution to the EKE variations are comparable.

The baroclinic source term $\overline{w'b'}$ is associated with the vertical shear in the flow and is very sensitive to the shape of the bottom topography. The depth of the bottom topography at the center of the Stream and the mean topographic slope between the center of the Stream and the shelf (defined as the $\Psi = 15 \text{ Sv}$ and $\Psi = 1 \text{ Sv}$ streamfunction contours, respectively) are shown Fig. 2.46. The correlation between the slope variations and $\overline{w'b'}$ clearly points to a local topographic stabilization interpretation.

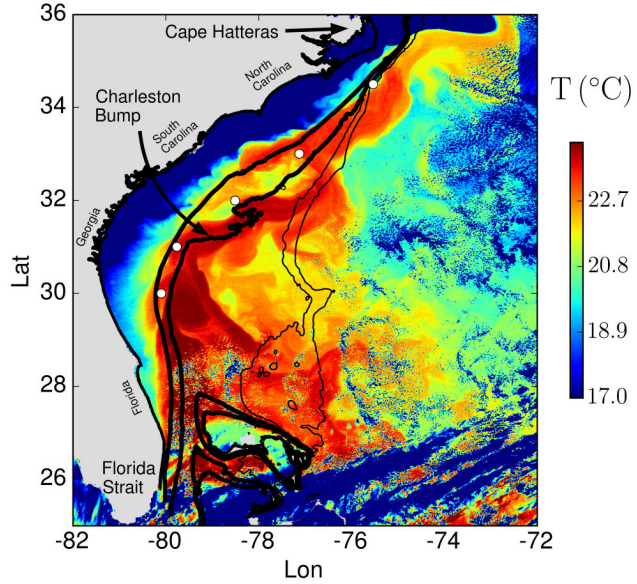


Figure 2.43 – Observed Sea Surface Temperature (SST) of the Gulf Stream on March 15, 2013. Data from MODIS-AQUA. Black contours indicate the 200 m, 600 m, 1000 m, and 2000 m isobaths. The warm Gulf Stream is deflected eastward at the Charleston Bump location. Large meanders form downstream of the Bump with frontal eddies in-between detraining water from the leading wave crest of the meander. The large frontal eddy visible at (77.5°W, 32.5°N) has additional smaller scale perturbations on its rim. From **Gula et al. (2016a)**.

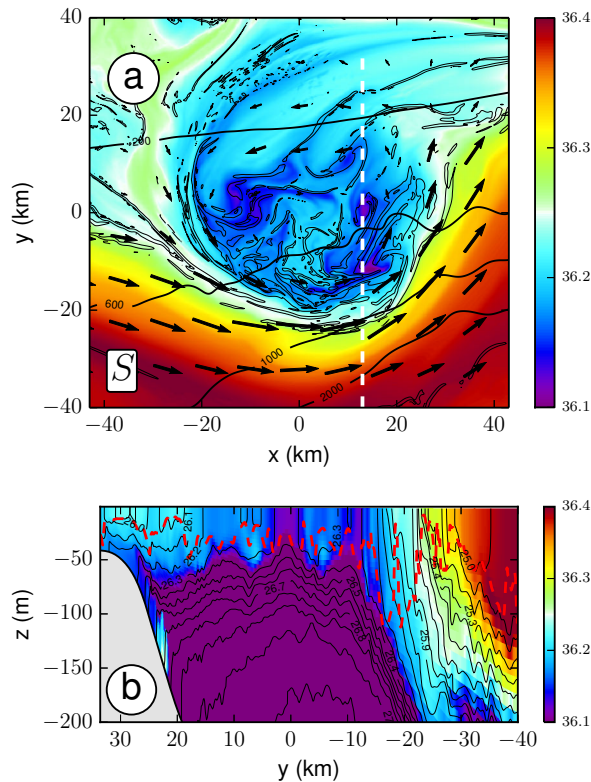


Figure 2.44 – (Top) salinity at $z = -10$ m (PSU, colors) and relative vorticity (at $\pm 2f$ in black contours) for a frontal eddy, showing the intra-frontal-eddy submesoscale vortices. Topography is shown in thin black contours for levels -200 m, -600 m, -1000 m, and -2000 m. (Bottom) vertical cross-shelf section of salinity along the white dashed line shown in the top panel. Density is shown in black contours. The dashed red line denotes the mixed-layer depth.

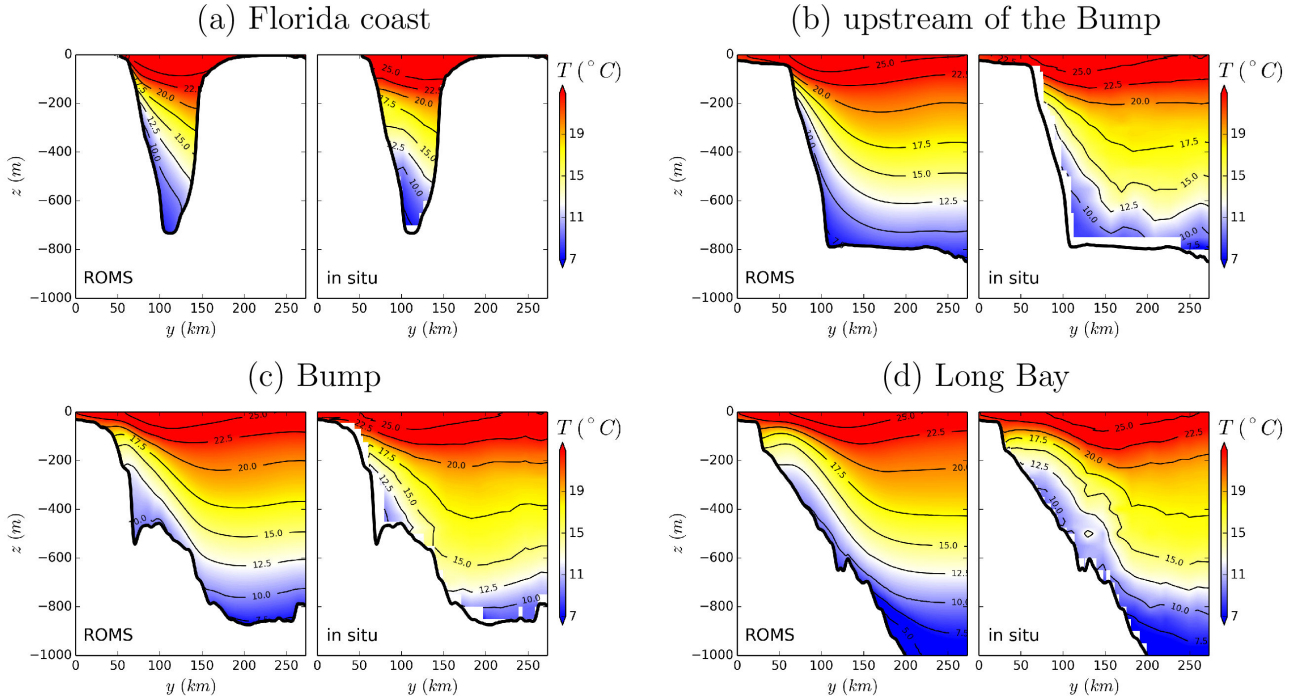


Figure 2.45 – Annual mean temperature from ROMS and statistical mean temperature from in-situ profile data (WOA; Locarnini *et al.* 2013) along vertical cross-shelf sections. Panels are plotted from upstream to downstream. From **Gula *et al.* (2015a)**.

The continental slope does not vary much between the Florida Strait and the Charleston Bump, as seen previously from Fig. 2.45 with values between $s = 0.01$ and $s = 0.02$. The slightly positive ratio between the slopes of the topography and the isotherms corresponds to a moderate stabilization of the flow. The first local maxima for the baroclinic source term at $x = 500$ km (between $29^\circ N$ and $30^\circ N$ in Fig. 2.35) coincides with a local minima in the slope. The large increase of $\overline{w'b'}$ corresponds to the region where the Stream is disrupted and loses contact with the slope (Fig. 2.45c). The mean slope felt by the flow decreases towards very small values and allows the flow to become strongly baroclinically unstable. Between the Charleston Bump and Cape Hatteras the slope of the topography gradually increases and $\overline{w'b'}$ decreases accordingly. Right after the Bump the ratio between the topography slope and the isotherms is close to 1 (Fig. 2.45d), leading to a strong stabilization of the flow. The slope becomes steeper downstream and almost vertical at Cape Lookout leading to another outburst of instability.

The use of linear stability results to interpret local instabilities of the flow can usually be made under the assumption that the slope variations in the along-stream direction occur on a scale large relative to the wavelength of the unstable modes. This is not the case here as the scale of the meanders is often similar to the scale of the along stream variations of topography (Fig. 2.43). Topographic variations at the Bump form a gap with a limited extent ($L \approx 100$ km) where the flow is unstable while the slope is stabilizing the flow upstream and downstream of this gap. Samelson & Pedlosky (1990) studied such a configuration in a two-layer QG model and showed that baroclinic instability can grow locally even when the unstable region has a limited extent, comparable or smaller than the wavelengths of unstable modes. Growth rates become small only for interval shorter than the Rossby deformation radius. The analysis in Samelson & Pedlosky (1990) shows that the unstable modes are trapped in the gap, they grow in time but decay in space downstream of the unstable region such that the maximum mode amplitudes occur near the downstream edge of the unstable interval. This explains the location of the EKE local maximum in Fig. 2.46 at the tail of the Bump.

The impact of topography is not as straightforward for barotropic instability mechanisms. There are different competing nonlinear effects due to the topography. On one hand, the slope acts to sharpen the cross-stream velocity and vorticity gradients and therefore increases growth rates of a barotropic shear type instability. On the other hand, the topography also acts to inhibit the eddying activity by increasing straining and limiting the cross-stream growth of the meanders.

The along-stream variations for the maximum cross-stream gradient of along-stream velocity u_y/f , which is the only contributing term in the shear (v_x+u_y) and horizontal strain ($S = \sqrt{(u_x - v_y)^2 + (v_x + u_y)^2}$), are shown Fig. 2.46c. The shear increases when the flow presses against the shelf due to a combination of bathymetric curvature and inertia effects. Variations of the shear match perfectly the variations of the inverse of the horizontal cross-stream distance between the center of the Stream (defined as the $\Psi = 11$ Sv streamfunction contour) and the shelf (defined as the $z = -50$ m isobath) shown Fig. 2.46c. The shear is maximum at the exit of the Straits of Florida (27°N), where the Stream is strongly squeezed against the shelf due to the narrow channel formed by the topography (Fig. 2.45a). There is a second maxima upstream of the Charleston Bump at about 30.5°N , where the curvature of the bathymetry toward northeast is maximum. The curvature locally peaks at 0.0040 km^{-1} , corresponding to a small radius of curvature of 250 km. Finally, a third shear maxima is visible upstream of Cape Lookout after the Stream has recovered from the Bump's seaward deflection and is again pressed against the slope. These three locations correspond to local minima of HRS and precede increases of HRS and corresponding outbursts of barotropic shear instability. HRS is anticorrelated with the derivative of the shear such that meanders grow when the shear is decreasing and meander growth is suppressed when the shear is increasing.

The patterns of HRS are better explained by looking at the life cycle of eddies that grow through barotropic shear instability and subsequently decay. Eddy generation originates from the mean velocity shear and is acting to reduce it. By analogy with an atmospheric storm track, there is eddy growth by Reynolds stress and downstream development of the eddies (Williams *et al.*, 2007). Interaction of the flow with the topography acts as an external forcing process to localize these oceanic storm tracks by sharpening the cyclonic side of the Stream at the three above mentioned locations. Regions of negative barotropic conversion are regions of eddy decay. Eddies are tilted with the increasing background shear and return energy and momentum to the mean flow following Orr mechanism (Orr, 1907). Eddy growth provides a deceleration of the mean flow in the region of positive HRS, and eddy decay provides an acceleration of the flow in the region of negative HRS.

Associated time-averaged eddy fluxes are essential to maintain and reshape the mean current. Eddy fluxes of momentum are acting to decelerate the Stream in the unstable regions, after the exit of the Straits of Florida and at the Charleston Bump, and accelerate it in stable regions in-between, especially between the Bump and Cape Lookout. The eddy fluxes of vorticity, buoyancy and PV are also downgradient in the Charleston Bump area and revert to upgradient in the area between the Bump and Cape Lookout. The pattern of eddy fluxes is explained in terms of eddy life cycle. Eddy growth regions are associated with downgradient eddy fluxes and eddy decay regions with upgradient eddy fluxes (Gula *et al.*, 2015a).

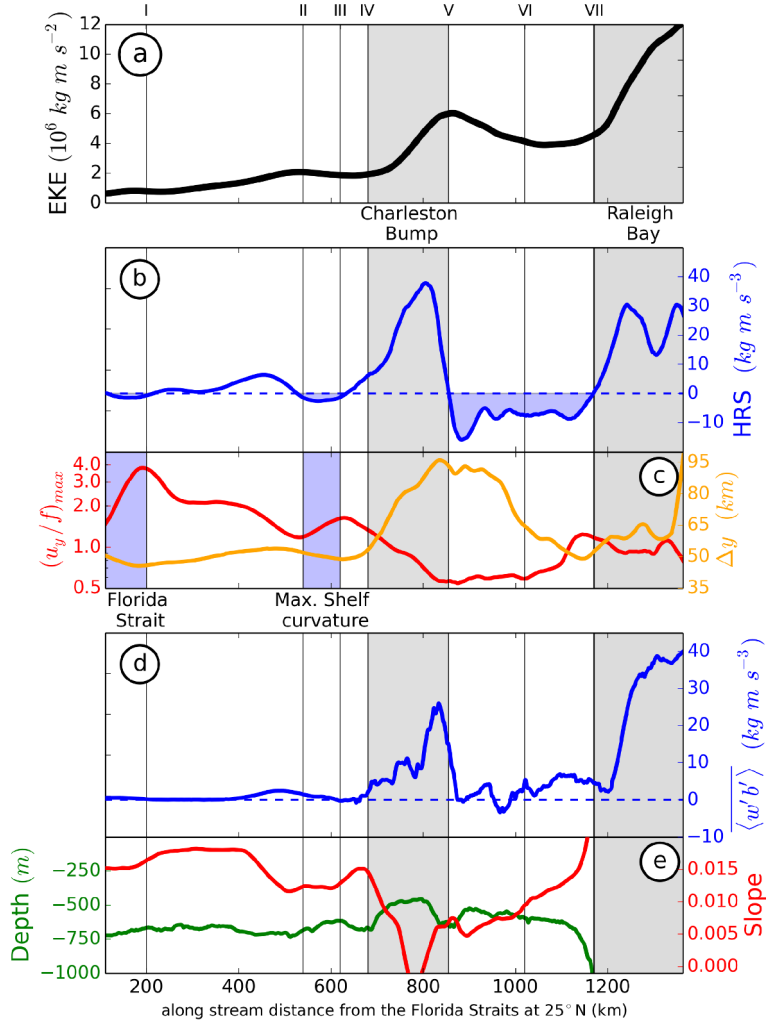


Figure 2.46 – Along-stream (a) Eddy kinetic energy EKE (black), (b) barotropic HRS energy conversion term (blue), (c) Maximum cross-stream gradient of along-stream velocity u_y/f (red) and horizontal cross-stream distance Δy (orange) between the center of the Stream (defined as the $\Psi = 11$ Sv streamfunction contour) and the shelf (defined as the $z = -50$ m isobath), (d) baroclinic $\langle w'b' \rangle$ (blue) energy conversion term, and (e) depth of the bottom topography at the center of the Stream (green) and mean topographic slope (red) between the center of the Stream and its inshore front (defined as the $\Psi = 11$ Sv and $\Psi = 1$ Sv streamfunction contours, respectively). u, v are the velocities along the local coordinates (x, y) defined as along and cross-stream directions, respectively. Locations of the Charleston Bump and Raleigh Bay correspond to the filled gray areas. From **Gula et al. (2015a)**

2.5 Submesoscale processes in the surface layer

In this subsection I present works on different submesoscale processes in the ocean surface layer. These include the submesoscale equivalent of the barotropic and baroclinic instability, which will be designated as **barotropic shear instability** (subsection 2.5.2) and **mixed-layer baroclinic instability** (subsection 2.5.3), respectively, as well as other mechanisms related to **frontogenesis** (subsection 2.5.1). Finally the role of each mechanism in the energy cascade will be discussed (subsection 2.5.4). This includes results from **Gula et al. (2014, 2016a); Klymak et al. (2016); McWilliams et al. (2015); Callies et al. (2015); McWilliams et al. (2019)** as well as various unpublished results.

2.5.1 Frontogenesis

Frontogenesis describes the theory for cross-front density gradients intensification, which has been originally developed in the atmospheric context (Hoskins, 1982) and later applied to the upper ocean (Capet *et al.*, 2008b). It involves the sharpening of favorably aligned lateral density gradients by a larger scale straining flow, disruption of the geostrophic balance for the along-front flow, and generation of an ageostrophic secondary circulation (Fig. 2.47, left). This secondary circulation acts to restore the geostrophic and hydrostatic force balances by advectively tilting isopycnals toward the horizontal, *i.e.*, by restratifying the flow.

A variant of this process applicable to cold filaments at finite Rossby number has been proposed by McWilliams *et al.* (2009). It is a related mechanism where the deformation flow acts on a favorably aligned cold filament (a surface density maximum formed by 2 parallel fronts with opposite-sign density gradient), causing an even more rapid narrowing and stronger surface convergence and downwelling at its center than for an isolated front (Fig. 2.47, right).

2.5.1.1 Filament frontogenesis

I have studied the life cycle of the intense submesoscale cold filaments in **Gula et al. (2014)** using a set of realistic, very high resolution simulations in the region of the Gulf Stream. An idealized study of the filament dynamics has later been presented in **McWilliams et al. (2015)**.

Elongated buoyancy filaments appear in virtually any high resolution image of the ocean surface. Filaments play an important role in oceanic biogeochemistry, affecting both lateral and vertical transport of tracers like nutrients, phytoplankton, and zooplankton larvae (Lehahn *et al.*, 2007). They are produced by the stirring and straining of the mesoscale eddies. These structures visible for instance in ocean color, sea surface temperature (SST), or Synthetic Aperture Radar (SAR) are typically of mesoscale length (30 – 100 km) and of much smaller submesoscale width (1 – 10 km or less). Example of cold filaments can be seen on the South Wall of the Gulf Stream in Fig. 2.48 at various stages of their life cycle.

The entire life cycle of filament F_0 is shown in Fig. 2.49. It is typical of most of the other filaments in the simulation. Panels (a-c) in Fig. 2.49 show a sequence of SST snapshots at intervals of a few hours that illustrates the sharpening temperature gradient and the filamentary intensification of F_0 . The sharpening of the filament happens very fast: between panels (a) and (c) the buoyancy gradient reaches a $\mathcal{O}(1 \text{ km})$ scale in about 12 hours.

A vertical cross section of the filament at the time of Fig. 2.49c shows the temperature contours and the 3D velocity field in Fig. 2.50. The vertical structure is typical of a cold filament structure (McWilliams *et al.*, 2009) with local outcropping of cold isotherms and a very small lateral width for

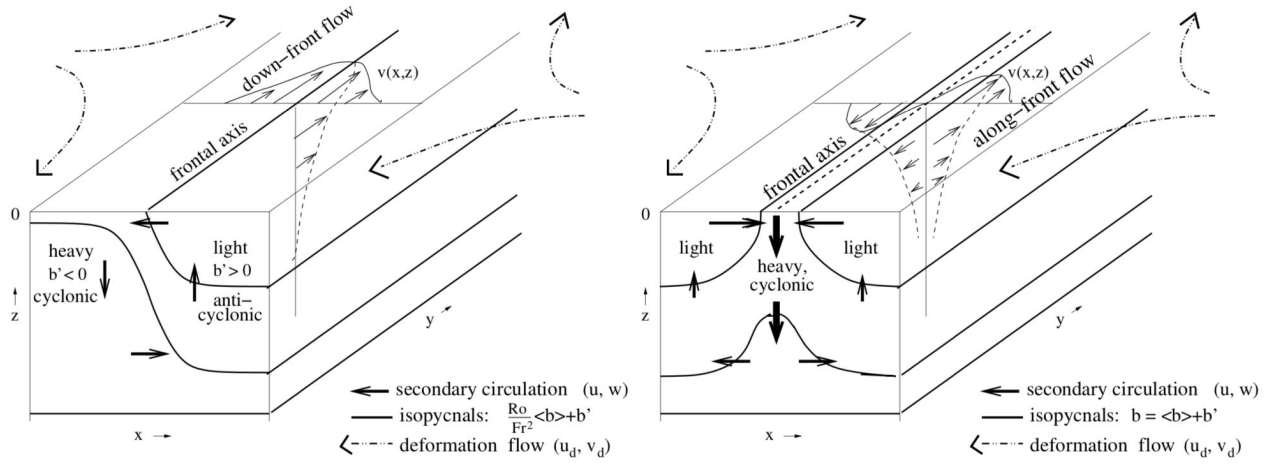


Figure 2.47 – Sketches of surface-layer frontogenesis caused by a large-scale deformation flow for a front (left) and a dense filament (right) configuration in $b(x,z)$. The along-axis flow is partly geostrophic, and the secondary circulation in the (x, z) plane is ageostrophic. With time the x gradients sharpen at a super-exponential rate, and Ro grows. With finite Ro , the downwelling $w < 0$ and cyclonic $\zeta/f > 0$ features dominate their opposite-sign counterparts. From McWilliams (2016).

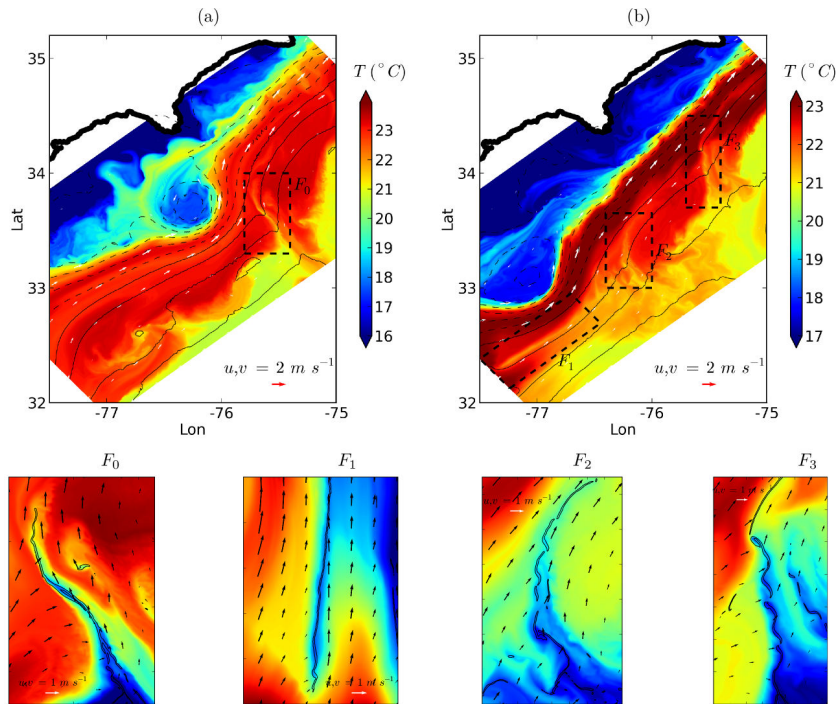


Figure 2.48 – Simulated SST for a region south of the Gulf Stream separation point at Cape Hatteras on March 18 (a) and March 13 (b). Surface velocities are the white vectors. The sea surface dynamic height is shown with thin black contour lines every 0.1 m. Bottom panels show the SST zoomed into the 4 black rectangles of the two top panels showing submesoscale cold filament intrusions corresponding to the F_0 , F_1 , F_2 , and F_3 cases, from left to right. The surface relative vorticity is shown with thin black contour lines, and surface velocity with black arrows. From Gula *et al.* (2014).

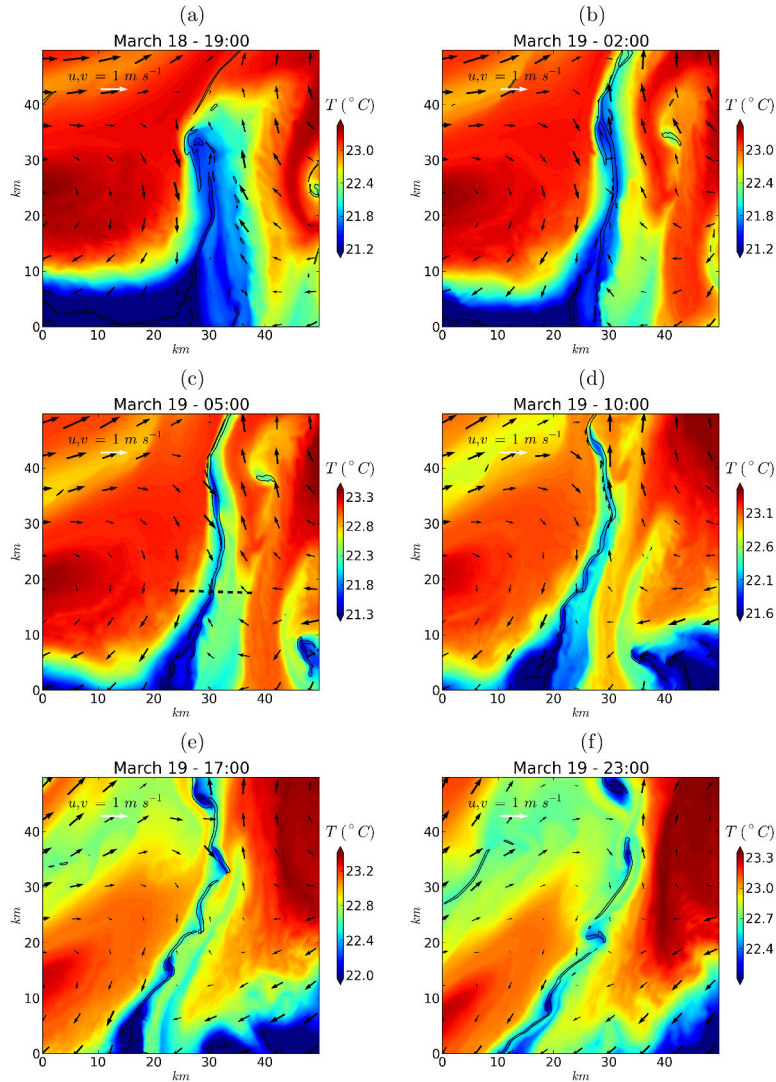


Figure 2.49 – SST (in colors), surface relative vorticity (black contours), and surface velocity (vectors) for the evolution of the cold filament F_0 shown Fig. 2.48. The mean velocity (over the plotted domain) has been subtracted from the plotted vectors. From **Gula et al. (2014)**.

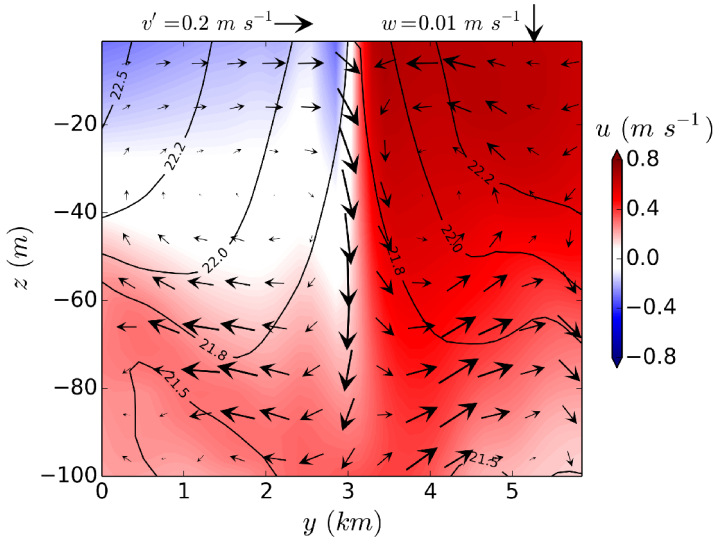


Figure 2.50 – Vertical section of along-front velocity (in colors), cross-front and vertical velocities (vectors) and temperature (black contours) along the dashed black line in Fig. 2.49. From **Gula et al. (2014)**.

the temperature and along-front velocity gradients ($\Delta L \approx 1\ km$). The vectors show the ageostrophic secondary circulation that forms two recirculation cells on each side of the filament. The secondary circulation acts to restore the geostrophic balance by advectively restratifying the flow, *i.e.*, tilting the isopycnals toward the horizontal by bringing warm/light fluid from the side toward the center of the filament. The convergence of the flow at the surface gives rise to a very strong and narrow downwelling in the filament middle. Instantaneous values of the vertical velocity can reach $\mathcal{O}(1\ cm\ s^{-1})$.

Such filaments are thus lines of strong oceanic surface convergence. This is illustrated by the release of Lagrangian particles in **Gula et al. (2014)**. The vertical mixing due to turbulence in the surface layer allows particles to horizontally cross the density gradients. Once particles have reached the center of the filament, they downwell adiabatically and move away within the pycnocline. This highlights the important role played by such submesoscale structures as sources of tracer injection.

2.5.1.2 Turbulent thermal wind

The traditional view for filaments and fronts, as well as most mesoscale currents, assumes that the basic cross-frontal momentum balance is geostrophic, meaning that the cross-front pressure gradient is in balance with the Coriolis force associated with the along-front velocity. By differentiating vertically the momentum equation and combining with the hydrostatic approximation, we get the well-known **thermal wind relation**:

$$\begin{aligned} -f \frac{\partial v_g}{\partial z} &= -\frac{\partial b}{\partial x} \\ f \frac{\partial u_g}{\partial z} &= -\frac{\partial b}{\partial y}, \end{aligned} \quad (2.11)$$

where x, y and u_g, v_g the along- and cross-front coordinates and geostrophic velocity components, respectively.

The different terms of the thermal wind balance are plotted in Fig. 2.51, for the filament F_1 during the frontogenesis process. Differences between panels (a) and (c) show that this balance fails in the

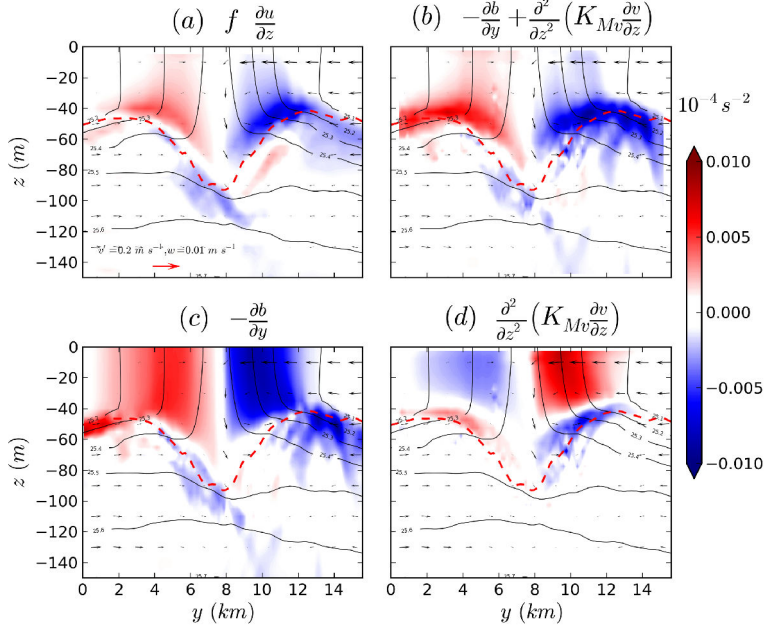


Figure 2.51 – Vertical sections of the different terms of the turbulent thermal wind balance for the filament F_1 in the cross-front direction y : (a) $f \frac{\partial u}{\partial z}$; (b) $-\frac{\partial b}{\partial y} + \frac{\partial^2}{\partial z^2} \left(K_{Mv} \frac{\partial v}{\partial z} \right)$; and (c) $-\frac{\partial b}{\partial y}$; and (d) $-\frac{\partial b}{\partial y} + \frac{\partial^2}{\partial z^2} \left(K_{Mv} \frac{\partial v}{\partial z} \right)$. Density is shown in black with a contour interval 0.1 kg m^{-3} . All quantities are averaged in the along-front direction. The dashed red line shows the depth of the boundary layer from the KPP-scheme. From **Gula et al. (2014)**.

mixed-layer. While the flow is in approximate thermal wind balance in the cross-front direction at the base of the boundary layer, there is a large discrepancy in the upper mixed-layer where the cross-front buoyancy gradient is still large, but the vertical gradient of along-front velocity becomes very small. The effect of vertical mixing of momentum due to turbulence in the surface layer is of the same order of importance as the pressure gradient and Coriolis forces (Fig. 2.51). A more complete picture involves considering vertical mixing of momentum in both equations such that:

$$\begin{aligned} -f \frac{\partial v_{ttw}}{\partial z} &= -\frac{\partial b}{\partial x} + \frac{\partial^2}{\partial z^2} \left(K_{Mv} \frac{\partial u_{ttw}}{\partial z} \right) \\ f \frac{\partial u_{ttw}}{\partial z} &= -\frac{\partial b}{\partial y} + \frac{\partial^2}{\partial z^2} \left(K_{Mv} \frac{\partial v_{ttw}}{\partial z} \right), \end{aligned} \quad (2.12)$$

where (u_{ttw}, v_{ttw}) is the sum of the part of the horizontal flow driven by the momentum mixing and the geostrophic components, and $K_{Mv}(x, y, z)$ is the mixing coefficient for momentum. Eq. 2.12 is a 1D coupled second order system for $(\frac{\partial u_{ttw}}{\partial z}, \frac{\partial v_{ttw}}{\partial z})$ and describes what can be called a **turbulent thermal wind (TTW)** balance.

Furthermore, solving this TTW balance provides a very reliable estimate of the ageostrophic secondary circulation sharpening the filament and of the corresponding vertical velocity in the surface layer. Given a buoyancy field, the mixing coefficient for momentum, and the surface stress, Eq. 2.12 can be solved directly to obtain the TTW horizontal flow (u_{ttw}, v_{ttw}) . Results are shown in Fig. 2.52 for F_1 at the same time and place as Fig. 2.51. The geostrophic components gives a very good approximation of the flow below the mixed-layer, except for local differences in the form of localized gravity waves signals. As seen in Fig. 2.51, the cross-front buoyancy gradient, corresponding to the geostrophic vertical shear, is much larger than the vertical velocity shear in the mixed-layer. This leads to much larger amplitudes for the geostrophic along-front velocity u_g at the surface compared to

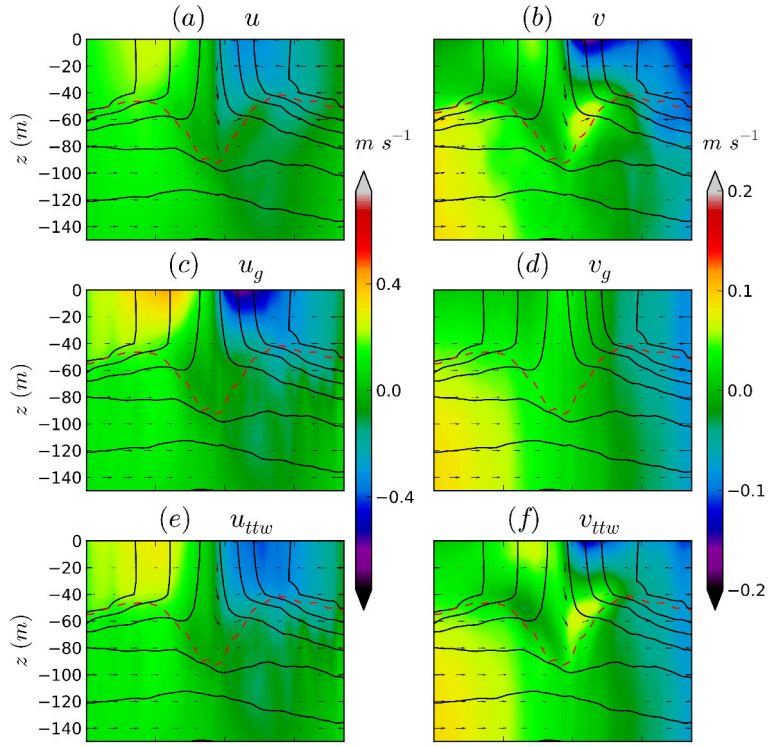


Figure 2.52 – Vertical sections of (left) along-front velocity u and (right) cross-front velocity v for the filament F_1 in the cross-front direction y . (a-b) Total horizontal velocity from the model (u, v), (c-d) geostrophic components of the horizontal flow (u_g, v_g), and (e-f) TTW associated flow (u_{ttw}, v_{ttw}). Density is shown in black with a contour interval 0.1 kg m^{-3} . All quantities are averaged in the along-front direction. The dashed red line shows the depth of the boundary layer from the KPP-scheme. From **Gula et al. (2014)**.

the real velocity u . The TTW associated along-front velocity u_{ttw} compensates these effects and gives a much more accurate estimate of the real velocity. The cross-frontal circulation in the mixed-layer is mostly driven by vertical mixing as there is no buoyancy gradient in the along-front direction. The cross-front velocity, which corresponds to the ageostrophic secondary circulation of the filament is well described by the TTW horizontal velocity v_{ttw} .

The associated vertical velocity w_{ttw} can be computed by integrating the continuity equation from bottom to top. The total vertical velocity and the vertical velocity computed from the TTW associated flow are shown in Fig. 2.53 for F_1 . As seen from both horizontal and vertical sections, most of the strong negative vertical velocity signal at the center of the filament is well described by TTW balance.

Thus, after the initial intensification of filaments by the ambient strain field, a sustained frontogenetic can ensue even if the strain abates, where the secondary circulation is due to TTW. The general picture is that dense filaments, which are created by the chaotic horizontal advection due to the mesoscale eddies, will further evolve frontogenetically by the interaction of boundary layer turbulence with the filament density structure that maintains the TTW secondary circulation.

An idealization of the cold filament of Fig. 2.50 has been used in **McWilliams et al. (2015)** with an approximate model of the surface buoyancy evolution assuming TTW balance. It has been shown that the vertical mixing itself causes a further horizontal frontogenesis through the induced secondary circulation. In the approximate model based on TTW, the central vorticity approaches a

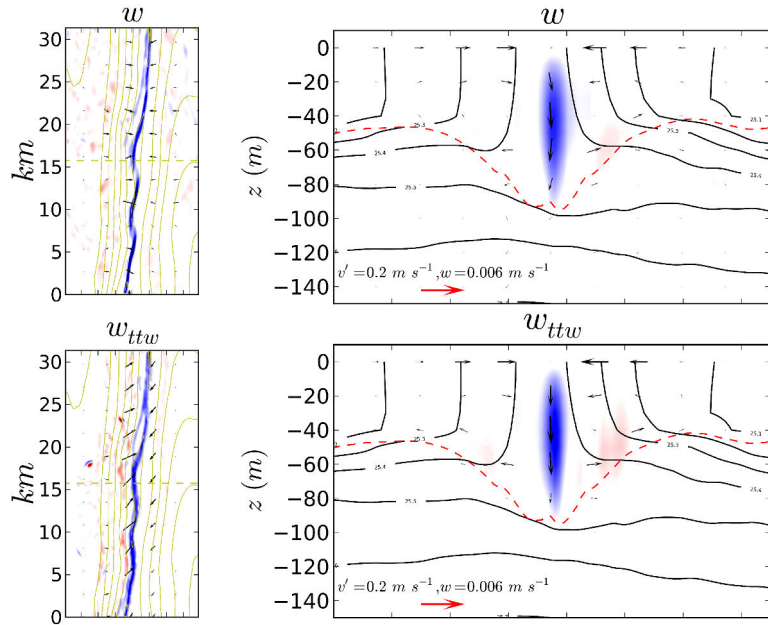


Figure 2.53 – (left) Instantaneous horizontal patterns of (top) w , (middle) w_{ttw} , and (bottom) $w_{GL81} = \nabla(K_M v \nabla b)/f^2$ for the filament F_1 at depth $z = -20$ m. Vectors show the horizontal velocity field: (top) (u_{div}, v_{div}) , (middle) $(u_{ttw} - u_g, v_{ttw} - v_g)$, and (bottom) (u_{GL81}, v_{GL81}) . (right) Vertical sections of (top) w , (middle) w_{ttw} , and (bottom) w_{GL81} for the filament F_1 in the cross-front direction y . All quantities are averaged in the along-front direction. Vectors show the cross-section velocity field: (top) (v_{div}, w_{div}) , (middle) $(v_{ttw} - v_g, w_{ttw})$, and (bottom) (v_{GL81}, w_{GL81}) . Density is shown in green and black contours. The dashed red line shows the depth of the boundary layer from the KPP-scheme. From Gula *et al.* (2014).

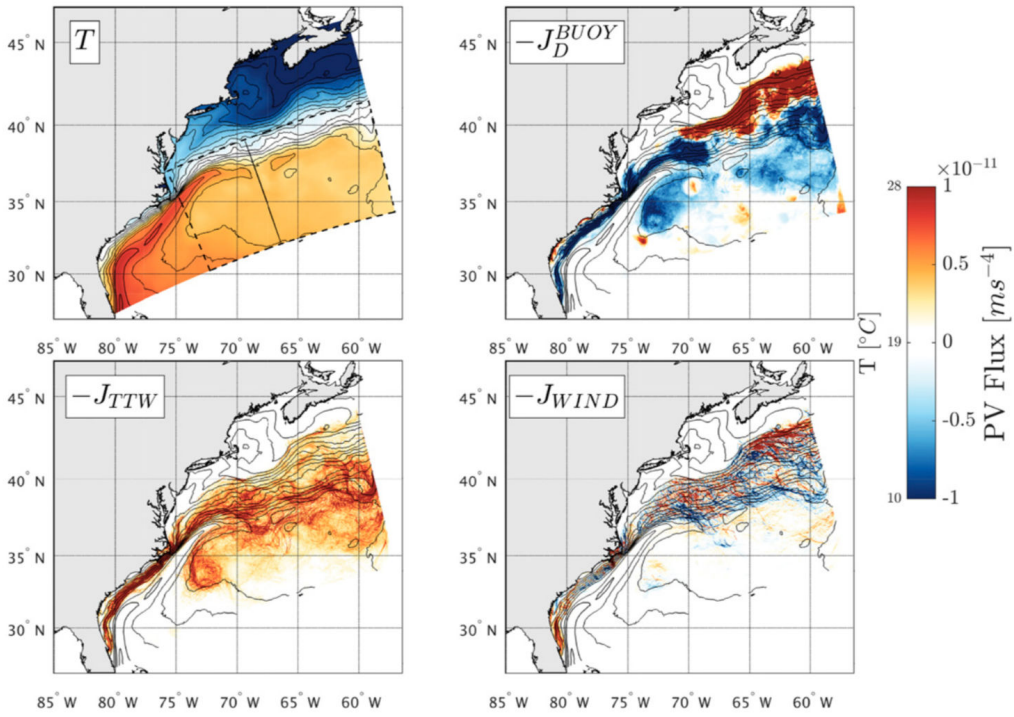


Figure 2.54 – Annual averaged surface fields from a 1.5-km run. Annual averages of the PV fluxes (J vectors) are calculated over the time-varying mode water outcropping. J_{WIND} , J_{BUOY} , and J_{TTW} correspond to the contribution of the wind, buoyancy fluxes, and TTW circulation, respectively, on the tendency of PV. From **Wenegrat et al. (2018b)**.

finite-time singularity, and in a more general hydrostatic model, the central vorticity and horizontal convergence are amplified by shrinking the transverse scale to near the model’s resolution limit within a short advective period on the order of a day. The evolution of fronts in TTW balance has been further studied by Crowe & Taylor (2018, 2019); Barkan *et al.* (2019).

2.5.1.3 Impacts for surface potential vorticity fluxes and creation of Mode Water

This balance has important applications, for example on the potential vorticity (PV) fluxes at the surface (**Wenegrat et al., 2018b**). The PV fluxes that arise through the TTW circulation (*i.e.*, the circulation due to the turbulent mixing of geostrophic momentum) are enhanced at strong horizontal buoyancy fronts. In some cases they may dominate both wind and surface buoyancy-flux-driven PV fluxes, and hence can lead to a net injection of PV onto outcropped isopycnals even during periods of surface buoyancy loss.

This has been illustrated using idealized and realistic CROCO simulations in the Gulf Stream, where it was demonstrated that injection of PV at the submesoscale reduces the rate of mode water PV removal by a factor of 2 and shortens the annual period of mode water formation by 3 weeks, relative to air-sea fluxes alone (Fig. 2.54). Submesoscale processes thus provide a direct link between small-scale boundary layer turbulence and the gyre-scale circulation, through their effect on mode water formation, with implications for understanding the variability and biogeochemical properties of ocean mode waters globally.

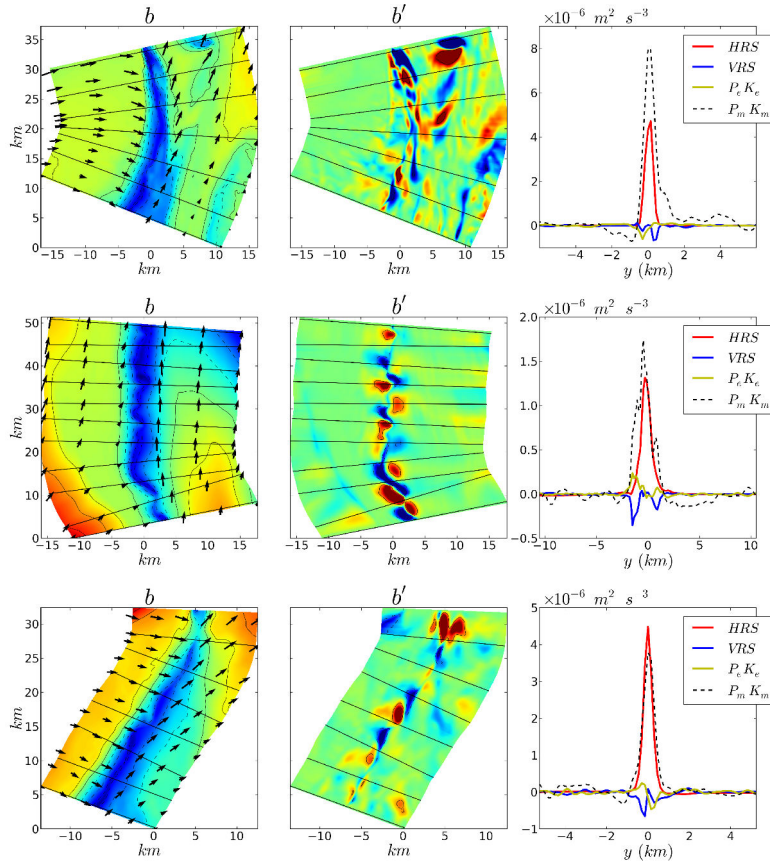


Figure 2.55 – Total surface buoyancy field b (left), perturbation field b' (middle) and instantaneous local energy conversions profiles HRS , HRS , $P_e K_e$ ($VBF = \overline{w'b'}$) and $P_m K_m = \overline{w\bar{b}}$ (right) computed for 3 different unstable cold filaments in their early stages of the instability process. (up) F_0 at the time of Fig. 2.49c, (middle) F_1 , and (bottom) F_2 . From **Gula et al. (2014)**.

2.5.1.4 Frontal arrest

The theory of frontogenesis does not explain how it will ultimately be arrested or destroyed. Mechanisms responsible for arrest might be the disappearance of the ambient strain triggering the frontogenesis in the first place, a negative tendency due to the vertical mixing, dissipation by horizontal diffusion, or an instability and eddy-feedback equilibration process. McWilliams & Molemaker (2011) show in a quasi-linear model that baroclinic instability during frontogenesis leads to frontal arrest by an eddy buoyancy-flux feedback.

In the previous cases, the sharpening of the filament is disrupted by fluctuations growing and breaking the along-front regularity of the filament (Fig. 2.49). This evolution is similar for all examples of filaments shown in (Fig. 2.48) The filaments ultimately fragment into a train of submesoscale vortices as a result of the instability process.

The energy source for these unstable perturbations is the horizontal Reynolds stress (as defined in subsection 2.4.1.1), transferring energy from the strong shear in the cross filament direction to the growing perturbations (Fig. 2.55). This is different from the frontal cases discussed in Capet *et al.* (2008b), where baroclinic conversion is the primary cause of the frontal instabilities. However, it is similar to the submesoscale instabilities that were studied in Molemaker *et al.* (2010). The difference in flow regimes where either baroclinic conversion, or barotropic shear conversion are dominant appears to be mostly a matter of horizontal scales. At larger submesoscales, instabilities are predominantly driven by release of potential energy through baroclinic conversion. At smaller horizontal scales, the

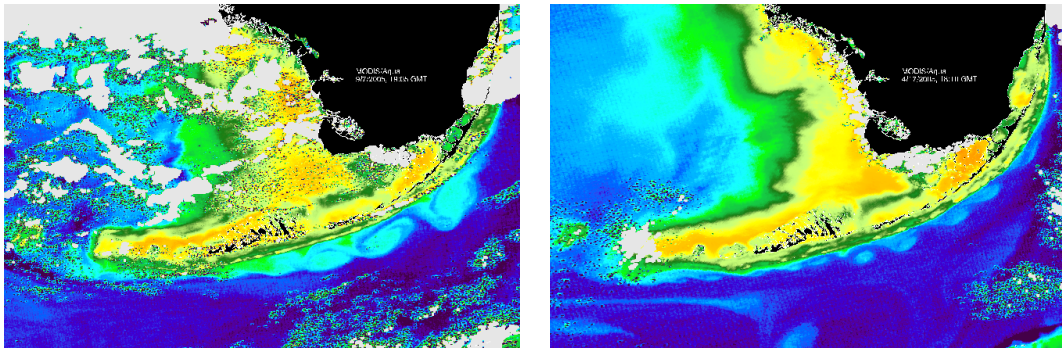


Figure 2.56 – Color index images of the Florida Keys, from MODIS, showing shear instability triggering along the Florida Keys.

horizontal shear grows until the dominant energy source is through horizontal Reynolds stress and barotropic shear conversion. In our case, the sharpening of the fronts that form the filaments is amplified such that they reach scales at which the horizontal shear instability is predominant despite the competition with the mixed-layer baroclinic instability.

This scenario for the frontal arrest has been confirmed using large-eddy simulations of an idealized dense filament by Sullivan & McWilliams (2018). Within less than a day, the frontogenesis is arrested at a small width (≈ 100 m), primarily by an enhancement of the turbulence through a small submesoscale, horizontal shear instability of the sharpened filament, followed by a subsequent slow decay of the filament by further turbulent mixing.

2.5.2 Barotropic Shear instability

Horizontal shear instability is an important mechanism for the arrest of intense filaments, and in general it is a mechanism that appears more and more predominant when we look at smaller and smaller scales. Unbounded flows with sufficiently strong shear layers are known to be unstable (Hide & Tingman, 1967). Following the classic analysis by Rayleigh (1880), an isolated two-dimensional vorticity filament is always unstable and expected to roll up into discrete vortices. However, the presence of a background strain can stabilize the horizontal shear instability of a vorticity filament (Dritschel *et al.*, 1991). The large scale strain field, usually associated with coherent vortices, is an explanation for the long-time persistence of vorticity filaments in a number of laboratory and numerical experiments of two-dimensional turbulence.

2.5.2.1 Shear instability in western boundary currents

There are many examples of horizontal shear instabilities generating submesoscale and mesoscale cyclones in western boundary currents. Such instabilities have been observed along the Florida Keys (Fig. 2.56), in the Gulf Stream between the Florida Straits and the Charleston Bump (Fig. 2.57), or in the Agulhas Current (Fig. 2.60).

The instability in the Gulf Stream has been documented and reproduced using high resolution simulations in **Gula *et al.* (2015b)**, see Fig. 2.58. The flow in the Florida Straits is strongly squeezed against topography, and the strain on the cyclonic side of the Gulf Stream is large south of 27°N where the Stream is in contact with the Florida Coast. The vorticity of the filament after separation of the flow from the coast becomes large compared to the background straining, such that the vorticity filament becomes unstable and rolls up into a string of submesoscale vortices (Fig. 2.58).

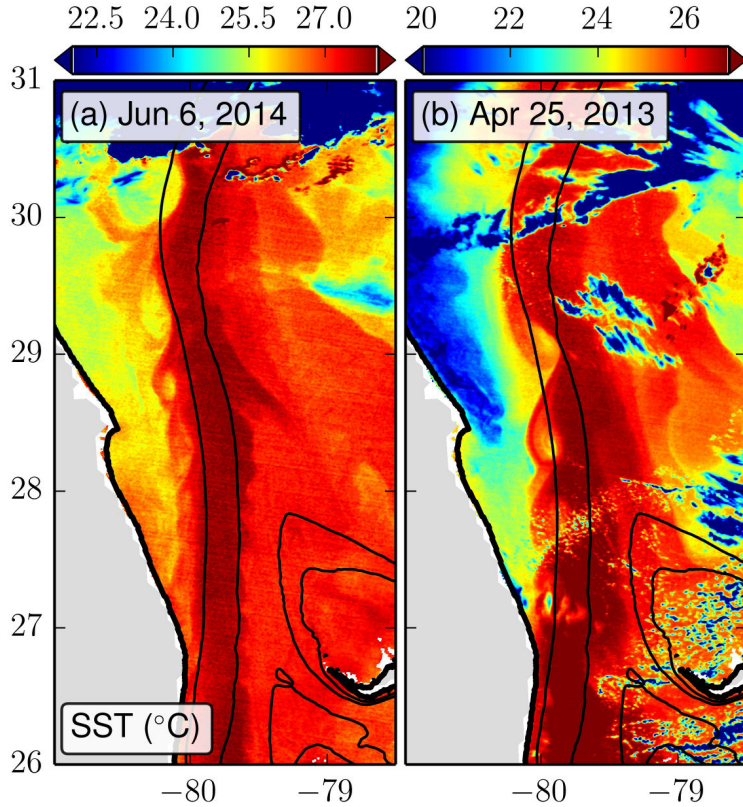


Figure 2.57 – Observed Sea Surface Temperature (SST) of the Gulf Stream along the Florida coast on June 06, 2014 (left), and April 25, 2013 (right). Bahamas contours are visible southeast of the domain. Data from MODIS-AQUA. Notice the Gulf Stream edge fluctuations on the shoreward side. Topography is shown in black contours by the 0 m, 200 m, and 600 m isobaths. From **Gula et al. (2015b)**.

A local eddy-mean analysis at the time of maximum fluctuation amplification (Fig. 2.58b,f) has confirmed that the main energy source for the perturbations is the horizontal shear of the mean flow (HRS). The instability is a larger scale analogous to the horizontal shear instability of submesoscale cold filaments described in subsection 2.5.1.4.

The story is quite similar in the Agulhas Current. Submesoscale cyclonic vortices develop in the region of Port Elizabeth (Fig. 2.60) due to horizontal shear instability processes. This has been first shown using glider measurements in **Krug et al. (2017)**, and the mechanism has been confirmed by a 1D linear stability analysis and an eddy kinetic energy budget with a high-resolution numerical simulation in **Tedesco et al. (2019)**, see Fig. 2.61. There is a remarkable agreement between the partial \overline{HRS} term computed from the glider data (using only cross-front derivative) and the full \overline{HRS} term computed from the model (Fig. 2.62).

As in the Gulf Stream, the spatial variability of barotropic instability is shaped by the background strain. A large strain aligned with the frontal axis intensifies the frontal shear upstream of 28°E and a weakening of the strain allows for the barotropic instability to trigger downstream.

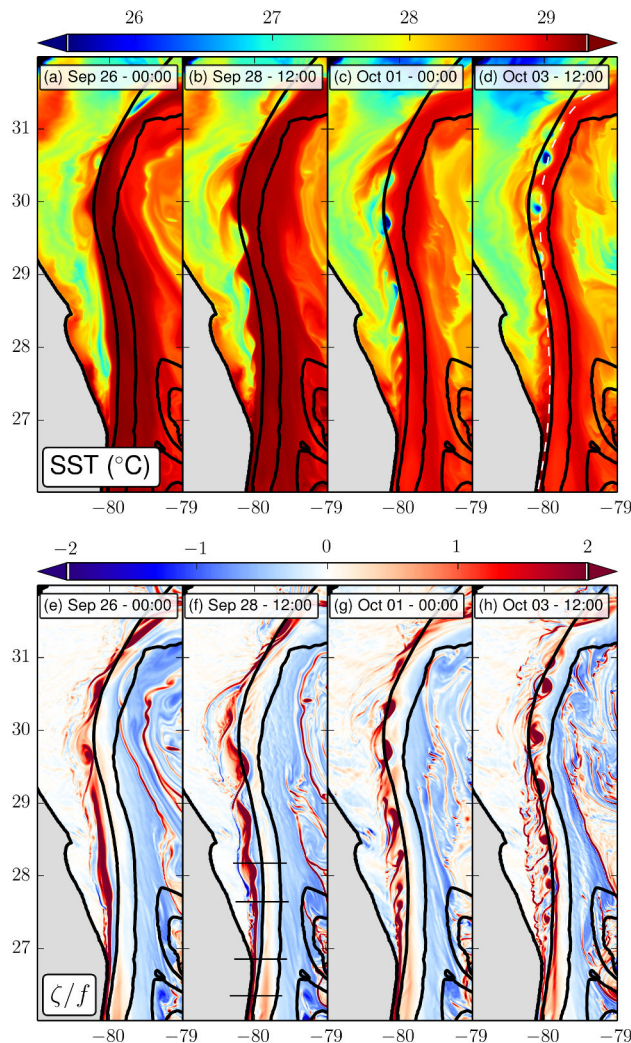


Figure 2.58 – Snapshots of SST (top) and surface relative vorticity normalized by f (bottom) from a model. Barotropic instability of the flow is visible between the Florida Straits and the Charleston Bump in the form of a cyclonic vortex street. Time interval between 2 panels is 2.5 days. Topography is shown in black contours at 0 m, 200 m, and 600 m isobaths. From **Gula et al. (2015b)**.

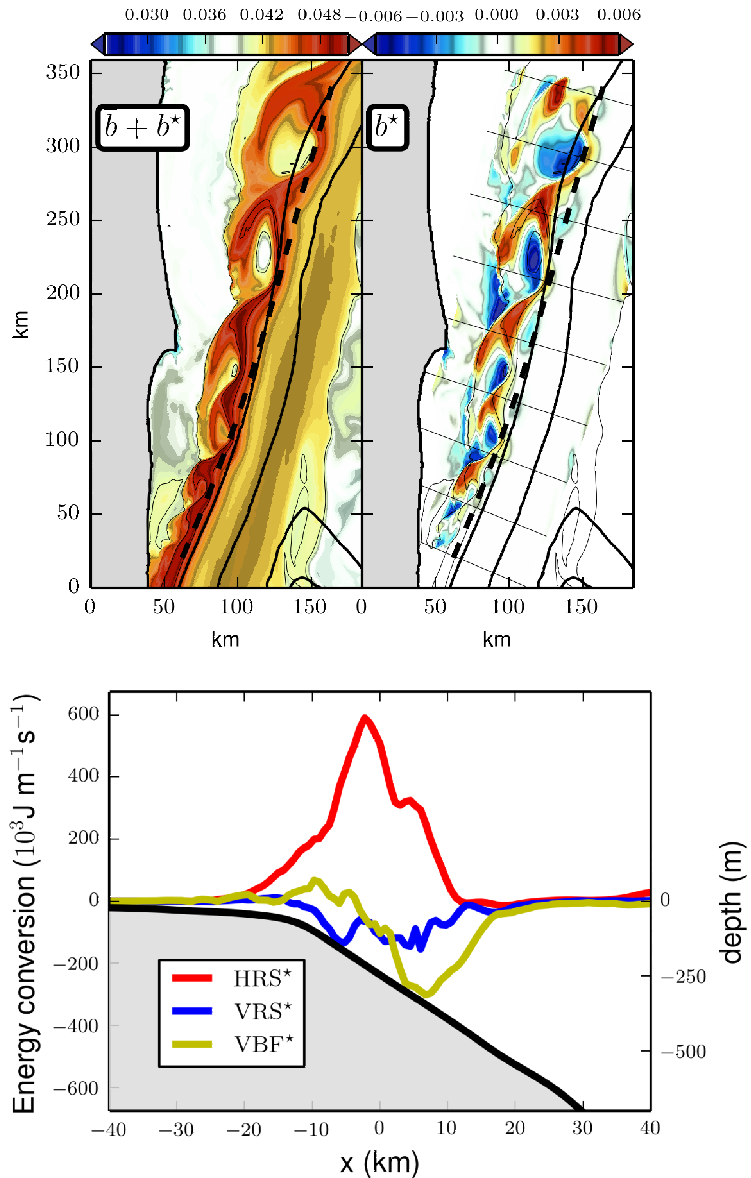


Figure 2.59 – (Top) total surface buoyancy field b with a black dashed line marking the along stream axis (top left), and perturbation field b^* after subtracting the along-front mean profile (top right) at the same time as in Fig. 2.58b. Unit is m s^{-2} . (Bottom) instantaneous local energy conversions profiles HRS*, VRS* and VBF* integrated in the along-stream direction y and in the vertical. The unit of the eddy conversion terms is $10^3 \text{ J m}^{-1} \text{s}^{-1}$. From **Gula et al. (2015b)**.

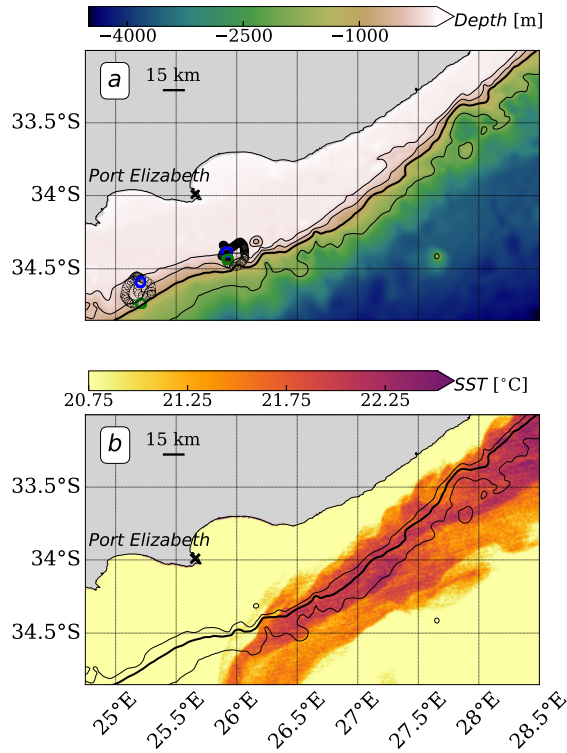


Figure 2.60 – (a) Black circles track two Seagliders when they sampled two submesoscale cyclonic features between the 19-April and the 20-May 2015 (**Krug et al., 2017**). The first and last measures inside these features are respectively marked with green and blue circles. The background colors represent the bathymetry. The thin black lines follow the 200, 500 and 2000 m isobaths. The bold black line is the 1000 m isobath, which corresponds to the Agulhas front location during the SAGE observations. (b) A snapshot of Sea Surface Temperature (SST) [$^{\circ}\text{C}$], from the denoised Moderate-Resolution Imaging Spectroradiometer (MODIS) on the 19-July-2010. The black lines represent the same isobaths than in (a), except for the 200 m which is not represented. Submesoscale meanders develop upstream of Port Elizabeth, between 28.5°E and 26°E . From **Tedesco et al. (2019)**.

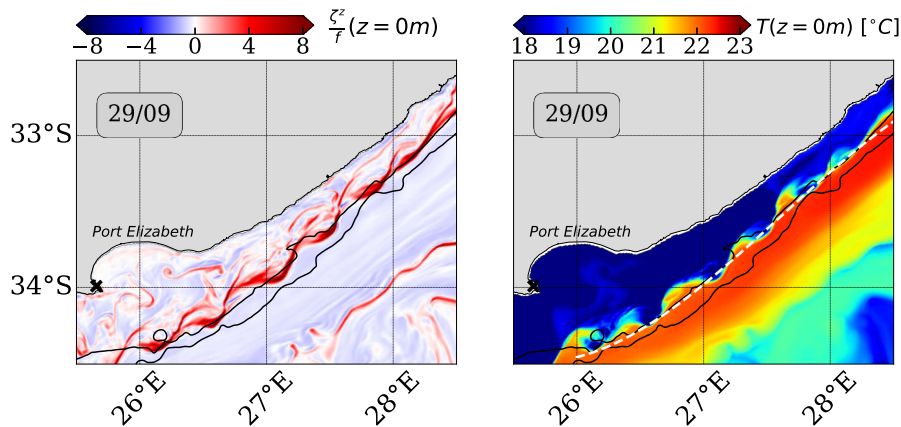


Figure 2.61 – Snapshots of the surface normalized vertical relative vorticity ($\bar{\zeta}$, on the left panel) and of the temperature (T [$^{\circ}\text{C}$], on the right panel) from the model. Black contours are the 200 and 1000 m isobaths. The vortex street develops along the front between 28°E and 26°E . From **Tedesco et al. (2019)**.

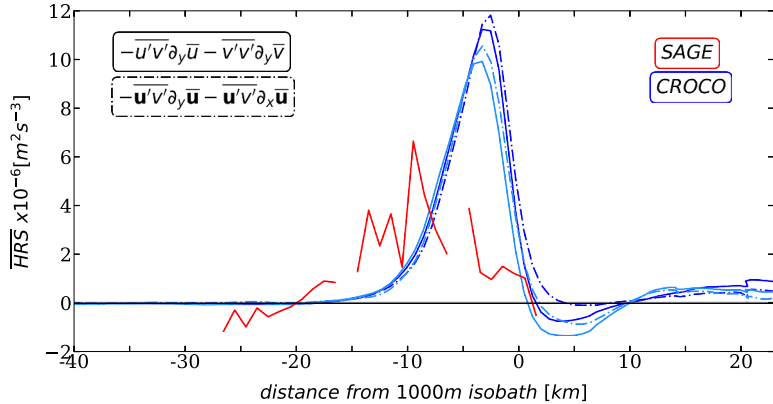


Figure 2.62 – Cross-front sections at the SAGE location (25.75°E , shown in Figure 2.60a) for surface observed (red) and modeled (blue) partial and full \overline{HRS} rate. The partial \overline{HRS} rate, only composed of the cross-front derivatives subterms ($-\overline{u'v'}\partial_y\bar{u} - \overline{v'v'}\partial_y\bar{v}$), is shown for the SAGE dataset as a plain red line and for the model in plain blue lines. The full \overline{HRS} rate, composed of the cross and along-front derivatives subterms ($-\overline{u'v'}\partial_x\bar{u} - \overline{v'v'}\partial_y\bar{u}$) is shown in dashed blue lines. The modeled partial and full \overline{HRS} rates are computed for different time periods : a one-month long (light blue lines) and five consecutive-months without Natal Pulses (dark blue lines). The bottom x-axis represents the cross-front distance from the 1000 m isobath, which represents the front position for the SAGE period. The comparison between the modeled partial and full \overline{HRS} rates shows that the cross-front derivatives are a good *proxy* of the full \overline{HRS} rate. The comparison between the modeled 1 and 5 months averages of the \overline{HRS} rates shows that the submesoscale eddies generation is a locally recurrent process. From Tedesco *et al.* (2019).

2.5.2.2 Inside frontal eddies and Natal Pulses

A very rich submesoscale structure can also be found inside the frontal eddies that are formed in western boundary currents. Such submesoscale features are visible in the observed satellite SST in Fig. 2.43, around the frontal eddy located at ($32.5^{\circ}\text{N}, 77.5^{\circ}\text{W}$). A detailed study of the emergent submesoscale interior of a Gulf Stream frontal eddy in a high resolution simulation is given in Gula *et al.* (2016a). The inside structure of the frontal eddy shows low salinity patches (Fig. 2.44) associated with vortical structures with high relative vorticity values ($\zeta > 2f$, Fig. 2.63).

These vortical structures are submesoscale cyclonic vortices which forms inside the frontal eddy due to a submesoscale instability of the front. The meandering of the front on the downstream face of the trough is an indication of this instability. To identify the nature of the instability processes that generate the intrusions, we can compute the eddy kinetic energy source terms, as defined in subsection 2.4.1.1, between the curved parallel flow and its meandering perturbations in a local reference frame aligned with the front following the methodology described in Gula *et al.* (2014). An example of such a decomposition for buoyancy is shown in Fig. 2.64.

The energy source for the perturbations is the horizontal shear of the mean flow. Other sources like the baroclinic term VBF and the vertical shear stress VRS are small. The vertical structure of the HRS term shows that it is surface-intensified and disappears below 50 m (Fig. 2.64d). The meander-induced frontogenesis sharpens the gradients on the upstream face of the trough, in particular the cross-front velocity shear u_y , and triggers submesoscale barotropic shear instability of the front in the sector where the strain rate is not quite so large.

A schematic summary of the submesoscale phenomena is shown in Fig. 2.65. The strong straining acts to sharpen the velocity gradient as well as stabilizing the barotropic shear instability on the up-

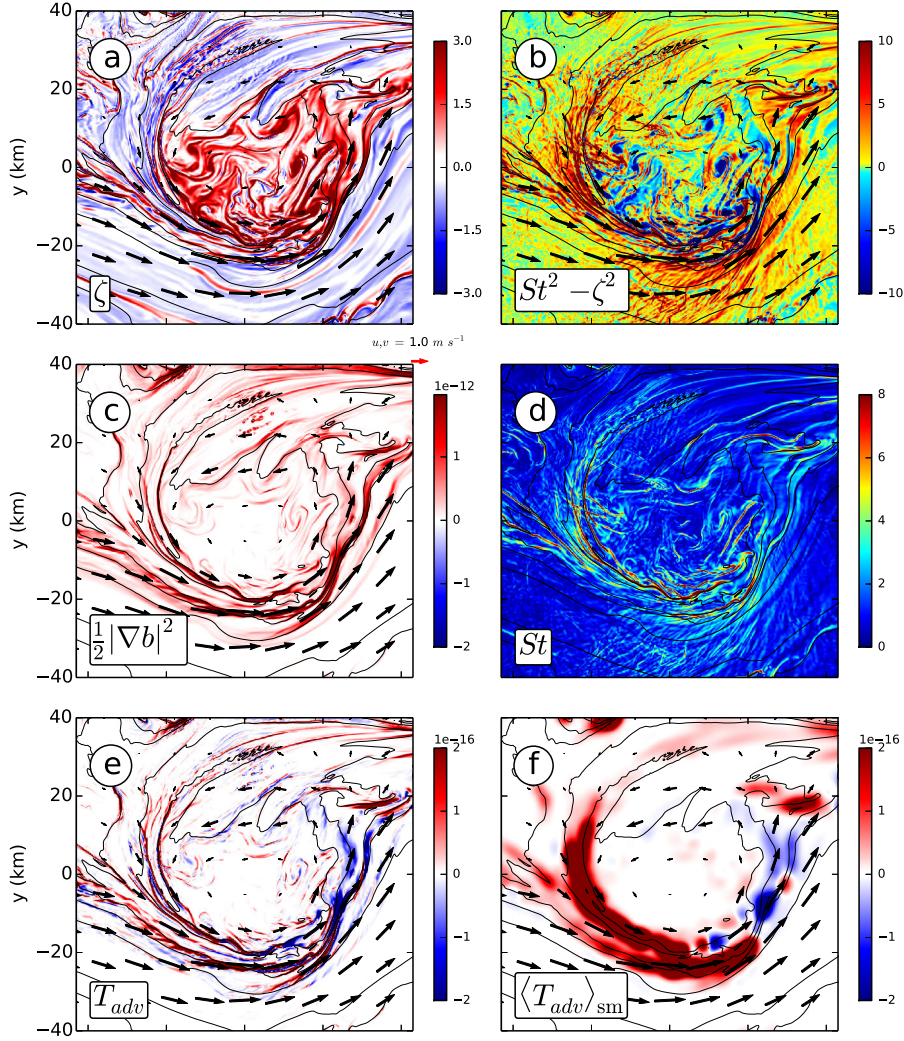


Figure 2.63 – Instantaneous horizontal patterns for the frontal eddy at $z = -10$ m for the frontal eddy of Fig. 2.44: (a) relative vorticity, $\zeta = v_x - u_y$, normalized by f , (b) Okubo-Weiss parameter $St^2 - \zeta^2$, normalized by f^2 , (c) frontal sharpness $0.5 \|\nabla b\|^2$ (*i.e.*, variance of the horizontal density gradient), (d) horizontal strain rate, $St = \sqrt{(u_x - v_y)^2 + (v_x + u_y)^2}$, normalized by f , and (e-f) frontal sharpness tendency due to 3D advection, T_{adv} . (f) is horizontally smoothed by using a convolution with a Gaussian kernel of half-width 5 km. Buoyancy is shown in thin black contours with an interval $2.5 \cdot 10^{-3} \text{ m s}^{-2}$. From **Gula et al. (2016a)**.

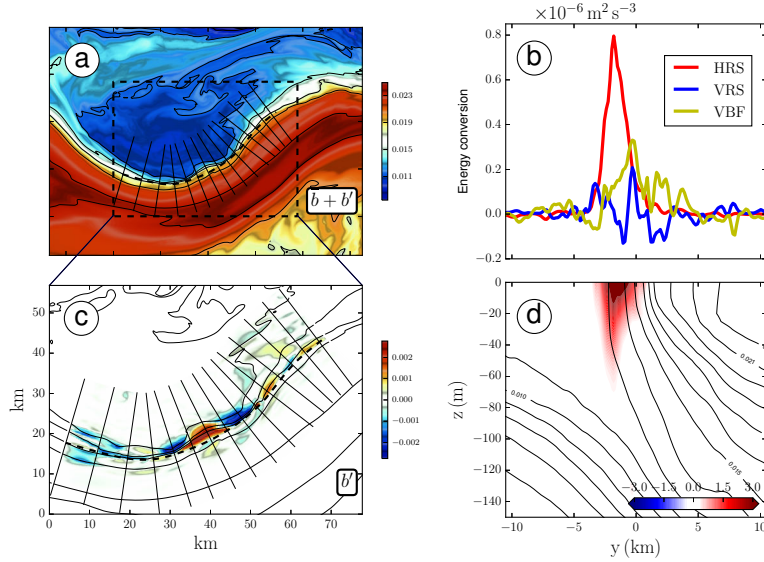


Figure 2.64 – (a) Total surface buoyancy field b with a black dashed line marking the along-front axis and black solid lines individual cross-sections and (c) perturbation field b' after subtracting the along-front mean profile for a frontal eddy. (b) instantaneous local energy conversions profiles HRS, VRS and VBF averaged in the along-front direction and over the upper 200 m and (d) vertical section of HRS averaged in the along-front direction. The unit of the eddy conversion terms is $10^{-6} \text{ m}^2 \text{ s}^{-3}$. From Gula *et al.* (2016a).

stream face of the trough. The strain weakens in the trough, the cross-front perturbations are allowed to grow, and the front becomes unstable. The small-scale meandering perturbations ultimately evolve into rolled-up vortices that are advected back into the interior of the frontal eddy.

Similar submesoscale structures, presumably also generated by horizontal shear instability, are visible in Natal Pulses propagating in the Agulhas Current (Fig. 2.66).

2.5.3 Mixed-layer baroclinic instability

The **mixed-layer instability** (MLI) is an equivalent of the classical interior baroclinic instability, happening inside the mixed-layer (Haine & Marshall, 1999; Boccaletti *et al.*, 2007). It differs from instabilities in the ocean interior because of the weak surface stratification. MLI draw its energy from the lateral buoyancy gradients – the potential energy source – and convert it to eddy kinetic energy. MLI generates horizontal structures at scales close to the mixed-layer Rossby deformation radius (usually around 1 - 10 km) instead of the first Rossby deformation radius (about 30 - 40 km at mid-latitude). It is one of the most important sources of submesoscale currents in the mixed-layer of the ocean, and it has been extensively studied over the last decade using submesoscale resolving numerical simulations (Capet *et al.*, 2008b; Mensa *et al.*, 2013) and more seldomly from in-situ observations (Buckingham *et al.*, 2017). It is a leading-order process in the mixed-layer buoyancy budget, acting to constantly restratify the surface ocean (Boccaletti *et al.*, 2007).

2.5.3.1 Seasonality of the open ocean MLI

High-resolution numerical simulations suggest that submesoscale flows are much stronger in winter than in summer in the region of the Gulf Stream (Mensa *et al.*, 2013). This is illustrated in Fig. 2.67 with snapshots from a simulation of the Gulf Stream region with a horizontal resolution of 750

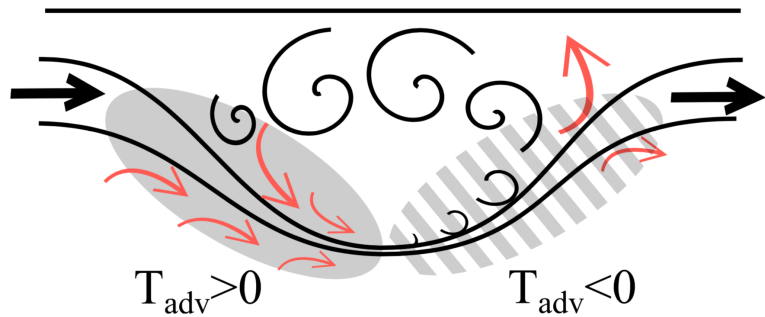


Figure 2.65 – Schematic diagram for the meander-induced frontogenesis, barotropic shear instability, and formation of submesoscale vortices in the propagating trough enclosing the frontal eddy. Black lines show isolines of vorticity and tracers. Perturbations are strain-elongated on the left, meandering in the lower middle, and rolled up vortices on the right. The plain and dashed gray filled area show the positive and negative frontal tendency regions induced by the mesoscale straining of the flow. From Gula *et al.* (2016a).

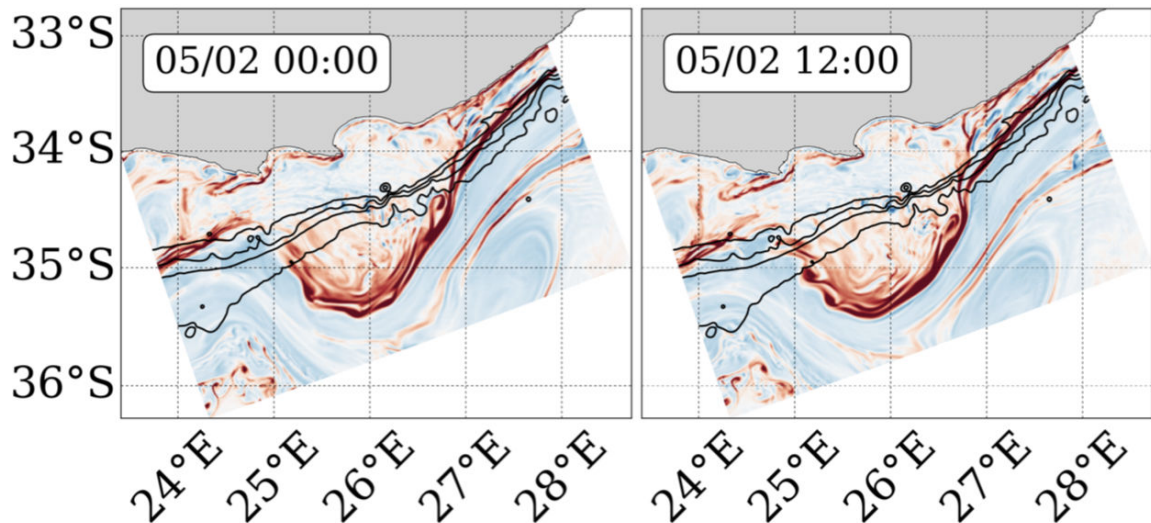


Figure 2.66 – Maps of surface normalized vertical relative vorticity (values between $\pm 2 f$) at snapshots during a Natal Pulse event when submesoscale eddies were seen to develop. Black lines represent the 200, 500, 1000 and 2000 m isobaths. Figure from P. Tedesco.

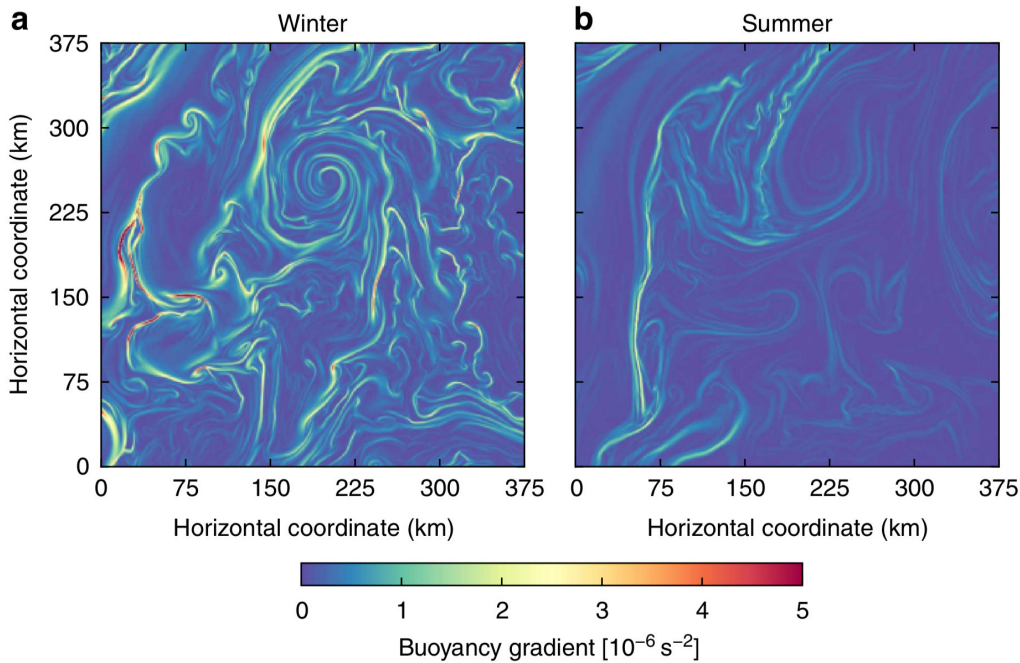


Figure 2.67 – Surface buoyancy gradient magnitudes from a numerical simulation in the Gulf Stream region in (a) winter (February 15) and (b) summer (August 15). The simulation domain is shown Fig. 2.68. Figure from **Callies *et al.* (2015)**.

m. The snapshots of surface buoyancy gradients show that fronts are strong in winter and much less pronounced in summer, except for the Gulf Stream front that persists throughout the year.

Surface kinetic energy spectra in the Sargasso Sea – the region of the open ocean excluding the Gulf Stream – are confirming this strong seasonal cycle (Fig. 2.69). The submesoscale energy levels are significantly higher in winter than in summer. This seasonal difference in submesoscale energy levels is reflected in how rapidly the energy falls off with wavenumber in the submesoscale range. In winter, the spectra are relatively flat and approximately follow a k^{-2} power law. In summer, the spectra in the range 20–100 km fall off more rapidly and approximately follow a k^{-3} power law.

This seasonal cycle is due predominantly to the mixed-layer baroclinic instabilities. In winter, when the mixed layer is deep (Fig. 2.70), instabilities grow on a time scale of about 1 day and at a horizontal scale between 1 and 10 km, subsequently energizing the entire submesoscale range through turbulent scale interactions. In summer, the mixed-layer is very shallow (Fig. 2.70), the instability is either damped out or fails to energize the submesoscale range because of the lack of a strong inverse cascade, when the mixed layer deformation radius (NH/f) is very small.

Observational evidence of this seasonal cycle for the submesoscale flows in the surface mixed layer have been presented in **Callies *et al.* (2015)** using data collected as part of two separate observational programmes: the Oleander project along a transect between Elisabeth, New Jersey, and Hamilton, Bermuda, occupied weekly in 2005–2013, and the Lateral Mixing Experiment (LatMix) along several straight transects off Cape Hatteras in June 2011 (summer) and just south of the Gulf Stream extension in March 2012 (winter) (Fig. 2.68).

Kinetic energy spectra computed from the data exhibit the same seasonal cycle than the simulations (Fig. 2.71). The winter spectra are consistent with turbulent dynamics induced by mixed-layer instabilities. In summer, the steep energy spectra are consistent with interior quasi-geostrophic turbulence. At scales smaller than 20 km, the spectra flatten out and roughly match the Garrett–Munk

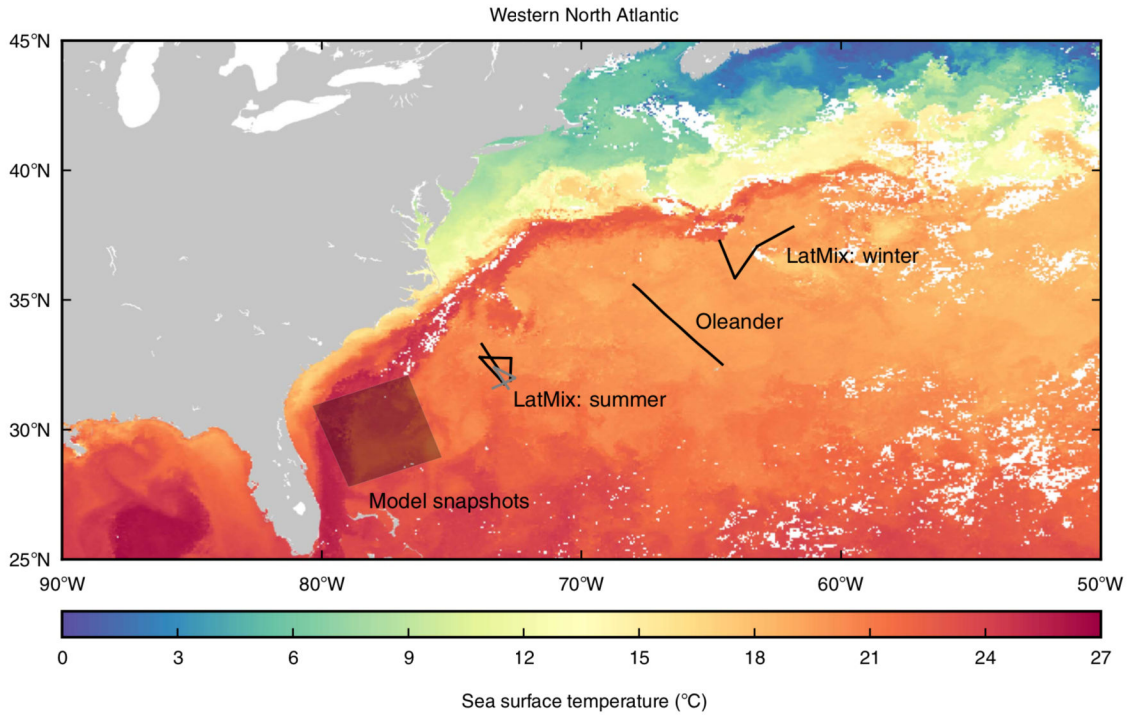


Figure 2.68 – Locations of velocity transects (black lines), of additional buoyancy transects (dark gray lines) and of the model snapshots shown in Fig. 2.67 (transparent shading). The colour shading shows sea surface temperatures on 13–20 March 2012 (8-day L3 MODIS Aqua composite of 4 mm nighttime temperature). Missing data are indicated by white shading. Figure from Callies *et al.* (2015).

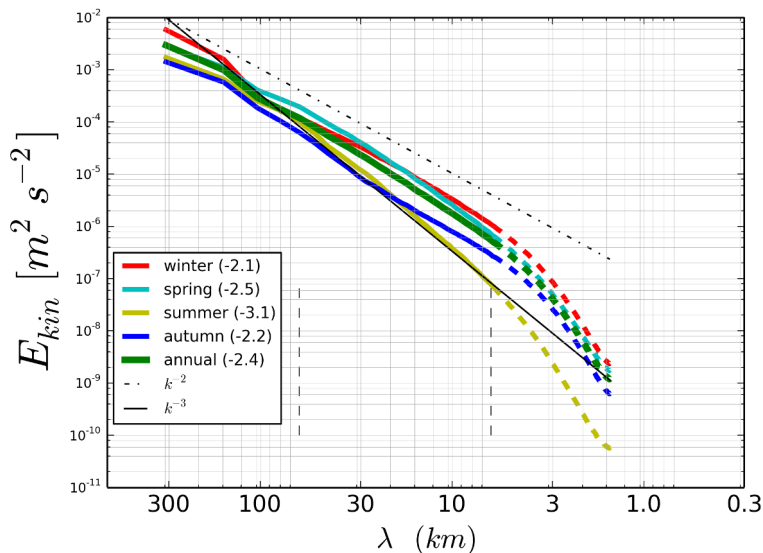


Figure 2.69 – Kinetic energy spectra for the domain of Fig. 2.68 excluding the Gulf Stream front averaged for the 4 seasons. The exponent n corresponding to the best k^{-n} fit between the dashed lines is indicated between parentheses.

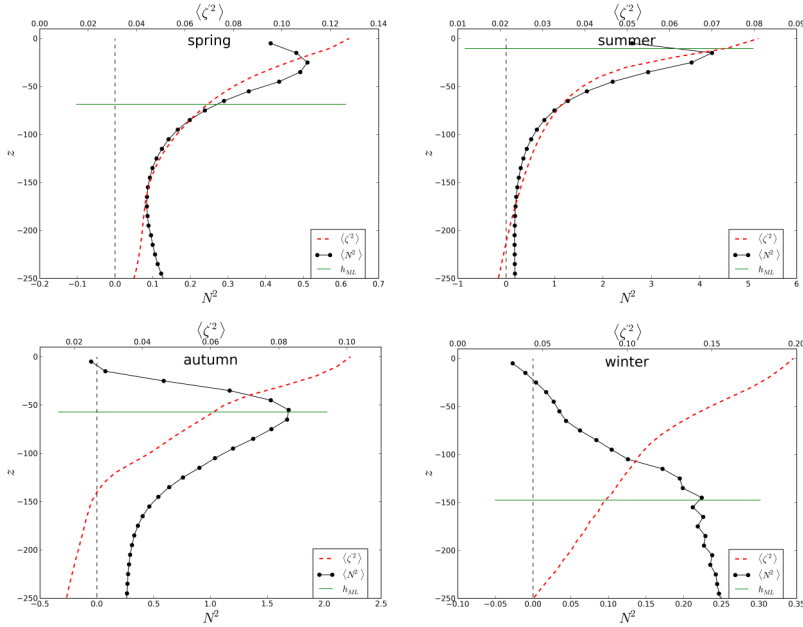


Figure 2.70 – Seasonal stratification, mixed-layer depth, and relative vorticity variance computed south of the Gulf Stream.

(GM) empirical model spectrum of internal waves (Munk, 1981). The emergence of this GM spectrum at scales below 20 km confirms that internal waves dominate these scales and mask an even more dramatic drop-off of geostrophic submesoscale motions in summer.

Inside the Gulf Stream, the dynamics is different than in the open ocean (Fig. 2.72). The submesoscale currents are driven primarily by the mesoscale-driven surface frontogenesis mechanism. The frontogenesis only depends on the presence of the jet and mesoscale eddy field, which do not undergo a strong seasonal cycle.

2.5.3.2 MLI inside the Gulf Stream

Some specific events of submesoscale instabilities inside the Gulf Stream have also been successfully sampled during the field experiments by the Office of Naval Research ("LATerally MIXing") in 2012 (Fig. 2.73). The 2012 LATMIX campaign is partly described in **Klymak et al. (2016)**. It consisted in high-resolution measurements of the north wall of the GS from 66°W to 60°W, about 850 km east of where the GS separates from the North American continental slope. A Lagrangian float was placed in the Gulf Stream front based on a brief cross-stream survey and programmed to match the density of the surface mixed layer (upper 30 m). The float moved downstream at a mean speed of 1.4 m/s. The R/V Knorr tracked the float and deployed a Chelsea Instruments TriAxus that collected temperature, salinity, and pressure (CTD) on a 200 m deep sawtooth with approximately 1 km lateral spacing in a 10 km box-shaped pattern relative to the float (Fig. 2.73, red). R/V Atlantis performed larger cross sections approximately 30 km across the front, trying to intercept the float on each front crossing (Fig. 2.73, magenta). R/V Atlantis was deploying a Rolls Royce Marine Moving Vessel Profiler equipped with a CTD that profiled to 200 m approximately every 1 km.

Signatures of instabilities are visible as submesoscale structures associated with cold water intrusions on the North Wall of the Gulf Stream in satellite images (Fig. 2.74, left). The R/V Atlantis have sampled through these intrusions on several occasions. The intrusions are visible in the vertical sections of temperature (Fig. 2.74, right), as the mixed layer water interleaves, with cold water entrained

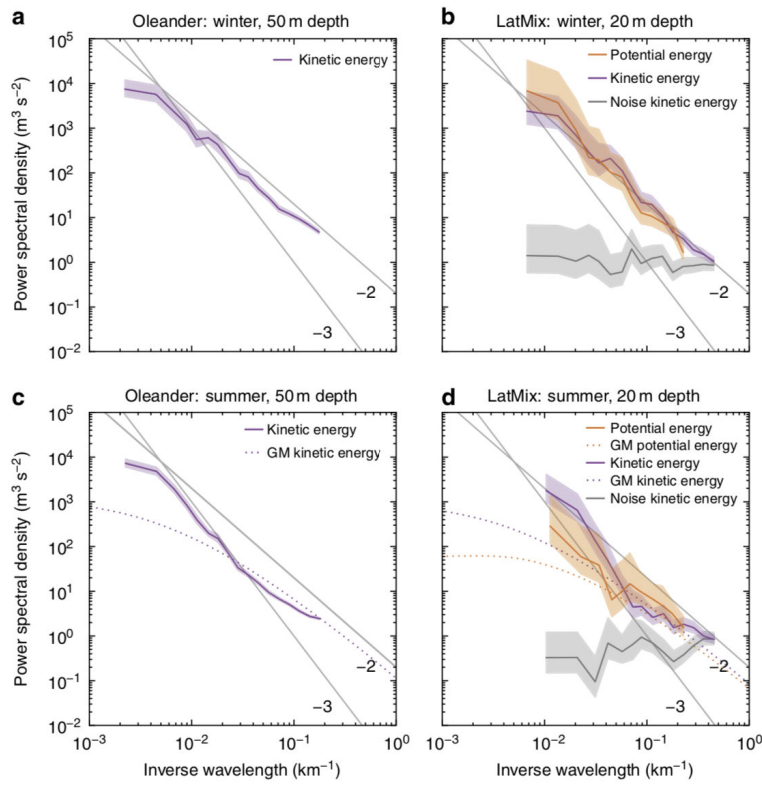


Figure 2.71 – (a) Kinetic energy spectrum at 50 m depth for the Oleander winter data. (b) Potential and kinetic energy spectra at 20 m depth for the LatMix winter experiment. (c) Kinetic energy spectrum at 50 m depth for the Oleander summer data. (d) Potential and kinetic energy spectra at 20 m depth for the LatMix summer experiment. The light shadings are 95% confidence intervals. Also shown are the GM model spectra for internal waves in the seasonal thermocline. Figure from **Callies et al. (2015)**.

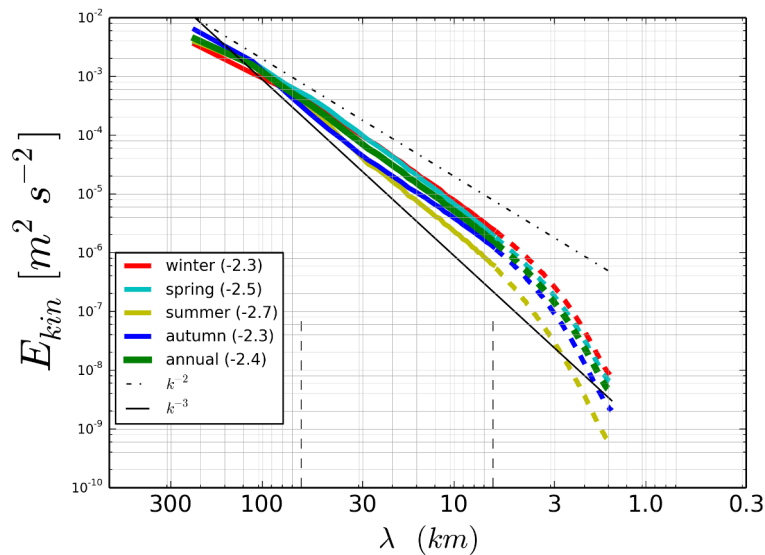


Figure 2.72 – Kinetic energy spectra for a region centered on the Gulf Stream front averaged for the 4 seasons. The exponent n corresponding to the best k^{-n} fit between the dashed lines is indicated between parentheses.

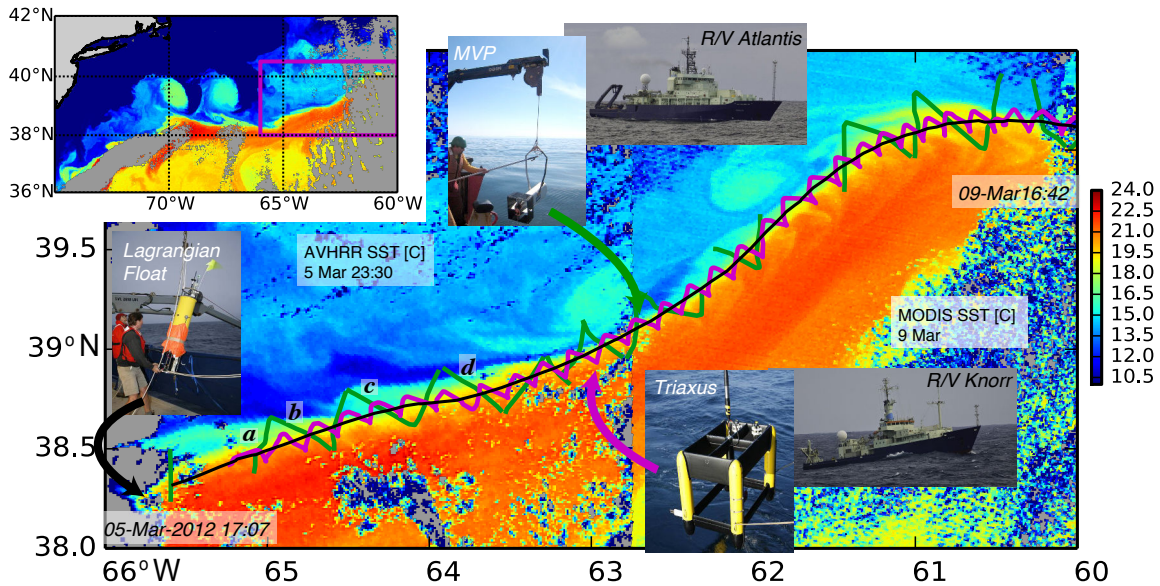


Figure 2.73 – Observed Sea Surface Temperature (SST) of the Gulf Stream on March, 8th 2012, during the Latmix campaign. Data from MODIS-AQUA. Notice the Gulf Stream edge fluctuations on the North Wall. Figure from **Klymak et al. (2016)**.

and warm water detrained from the main stream. These instabilities are confined to the mixed layer, which is here about 100 m deep, and do not appear to have a signature in the deeper water. These signatures are thus different than the streamers described in **Klymak et al. (2016)**, which penetrate deeper than the mixed-layer and are related to horizontal shear instability.

A more detailed identification of the instability mechanism is difficult to achieve using the limited in-situ observations. However we can rely on submesoscale-resolving realistic simulations of the Gulf Stream which have been performed in parallel of the campaign. A simulation of the Gulf Stream North-Wall performed during wintertime using the ROMS model with $\delta x = 500$ m (see a vorticity snapshot in Fig. 2.5) is able to reproduce the observed cold intrusions and can be used to investigate the energy source for the generation of these submesoscale currents (Fig. 2.75).

To identify the nature of the instability processes that generate the intrusions, we can compute the eddy kinetic energy source terms (as defined in subsection 2.4.1.1) between the curved parallel flow and its meandering perturbations in a local reference frame aligned with the front following the methodology described in **Gula et al. (2014)**. The dominance of the VBF term associated with its vertical structure demonstrate that these instabilities are indeed MLIs. They are acting to restratify the Gulf Stream mixed-layer as well as exchanging water laterally across the Gulf Stream North Wall. The actual cross-front transport they mediate as well as their potential contribution to the formation of "18°Water" remain to be quantified.

An interesting property of these cross-wall intrusions is that they are more prevalent in specific sections of the Gulf Stream meanders. They are usually visible in the meander sector downstream of the trough, but not in the meander sector upstream of the trough (Fig. 2.75). As explained in **McWilliams et al. (2019)**, the sharpness of the North Wall front is modulated depending on the phase of the meander. The front is sharper in the meander sector upstream of the trough, where the positive straining and frontogenetic tendency act to increase gradients in the cross-front direction. Downstream of the trough, the frontolytic tendency weakens cross-front gradients and allows cross-front perturbations to grow. The instability is thus stabilized upstream of the trough and develops preferentially upstream of the trough (Fig. 2.77).

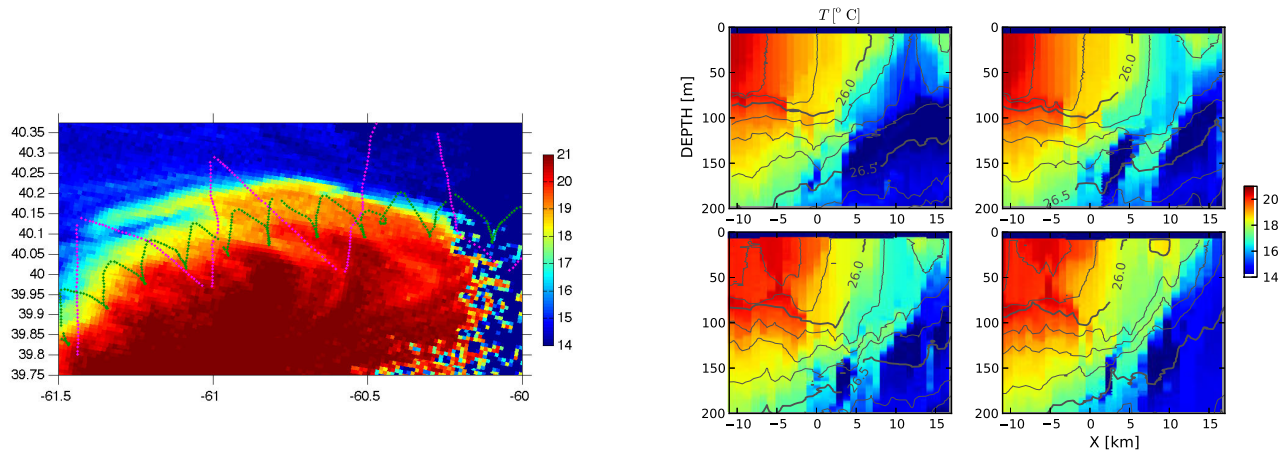


Figure 2.74 – (Left) Observed Sea Surface Temperature (SST) of the Gulf Stream on Mar 08, 2012 at the top of a meander. Data from MODIS-AQUA. MLI are visible as cooler water intruding into the Gulf Stream. (Right) Temperature sections through the instabilities showing that they are confined to the mixed layer.

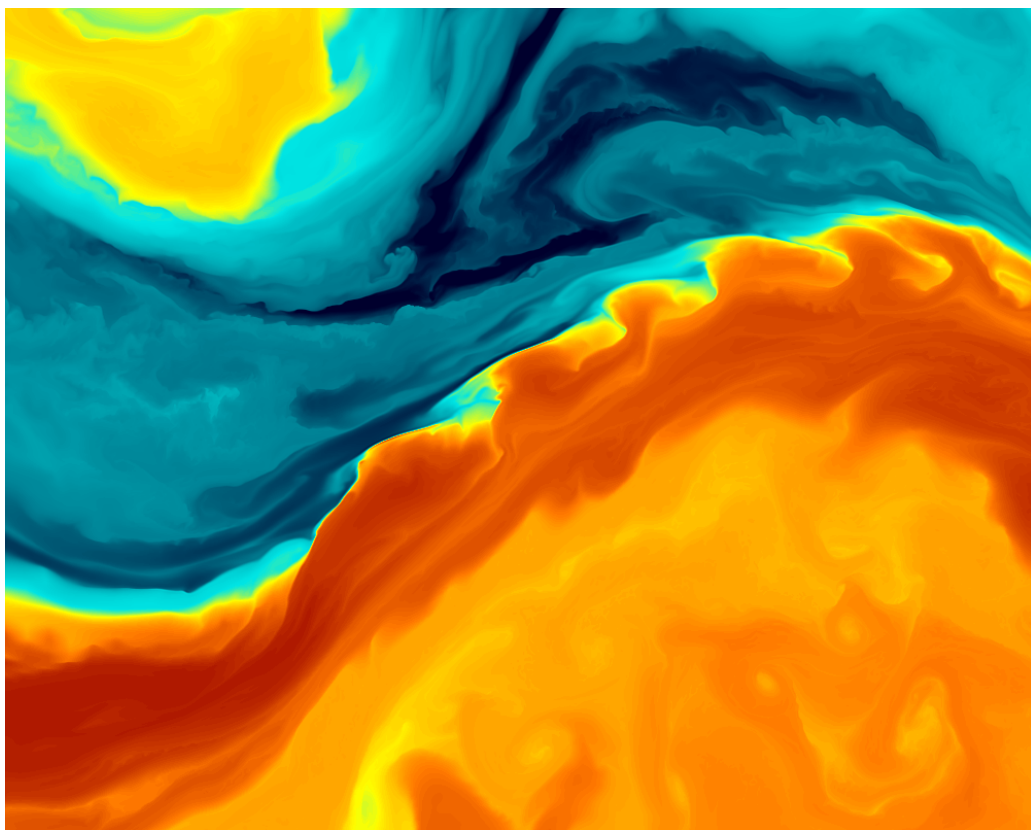


Figure 2.75 – Simulated Sea Surface Temperature (SST) for a section of the Gulf Stream North Wall showing submesoscale baroclinic "commas" instabilities.

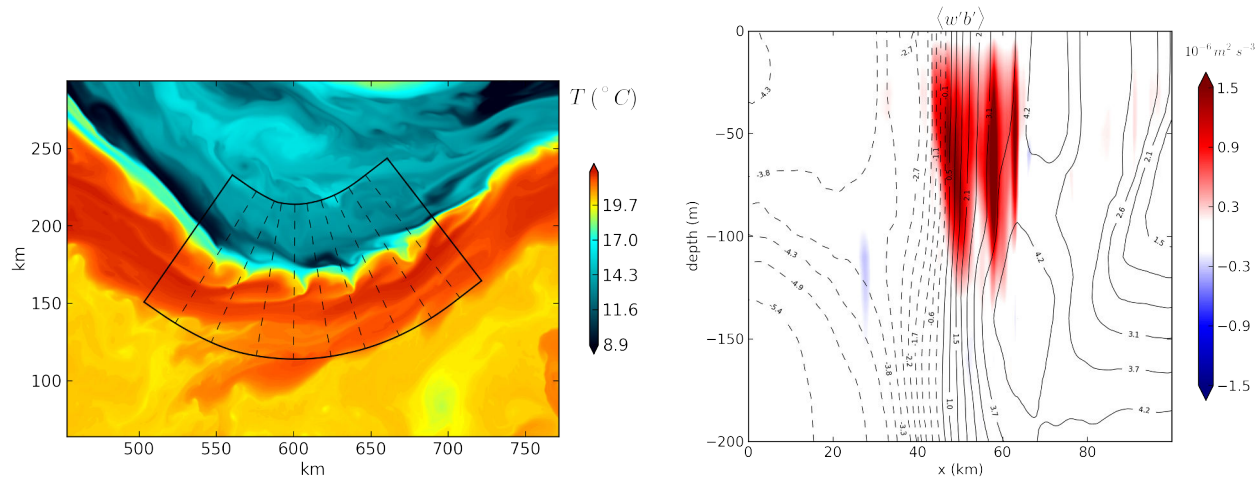


Figure 2.76 – (a) Modeled SST and (b) VBF = $\langle w'b' \rangle$ term averaged in the along-front direction.

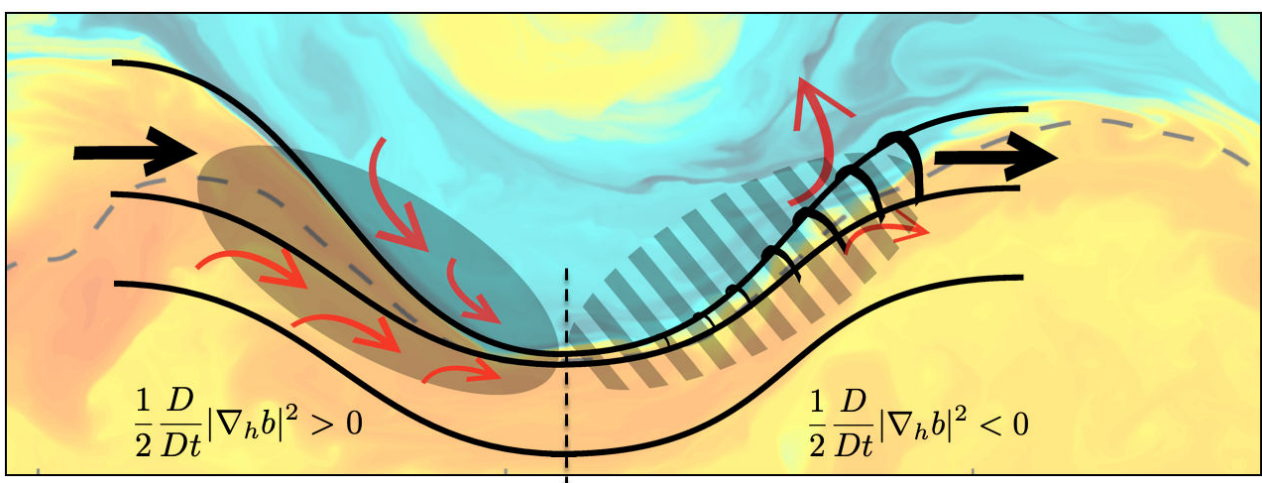


Figure 2.77 – Schematic of the effect of mesoscale straining on the development of the instability.

2.5.4 Interpreting the energy cascade

How do the various submesoscale processes contribute to the energy cascade?

On one hand, the **mixed-layer baroclinic instability** is a mostly balanced process that is expected to drive a **turbulent inverse energy cascade** (Boccaletti *et al.*, 2007). It is similar to what happens for the classical interior baroclinic instability, except that energy is injected at a scale close to the mixed-layer Rossby deformation radius (usually around 1 - 10 km) instead of the first Rossby deformation radius (about 30 - 40 km at mid-latitude). From there, energy will cascade toward larger scales through merging of eddies.

On the other hand, **ageostrophic processes** drive a **forward energy cascade** en route to dissipation. Frontogenesis is an efficient mechanism to cascade energy to small scales (Capet *et al.*, 2008c; Molemaker *et al.*, 2010). Ageostrophic instabilities like frontal shear instability, gravitational, symmetric or centrifugal instabilities are also efficient to drive a direct cascade toward smaller scales and dissipation (D'Asaro *et al.*, 2011; Thomas *et al.*, 2013), eventually by triggering secondary instabilities such as Kelvin-Helmholtz instabilities (Taylor & Ferrari, 2009).

In the following subsections, we will diagnose the direction and intensity of the energy cascade using realistic submesoscale-resolving simulations.

2.5.4.1 The spectral approach

The traditional approach is to diagnose the direction of energy fluxes in the Fourier space by computing the kinetic energy spectral flux. This is done by integrating in k the advective term in the energy balance and assuming that the flux vanishes at the highest wavenumber, k_{max} :

$$\Pi(k)_{sp} = \int_k^{k_{max}} -\hat{u}_h^* \cdot (\widehat{u_h \cdot \nabla}) u_h dk \quad (2.13)$$

An inverse transfer to larger scales corresponds to $\Pi(k)_{sp} < 0$, and a forward transfer to smaller scales and dissipation to $\Pi(k)_{sp} > 0$. Example of kinetic energy spectral fluxes are shown for different regions in Fig. 2.78. All of the small-submesoscale nested grids show a robust forward KE cascade range, with inverse cascade at larger scales, but only if the divergent part of the flow is included in the calculation.

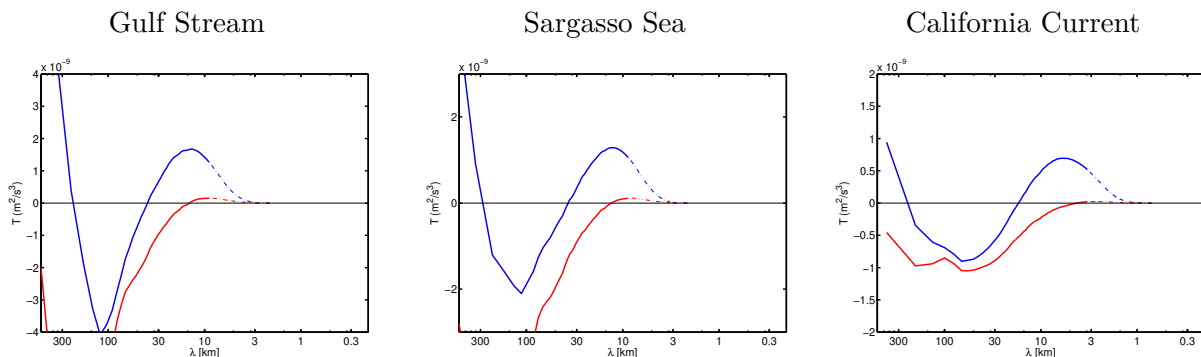


Figure 2.78 – Kinetic energy spectral flux $\Pi(k)_{sp}$ at the surface for simulations of the Gulf Stream ($dx = 500$ m), Sargasso Sea ($dx = 500$ m), and California Current ($dx = 150$ m). The blue line is computed using the total velocity ($u = u_r + u_d$), the red line using only the rotational part of the flow (u_r) .

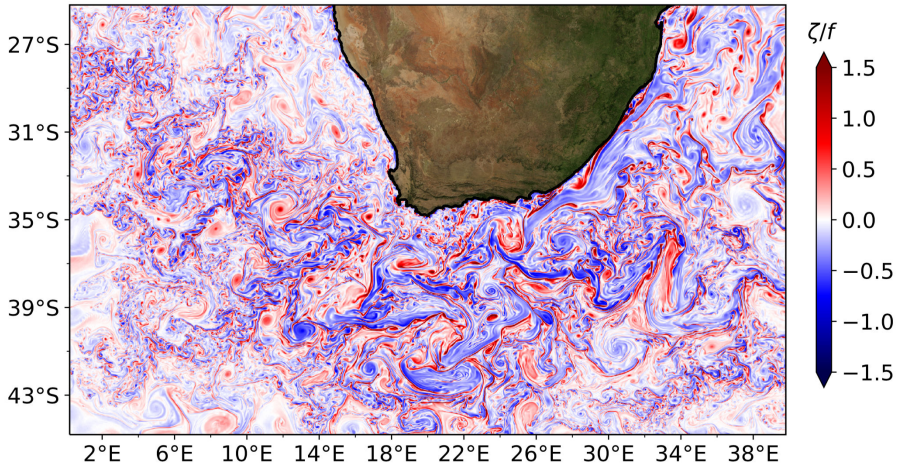


Figure 2.79 – Snapshot of relative vorticity normalized by f in the $1/60^\circ$ domain. Figure From **Schubert et al. (2019a)**.

2.5.4.2 The coarse-graining approach

The kinetic energy spectral flux has some limitations as it relies on hypothesis of a homogeneous and isotropic turbulence as well as zero flux at the smallest scales. An alternative way to diagnose energy fluxes uses the **coarse-graining approach** (Leonard, 1975; Germano, 1992), which allows a direct quantification of the energy fluxes between different spatial scales and is suitable for spatially inhomogeneous flows. The method is widely used in fluid dynamics, but its application to physical oceanography is quite recent (Aluie *et al.*, 2018). The principle is to apply a spatial filter, either in a form of gaussian or top-hat filter with a specific length scale l , to the dynamical equations. Then, one can derive an equation for the coarse-grained or (low pass) kinetic energy of the flow, which contains all length scales larger than l . The equation will include an energy flux term $\Pi(k)_{cg}$ which quantifies the energy transferred from scales smaller than l to the coarse-grained flow. The advantages of this method are that it does not require any hypothesis on the turbulence regime and can be applied locally in space and time.

2.5.4.3 Application to the Agulhas Current

The following results are part of an ongoing work undertaken in collaboration with R. Schubert and A. Biastoch (GEOMAR, Kiel, Germany). An article have recently been submitted (**Schubert et al., 2019a**).

We use a set of NEMO nested simulations in the Agulhas Current region. The higher resolution nest is $1/60^\circ$ (Fig. 2.79). The simulations setup is described in Schwarzkopf *et al.* (2019). The dynamics of the submesoscale permitting nest is described in more details in Schubert *et al.* (2019b). It is shown that the mesoscale dynamics is more realistic when small-scale features are resolved. Results of an eddy-detection algorithm applied to the model outputs as well as to a gridded sea-surface height satellite product show that in particular strong cyclones are much better represented when submesoscale flows are resolved in the model (Schubert *et al.*, 2019b). The impact of submesoscale dynamics on the mesoscale structures prompted a more detailed analysis of the direction of energy fluxes in the presence of submesoscale and how the different submesoscale dynamical processes could contribute an inverse or a direct energy cascade.

Surface scale energy fluxes have been computed using both a spectral and a coarse-graining approach from the model outputs (Fig. 2.80). They attribute the strengthening of the mesoscale eddies

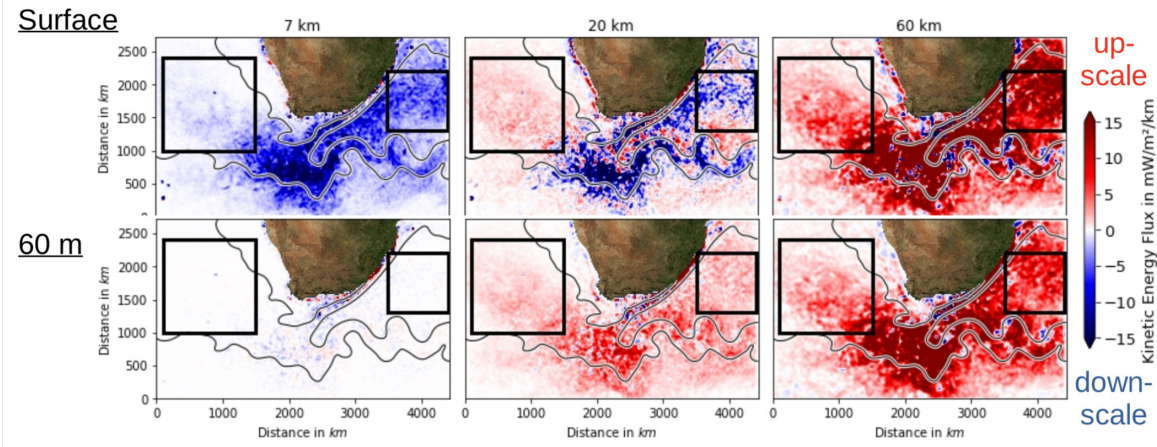


Figure 2.80 – Kinetic energy fluxes across different scales: 7 km, 20 km, and 60 km, from left to right, at the surface (top) and 60 m depth (bottom) for a winter snapshot for the $1/60^\circ$ simulation. Red indicates a transfer of energy towards larger scales (inverse cascade) and blue indicates a transfer of energy towards smaller scales (direct cascade). Figure from **Schubert et al. (2019a)**.

to the almost full resolution of the inverse cascade in the $1/60^\circ$ configuration. A strong inverse cascade is found to reach down to scales of 10 km, especially in the open-ocean, and follows a strong seasonal cycle with much stronger upscale fluxes in winter-time. This inverse cascade leads on average to 7 times more energy flux into mesoscales larger than 100 km in the $1/60^\circ$ model compared to the $1/20^\circ$ model without submesoscale activity.

This inverse cascade at small scales is mostly driven by MLI, as seen from the vertical structure of the fluxes (Fig 2.81) as well as their spatial location and seasonality. On the other hand, the downscale fluxes triggering a direct cascade are intensified at the surface at small scales (Fig 2.81). Horizontal maps are showing that these fluxes are intense in frontogenetic regions. They are triggered by frontogenesis processes and ageostrophic instabilities like symmetrical instability.

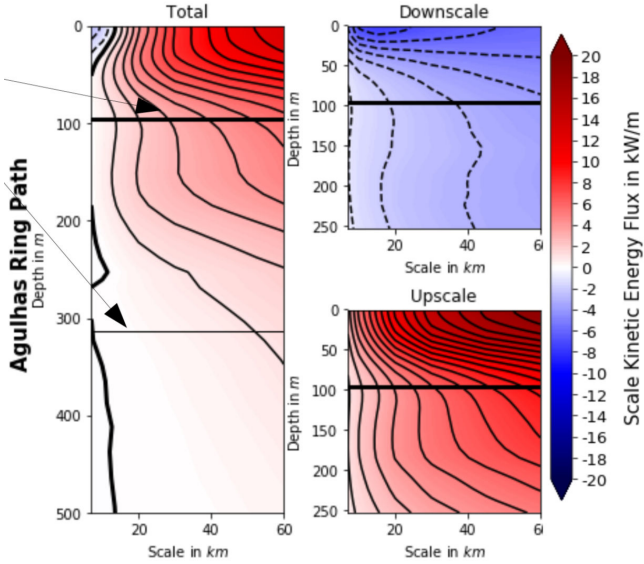


Figure 2.81 – Kinetic energy flux versus scale l at different depths for a winter snapshot of the $1/60^\circ$ simulation in the Agulhas ring path (left box in Fig. 2.80). Red indicates a transfer of energy towards larger scales (inverse cascade) and blue indicates a transfer of energy towards smaller scales (direct cascade). The arrows indicate the mean and maximum mixed-layer depth. Figure from **Schubert et al. (2019a)**.

2.6 Surface signature of submesoscale processes and internal waves

In this subsection I present works related to the surface signature of submesoscale processes and internal waves in the velocity and SSH fields, which include results on the separation between balanced and unbalanced motions (subsection 2.6.1), the modulation of the internal tides signature at the surface by the stratification (subsection 2.6.2) and the surface signature of lee waves (subsection 2.6.3). Some of these results have been published in **Chelton et al. (2019); Lahaye et al. (2019a); De Marez et al. (2019)**, which include the studies led by N. Lahaye during his postdoctoral studies and by C. De Marez during his M2 internship, as well as some unpublished works.

2.6.1 Separation between balanced and unbalanced motions

Submesoscale currents are difficult to measure as they are too small for most satellite footprints, and in particular the current generation of satellite altimeters (≈ 100 km). In the near future, satellite measurements from the Surface Water and Ocean Topography mission (SWOT, Fu & Ferrari, 2008) will provide a global coverage of SSH at unprecedented resolution (a few 10s km). However, reconstructing the geostrophic surface velocity from SSH is a challenging task at these scales. An extensive study on the capability of the SWOT mission, as well as the Doppler scatterometer mission WaCM, to measure the ocean surface velocity and vorticity is given in **Chelton et al. (2019)**.

One important issue is the presence of unbalanced motions, such as internal waves and ageostrophic submesoscale currents, in the SSH field, which contaminates the estimates of the surface geostrophic velocity. Our ability to compute the geostrophic surface velocity from SSH measurements will thus depend on our capacity to disentangle the signals associated with balanced and unbalanced motions.

To estimate the scales at which the geostrophic approximation is valid, we can compute the energy spectra for the rotational and divergent part of the flow, as well as for the currents estimated from geostrophic and cyclogeostrophic approximations, for a realistic simulation including the impact of

high-frequency wind forcings and internal tides. We show below results for the Sargasso Sea (Fig. 2.82), which has active mesoscale eddies driven by the nearby Gulf Stream, and a strong seasonal cycle of submesoscales at the surface. The simulation includes a realistic level of internal waves (including near-inertial waves, lee waves, and internal tides) as seen from a comparison with the Garret-Munk Spectra.

The surface velocities are decomposed into a divergent and a non-divergent (rotational) part using a Helmholtz decomposition of a 3D incompressible flow. The divergent part of the flow is computed by solving a Poisson equation for the divergence of the flow using a multigrid solver with Dirichlet boundary conditions. The rotational part of the flow is not formally equal to the geostrophic part but can be considered as a good proxy. We can compare the importance of the divergent and rotational parts by looking at their respective power spectra (Fig. 2.82). The ratio of divergent to rotational energy gives a good indication of the degree to which the flow is balanced. The ratio should be small (< 0.1) for geostrophically balanced flow and become larger as non-balanced ageostrophic dynamics related to intense vortices, fronts, instabilities, and internal waves become important. The ratio increases as the wave length decreases and peaks at a scale limited by model diffusion (estimated as 8 dx and shown by dashed lines in Fig. 2.82). The ratio is close to zero and the flow mostly balanced for the large mesoscales (> 100 km), but becomes significant (> 0.1) at scales smaller than 50 km.

There is a strong seasonal variation of this ratio, related to the strong seasonal cycle of submesoscales in this region (**Callies et al., 2015**). During winter the mixed-layer is deeper and efficiently feed energy to the partially balanced submesoscale currents through mixed-layer instability. During summer the mixed-layer is very shallow and submesoscale currents are weaker, often dominated by internal waves. This reflects into the ratio of divergent to rotational velocities (Fig. 2.82), which is much larger in summer than in winter. In the summer season the ratio becomes larger than 0.1 at scales smaller than about 100 km. This is similar to the seasonal cycle observed in other regions of the world such as the Northwestern Pacific (Rocha *et al.*, 2016a; Qiu *et al.*, 2017) or the Drake Passage (Rocha *et al.*, 2016b). The transition scale between the balanced and unbalanced motions will strongly depend on the local dynamics, which varies between regions and seasons. This transition scale has been estimated globally in Qiu *et al.* (2018); Torres *et al.* (2018).

2.6.2 The signature of internal waves at the surface

Another factor in the seasonal variation of the transition scale between the balanced and unbalanced motions is that the internal waves can be surface-amplified in summer. A mechanism has been proposed by D'Asaro (1978), to show that the presence of a mixed layer and underlying density gap could support the existence of interfacial waves excited from the interior wave field, resulting in a drastic amplification of the surface kinetic energy near the surface.

We have tested this mechanism in **Lahaye et al. (2019a)** using results from high-resolution realistic simulations over the north Mid-Atlantic Ridge, which is a region with energetic tides. Taking the ratio of the spectral density in summer over the one in winter clearly exhibits the different behavior between the internal waves and the submesoscale currents (Fig. 2.83). The internal waves are more energetic in summer (red patch in Fig. 2.83, b), especially for the vertical modes higher than the first baroclinic mode – the latter being roughly as intense in both seasons. On the contrary, the submesoscale motions are more energetic in winter (blue patch in Fig. 2.83, b).

We have revisited the mechanism of D'Asaro (1978) by solving the linear wave problem with a realistic stratification and shown that the linear dynamics of internal waves captures the essential properties of this amplification. In particular, we found that modes 2–4 are greatly amplified in summer (Fig. 2.83, c), as previously reported, while internal modes are all attenuated in winter, due to a deeper mixed layer and the absence of a sharp density gap at its base (Fig. 2.83, d).

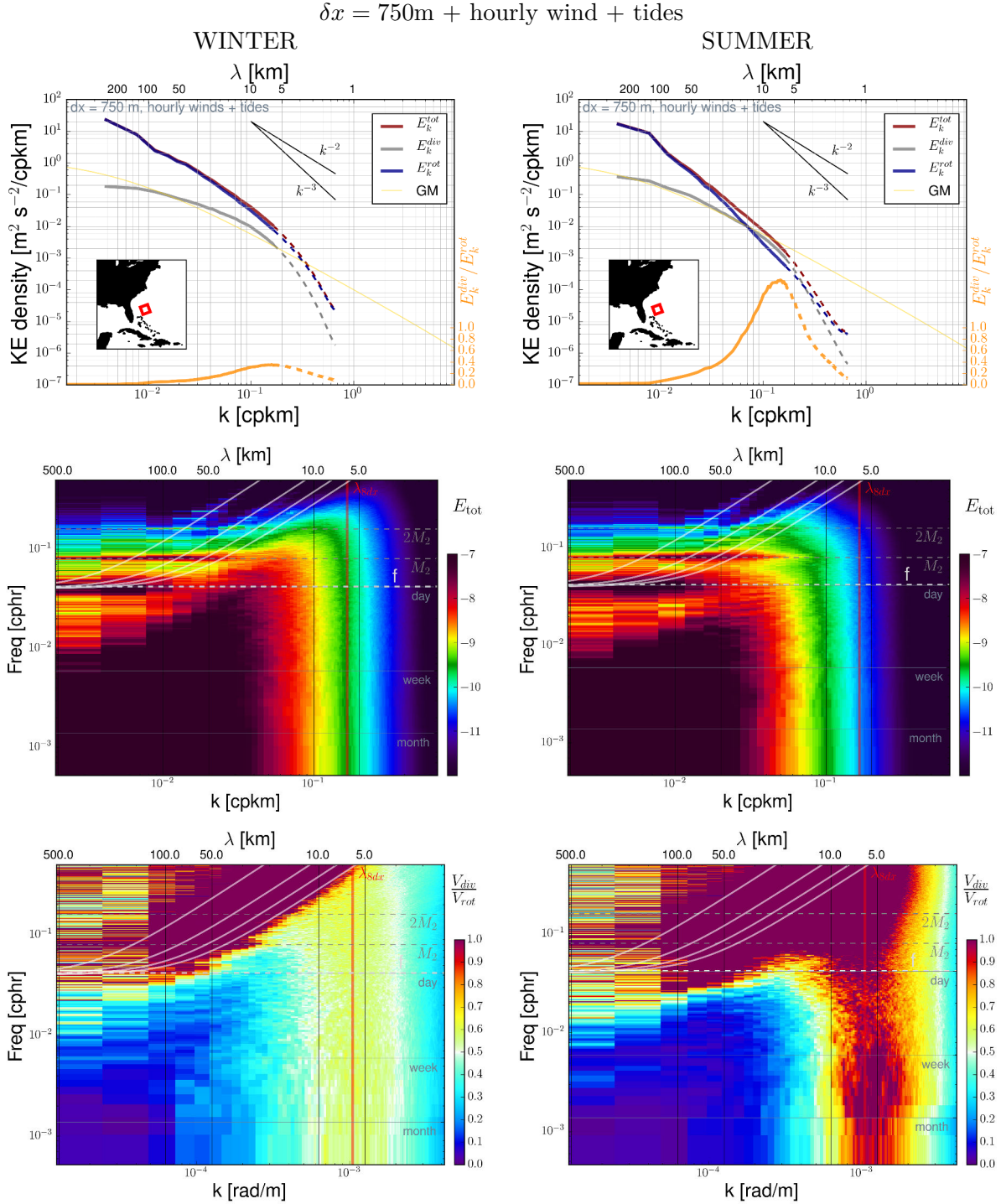


Figure 2.82 – Seasonal variations of rotational and divergent surface kinetic energy spectra in the Sargasso Sea. (top) Horizontal wavenumber spectrum of the rotational (red) and divergent part of the surface currents (grey) in summer (left) and winter (right) for a simulation with $\delta x = 750$ m, hourly wind and tidal forcings. The spectra are computed hourly over the domain shown in the inserts in the bottom panels during one year of simulation. The thin yellow line shows the Garrett–Munk spectrum using the scalings from Munk (1981). (middle) Horizontal wavenumber-frequency spectrum of surface kinetic energy $E(k, \omega)$, and (bottom) Ratio of rotational and divergent surface kinetic energy $\sqrt{E^{div}(k, \omega)/E^{rot}(k, \omega)}$, and (bottom) The ratio $E^{div}(k)/E^{rot}(k)$ is shown at the bottom. White lines in the middle and bottom panels show the dispersion relations for inertia-gravity waves from mode 1 through mode 4.

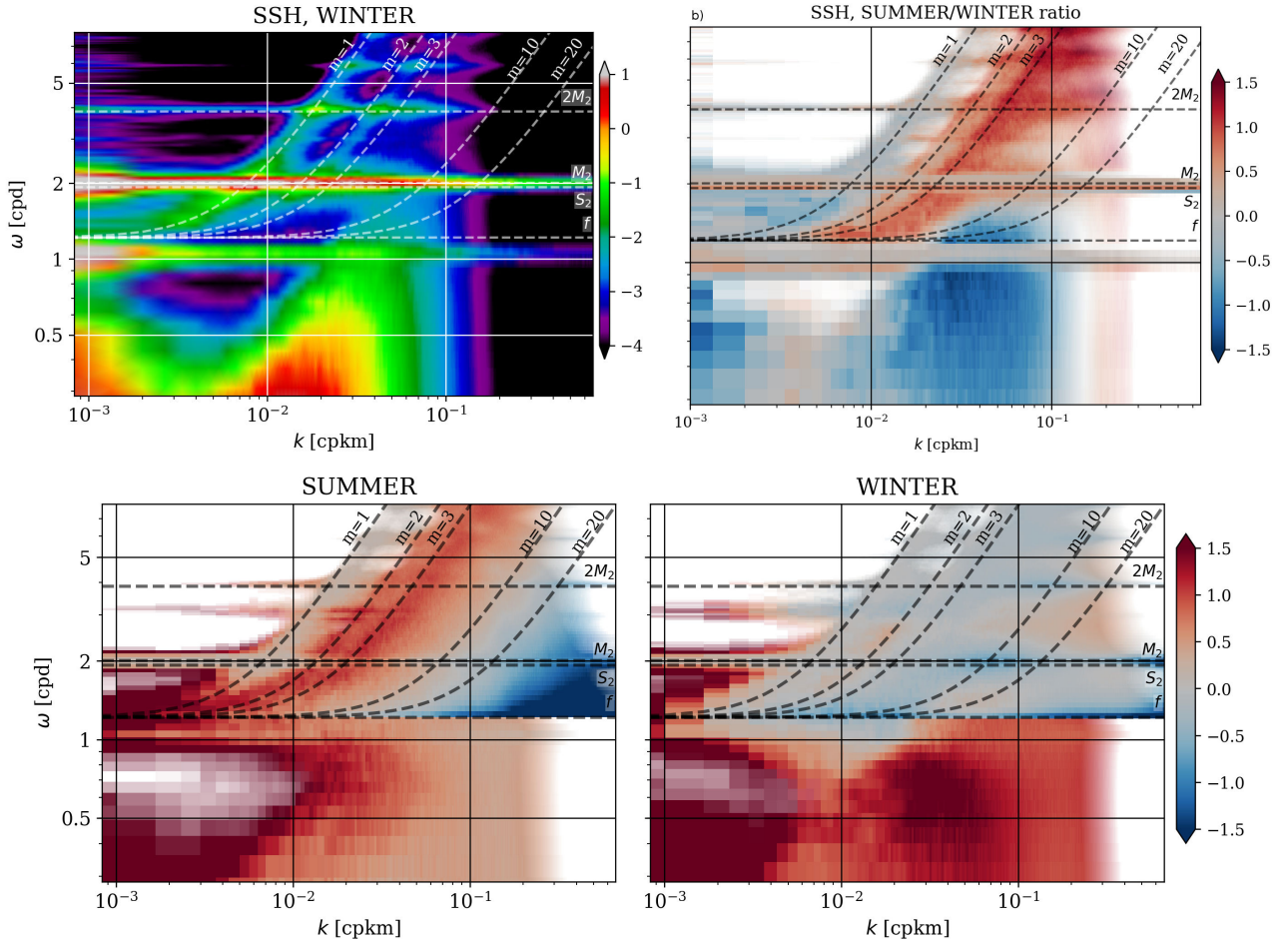


Figure 2.83 – Power spectral density in the (k, ω) space (all plots are in log scale). Upper row: Sea surface height variance in winter (a) and summer/winter ratio (b). Lower row: surface/interior amplitude ratio $R(k, \omega)$ in summer (e) and in winter (f). Ratios are displayed only where the corresponding spectral density is large enough, with colors fading to white in the range $(10^{-3}, 10^{-2})$ for A^2 and $(10^{-4}, 10^{-2.5})$ for the SSH. From Lahaye *et al.* (2019a).

We have also shown that the details of the stratification profile are important for the amplification/attenuation role of the mixed layer. In particular, the sharpness of the density gradient changes the surface/interior kinetic energy ratio cutoff rate as well as the width and magnitude of the amplification peak. We also evidenced the potential impact of horizontal (sub)mesoscale inhomogeneities in the stratification near the surface on the internal wave activity, especially in winter. All together, these could result in strong horizontal and time dependence of the global sea-surface signature of internal waves, which would need further investigation.

2.6.3 Lee waves signature at the surface

The signature of internal waves can also be observed using synthetic aperture radars (SAR) or sun glitter images through their surface roughness signature. Quasi-stationary wavefront-like patterns – signature of lee waves – are seen over the Charleston Bump, where the Gulf Stream interacts with seamounts (Fig. 2.84). Similar signals have also been observed in this area through their impact on patchiness in seabird distribution (Haney, 1987).

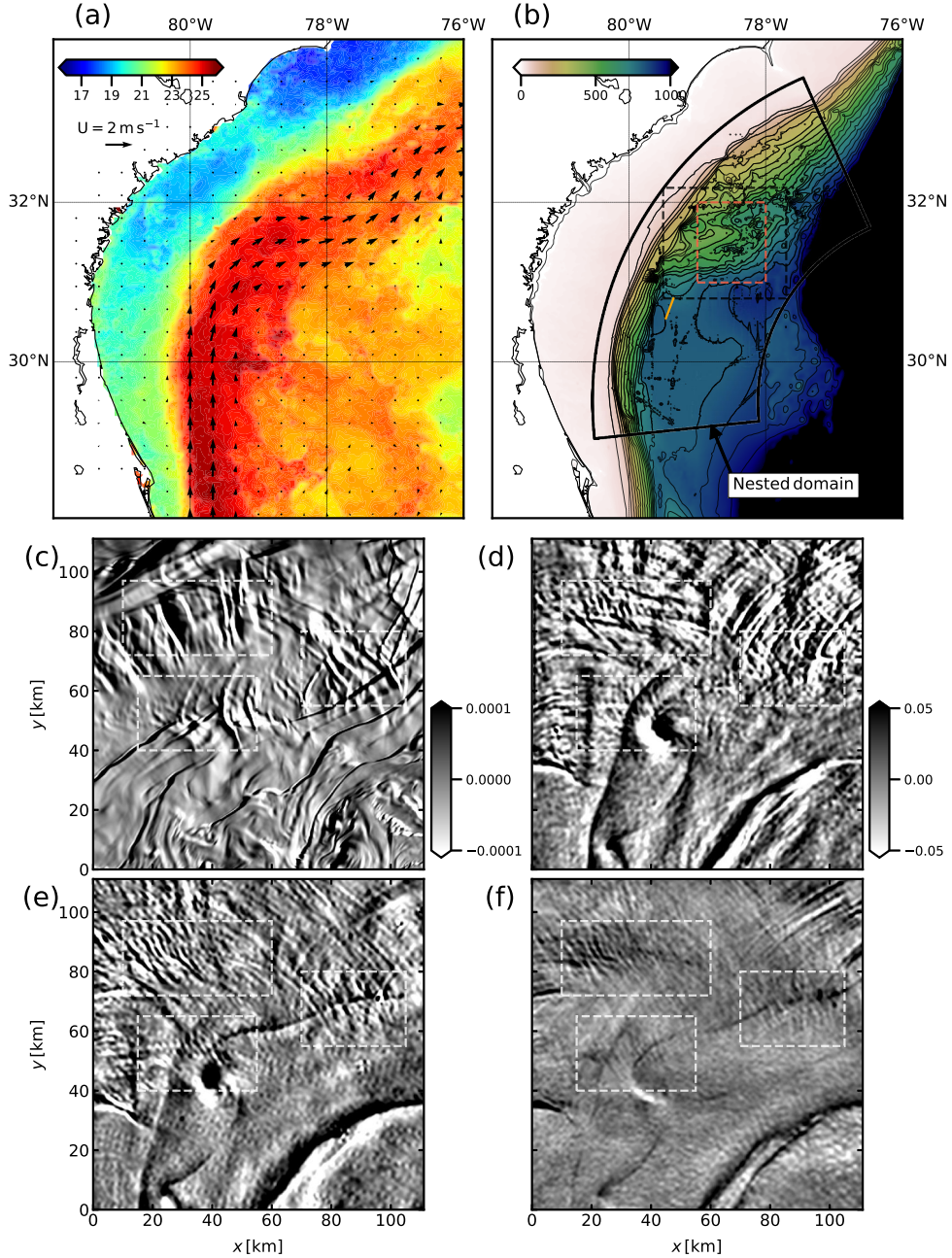


Figure 2.84 – (a) Sea Surface Temperature over the Gulf Stream region on 2010/04/01 and surface currents from AVISO on 2010/03/31. (b) Bathymetry [in m] from the SRTM30_PLUS dataset, black contours are isobaths from the surface to 1000 m depth every 50 m. The red dashed rectangle indicates the area of the zoom presented in panels (c,d,e,f). (c) Estimation of the surface roughness [in s^{-1}] in the LEEWA simulation. The coordinate (0,0) corresponds to 79°W 31°N. (d,e,f) Surface roughness [in arbitrary units] from Sun-glitter measured on 2010/04/01 by 3 different satellites (TERRA, AQUA, and Envisat) with (MODIS, MODIS, and MERIS) instruments in the same area than (c). White dashed rectangles indicate places where a qualitatively similar roughness patterns appears in both the simulation and the satellite observations. From **De Marez et al. (2019)**.

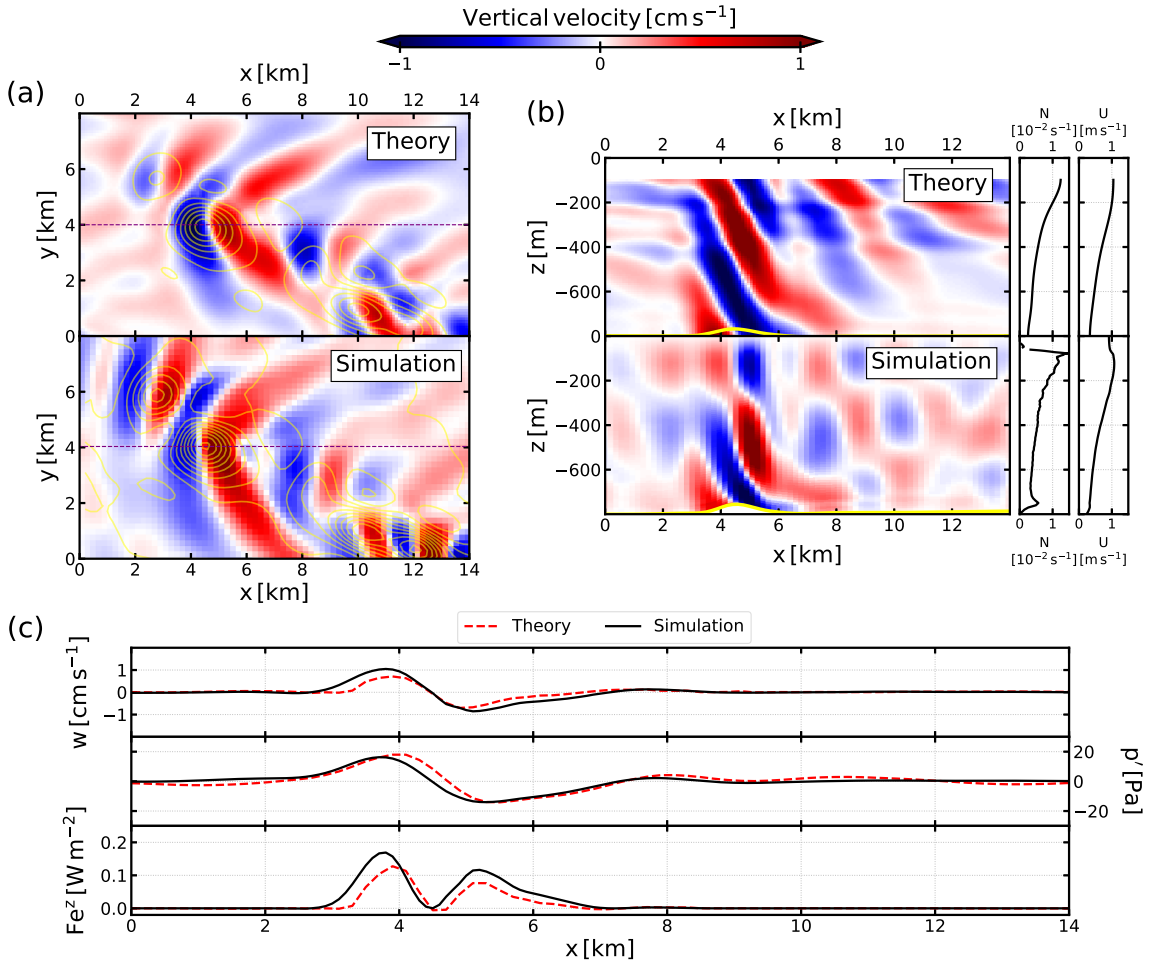


Figure 2.85 – Comparison between the 3D hydrostatic linear theory and time-lowpass outputs from the LEEWA simulation (around the location presented by the orange line in Fig. 2.84). (a) Horizontal sections at 500 m depth of vertical velocity. Yellow contours indicate 5 m-separated isobaths. (b) Vertical sections taken above an isolated seamount (see purple line in (a)) and profiles of stratification N and along-section velocity U . Bold yellow line indicates the bathymetry. (c) Values of vertical velocity w , pressure anomaly p' and vertical energy flux Fe^z at the bottom of sections (b). From **De Marez et al. (2019)**.

Realistic simulations in the Gulf Stream ($\delta x < 300$ m) have been used in **De Marez et al. (2019)** to study the generation of lee waves at this location. The generation of lee waves in the model is in qualitative agreement with observations from satellite observations. Linear theory is able to reproduce the essential properties of observed lee waves, at least as far as their amplitude, wavelength of generation, and associated vertical energy flux are concerned (Fig. 2.85). These waves are mostly in hydrostatic and linear regime according to typical dimensionless numbers.

Furthermore, we have shown that small scale topographic features strongly impact the structure of the Gulf Stream, and that lee waves may play an active role in this topographic control. This is particularly important since these areas are most of the time omitted in global studies of lee waves.

2.7 Submesoscale processes in the bottom layer

In this section I present works focused on submesoscale processes in the ocean bottom layer, and in particular the turbulence in the wake of topography due to the frictional effects. A description of the topographic drag and its impact on horizontal shear instability processes discussed previously (**Gula et al., 2015a,b; Tedesco et al., 2019**) are presented in subsection 2.7.1. The triggering of centrifugal instability and its impact on energy dissipation and mixing (**Gula et al., 2016a,b**) is described in subsection 2.7.2. The generation of submesoscale coherent vortices in the wake of topography (**Vic et al., 2015; Morvan et al., 2019; Gula et al., 2019; Le Corre et al., 2019b,a; Smileneova et al., 2019**) is discussed in 2.7.3.

2.7.1 The topographic drag

The topographic drag against the slope is a strong source of relative vorticity and potential vorticity (Molemaker *et al.*, 2015; McWilliams, 2016). A boundary slope current moving anticyclonically/-cyclonically around a basin (meaning that the flow has the coast on its left/right in the Northern Hemisphere) can generate highly positive/negative relative vorticity and potential vorticity values within the sloped turbulent bottom boundary layer (Fig. 2.86).

Due to these effects, a flow past a seamount may generate a turbulent topographic wake as seen from idealized (Srinivasan *et al.*, 2019) or realistic simulations (**Gula et al., 2019**) with generation of both cyclonic and anticyclonic vorticity (Fig. 2.87), leading to instabilities and potentially formation of coherent vortices. This is similar to the dynamics of an island wake, which forms as a von Karman street with alternating cyclones and anticyclones (Stegner, 2014).

The same process can happen for any type of current (jet, vortex or tidal current) flowing along a sloped topography. The sign of the vorticity will depend on the orientation of the current relative to the topography. The anticyclonic case applies for example to the California Undercurrent, where the topographic drag generates a narrow strip of large negative vertical vorticity, which become unstable when it separates from the topography and may form anticyclonic mesoscale eddies (Molemaker *et al.*, 2015). It will apply as well to a lot of deep currents, which are biased toward prograde currents (flowing with the coast on its right in the northern hemisphere) in the ocean interior as a result of the Neptune Effect (Holloway, 1987). It also applies to the anticyclonic side of the Gulf Stream, where it flows along the Bahamas (**Gula et al., 2016b**), see subsection 2.7.2.

The cyclonic case applies for example to the Gulf Stream along the U.S. seaboard. There, the topographic drag plays an important role in amplifying the horizontal cyclonic shear of the jet. The interaction of the Gulf Stream with the continental slope leads to injection of positive relative vorticity, intensification of the shear and triggering of the horizontal shear instability described in subsection 2.5.2.1 and **Gula et al. (2015a,b)**. On the contrary, the bottom friction does not seem to play a leading role in modulating the Agulhas Current's horizontal shear (**Tedesco et al., 2019**).

Arrested coastal waves (subsection 2.4.2.2) is another mechanism by which vorticity can be created and energy dissipated when a flow is retrograde, *i.e.*, in the direction opposite to the Kelvin wave propagation direction (**Gula & Zeitlin, 2010**) and (Dewar & Hogg, 2010). However no indications of flow arrest have been observed in the various cases described above, and further work is needed to evaluate the impact of such process in realistic flows.

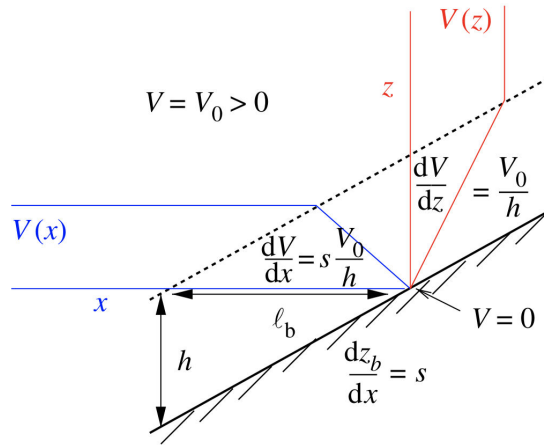


Figure 2.86 – Sketch of the along-slope velocity structure $V(x, z)$ for a uniform interior flow and a turbulent BBL over a bottom slope with $s = \partial_x z > 0$. With a uniform interior velocity V_0 , the drag generates a vertical shear profile $\partial_z V > 0$ within the BBL that also projects as a horizontal shear layer with vertical vorticity $\zeta = \partial_x V < 0$ and width $\ell_b \sim h_b/s$. This vorticity injection sets up a topographic wake leading to instabilities if there is a subsequent current separation from the boundary. From Molemaker *et al.* (2015).

2.7.2 Centrifugal instability and dissipation

The anticyclonic case is particularly interesting as it can trigger **centrifugal instability**, which has a strong impact on energy dissipation and mixing Gula *et al.* (2016b). Following the sequence of processes described in the context of the California Undercurrent (Molemaker *et al.*, 2015; Dewar *et al.*, 2015), relative vorticity can locally become much less than $-f$, where f is the Coriolis frequency, and Ertel's potential vorticity (PV) becomes negative, which is a criterion for ageostrophic centrifugal instability (Hoskins, 1974).

This mechanism has been shown to be very efficient at dissipating energy in the context of the Gulf Stream, which is constrained by the Great Bahama Bank and the Little Bahama Bank on its anticyclonic side (Fig. 2.88a). At this location, the current is strong and the topography steep, such that the topographic drag against the slope leads to very large negative vertical vorticity values (Fig. 2.88a,b), and very low PV values (Fig. 2.89). Then the separation of the negative PV strip from the slope leads to intense small-scale instabilities and energy dissipation in the separated wake (Fig. 2.89).

Centrifugal (or inertial) instability is triggered when the relative vorticity is smaller than $-f$ and extracts its energy mostly from the lateral shear ($HRS > 0$, Thomas *et al.* (2013)). It has been checked in the model that the positive conversions from mean to eddy kinetic energy seen in the regions of sustained negative potential vorticity generation (Fig. 2.90b,d) are due to the lateral shear, while the vertical buoyancy flux term (Fig. 2.90e) is negative in the region of instability.

Locations of sustained generation of centrifugal instability correspond to eddy kinetic energy dissipation maxima (Fig. 2.90a,c). Where the current directly interacts with the topography (*i.e.*, upstream from the Bimini Islands), there is dissipation of mean kinetic energy due to the vertical mixing occurring in the bottom boundary layer that is directly triggered by the bottom drag. Downstream from the generation sites the dissipation is also dominated by the vertical mixing terms, but in the ocean interior, outside of the surface and bottom boundary layers, where it represents the parameterization of small Richardson number processes and static instabilities (Large *et al.*, 1994). The vertically integrated dissipation rates of eddy kinetic energy reach values up to $8 \times 10^{-4} \text{ W m kg}^{-1}$ instantaneously at 26°N following separation of the negative PV strip from the slope (Fig. 2.89b). It is of the same or-

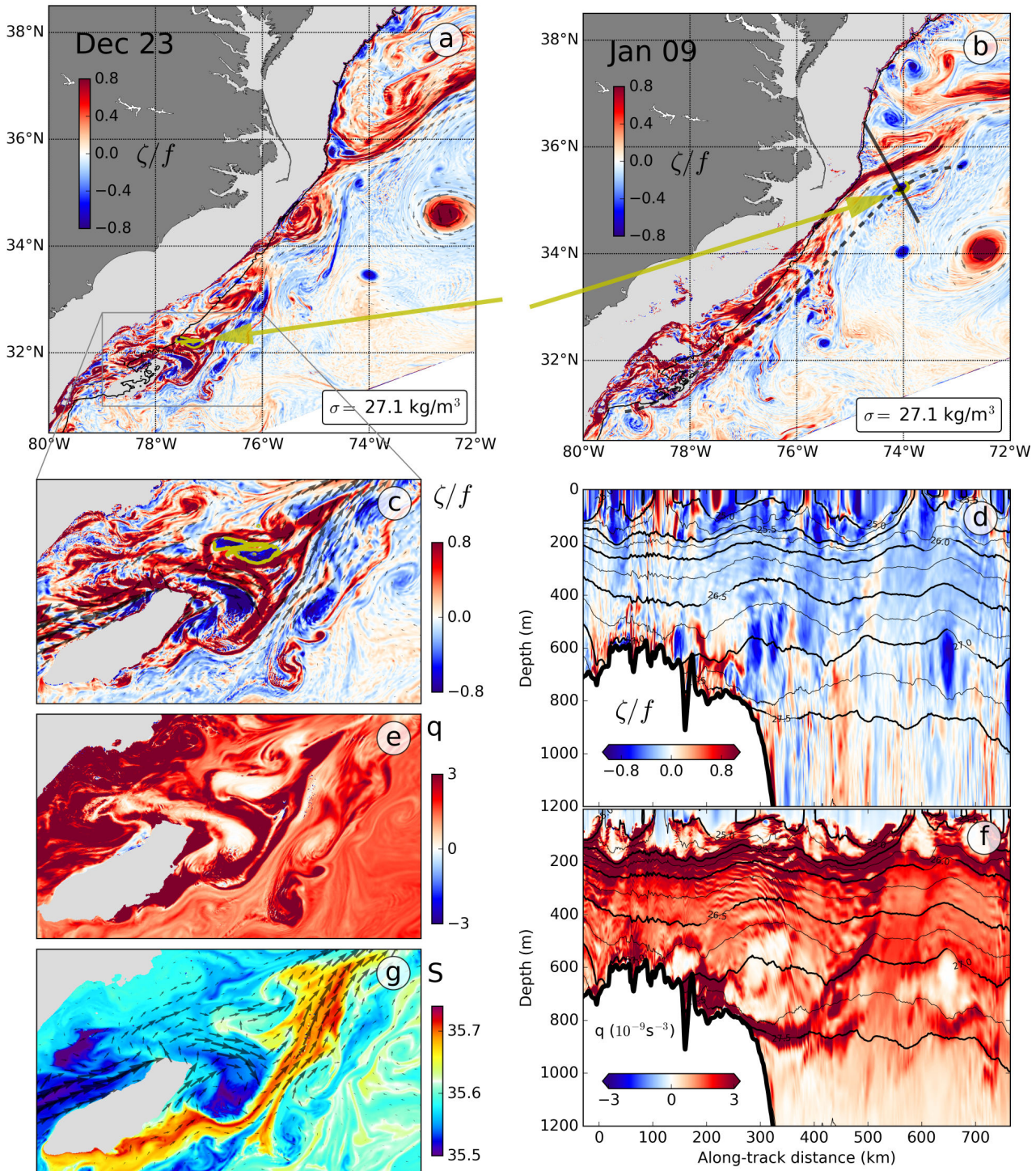


Figure 2.87 – Generation of SCVs in the lee of the Charleston Bump. (a,b) Snapshots of the relative vorticity ζ (normalized by f) on the 27.1 kg m^{-3} isopycnal: (a) shortly after the generation of several SCVs and (b) 2 weeks later. Yellow contours and arrows on panels a, b, and c indicate the location of the water masses forming the core of the SCV; 600 m isobath is shown in black. (c,e,g) zooms of panel a showing relative vorticity, PV (in s^{-3}), and salinity. (d) Relative vorticity and (f) PV in the along-stream direction (shown as a dashed gray line in panel b) at the time of panel b. Black contours showing potential density are repeated on panels d and f. From Gula *et al.* (2019).

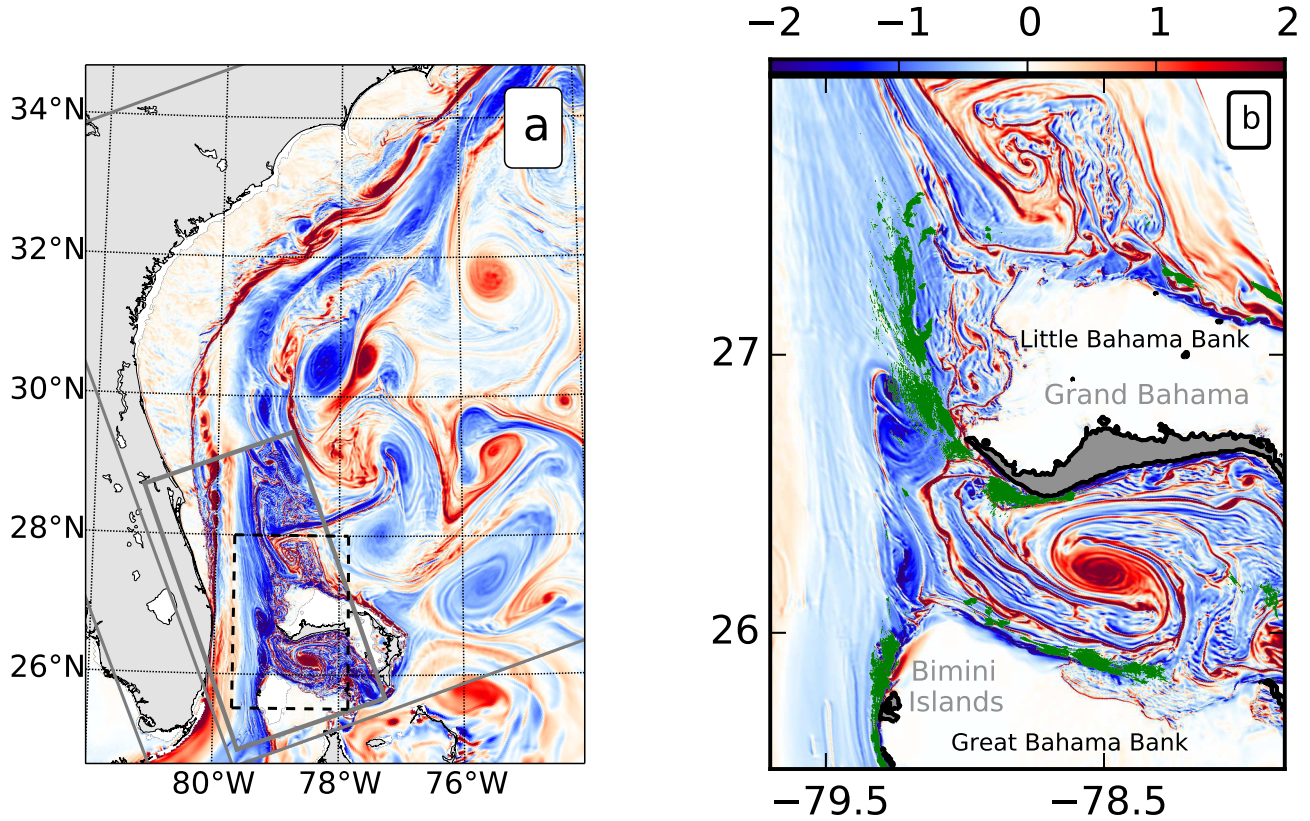


Figure 2.88 – Topographic generation of negative vorticity along the Bahamas Banks. (a) Instantaneous surface relative vorticity $\zeta = v_x - u_y$, normalized by f , for the Gulf Stream along the southeast U.S. seaboard as simulated by ROMS. The boundaries of the successive nested domains ($\Delta x = 2.5, 0.75$ and 0.25 km) are delineated by thick gray lines. (b) Zoomed-in view of the Gulf Stream along the Bahamas Banks. Green contours show region of high energy dissipation (depth-integrated energy dissipation $\langle \epsilon \rangle > 2 \times 10^{-4}$ W m kg $^{-1}$). Localized regions with negative vorticity and high energy dissipation rates are created by the currents flowing along the topographic slopes of the Bahamas Banks. From Gula *et al.* (2016b).

der as the dissipation rates observed in an intense surface front within the Kuroshio Current (D'Asaro *et al.*, 2011) integrated over the mixed-layer.

The eddy kinetic energy dissipation rates averaged over a 3 months period (Fig. 2.90c) have values up to 2×10^{-4} W m kg $^{-1}$, which are only slightly smaller than the instantaneous values. This shows how remarkably sustained are the topographic generation of vorticity and the subsequent centrifugal instability. About a third of the energy extracted from the mean flow by the instability processes and small scale turbulence is locally dissipated. Scaling up this value to the entire ocean leads to a global dissipation rate of 0.05 TW, *i.e.*, in the range of 0.01 - 0.1 TW, which represents a significant route toward dissipation for the geostrophic currents, compared to the 0.8 TW (10^{12} W) that the wind provides (Ferrari & Wunsch, 2010).

The presence of recurrent cyclonic eddies on the cyclonic side of a current along the slope, as a results of the baroclinic or barotropic instability of the mean current, will also induce local reversals of the current and trigger the sequence of processes described here leading to centrifugal instability. An example is shown for a frontal eddy in the Gulf Stream in Fig. 2.91.

Recent observational works by Ruan *et al.* (2017) in the southern Drake Passage have highlighted the importance of topographically generated submesoscale flows over continental slopes. Another re-

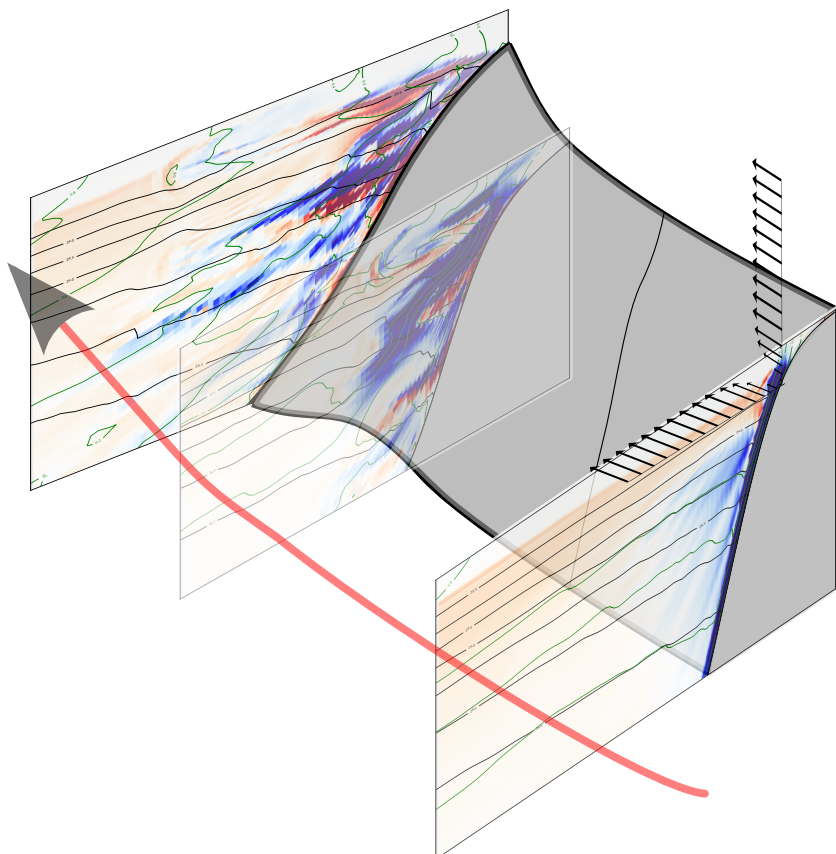


Figure 2.89 – . Snapshots of potential vorticity (PV, in 10^{-8} s^{-3}) along the Bahamas Banks showing generation of negative PV and the onset of centrifugal instability in the wake. Adapted from **Gula et al. (2016b)**.

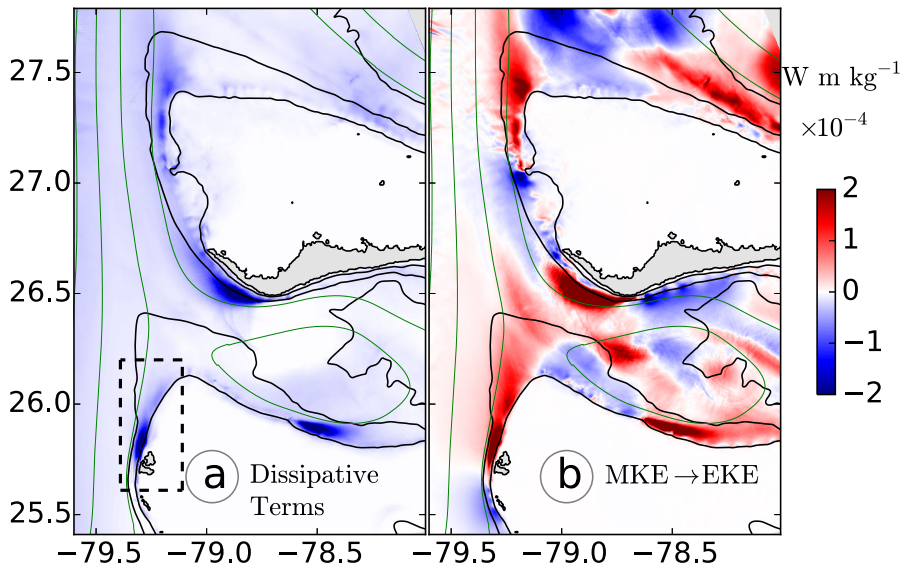


Figure 2.90 – **Energy dissipation and mixing.** Time mean depth integrated terms of the eddy kinetic energy (EKE) equation : (a) dissipative terms, (b) conversion from mean kinetic energy (MKE) to EKE. The mean transport streamfunction is shown in green with a 5 Sv interval ($1 \text{ Sv} = 10^6 \text{ m}^{-3} \text{s}^{-1}$). Units for energy rates are W m kg^{-1} . Topography is shown in black contours at 0 m, 100 m, 500 m, and 1000 m isobaths. From **Gula et al. (2016b)**.

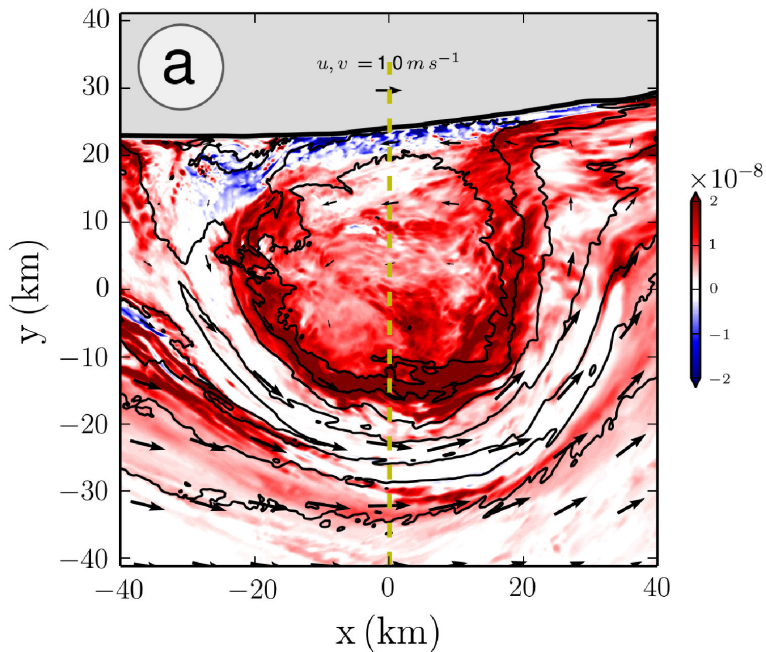


Figure 2.91 – Horizontal section at $z = -100 \text{ m}$ of potential vorticity q (colors) and density (black contours) at the center of a frontal eddy plotted in Fig. 2.63 along the cross-stream direction y . Notice in particular the negative potential vorticity created by drag from the southward frontal-eddy flow along the slope. From **Gula et al. (2016a)**.

cent observation program have also sampled very strong mixing mechanisms in an abyssal boundary current in the Orkney Passage, by which deep-ocean waters are rapidly laundered through intensified near-boundary turbulence and boundary–interior exchange (Naveira Garabato *et al.*, 2019). These observations confirm the importance of submesoscale instabilities in deep boundary currents for the generation of near bottom mixing, the export of buoyancy and ultimately for the closure of the overturning circulation. This is an important motivation for my project, which is described in section 3.2.

2.7.3 Generation of Submesoscale Coherent Vortices

The topographic wakes also lead to the formation of subsurface submesoscale eddies, known as Submesoscale Coherent Vortices (SCVs) (McWilliams, 1985) or Intra Thermocline Eddies (ITEs) (Dugan *et al.*, 1982). SCVs are usually defined as energetic eddies with a radius smaller than the Rossby deformation radius, a structure localized in the vertical, and an interior velocity maximum (McWilliams, 1985). They can be very long-lived (>1 year) and travel far from their origins, being primarily advected by mesoscale and mean currents.

SCVs have been observed in most regions of the globe (see reviews in McWilliams (1985); Kostianoy & Belkin (1989)). One of the most well-known types of SCVs are the Meddies (even if they are often closer to mesoscale than submesoscale) formed at the exit of the Mediterranean Sea (McDowell & Rossby, 1978), which spread salty Mediterranean waters in the subtropical Atlantic ocean. SCVs also form in eastern boundary regions such as along the West African coast (Kostianoy & Rodionov, 1986a,b). These SCVs are essential for spreading oxygen-poor and nutrient-rich waters into the interior of gyres (Frenger *et al.*, 2018). More generally, SCVs can be generated by interaction of boundary currents with topography, as in the Beaufort Gyre in the Arctic Ocean (Manley & Hunkins, 1985; D’Asaro, 1988), in the Mediterranean Sea along Sardinia (Bosse *et al.*, 2015), at the tail of the Grand Banks (Bower *et al.*, 2013), and over the Mid-Atlantic Ridge (Vic *et al.*, 2018). They also form from wintertime deep convection, as observed in the Labrador Sea (Clarke, 1984; Lilly & Rhines, 2002) and the northwestern Mediterranean Sea (Testor & Gascard, 2003; Bosse *et al.*, 2016, 2017) where they are essential for spreading the newly formed deep waters within ocean basins.

SCVs are challenging to detect because of their small horizontal scale. Most observations of SCVs come from hydrographic profiles, and it is difficult to get more than one profile in a given SCV as the horizontal resolution of ship-based hydrographic measurements or Argo float profiles are typically of the same order as the radius of an SCV. Most SCVs do not have a measurable surface expression; only larger mesoscale subsurface eddies can be detected using altimetry (Assassi *et al.*, 2016). Thus, it is difficult to target a specific structure during a field campaign and most observations of SCVs come about by chance.

Recently we have presented new seismic images (Fig. 2.92) and glider sections of the Gulf Stream front along the U.S. eastern seaboard that capture deep, lens-shaped submesoscale features (Fig. 2.93) in **Gula *et al.* (2019)**. These features have radii of 5–20 km, thicknesses of 150–300 m, and are located at depths greater than 500 m. These are typical signatures of anticyclonic submesoscale coherent vortices.

A submesoscale-resolving realistic simulation, which reproduces submesoscale coherent vortices with the same characteristics, has been used to analyze their generation mechanism. Submesoscale coherent vortices are primarily generated where the Gulf Stream meets the Charleston Bump, a deep topographic feature, due to the frictional effects and intense mixing in the wake of the topography (Fig. 2.87). These submesoscale coherent vortices can transport waters from the Charleston Bump’s thick bottom mixed layer over long distances and spread them within the subtropical gyre. Their net effect on heat and salt distribution remains to be quantified.

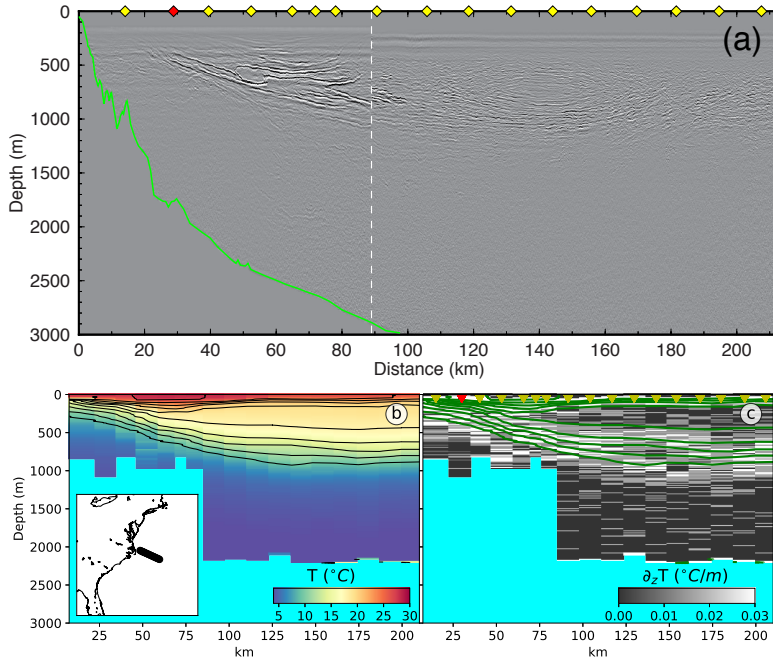


Figure 2.92 – **Submesoscale lenses in the Gulf Stream front.** (a) Seismic image across the Gulf Stream front (see insert (b) for location). Yellow (Red) diamonds show locations of XBT (XCTD) casts. Seafloor is highlighted by a green line. White dashed line denotes transition from Line 1 (eastern portion) to Line 1A (western portion), which was collected after data collection was stopped to repair one of the airgun arrays (time difference at transition between lines is approximately 5 hours). (b) Temperature and (c) vertical gradient of temperature from the XBT and XCTD casts along the section. From **Gula et al. (2019)**.

Other examples of SCVs in the Gulf of Oman have been studied in **Vic et al. (2015)** and **Morvan et al. (2019)**. SCVs are generated there due to eddy-topography interactions leading to the formation of intense frictional boundary layers that detach from the slope due to rotation of the flow around mesoscale structures (Fig 2.94). These SCVs can trap Persian Gulf Waters (PGW) and contribute to its redistribution from the boundaries to the interior of the Gulf of Oman.

The idealized simulations in **Morvan et al. (2019)** have also highlighted a second possible mechanism for the generation for SCVs. This second mechanism is inviscid and allows SCVs to be generated even in simulations without bottom drag nor a parameterized bottom boundary layer (simulation NO-BBL in Fig. 2.95). This mechanism corresponds to **baroclinic instability** arising at depth (below 300 m in this configuration) due to the weaker stratification. The source of energy for the perturbations is the vertical buoyancy flux (VBF) and not the Horizontal Reynolds Stress (HRS) as in the case of SCVs generated by a frictional boundary layer. This is a counterpart of the mixed-layer baroclinic instability, happening in weakly stratified layers over sloping topography, as explained in Wenegrat *et al.* (2018a). This mechanism is suspected to play a crucial role for the restratification of the bottom layer, thus allowing sustained water mass transformation, and directly affect the strength and structure of the abyssal overturning circulation (Callies, 2018). This is further discussed in section 3.2.

2.7.4 SCVs feeding the Rockall Trough anticyclone

A persistent, non-stationary, deep anticyclonic vortex has been identified in the Rockall Trough (RT), northeast North Atlantic, using altimetry, high-resolution ship-board wintertime Conductivity-Temperature-Depth and mesoscale-resolving model output data in **Smilenova et al. (2019)**, see Fig.

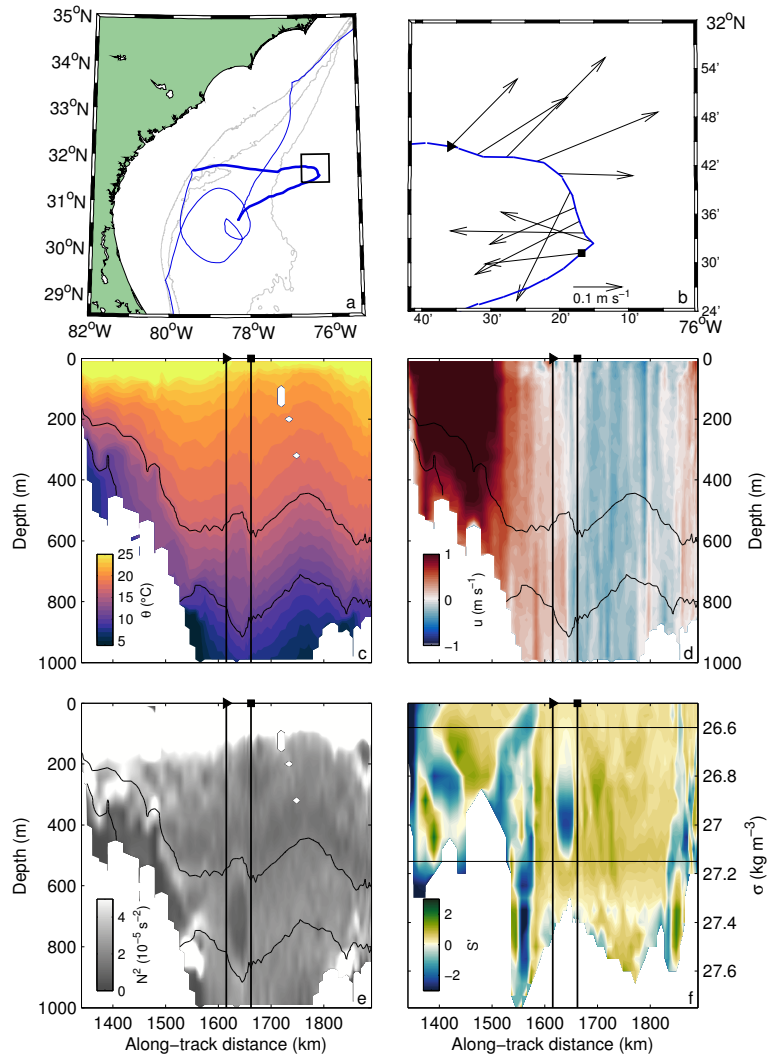


Figure 2.93 – Glider observations of an SCV adjacent to the Gulf Stream in May–June 2017. (a) Trajectory of the glider in and near the Gulf Stream from central Florida to North Carolina (blue); the bold portion is plotted in subsequent panels. The Charleston Bump is the topographic feature outlined by the 500-m isobath near 31.5°N ; the 200-m and 1000-m isobaths are also drawn. (b) Zoomed view of the glider’s trajectory from 25 May (triangle) to 28 May (square) in the box drawn in (a) with horizontal currents vertically averaged between 500 m and 900 m. Along-track transects of (c) potential temperature θ , (d) eastward velocity u , and (e) Brunt-Väisälä frequency N^2 . (f) Along-track transect of salinity anomaly S' along isopycnals normalized by the standard deviation of salinity along each isopycnal. In c–f, the SCV is bracketed by the vertical lines and the 26.6 and 27.15 kg m^{-3} isopycnals (thin black lines); the vertical lines also bracket the dives for which velocity vectors are shown in (b) with positions denoted by the triangle and square in (b). From **Gula et al. (2019)**.

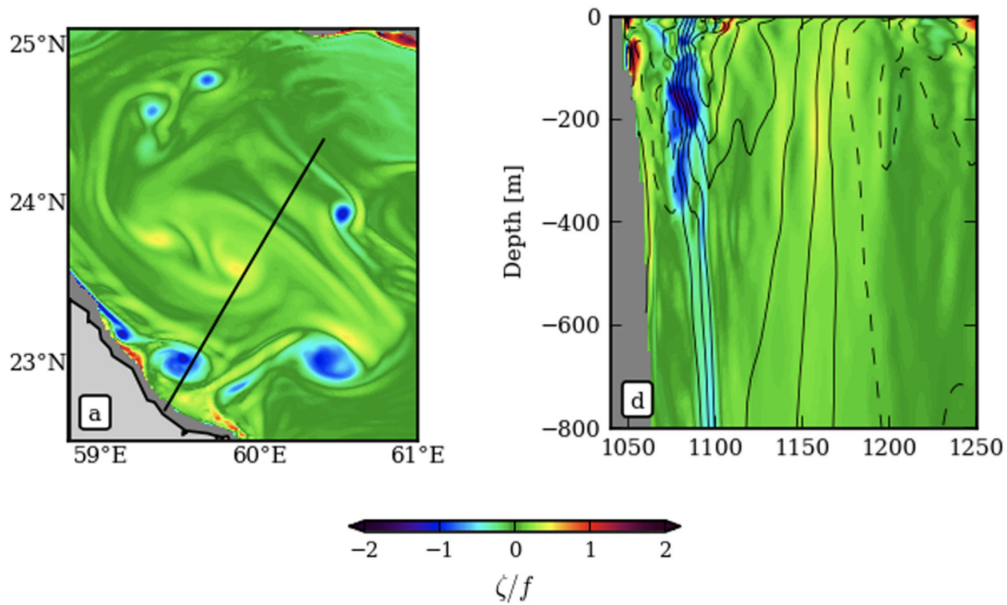


Figure 2.94 – Horizontal section at $z = -200$ m and vertical section of relative vorticity in the Gulf of Oman showing the generation of anticyclonic SCVs due to interactions of a mesoscale cyclone with the topography. From **Vic et al. (2015)**.

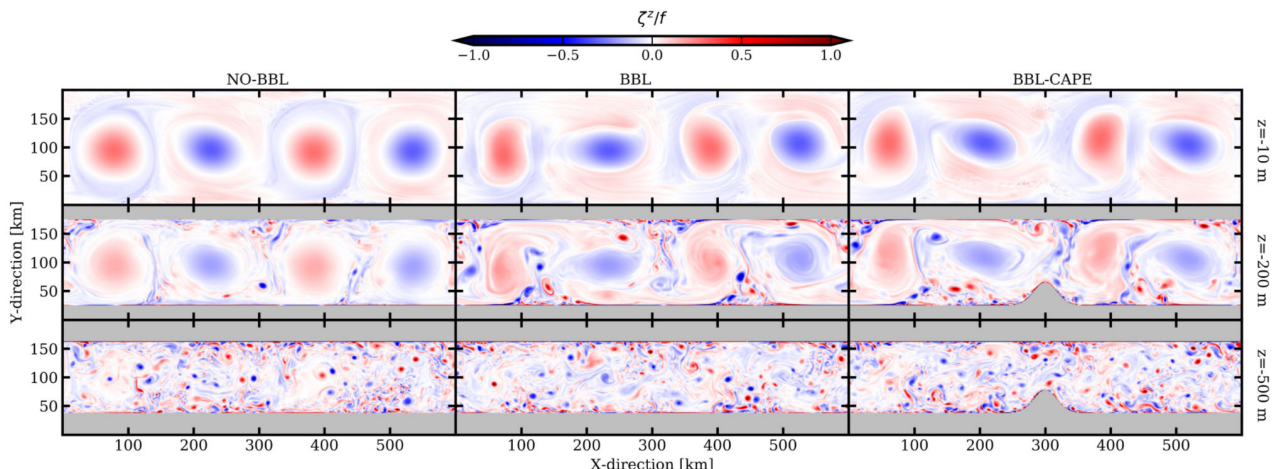


Figure 2.95 – Vertical relative vorticity field normalized by the Coriolis frequency at day 200 and 10, 200 and 500 meter depth for the NO-BBL, BBL, and BBL-CAPE experiments.. From **Morvan et al. (2019)**.

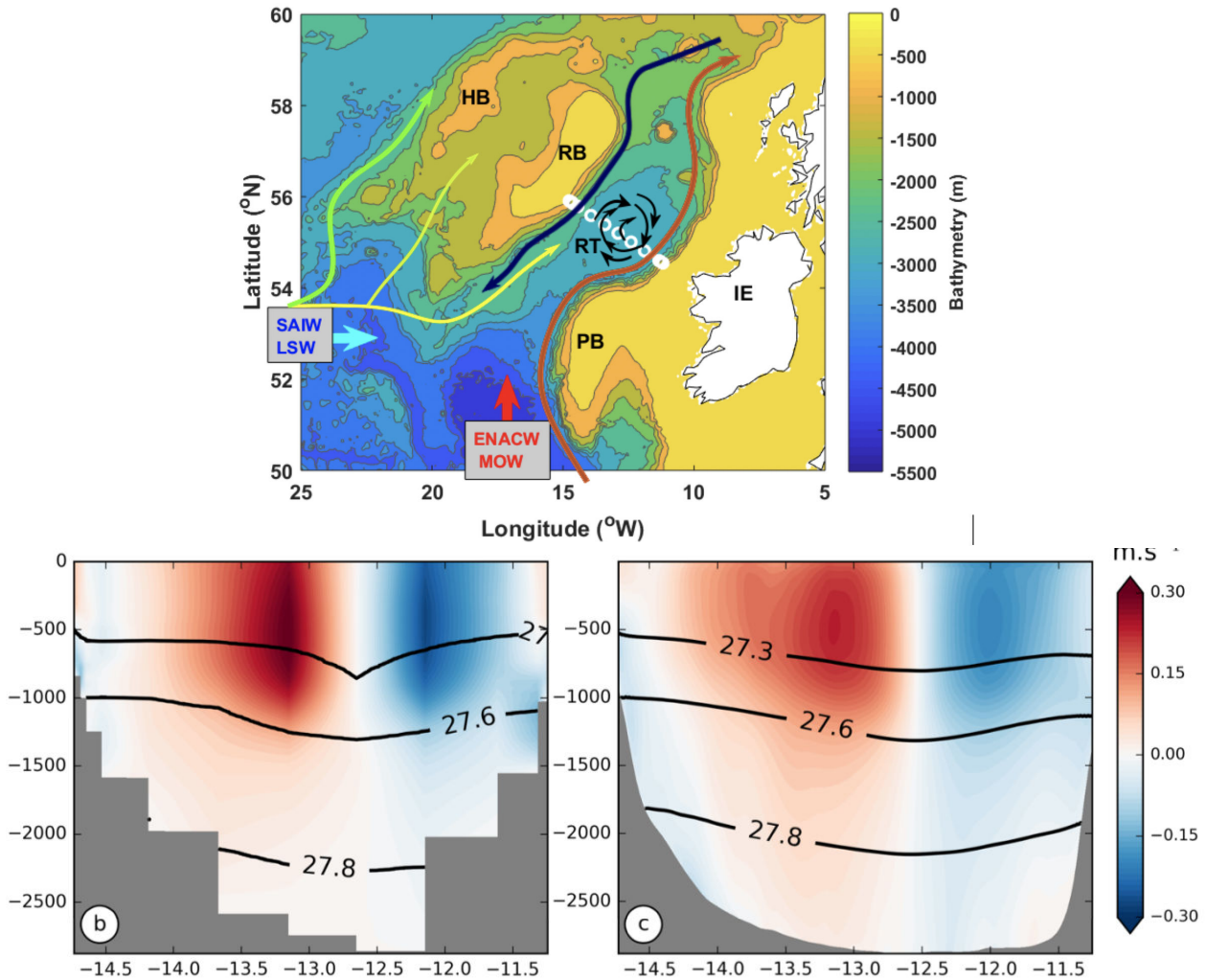


Figure 2.96 – (a) Mean currents pathways in the Rockall Trough (RT) represented by coloured arrows with survey transect line stations (white circles) shown. (b-c) Vertical sections of potential density (black contours) and cross-section velocity (colors) along the survey transect line from in-situ observations in January 2011 (a) and from the model (b). From Smilenova *et al.* (2019); Le Corre *et al.* (2019b)

2.96. The anticyclone is centred at approximately 55°N, 12°W, it has a radius about 40 km, a warm and salty core made of Mediterranean Overflow Water (MOW), a velocity maximum at around 500 m depth and it reaches down to 2000 m depth.

We have shown using the model outputs that the main source of anticyclonic vorticity for the RT anticyclone is the divergence of eddy vorticity fluxes, mostly due to the merging of submesoscale anticyclonic vortices shed from the slope current flowing poleward along the eastern Rockall Trough slope (**Le Corre *et al.*, 2019b,a**). The slope current, modulated by the background eddy field, generates large horizontal potential vorticity gradients due to frictional effects along the Rockall Trough south-eastern slope. Intense negative vorticity filaments are formed, subsequently detaching from the slope, encapsulating Mediterranean Overflow Water as they become unstable and grow into submesoscale anticyclonic vortices. These Mediterranean Overflow Water-rich vortices are advected into the trough, consequently merging with the Rockall Trough anticyclone and sustaining it (Fig. 2.97).

This input of anticyclonic vorticity is balanced by topographic effects through the bottom pressure torque and the bottom drag curl acting as anticyclonic vorticity sinks. The intensification of the RT

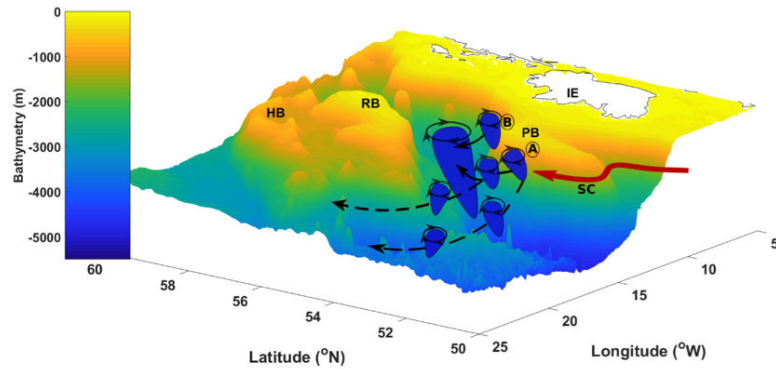


Figure 2.97 – Schematic representation of the bottom topography - slope current interactions in the southern Rockall Trough, where circled A and B denote ‘hot spots’ for flow separation due to bottom topography - slope current induced baroclinic/barotropic instabilities. Generated small-scale vortices along the east banks of the trough propagate both north-eastward into the trough, thus feeding and sustaining the Rockall Trough anticyclone, and westward into the subpolar northeast NA. Letter annotations in figure as follows: PB - Porcupine Bank, HB - Hatton Bank, RB - Rockall Bank, SC - Slope current, IE - Ireland. From **Smilenova et al. (2019)**.

anticyclone implies a barotropization of its structure, which results in an intensification of the bottom currents. These currents are responsible for a positive drag curl and positive bottom pressure torque counteracting the intensification of the RT vortex.

2.8 Impacts of submesoscale and internal waves in the deep ocean

In this section I present some results showing the variability of deep currents due to submesoscale processes and internal waves (subsection 2.8.1), their impact on the mean deep circulation (subsection 2.8.2), and the dispersion of biogeochemical tracers in the deep ocean (subsection 2.8.3). These results have been published in **Vic et al. (2018)**; **Lahaye et al. (2019b, 2020)**, which were studies led by C. Vic and N. Lahaye during their postdoctoral studies.

2.8.1 Submesoscale and internal waves in the deep ocean

The circulation in the deep ocean is far more complex than previously thought. The various submesoscale processes related to flow-topography interactions described in section 2.7 are important sources of variability, leading to intense submesoscale turbulence in regions with rough topography (Fig. 2.7). Using high-resolution modeling of the North Mid-Atlantic Ridge (MAR), we have shed light on a submesoscale regime of oceanic turbulence over the MAR at 1500 m depth, contrasting with open-ocean – i.e., far from topographic features – regimes of turbulence, dominated by mesoscales (Fig. 2.98). Away from the MAR the energy spectra is consistent with the quasi-geostrophy theory ($E \propto k^{-3.0}$). Close to the MAR, the slope of the spectra becomes flatter ($E \propto k^{-2.4}$), indicating energized submesoscale motions.

Another fundamental ingredient of the currents variability over the MAR is the tidal forcing. The frequency spectra of kinetic energy and temperature variance from models and observations below 1500 m over the MAR (close to the Lucky Strike site) are shown in Fig. 2.99. Strong peaks appear at diurnal and semi-diurnal frequencies and at their harmonics due to tidal forcings, with a good agreement between the observations and the simulation. Comparing the simulation without meso/submesoscale variability (luckyto = Tides only) with the fully realistic simulation (luckyt = With tides) reveals that the meso/submesoscale variability allows for more intense wave-wave interactions which fills energy in between the tidal harmonic peaks (M_2 , M_4 , ...). The numerical model still lacks energy in the near-inertial band ($\approx 0.5 - 2$ cpd) and in between the tidal harmonic peaks. This can be explained by limitations in the model surface forcings frequency (daily winds), the barotropic tidal forcing at the boundaries which exclude internal waves generated outside of the domain, and a too coarse resolution unable to resolve all wave-wave interaction mechanisms. The lack of energy in the near-inertial band can also explain the weaker harmonics generated through wave-wave interaction (van Haren, 2016).

The internal tide dynamics over the North MAR has been studied in more details in **Lahaye et al. (2020)**. The realistic high resolution simulation has been used to understand how the internal tide propagates, gets dispersed and dissipated over the ridge. Using a vertical mode decomposition, we showed that the topographic scattering is a key process to generate small wavenumber internal tide over the ridge, thus enhancing dissipation there.

2.8.2 Impacts of submesoscale and internal waves on the mean circulation

The circulation in the rift valley along the Azores sector of the North Mid-Atlantic Ridge has been studied using a more extensive dataset of *in-situ* observations from several surveys, combined with the high-resolution modeling in **Lahaye et al. (2019b)**. The results have shown the presence of a mean deep current with an up-valley branch intensified along the right inner flank of the valley (looking downstream), and a weaker down-valley branch flowing at shallower depth along the opposite flank. The variability of this current is important, and consists of vortex turbulence taking place within the valley and of strong variation of the intensity of the flow, in particular in sill overflows. This variability is caused by the overlying mesoscale turbulence interacting with the topography and the deep currents.

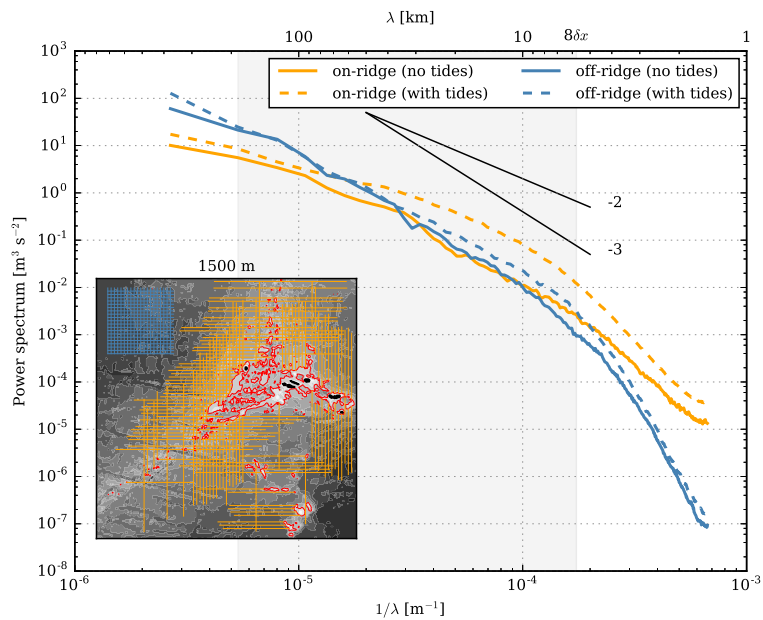


Figure 2.98 – Horizontal velocity power spectra E at 1500 m in $\delta x = 750$ m ROMS simulations over the Mid-Atlantic Ridge with and without tides. Solid (dashed) lines are for the simulation without (with) tides. Blue (orange) lines are for the off-ridge (on-ridge) areas. Spectra are computed for the cross-segment velocities (see segments in inset map) and averaged on 10 days. The gray shaded area is the spectral space in which power regressions $E \propto k^{-\alpha}$ are computed ($k = 2\pi/\lambda$). Without tides, $\alpha_{\text{off-ridge}} = 3.0$ and $\alpha_{\text{on-ridge}} = 2.4$. For indication, k^{-2} and k^{-3} are shown in black lines. In the inset map, blue segments are chosen to be in the open ocean whereas orange segments intersect the outcropping topography at 1500 m (red contour). All segments have a length of 400 km, which allow spectra to span more than two orders of magnitude of spatial scales (the Nyquist wavelength is $2 \times \delta x \sim 1.5$ km). From **Vic et al. (2018)**.

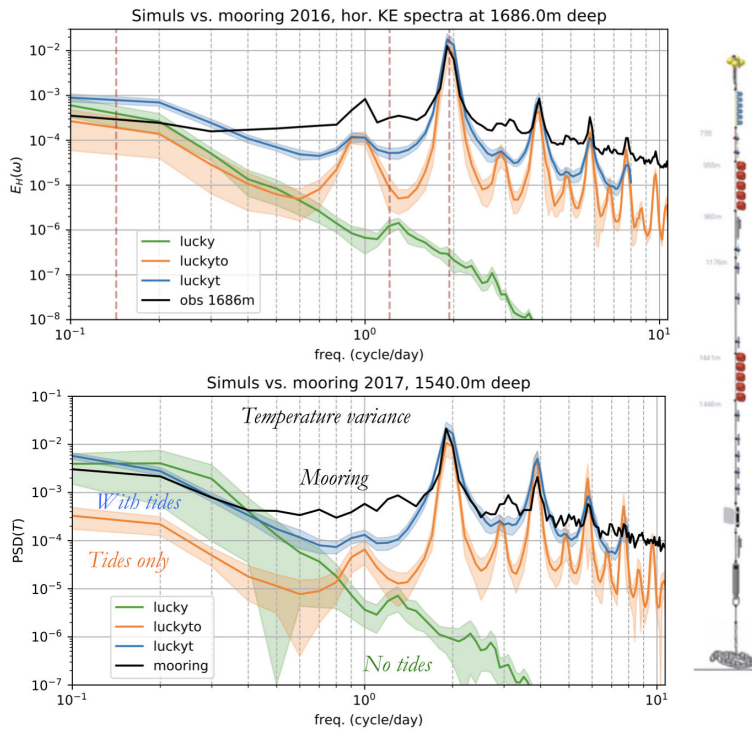


Figure 2.99 – Power spectra of horizontal velocity at 1686 m depth (top) and temperature at 1540 m depth (bottom) at the location of the Lucky Strike site on the MAR from in-situ observations (in black) and simulations (lucky = ‘No tides’, luckyto = ‘Tides only’, luckyt = ‘With tides’ or ‘Full Forcing’). Adapted from Lahaye *et al.* (2019b).

The internal tide dynamics plays a significant role in forcing the mean current. Internal tides generate significant mixing over the MAR, and the density gradient resulting from bottom-enhanced mixing over the sloping topography can generate mean currents (*e.g.*, St. Laurent *et al.*, 2001; Thurnherr *et al.*, 2005; Clément & Thurnherr, 2018). But the role of mesoscale eddies in transferring momentum to the mean field (Holloway, 1992) is important as well. The mean circulation in simulations with partial forcings (No tides, Tides only, Full Forcing) is shown in Fig. 2.100. Both simulations with incomplete forcing exhibit a low-frequency circulation at depth, with a magnitude comparable (although weaker) to the reference run, thus showing that both dynamical components present in each run – the tides and the mesoscale turbulence – play a role of comparable importance in generating this deep flow.

2.8.3 Impact on dispersion of hydrothermal effluents and larvae

These complex abyssal flows over mid-ocean ridges drive the transport properties of biogeochemical constituents. In particular, hydrothermal vent effluents and larvae may be dispersed and transported long distances by deep ocean currents. The impacts of submesoscale and tidal currents on larval dispersion and connectivity among vent populations have been investigated in Vic *et al.* (2018) by releasing neutrally buoyant Lagrangian particles at the Lucky Strike hydrothermal vent in simulations with different forcings.

Submesoscale currents have been found to significantly increase both the horizontal and vertical relative dispersion of particles at $O(1\text{-}10)$ km and $O(1\text{-}10)$ days, resulting in an increased mixing of the cloud of particles. Particles can be trapped in submesoscale coherent vortices, which enable transport over long time and distances. Tidal currents and internal tides roughly double the vertical dispersion.

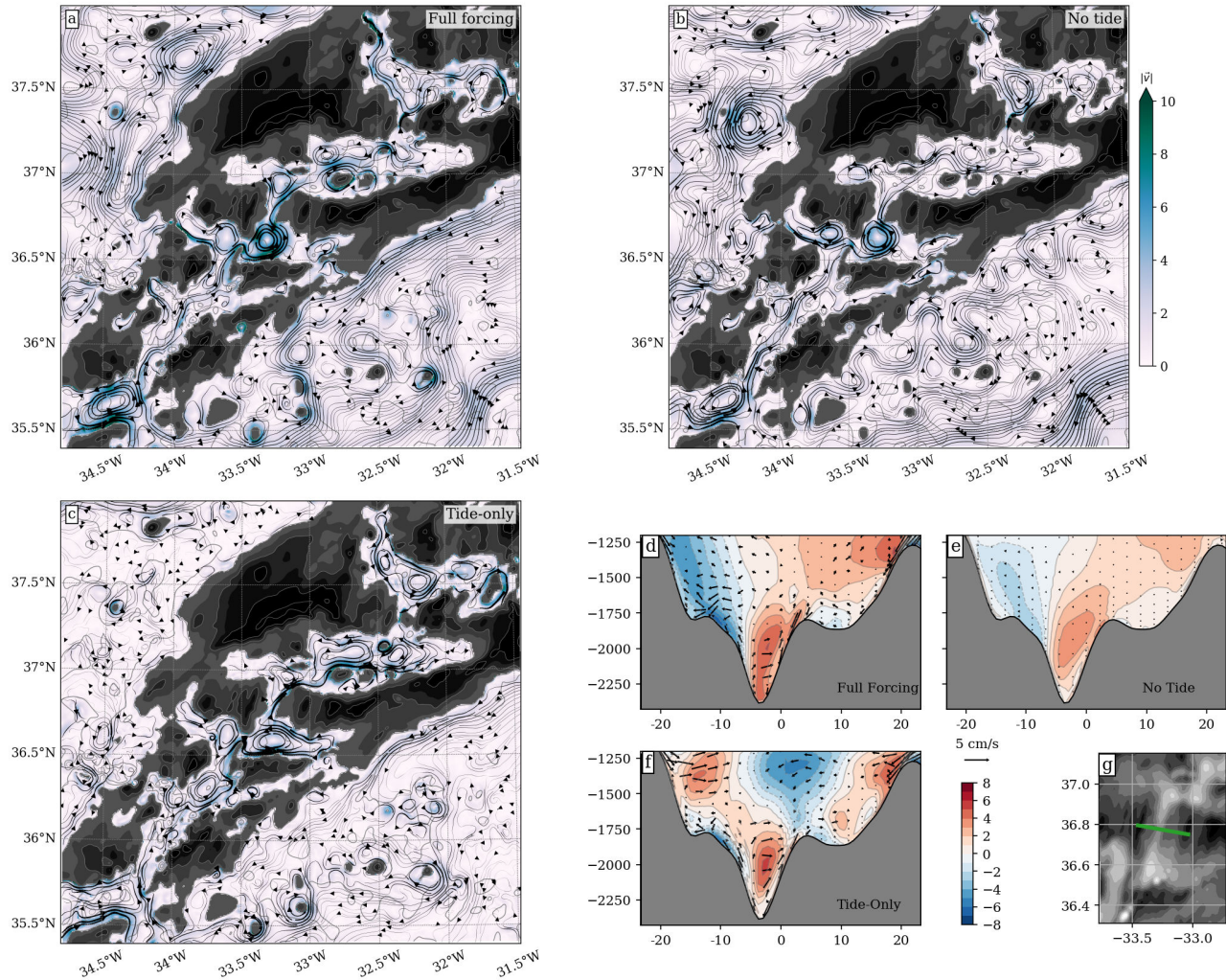


Figure 2.100 – Comparison of different simulations with different forcing, as seen from the mean horizontal current at 2000 m (a, b, c) and the vertical structure across a section in the Famous segment (d, e, f, and localization of the section in g). The different configurations correspond to full forcing (a, d), no tide (b, e) and tide-only (c, f). From Lahaye *et al.* (2019b).

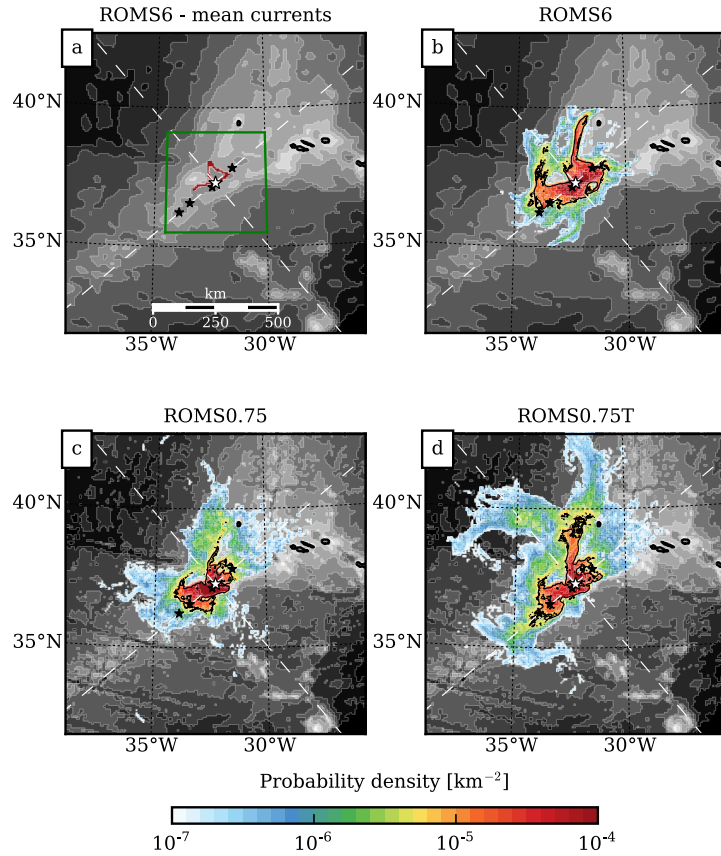


Figure 2.101 – Probability density of particles after 180 days, using (a) time mean currents from a $\delta x = 6$ km simulation, (b) a $\delta x = 6$ km simulation, (c) a $\delta x = 750$ m simulation without tides and (d) a $\delta x = 750$ m simulation with tides. Particles are released at the Lucky Strike site (white star) below 1400 m. The black stars are the principal hydrothermal vents in the area, from northeast to southwest : Menez Gwen, Menez Hom, Saldanha and Rainbow. Background shades of gray is the model bathymetry with 500-m contour interval. From **Vic et al. (2018)**.

Specifically, particles undergo strong tidally-induced mixing close to rough topographic features, which allows them to rise up in the water column and to cross topographic obstacles.

The impact of submesoscale and tidal currents on connectivity between vents for the mussel *Bathymodiolus* is illustrated in Fig. 2.101, which shows the probability density after 180 days for larvae released at the Lucky Strike vent. This suggests that the connectivity is enhanced between MAR hydrothermal sites (mainly, Saldanha and Rainbow) at PLD-relevant time scales when considering submesoscales and tidal currents, and challenges recent results of Breusing *et al.* (2016) who find that connectivity of larvae over one generation (one PLD) between known hydrothermal vents in unlikely.

2.9 Bonus

2.9.1 Retroaction of the atmosphere

The **coupling with the atmosphere** is an important aspect that I have not mentioned in this manuscript so far. Taking into account the retroaction of the ocean currents on the atmosphere – **the current feedback**– has a strong impact on the atmosphere and ocean (Renault *et al.*, 2016b). The current feedback acts as an oceanic eddy killer at mesoscale, and can dissipate up to 20 - 30 % of the

eddy kinetic energy. Taking into account this effect has been shown to stabilize the Gulf Stream separation in a model and improve its characteristics compared to observations **Renault *et al.* (2016a)**.

The impact of the current feedback has also been tested at the submesoscale using high-resolution coupled oceanic and atmospheric models for the Central California region in **Renault *et al.* (2018)**. It has been shown that the current feedback dampens the submesoscale variability by $\approx 17\%$ by inducing an ocean sink of energy and by being a source of atmospheric energy related to induced Ekman pumping velocities. However, those additional vertical velocities also cause an increase of the injection of energy by baroclinic conversion into the submesoscale currents, partially counteracting the sink of energy by the stress coupling.

Project: Impacts of submesoscale processes on the oceanic circulation

A significant part of my research over the last few years has been dedicated to understanding the dynamics of submesoscale processes in the surface and bottom layers of the ocean. While there are still a lot of unanswered questions about the dynamics of these processes, the main focus of my research in the next few years will be to try to quantify and parameterize the **impacts of these processes on the large-scale circulation**.

Deep submesoscale processes can act as sinks of energy from the mesoscale balanced dynamics and can trigger a direct route toward dissipation (**Gula et al., 2016b**), but their **impact in the global energy budget** remains to be quantified. They also generate strong **mixing at the bottom of the ocean**, which can drive upwelling of water masses along topographic slopes (Ruan *et al.*, 2017; Naveira Garabato *et al.*, 2019). They may also be instrumental in driving the **restratification at the bottom of the ocean** and exporting buoyancy outside of the bottom mixed layer (Callies, 2018). They also can generate **long-range anomalous transport of water properties or biogeochemical tracers in the ocean interior** in the form of submesoscale coherent vortices (SCV's) (McWilliams, 1985). Furthermore submesoscale motions strongly influence **tracer dispersion and transport in the deep ocean** (**Vic *et al.*, 2018**).

The **surface submesoscale currents** modify momentum, buoyancy and gas exchange between the ocean and atmosphere, and are therefore instrumental in Earth's climate system. Submesoscale motions also generate strong vertical velocities that **drive exchanges between the surface mixed-layer and the ocean's interior**. They drive nutrient fluxes upward into the euphotic zone, and act to subduct organic carbon into the ocean's interior (Mahadevan, 2016). They modify fluxes of potential vorticity at the surface and **impact the budget of mode waters** in subtropical gyres, with implications for the gyre circulation (**Wenegrat *et al.*, 2018b**).

Unfortunately, **these processes are not resolved for climate-scale ocean models**, which have to rely on parameterisations. The current generation of climate models does not have sufficient resolution to represent submesoscale processes. In the surface layer, it can lead to wrong mixed-layer properties. In the deep ocean, it can lead to large biases in the representation of mixing and water-masses transformations. In the ongoing CMIP6 exercise, ocean models will typically have a $\frac{1}{4}$ degree resolution, allowing for mesoscales but not totally resolving them (Griffies *et al.*, 2016). One can expect that truly mesoscale-resolving ocean models will be a standard for climate studies a decade from now. However, effects of submesoscale processes and internal waves will still have to be parameterized. Such parameterisations exist to account for wave-driven mixing (MacKinnon *et al.*, 2017), and some aspects of surface submesoscale instabilities (Fox-Kemper *et al.*, 2008; Bachman *et al.*, 2017), but no parameterization currently accounts for most submesoscale effects.

This project aims at better **understanding, quantifying and parameterizing the effects of submesoscale processes on the large-scale circulation**. Building on my previous works, which aimed at characterising deep submesoscale processes in realistic set-ups, this project will move up a gear and tackle effects of these processes on an unprecedented scale using cutting-edge realistic modelling with the CROCO model. A terrain-following model will be used for the first time at sub-

kilometre resolution over the full Atlantic ocean. Such model is particularly advantageous to study flow-topography interactions as it permits very high vertical resolution in the bottom boundary layer everywhere in the domain, and because it uses a cleaner formulation of the bottom boundary condition. A hierarchy of simulations will be built to be able to characterise processes driving submesoscale turbulence and will constitute a unique set of simulations to test theory related to submesoscale processes and internal waves and quantify their effects on the large scales. Finally, this project will explore ways of parameterizing them for climate-scale ocean models using machine learning methods.

The following project is decomposed into 4 work packages (WP) : a technical one (WP1, involving the realization of a new set of simulations), and 3 scientific work packages (WP2 – 4). WP2 aims at understanding submesoscale turbulence and internal waves generation at the bottom of the ocean and their impact on water-mass transformations. WP3 focuses on the generation and life-cycle of submesoscale coherent vortices in the interior, and their impact on horizontal tracer dispersion and transport. WP4 investigates the impacts of the surface submesoscale turbulence for the vertical fluxes of tracers between the surface and the interior. The project timeline is presented on the last page.

3.1 Modeling the Atlantic ocean at submesoscale

This part of the project will benefit from a lot of help from 2 engineers from LOPS (G. Cambon and S. Theetten). A PRACE project related to this project has been awarded in full (20 million core hours on Joliot Curie – SKL, <http://www.prace-ri.eu/18th-project-access-call-awarded-projects/>). The allocation runs from April, 1st 2019 to April, 1st 2020, and the numerical simulations are underway.

To investigate the impacts of the submesoscale processes and internal waves on larger scales, we need a realistic simulation with high enough resolution to resolve (at least partially) submesoscale dynamics, with realistic levels of internal waves, and with a large enough domain to fully contain the basin scale circulation. A basin scale domain is especially critical to simulate realistic level of internal tides at a given location, as they can be generated remotely.

The model used is of course the Regional Oceanic Modeling System (ROMS) (Shchepetkin & McWilliams, 2005), in its Coastal and Regional Ocean COMmunity (CROCO) version. A full Atlantic simulation will be run with the CROCO model in a framework as realistic as possible, which includes realistic sources of internal waves (hourly winds and tides) and geothermal forcings (Fig. 3.1). Different versions will be run with a gradual increase in resolution from mesoscale resolving (12 km / 50 lev., 6 km / 50 lev. and 3 km / 100 lev.), to submesoscale permitting (1 km, 200 lev.). The “most realistic” configuration will be submesoscale permitting ($dx < 1 \text{ km}$, 200 vertical levs.) and corresponds to a **10500 x 14000 x 200 points** domain. A duration of approximately 18 months is planned, starting from the equilibrated 3 km run, for 2 sensitivity runs with or without high-frequency wind forcings. All simulations will be carefully validated by comparing the relevant metrics (structure of the mean currents, mesoscale variability, internal waves energy levels, etc.) to available observations (satellite, drifters, gliders, moorings, Argo floats, etc.). The outputs of the simulations will be distributed to the scientific community and will serve multiple scientific objectives through numerous collaborations.

3.2 Impacts of deep submesoscale turbulence (and internal waves) on the large scale circulation

Most of the project described in this section is included in the ANR JCJC project DEEPER (Impacts of Deep submesoscale Processes on the ocean circulation, PI: J. Gula), which has been funded for the period 2020-2024. The full proposal is available here: <http://stockage.univ-brest.fr/~gula/Work/deeper.pdf>. It includes numerous collaborations detailed in the document and fundings for a postdoctoral fellow (2

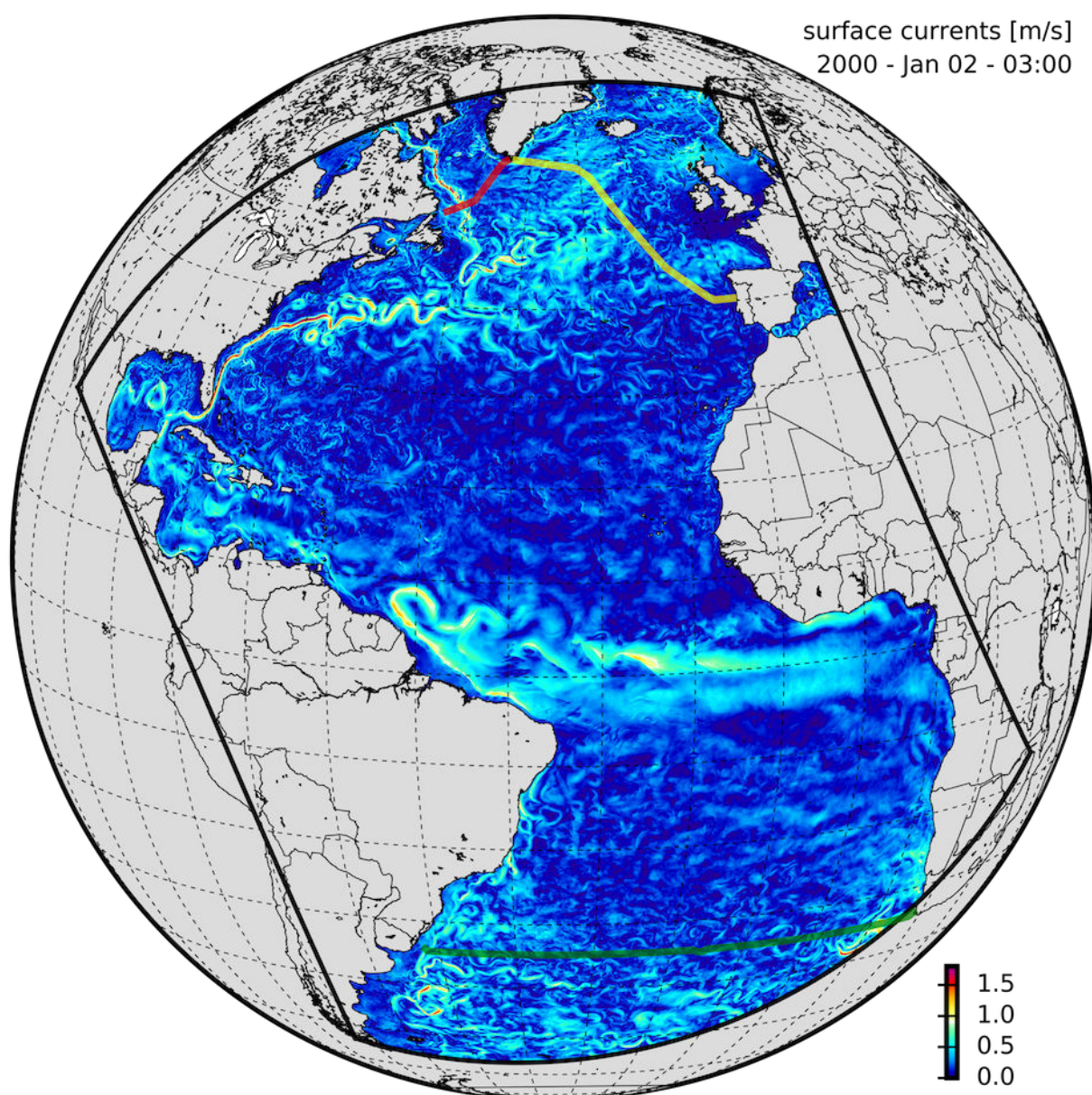


Figure 3.1 – Snapshot of surface currents amplitude for a 3-km resolution Atlantic simulation.

years) and a PhD student.

Theoretical and process studies are now just beginning to highlight the role played by submesoscale processes in the bottom layer. But we still miss a clear picture of their phenomenology, we do not know how they are affected by the internal wave field and we have not quantified their impacts on the large scale circulation. In particular, there is a dynamic link between deep small-scale turbulence and large-scale overturning circulation. That is, changes in dense water will necessarily have an impact on overturning circulation and, ultimately, climate. Observations have confirmed that intense bottom currents interacting with sloping topography could generate submesoscale processes with important implications for mixing and cross-density upwellings (Ruan *et al.*, 2017; Naveira Garabato *et al.*, 2019). But these effects cannot be resolved in climate-scale ocean models, and no parameterization currently accounts for their effects.

The goals of WP2 are (1) to quantify for the first time the impacts of deep submesoscale processes on mixing and turbulent fluxes of buoyancy in the Atlantic Ocean; (2) to explore ways of parameterizing them for climate-scale ocean models. It is organized around 3 different subparts, which have been designed to test the following hypotheses:

- H1: Submesoscale turbulence generated over sloping topography is a significant source of diapycnal mixing, and can drive intense localized upwelling of deep waters.
- H2: Submesoscale baroclinic instability and deep frontogenesis drive the restratification of the bottom boundary layer and help sustain water mass transformations.
- H3: Taking into account bottom submesoscale processes will modify the deep circulation, the large-scale distribution of water masses, and the meridional overturning circulation.

3.2.1 Quantify impacts of submesoscale turbulence on the large scale circulation

This part of the project will also involve P. Tedesco, who is a PhD Student supervised by J. Gula, P. Penven, and C. Menesguen, working on “the dissipation of mesoscale eddies in the ocean”. She is financed by LabexMer and Ifremer until Oct. 2020. The third year of the PhD will naturally fall in line with the analysis of the energy balance for the Atlantic simulations.

The first part aims at quantifying how submesoscale processes and internal waves modify the large-scale budgets of energy, buoyancy, and Potential Vorticity (PV). To this end, complete budgets of momentum, energy, tracers (T , S , b) and potential vorticity, including horizontal and vertical turbulent fluxes of all quantities, will be computed for the simulations at different resolutions, from mesoscale resolving (12 km / 50 lev., 6 km / 50 lev. and 3 km / 100 lev.) to submesoscale permitting (1 km, 200 levs.), and for the different setups, with or without NIW and tides.

3.2.1.1 Energy and buoyancy budgets

To characterize the presence and impact of submesoscale processes, we will first quantify the potential and kinetic energy for the time-mean flow and the eddies, traditionally known as the Lorenz energy cycle. We will also quantify how the different terms, in particular terms involving eddy-mean flow interactions, change with the resolution of the model and subsequently how energy dissipation is impacted. We will also investigate how the submesoscale dynamics play a role in fluxing energy across scales using methods such as coarse-graining (Aluie *et al.*, 2018). We will similarly compute the buoyancy budget over the Atlantic Ocean, and compare eddy buoyancy fluxes in the different simulations.

3.2.1.2 Impact of the internal waves

To disentangle the role of internal waves versus submesoscale processes, and study the interactions between the two, we will use the additional experiments where sources of internal waves are switched off alternatively. We will be able to get a more global picture of the impact of NIW and tides on the energy budget. We will quantify the energy directly extracted from the geostrophic currents by the waves, and see if it can lead to a “stimulated imbalance” (Barkan *et al.*, 2017), which catalyzes a forward energy cascade from mesoscale down to dissipative processes. Furthermore, we will be able to evaluate the vertical decay scale of near-inertial energy (Jochum *et al.*, 2013), which can have strong implications for bottom mixing (Clément & Thurnherr, 2018).

3.2.1.3 Potential vorticity budget

Another central quantity in oceanography, which can give insights to the gyres dynamics, is the Potential Vorticity (PV). PV is only modified by diabatic processes. For instance, it has been shown that PV fluxes are modified by submesoscale turbulence at the surface, with potentially strong impacts for the rate of formation of the 18 degree mode water (**Wenegrat *et al.*, 2018b**). In the present context, mixing and friction near the bottom boundary can create PV anomalies that can then lead to baroclinic instability and generation of eddies, spreading water mass properties within the ocean interior. There exists strong constraints on the evolution of the net PV in diabatic evolution and specific methodologies to calculate PV so as to verify these constraints (**Morel *et al.*, 2019**). We will use these diagnostics to calculate and interpret PV budgets, focusing on the production and spreading of the Mode Water. The emergence of submesoscale vortices from baroclinic instability and their impact on the generation of Mode Water and subsequently on modification of the large scale gyre dynamics, will be investigated in terms of the bottom PV fluxes.

3.2.2 Characterise processes responsible for water-mass transformations

This part of the project will be led by the Postdoc hired in the context of the ANR DEEPER. It will be a collaboration with J. Callies (Caltech), L. Thomas (Stanford), and X. Capet (LOCEAN). It will also be linked to other projects related to observation campaigns at different sites as detailed below.

This part aims at identifying and better understanding **the processes generating mixing and driving water-mass transformations**. We will first evaluate the intensity and localisation of energy dissipation and mixing in the different simulations and compare them to bulk estimates and observations from microstructure measurements (Waterhouse *et al.*, 2014). The thickness of the bottom boundary layer is another diagnostic that will be used to compare the simulations to observations (Banyte *et al.*, 2018). We will finally compute water-mass transformations in the simulation and evaluate the differences depending on the resolution and forcings used. Then we will try to disentangle the contribution of the different processes to deep ocean mixing, to determine where it is predominantly associated with internal waves breaking (internal tides, near-inertial waves, lee waves, or the formation of hydraulic jumps) and where submesoscale turbulence contributes significantly. We will also investigate which processes are driving the restratification of the bottom boundary layer.

We will identify **critical locations**, with intense bottom mixing and turbulent fluxes, and investigate the processes at play by means of high-resolution regional simulations and idealized process studies. Nested simulations with the CROCO model will be used to study specific regions at higher resolution and check how sensitive the processes are to the horizontal and vertical resolution, and the choices for the numerical schemes. For the highest resolution nests, we will take advantage of the recently developed **non-hydrostatic version of CROCO** (Roullet *et al.*, 2017) to relax the hydrostatic approximation and evaluate a possible impact on the dynamics. Identified processes will be further studied by designing idealized simulations. If possible, we will try to use theory to develop

some scaling-laws for the impact of the processes for mixing and buoyancy fluxes.

A few locations are already being studied in the context of other projects, in particular motivated by the presence of observational programs at the same location:

(1) **The Reykjanes Ridge** is a key topographic structure stretching at the crossroad of the Atlantic Meridional Overturning Circulation (AMOC) upper and lower limbs. Despite its crucial role in generating irreversible mixing leading to water mass transformation, the mixing scenario – *i.e.*, where? when? mechanisms at play? – remains obscure, hence strong biases are found in global simulations. By using a suite of in situ data collected during the “**The Reykjanes Ridge Experiment**” (**RREX**), in combination with realistic high-resolution simulations, we will document the geography and time variability of energy dissipation and mixing, and assess the contributions from the several processes potentially at play, *i.e.*, tides, (sub)mesoscale interactions with topography and NIW.

This part of the project will be led by C. Vic (ISBlue postdoctoral student at LOPS from March 2019 to March 2021, supervised by B. Ferron, V. Thierry and I).

(2) **The Mid-Atlantic Ridge south of the Azores** is a region with strong generation of internal tides and submesoscale turbulence (Vic *et al.*, 2018). One specific aim is to understand more precisely the turbulence around the **Lucky Strike hydrothermal vent**, located on the Mid-Atlantic Ridge, and to revisit the hydrothermal plume dynamics in a real turbulent flow environment. We have access to in-situ data (moorings + ADCP) on the Lucky Strike site as part of the **European observatory EMSO-Azores**. We will develop ultra-high resolution ocean models – down to 10 m grid size – at the Lucky Strike site to investigate energy dissipation, diapycnal mixing and transport of species near the seafloor and across the water column.

This part of the project will be led by a PhD student hired in the context of the iAtlantic H2020 project. <http://www.iatlantic.eu/>, supervised by G. Roullet and I. It is a follow-up of the work by C. Vic (2016), N. Lahaye (postdoc 2017-2019) and G. Crystle (currently PhD with G. Roullet).

(3) **The Orkney Passage (OP)** is a narrow passage between the Weddell Sea and the Scotia Sea where dense waters are modified prior to joining the lower limb of the overturning circulation cell (Fig. 3.2). Turbulent mixing processes within the OP are critical for setting properties of abyssal waters flowing out of the Weddell Sea. One turbulent mixing mechanism expected to have such effects is frictionally-induced modification in potential vorticity (PV) and associated centrifugal instability (Naveira Garabato *et al.*, 2019). This part of the project will focus on the analysis and interpretation of moored observations and model simulations. The observations have been collected at high temporal and spatial resolution as part of the **Dynamics of the Orkney Passage Outflow (DynOPO)** project. Three of seven moorings were spaced 5 km apart and therefore permit calculations of PV at submesoscale resolution (1-10 km). Furthermore, thermistors on several moorings can be used to infer changes in turbulent properties over the two-year record (2015-2017). The goals of the project are to (1) enhance understanding of energy and buoyancy fluxes by closely examining moorings and high-resolution model data, (2) identify a relationship between volume transport and fluxes within OP and (3) identify regions conducive to centrifugal instability. The full proposal can be downloaded here: http://stockage.univ-brest.fr/~gula/Work/CIOP_proposal.pdf.

This part of the project will be led by C. Buckingham, who has been awarded a European Marie Curie fellowship (H2020-MSCA-IF-2017) to come work at LOPS under my supervision. This is a collaboration with Alberto Naveira Garabato (Southampton), Sonya Legg (Princeton) and Stephen Griffies (NOAA/GFDL).

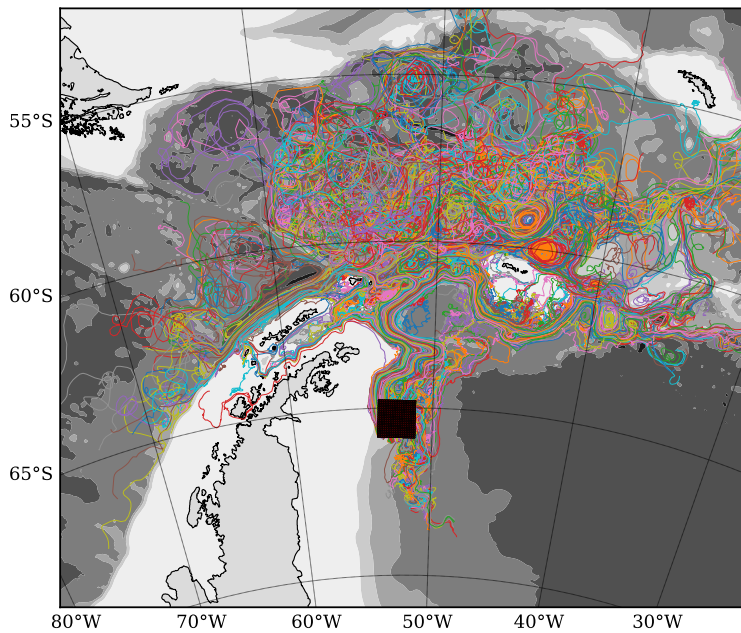


Figure 3.2 – Lagrangian particles trajectories in a regional simulation of the Weddell Sea and Drake Passage. Figure from C. Vic.

(4) **The Gulf Stream** is an ideal place to study the interaction of geostrophic flows with topography. As it flows past the New England Seamounts, high amplitude lee waves as well as intense turbulent wakes are visible in the lee of topography in models (Fig. 3.3). Very high levels of diapycnal mixing have also been inferred in this region based on Argo estimates and inverse models (A. Mashayek, personal communication). This is prompting interest for the design of a new observational program and a more detailed investigation using new simulations with CROCO-NH to better resolve the processes at play.

*This work will be a collaboration with A. Mashayek (Imperial College London). A NERC/NSF project targeting *in-situ* experiments in this region is currently being discussed with U.S. and U.K. partners.*

3.2.3 Parameterise impacts of deep submesoscale using machine learning

This part of the project will be led by the PhD student hired in the context of the ANR DEEPER. It will be a collaboration with P. Tandeo, R. Fablet (IMT-A), J. Le Sommer, W.K. Dewar (IGE), and G. Roullet (LOPS).

The sub-grid scale turbulence is taken into account in ocean models through the Reynolds stress terms in the momentum and tracer equations (“eddy” momentum and tracer fluxes). These terms can be computed using different types of closures, based on different physical principles, which provide a relation between the Reynolds fluxes and the resolved model variables. Some parameterizations are already used in ocean models to incorporate effects of some specific unresolved processes, such as the effect of internal waves (MacKinnon *et al.*, 2017) or the effects of submesoscale mixed-layer instability (Fox-Kemper *et al.*, 2008), and symmetrical instability (Bachman *et al.*, 2017). However, no parameterizations are currently able to incorporate effects of deep submesoscale processes in mesoscale resolving models. Designing a parameterization based on physical principles for a specific dynamical process is a long and uncertain task. But it is now possible to use empirical data-driven methods,

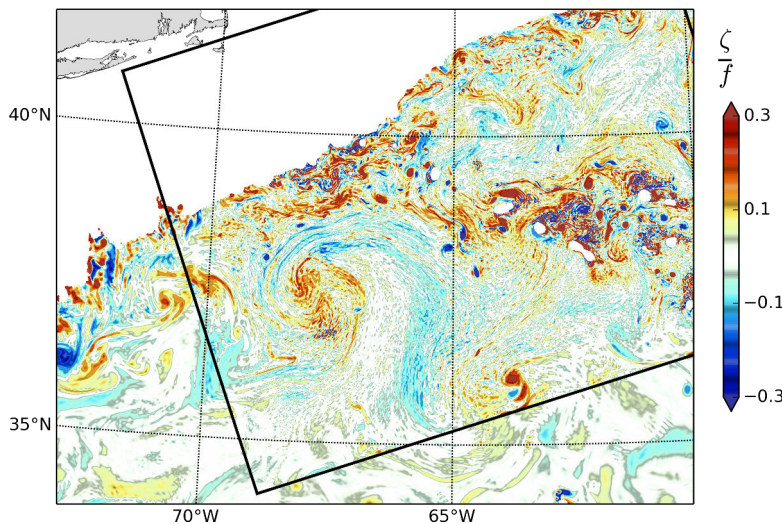


Figure 3.3 – Snapshot of Relative vorticity at 3000 m depth in a ROMS simulation of the Gulf Stream ($\text{dx} = 500 \text{ m}$)

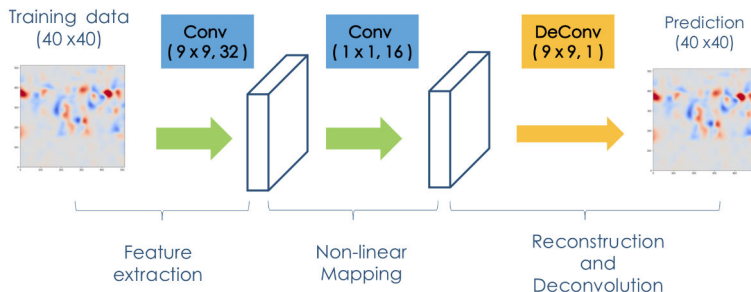


Figure 3.4 – Architecture of the Deep Neural Network used in Fig 3.5. Figure from Yan Feier.

based on machine learning algorithms, that allow to extract the information without knowing all underlying physical principles.

One way to predict Reynolds stresses without knowing a priori all underlying physical principles is to use **machine learning** methods, and in particular, a **deep neural network (DNN)**. The DNN transforms input data through multiple layers of nonlinear interactions (*e.g.*, Fig. 3.4). The DNN has proved very efficient to find intricate structures in high-dimensional data (LeCun *et al.*, 2015) and it has gained a lot of attention in the last few years for its ability to be successful in different domains such as playing the game of Go (Silver *et al.*, 2016). The concepts behind deep learning are not that recent, but can now take advantage of the growing computational power and the large amount of data available to train the DNN. Such methods have been successfully applied to parameterize Reynolds stresses for Reynolds-averaged Navier-Stokes (RANS) models (Ling *et al.*, 2016) or large eddy simulations (LES) (Vollant *et al.*, 2017).

More recently, DNN have been able to successfully replicate the spatiotemporal variability of the Reynolds stresses for momentum in an idealized quasi-geostrophic ocean model (Bolton & Zanna, 2019). We have reproduced the same results using an improved version of the DNN (Fig. 3.4) and applied it to a realistic Atlantic model during the M2 internship of Yan FeiEr (Fig. 3.5). We have found that this approach can give accurate generalization of spatial and temporal variability of subgrid eddy momentum forcings for mesoscale eddies in a western boundary current region, even trained by a limited amount of data. The data-driven parameterizations are a very promising path for ocean models in the future.

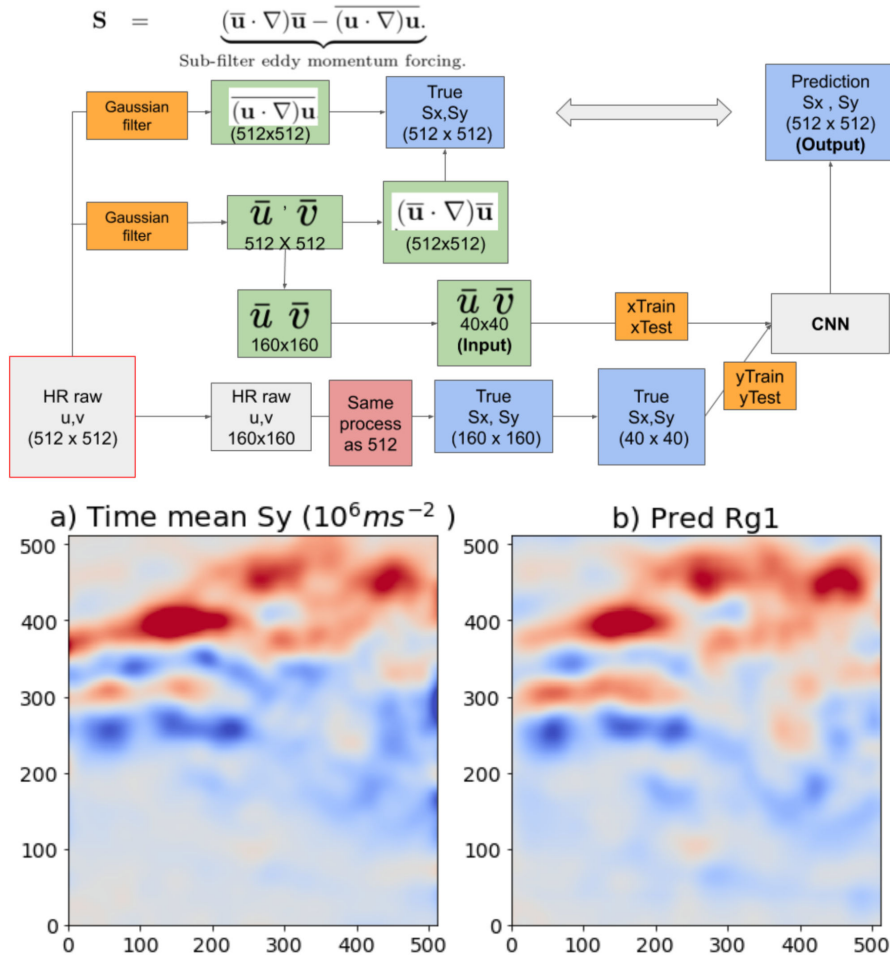


Figure 3.5 – (top) Implementation details, and (bottom) example of the time-mean prediction for the meridional eddy momentum forcing in a Gulf Stream simulation. Figure from Yan Feier.

We are now planning to apply a DNN along the same lines for the submesoscale turbulence. The objective will be to predict Reynolds stress corrections to the momentum and tracer equations for a mesoscale resolving (typically 12 km) simulation using the DNN. The DNN will be built in Python using Keras and TensorFlow. It will be trained to relate coarse-grained turbulent Reynolds stresses to coarse-grained horizontal velocities and tracers computed from the highest resolution simulation (1 km) including tides and high-frequency winds from WP1. We will also apply the DNN to another simulation: eNATL60, a North Atlantic NEMO simulation with different vertical coordinates (z-coordinates) and numerical schemes. The goal will be to evaluate the sensitivity of the approach to numerics and model discretisation. This task will imply to design a common framework of tools for both models that are able to deal with very large datasets. We will rely on the Pangeo software ecosystem (<https://pangeo.io/>) for this purpose.

3.3 Impacts of submesoscale coherent vortices

This part of the project will be led by A. Chouksey, who is a PhD student (2019-2022) supervised by X. Carton and I, funded by CNRS and Région Bretagne. The work will be done in collaboration with Jim McWilliams (UCLA) and Loic Houpert (NOCS).

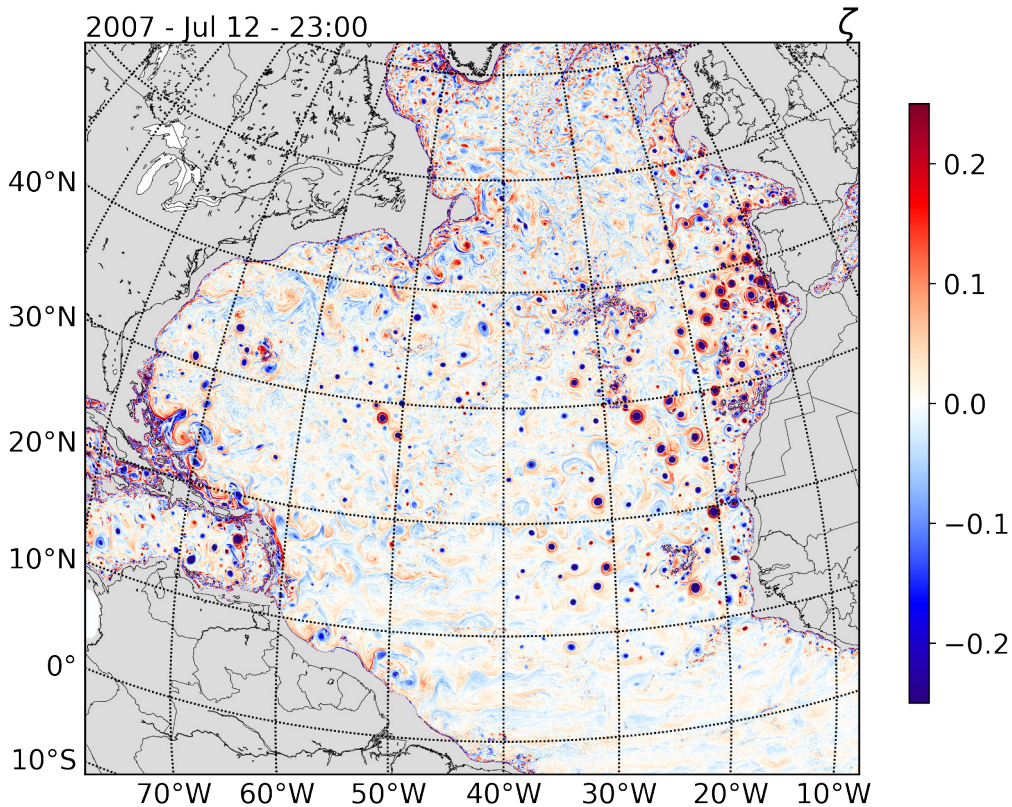


Figure 3.6 – Snapshot of relative vorticity at 1000 m depth in a 3-km resolution Atlantic simulation.

Ocean eddies contribute significantly to global fluxes of heat, salt, carbon and biogeochemical tracers. Surface intensified mesoscale eddies, with radii larger than the Rossby deformation radius (30-200 km), have been studied extensively using altimetric observations. However, we know much less about the contribution of subsurface eddies, particularly submesoscale (1-30 km) subsurface eddies due to the sparsity of in situ observations. SCVs can generate long-range anomalous transport of water properties and biogeochemical tracers; for instance, an SCV transporting water from Baja California was sampled near Hawaii (Lukas & Santiago-Mandujano, 2001). Historical observations of SCVs provide glimpses of the ocean interior richness, and suggest that it is populated by a large number of deep submesoscale structures, but the ocean is still largely undersampled and observational data remains limited. Furthermore, global or basin-scale models do not usually have a resolution sufficient to resolve submesoscale processes. Thus, we still do not have a quantitative assessment of the numbers and impact of SCVs for the ocean circulation.

Furthermore, observations show a larger number of anticyclonic SCVs than cyclonic SCVs, but the reason why anticyclones dominate over cyclones is still an unresolved issue (McWilliams, 2016). We do not know if it is related to an asymmetry of the generation processes or to different stability properties of the SCVs after their formation. Quasi-geostrophic theory does not predict any asymmetry between cyclones and anticyclones related to the generation process, nor their stability. The generation of vortices in the lee of topography is also symmetric and does not explain the dominance of anticyclones.

The aim of this part of the project is to provide **the first census of SCVs in the Atlantic Ocean** and **quantify their impact on the large scale circulation** using in situ observations from moorings, gliders and Argo floats, and the Atlantic simulation from WP1. In addition, the project will investigate the processes responsible for the generation and destruction of the SCVs, and for their propagation. Finally, it will also tackle a long standing question in oceanography: *why are there more*

submesoscale anticyclones than cyclones in the interior ocean?

3.3.1 Basin scale statistics for SCVs

Moorings, argo data and model outputs will be used to compute basin scale statistics on the presence and structure of SCVs. After the detection of submesoscale eddies we will be able to perform statistics of eddy characteristics: hydrographic signatures at the eddy cores, vertical distribution of hydrographic anomalies, and vertical and horizontal scales; and to analyze their spatial and temporal variability. The numerical outputs from the model will be used to track long-lived SCVs. We aim to compile statistics of the structure and propagation of these eddies: amplitude, radius, lifespan, propagation speed, propagation distance, preferred trajectories, formation and dead zones, etc. We will also look at the ratio between cyclonic and anticyclonic SCVs in the different regions, and check how it varies depending on the SCVs age and origin. In particular we will check if the ratio matches the ratio of prograde versus retrograde currents, or if it is related to a different behaviours for the cyclones and anticyclones after their generation.

3.3.2 Generation mechanisms and life-cycle of SCVs

The previous statistics will provide knowledge on the preferred eddy formation and decay regions. Then, using targeted realistic and/or idealized numerical simulations, we aim to investigate: the generation mechanisms of SCVs in the different regions; the mechanisms driving SCVs trajectories (e.g. advection by mean currents, interactions with the mesoscale eddies); the interactions between SCVs (cyclonic and/or anticyclonic) possibly leading to erosion, fusion or alignment of SCVs; the mechanisms leading to SCVs destruction (e.g. large scale current shear and strain, interactions with topography); the mechanisms potentially leading to different stability properties for the cyclones and anticyclones.

3.3.3 Impacts on the large scale circulation

Finally, we plan to assess, for the first time, the contribution of SCVs to the temperature, salinity and energy budget in the Atlantic Ocean, and determine how important they are to the ventilation of the interior ocean and to the transport of water masses in the deep ocean.

3.4 Impacts of submesoscale fronts on the vertical fluxes of tracers

The submesoscale drive significant vertical energy propagation, which strongly control exchanges between the surface layer and the ocean interior. Submesoscale instabilities act to re-stratify the mixed-layer, which could potentially inhibit vertical exchanges. However, the very large vertical velocities that are generated at the submesoscale fronts and filaments induce a net flux of tracers through the base of the mixed-layer (Balwada *et al.*, 2018). Submesoscale variability thus provides a pathway connecting the ocean surface with the interior, hence its correct representation in ocean models might contribute to closing a current knowledge gap.

The competition between the different type of submesoscale processes and their impact on vertical tracer fluxes at truly submesoscale resolving resolutions will be the topic of dedicated realistic and idealized studies (ongoing collaboration with R. Barkan, U. of Tel Aviv). This is also highly relevant in the context of two international observationally-based programs in which I am participating: APERO, which focuses on carbon export (4.1), and EUREC4A-OA, which focuses on air-sea interactions (4.2).

The meso- and submesoscale drive significant vertical energy propagation, which strongly control exchanges between the surface layer and the ocean interior, and in turn maintain anomalies in SST and other variables. Submesoscale instabilities act to re-stratify the mixed-layer, which could potentially inhibit vertical exchanges. However, the very large vertical velocities that are generated at the

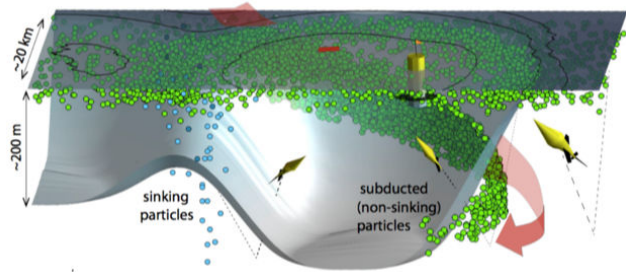


Figure 3.7 – Diagram showing the impact of the advection generated by an eddy on the sinking of particles. Figure from Denver et al., 2017)

submesoscale fronts and filaments generate a net flux of tracers through the base of the mixed-layer (Balwada *et al.*, 2018). Meso- to submesoscale variability thus provides a pathway connecting the ocean surface with the interior, hence its correct representation in ocean transport models might contribute to closing this current knowledge gap.

The competition between the different type of submesoscale processes and their impact on vertical tracer fluxes at truly submesoscale resolving resolutions will be the topic of dedicated realistic and idealized studies (ongoing collaboration with R. Barkan, U. of Tel Aviv). This is also highly relevant in the context of two international observationally-based programs in which I am participating: **APERO**, which focuses on carbon export (3.4.1), and **EUREC4A-OA**, which focuses on air-sea interactions (3.4.2).

3.4.1 Impact of submesoscale dynamics on the fate of exported particles in the deep ocean

This part of the project will be led by Lu Wang, who is undertaking a PhD project (2019-2022) supervised by L. Memery (LEMAR) and I, funded by ISblue.

Oceans play a critical role for the carbon cycle through their fixation of organic matter from dissolved carbon dioxide in the surface ocean and the export of this fixed organic carbon to the deep ocean, where that carbon may be sequestered from the atmosphere on time scales of months to millennia. So far carbon export has been thought of as a 1D vertical process, and 3d motions of the oceans have not been considered (Fig. 3.7).

The meso- and submesoscale currents play an important role as they not only create a very strong heterogeneity on the particle production at the surface, but they also drive the vertical velocities that control for the most part exchanges between the surface layer and the ocean interior. The net impact of submesoscale currents may be to enhance both upward nutrient inputs into the surface layer (fertilizing effect on primary production), and tracer and particle subduction from the surface layer to the interior (export). This result remains to be carefully quantified in fully realistic conditions and under different dynamical regimes. The impact on tracer subduction may depend on the type of mesoscale and submesoscale processes dominating the upper ocean dynamics.

We will use Atlantic simulations (see section 3.1) as well as local simulations (200 m), resolving the smaller frontal scales. The Atlantic run will be used to define the characteristics of different dynamical and biological production regimes (North-East Atlantic, African upwelling, Gulf Stream, Sargasso Sea, Labrador Sea, etc.) that will be selected to run higher resolution local (400x400 km) simulations. Particles will be released at the surface following observed ocean color patterns. We will use a code of Lagrangian trajectories, suited for particles, e.g. taking into account behavior rules (sinking, particle interaction). This work will also serve as a preparation for the APERO (Assessing

marine biogenic matter Production, Export and Remineralisation : from the surface to the dark Ocean) campaign that is planned in the Porcupine Plain in 2021 or 2022. This work will explore and quantify the (de)correlation of the particle flux sampled in the traps in the deep ocean with the spatio temporal distribution of surface particles, generated by biological production, and come up with relations between the characteristics of the surface turbulence regime and the particle spectra at depth.

3.4.2 Impact of submesoscale on air-sea exchanges

*This part of the project is included in the project EUREC4A-OA (*Improving the representation of small-scale nonlinear ocean-atmosphere interactions in Climate Models by innovative joint observing and modelling approaches*, PI: S. Speich), which has been submitted to the JPI-Oceans call in June 2019. The proposal includes fundings for a postdoc at LOPS, supervised by X. Carton and I.*

Air-sea exchange of heat, freshwater and constituents is controlled by a multitude of physical, biogeochemical and biological processes that vary in importance by region but also in time. The EUREC4A-OA project seeks to advance our understanding of ocean-atmosphere exchanges at the ocean small-scale by two complementary approaches: 1) by compiling an unprecedented set of observations of, in parallel, the ocean, the atmosphere and their exchanges at the ocean small-scale and resolving statistics of the diurnal cycle and 2) by combining the observations with a large hierarchy of ocean, atmosphere and ocean- atmosphere coupled models for exploring the nature of air-sea interactions and ocean dynamics at these scales.

EUREC4A-OA will take advantage of the international EUREC4A airborne field campaign from 18 Jan to 20 Feb 2020 over the Northwest Tropical Atlantic, near Barbados (www.eurec4a.eu) and add an international ocean-atmosphere in-situ component that will resolve, for the very first time, the submeso- and meso-scale processes in the ocean and atmosphere boundary layers. This will be achieved by implementing a set of innovative ocean-atmosphere measurements via the deployment in parallel of a large number of observing platforms (research vessels with augmented observing capabilities, drones, underwater gliders, and newly developed drifters, profiling floats, air-sea fluxes buoys and saildrones). The project will develop an unparalleled hierarchy of numerical simulations (ranging from Large Eddy Simulations, LES – including coupled ocean-atmosphere LES – to global high-resolution ocean- atmosphere simulations and ESMs) of the ocean and of the ocean-atmosphere systems explicitly resolving scales as small as 10 meters and the direct interactions of the ocean-atmosphere systems.

My involvement in the project will be in the identification and investigation of the mechanisms associated with meso and submesoscale ocean structures. We will use observational data and numerical simulations with (1) submesoscale-resolving ocean component, (2) an eddy-resolving ocean component and (3) a non-eddy-resolving component. We will investigate the dynamics of eddies (stability and interactions) under atmospheric forcing modified by the ocean mesoscale activity, the effect of eddies on heat and momentum uptake, on their horizontal and vertical transport, the effect of sub-mesoscale fronts and instabilities (the intense vertical flows in frontal structures versus the re-stratification by mixing layer instabilities) and finally the effect of the Amazon and Orinoco rivers through the generation of fronts and changes in the properties of the mixed-layer.

3.5 Resources

I will invest most of my time in this project. It will also rely on multiple collaborations with engineers and researchers, and hiring of several postdocs and PhD students, as detailed for each of the WP described previously. This is summarized in the project's timeline in Fig. 3.9.

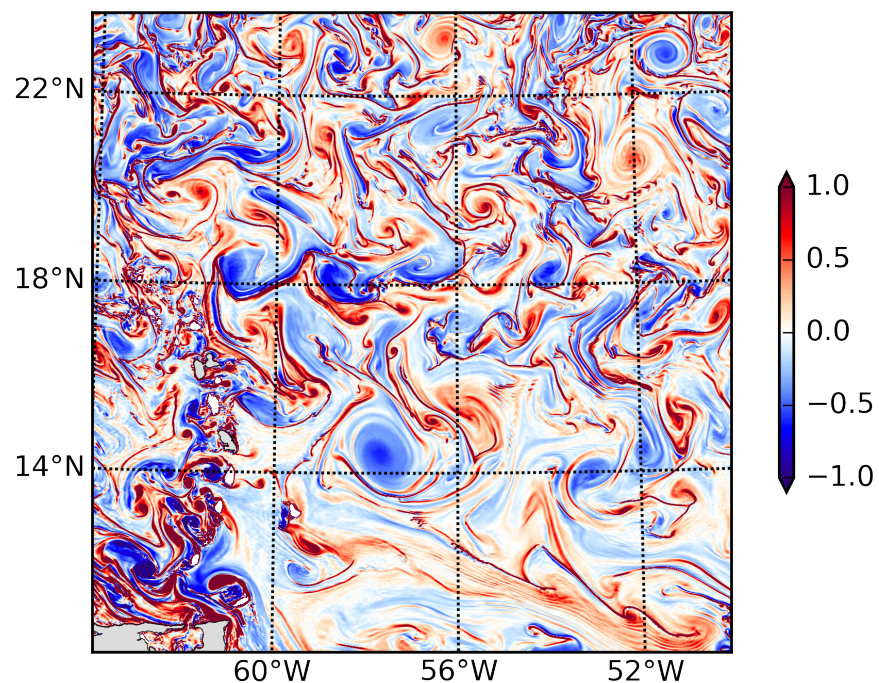


Figure 3.8 – Relative vorticity from a 3-km resolution model in the region chosen for the EUREC4A-OA campaign.

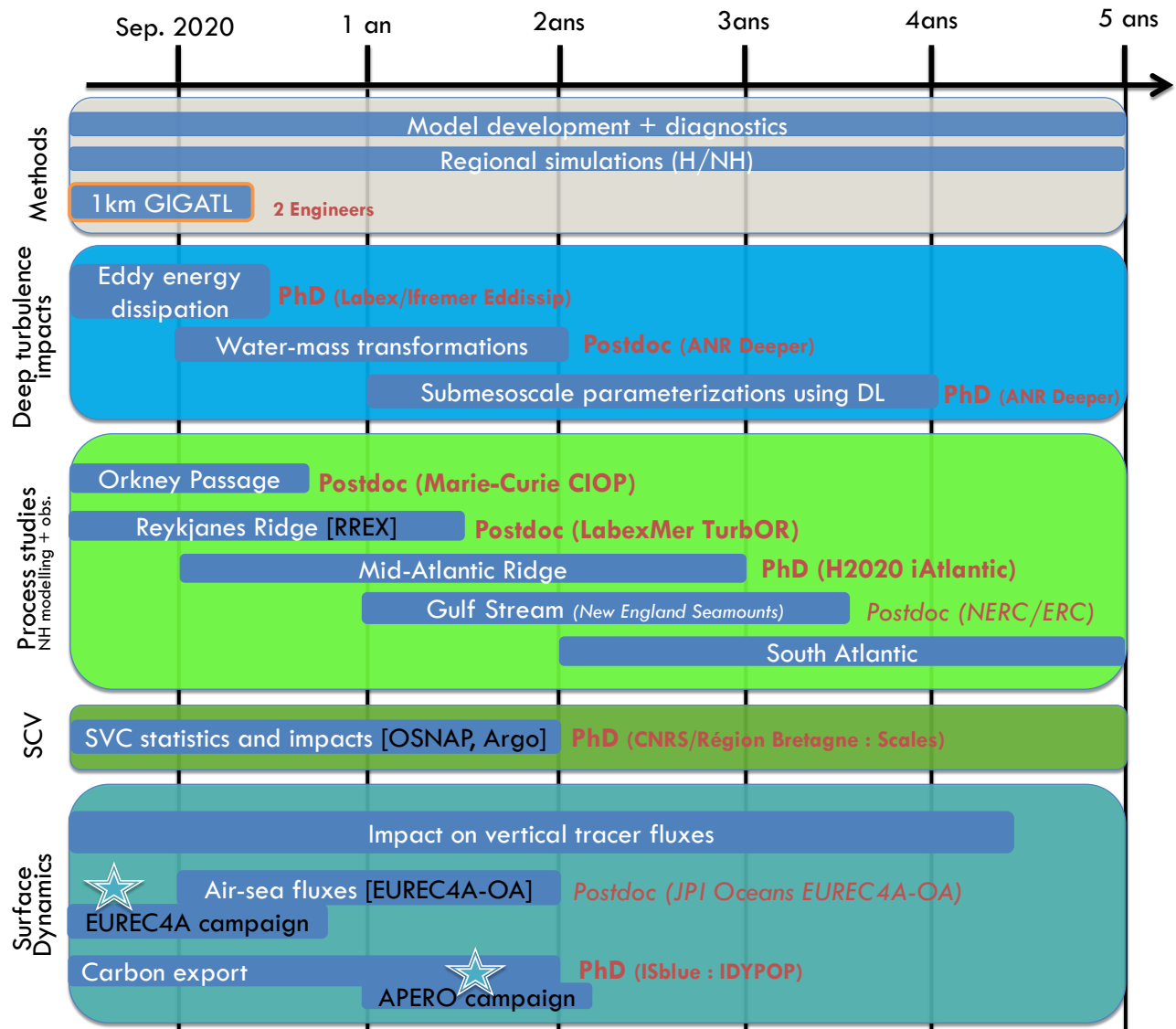


Figure 3.9 – Timeline of the project. Engineers, PhD and postdoctoral students involved in the project are indicated in red, bold if already funded, italic otherwise.

Bibliography

- AKEN, HENDRIK M. VAN 1995 Mean currents and current variability in the iceland basin. *Netherlands Journal of Sea Research* **33** (2), 135 – 145.
- ALUIE, HUSSEIN, HECHT, MATTHEW & VALLIS, GEOFFREY K. 2018 Mapping the energy cascade in the north atlantic ocean: The coarse-graining approach. *Journal of Physical Oceanography* **48** (2), 225–244.
- ARDHUIJN, F., GILLE, S.T., MENEMENLIS, D., ROCHA, C.B., RASCLE, N., CHAPRON, B., GULA, J. & MOLEMAKER, M.J. 2017 Small-scale open-ocean currents have large effects on wind-wave heights. *J. Geophys. Res.* **122**.
- VON ARX, W.S., BUMPUS, D.F. & RICHARDSON, W.S. 1955 On the fine-structure of the Gulf Stream front. *Deep Sea Research (1953)* **3** (1), 46–65.
- ASSASSI, C., MOREL, Y., VANDERMEIRSCH, F., CHAIGNEAU, A., PEGLIASCO, C., MORROW, R., COLAS, F., FLEURY, S., CARTON, X., KLEIN, P. & CAMBRA, R. 2016 An index to distinguish surface- and subsurface-intensified vortices from surface observations. *J. Phys. Oceanogr.* **46** (8), 2529–2552.
- BACHMAN, S.D., FOX-KEMPER, B., TAYLOR, J.R. & THOMAS, L.N. 2017 Parameterization of frontal symmetric instabilities. I: Theory for resolved fronts. *Ocean Modelling* **109**, 72 – 95.
- BALWADA, DHRUV, SMITH, K. SHAFER & ABERNATHEY, RYAN 2018 Submesoscale vertical velocities enhance tracer subduction in an idealized antarctic circumpolar current. *Geophysical Research Letters* **45** (18), 9790–9802.
- BANYTE, D., SMEED, D. A. & MORALES MAQUEDA, M. 2018 The weakly stratified bottom boundary layer of the global ocean. *Journal of Geophysical Research: Oceans* **123** (8), 5587–5598.
- BARKAN, ROY, MOLEMAKER, M. JEROEN, SRINIVASAN, KAUSHIK, McWILLIAMS, JAMES C. & D'ASARO, ERIC A. 2019 The role of horizontal divergence in submesoscale frontogenesis. *Journal of Physical Oceanography* **49** (6), 1593–1618.
- BARKAN, ROY, WINTERS, KRAIG B. & McWILLIAMS, JAMES C. 2017 Stimulated imbalance and the enhancement of eddy kinetic energy dissipation by internal waves. *Journal of Physical Oceanography* **47** (1), 181–198.
- BECKMANN, A. & HAIDVOGEL, D.B. 1993 Numerical simulation of flow around a tall isolated seamount. Part I: Problem formulation and model accuracy. *J. Phys. Oceanogr.* **23**, 1736–1753.
- BOCCALETTI, G., FERRARI, R. & FOX-KEMPER, B. 2007 Mixed layer instabilities and restratification. *J. Phys. Oceanogr.* **37**, 2228–2250.
- BOLTON, THOMAS & ZANNA, LAURE 2019 Applications of deep learning to ocean data inference and subgrid parameterization. *Journal of Advances in Modeling Earth Systems* **11** (1), 376–399.
- BOSSE, ANTHONY, TESTOR, PIERRE, HOUPERT, LOÏC, DAMIEN, PIERRE, PRIEUR, LOUIS, HAYES, DANIEL, TAILLANDIER, VINCENT, DURRIEU DE MADRON, XAVIER, D'ORTENZIO, FABRIZIO, COPOLA, LAURENT, KARSTENSEN, JOHANNES & MORTIER, LAURENT 2016 Scales and dynamics of submesoscale coherent vortices formed by deep convection in the northwestern Mediterranean Sea. *J. Geophys. Res. Oceans* **121** (10), 7716–7742.

- BOSSE, ANTHONY, TESTOR, PIERRE, MAYOT, NICOLAS, PRIEUR, LOUIS, D'ORTENZIO, FABRIZIO, MORTIER, LAURENT, GOFF, HERVÉ LE, GOURCUFF, CLAIRE, COPPOLA, LAURENT, LAVIGNE, HÉLOÏSE & RAIMBAULT, PATRICK 2017 A submesoscale coherent vortex in the Ligurian Sea: From dynamical barriers to biological implications. *J. Geophys. Res. Oceans* **122** (8), 6196–6217.
- BOSSE, ANTHONY, TESTOR, PIERRE, MORTIER, LAURENT, PRIEUR, LOUIS, TAILLANDIER, VINCENT, D'ORTENZIO, FABRIZIO & COPPOLA, LAURENT 2015 Spreading of Levantine Intermediate Waters by submesoscale coherent vortices in the northwestern Mediterranean Sea as observed with gliders. *J. Geophys. Res. Oceans* **120** (3), 1599–1622.
- BOWER, A.S., HENDRY, R.M., AMRHEIN, D.E. & LILLY, J.M. 2013 Direct observations of formation and propagation of subpolar eddies into the Subtropical North Atlantic. *Deep-Sea Res.* **85**, 15–41.
- BREUSING, CORINNA, BIASTOCH, ARNE, DREWS, ANNIKA, METAXAS, ANNA, JOLLIVET, DIDIER, VRIJENHOEK, ROBERT C., BAYER, TILL, MELZNER, FRANK, SAYAVEDRA, LIZBETH, PETERSEN, JILLIAN M., DUBILIER, NICOLE, SCHILHABEL, MARKUS B., ROSENSTIEL, PHILIP & REUSCH, THORSTEN B.H. 2016 Biophysical and population genetic models predict the presence of “phantom” stepping stones connecting mid-atlantic ridge vent ecosystems. *Current Biology* **26** (17), 2257 – 2267.
- BUCKINGHAM, CHRISTIAN E., KHALEEL, ZAMMATH, LAZAR, AYAH, MARTIN, ADRIAN P., ALLEN, JOHN T., NAVEIRA GARABATO, ALBERTO C., THOMPSON, ANDREW F. & VIC, CLÉMENT 2017 Testing munk's hypothesis for submesoscale eddy generation using observations in the north atlantic. *Journal of Geophysical Research: Oceans* **122** (8), 6725–6745.
- BUCKINGHAM, CHRISTIAN E., NAVEIRA GARABATO, ALBERTO C., THOMPSON, ANDREW F., BRANNIGAN, LIAM, LAZAR, AYAH, MARSHALL, DAVID P., GEORGE NURSER, A. J., DAMERELL, GILLIAN, HEYWOOD, KAREN J. & BELCHER, STEPHEN E. 2016 Seasonality of submesoscale flows in the ocean surface boundary layer. *Geophysical Research Letters* pp. n/a–n/a, 2016GL068009.
- CALLIES, JÖRN 2018 Restratification of abyssal mixing layers by submesoscale baroclinic eddies. *Journal of Physical Oceanography* **48** (9), 1995–2010.
- CALLIES, J., FERRARI, R., KLYMAK, J. & GULA, J. 2015 Seasonality in submesoscale turbulence. *Nat. Commun.* **6**, 6862.
- CAPET, X.J., MCWILLIAMS, JAMES C., MOLEMAKER, M.J. & SHCHEPETKIN, A.F. 2008a Mesoscale to submesoscale transition in the California Current System. Part I: Flow structure, eddy flux, and observational tests. *J. Phys. Oceanogr.* **38**, 29–43.
- CAPET, X.J., MCWILLIAMS, JAMES C., MOLEMAKER, M.J. & SHCHEPETKIN, A.F. 2008b Mesoscale to submesoscale transition in the California Current System. Part II: Frontal processes. *J. Phys. Oceanogr.* **38**, 44–64.
- CAPET, X., MCWILLIAMS, J. C., MOLEMAKER, M. J. & SHCHEPETKIN, A. F. 2008c Mesoscale to submesoscale transition in the california current system. part iii: Energy balance and flux. *Journal of Physical Oceanography* **38** (10), 2256–2269.
- CHARNEY, J.G. 1947 The dynamics of long waves in a baroclinic westerly current. *J. Met.* **4**, 135–163.
- CHELTON, DUDLEY B., DESOEKE, ROLAND A., SCHLAX, MICHAEL G., EL NAGGAR, KARIM & SIWERTZ, NICOLAS 1998 Geographical variability of the first baroclinic rossby radius of deformation. *Journal of Physical Oceanography* **28** (3), 433–460.
- CHELTON, DUDLEY B., SCHLAX, MICHAEL G. & SAMELSON, ROGER M. 2011 Global observations of nonlinear mesoscale eddies. *Progress in Oceanography* **91** (2), 167 – 216.

- CHELTON, DUDLEY B., SCHLAX, MICHAEL G., SAMELSON, ROGER M., FARRAR, J. THOMAS, MOLEMAKER, M. JEROEN, MCWILLIAMS, JAMES C. & GULA, JONATHAN 2019 Prospects for future satellite estimation of small-scale variability of ocean surface velocity and vorticity. *Progress in Oceanography* **173**, 256 – 350.
- CHELTON, DUDLEY B., SCHLAX, MICHAEL G., SAMELSON, ROGER M. & DE SZOKE, ROLAND A. 2007 Global observations of large oceanic eddies. *Geophys. Res. Lett.* **34** (15).
- CLARKE, R.A. 1984 Transport through the Cape Farewell-Flemish Cap section. *Rapports et procès-verbaux des réunions - Conseil international pour l'exploration de la mer* **185**, 120–130.
- CLÉMENT, LOUIS & THURNHERR, ANDREAS M. 2018 Abyssal upwelling in mid-ocean ridge fracture zones. *Geophysical Research Letters* **45** (5), 2424–2432.
- CROWE, MATTHEW N. & TAYLOR, JOHN R. 2018 The evolution of a front in turbulent thermal wind balance. part 1. theory. *Journal of Fluid Mechanics* **850**, 179–211.
- CROWE, MATTHEW N. & TAYLOR, JOHN R. 2019 The evolution of a front in turbulent thermal wind balance. part 2. numerical simulations. *Journal of Fluid Mechanics* **880**, 326–352.
- CSANADY, GABRIEL T. 1997 On the theories that underlie our understanding of continental shelf circulation.
- DANIAULT, NATHALIE, LHERMINIER, PASCALE & MERCIER, HERLÉ 2011 Circulation and transport at the southeast tip of greenland. *Journal of Physical Oceanography* **41** (3), 437–457.
- DANIOUX, E., VANNESTE, J., KLEIN, P. & SASAKI, H. 2012 Spontaneous inertia-gravity-wave generation by surface-intensified turbulence. *J. Fluid Mech.* **699**, 153–173.
- D'ASARO, E.A. 1988 Generation of submesoscale vortices: A new mechanism. *J. Geophys. Res.* **93** (C6), 6685–6693.
- D'ASARO, E.A., LEE, C., RAINVILLE, L., HARcourt, R. & THOMAS, L. 2011 Enhanced turbulence and energy dissipation at ocean fronts. *Science* **332** (318).
- D'ASARO, E. A. 1978 Mixed layer velocities induced by internal waves. *Journal of Geophysical Research* **83**, 2437–2438.
- D'ASARO, ERIC A., SHCHERBINA, ANDREY Y., KLYMAK, JODY M., MOLEMAKER, JEROEN, NOVELLI, GUILLAUME, GUIGAND, CÉDRIC M., HAZA, ANGELIQUE C., HAUS, BRIAN K., RYAN, EDWARD H., JACOBS, GREGG A., HUNTLEY, HELGA S., LAXAGUE, NATHAN J. M., CHEN, SHUYI, JUDT, FALKO, MCWILLIAMS, JAMES C., BARKAN, ROY, KIRWAN, A. D., POJE, ANDREW C. & ÖZGÖKMEN, TAMAY M. 2018 Ocean convergence and the dispersion of flotsam. *Proceedings of the National Academy of Sciences* **115** (6), 1162–1167.
- DE MAREZ, C., LAHAYE, N. & GULA, J. 2019 Interaction of the gulf stream with small scale topography : a focus on lee waves. *submitted to Sci. Rep.* .
- DEWAR, W.K. & BANE, JR., J.M. 1989a Gulf Stream dynamics. Part I: Eddy energetics at 73w. *J. Phys. Oceanogr.* **19**, 1574–1587.
- DEWAR, W.K. & BANE, JR., J.M. 1989b Gulf Stream dynamics. Part II: Eddy energetics at 73w. *J. Phys. Oceanogr.* **19**, 1574–1587.
- DEWAR, W.K. & HOGG, A.M. 2010 Topography inviscid dissipation of balanced flow. *Ocean Modelling* **32**, 1–13.

- DEWAR, W.K., MOLEMAKER, M.J. & MCWILLIAMS, JAMES C. 2015 Centrifugal instability and mixing in the California Undercurrent. *J. Phys. Oceanogr.* **45**, 1224–1241.
- d'ORGEVILLE, M., PELTIER, W.R., ERLER, A. & GULA, J. 2014 Climate change impacts on great lakes basin precipitation extremes. *J. Geophys. Res.* **119**, 10799–10812.
- DRAZIN, P.G. & REID, W.H. 1981 *Hydrodynamic Stability*. Cambridge University Press.
- DRITSCHEL, D.G., HAYNES, P.H., JUCKES, M.N. & SHEPHERD, T.G. 1991 The stability of a two-dimensional vorticity filament under uniform strain. *J. Fluid Mech.* **230**, 647–665.
- DUGAN, J. P., MIED, R. P., MIGNEREY, P. C. & SCHUETZ, A. F. 1982 Compact, intrathermocline eddies in the Sargasso Sea. *J. Geophys. Res. Oceans* **87** (C1), 385–393.
- EADY, E.T. 1949 Long waves and cyclone waves. *Tellus* **1**, 33–52.
- FERRARI, R. & WUNSCH, C. 2009 Ocean circulation kinetic energy: Reservoirs, sources, and sinks. *Annu. Rev. Fluid Mech.* **41**, 253–282.
- FERRARI, R. & WUNSCH, C. 2010 The distribution of eddy kinetic and potential energies in the global ocean. *Tellus* **62A**, 92–108.
- FISCHER, JÜRGEN, SCHOTT, FRIEDRICH A. & DENGLER, MARCUS 2004 Boundary circulation at the exit of the labrador sea. *Journal of Physical Oceanography* **34** (7), 1548–1570.
- FJØRTOFT, R. 1950 Application of integral theorems in deriving criteria of stability for laminar flows and for the baroclinic circular vortex. *Geophys. Publ.* **17**, 1–52.
- FLÓR, J.-B., SCOLAN, H. & GULA, J. 2011 Frontal instabilities and waves in a differentially rotating fluid. *J. Fluid Mech.* **685**, 532–542.
- FOX-KEMPER, BAYLOR & FERRARI, RAFFAELE 2008 Parameterization of mixed layer eddies. part ii: Prognosis and impact. *Journal of Physical Oceanography* **38** (6), 1166–1179.
- FOX-KEMPER, B., FERRARI, R. & HALLBERG, R. 2008 Parameterization of mixed layer eddies. Part I: Theory and diagnosis. *J. Phys. Oceanogr.* **38**, 1145–1165.
- FRENGER, IVY, BIANCHI, DANIELE, STÜHRENBERG, CAROLIN, OSCHLIES, ANDREAS, DUNNE, JOHN, DEUTSCH, CURTIS, GALBRAITH, ERIC & SCHÜTTE, FLORIAN 2018 Biogeochemical role of subsurface coherent eddies in the ocean: Tracer cannonballs, hypoxic storms, and microbial stewpots? *Global Biogeochem. Cy.* **32** (2), 226–249.
- FU, LEE-LUENG & FERRARI, RAFFAELE 2008 Observing oceanic submesoscale processes from space. *Eos, Transactions American Geophysical Union* **89** (48), 488–488.
- GERMANO, M. 1992 Turbulence: the filtering approach. *Journal of Fluid Mechanics* **238**, 325–336.
- GLENN, S.M. & EBBESMEYER, C.C. 1994 The structure and propagation of a Gulf Stream frontal eddy along the North Carolina shelf break. *J. Geophys. Res.* **99** (C3), 5029–5046.
- GRAY, A. & RISER, S. 2014 A global analysis of Sverdrup balance using absolute geostrophic velocities from Argo. *J. Phys. Oceanogr.* p. in press.
- GRIFFIES, S. M., DANABASOGLU, G., DURACK, P. J., ADCROFT, A. J., BALAJI, V., BÖNING, C. W., CHASSINET, E. P., CURCHITSER, E., DESHAYES, J., DRANGE, H., FOX-KEMPER, B., GLECKLER, P. J., GREGORY, J. M., HAAK, H., HALLBERG, R. W., HEIMBACH, P., HEWITT, H. T., HOLLAND, D. M., ILYINA, T., JUNGCLAUS, J. H., KOMURO, Y., KRASTING, J. P., LARGE, W. G., MARSLAND, S. J., MASINA, S., McDougall, T. J., NURSER, A. J. G., ORR,

- J. C., PIRANI, A., QIAO, F., STOUFFER, R. J., TAYLOR, K. E., TREGUIER, A. M., TSUJINO, H., UOTILA, P., VALDIVIESO, M., WANG, Q., WINTON, M. & YEAGER, S. G. 2016 Omip contribution to cmip6: experimental and diagnostic protocol for the physical component of the ocean model intercomparison project. *Geoscientific Model Development* **9** (9), 3231–3296.
- GRISOUARD, NICOLAS & THOMAS, LEIF N. 2016 Energy exchanges between density fronts and near-inertial waves reflecting off the ocean surface. *Journal of Physical Oceanography* **46** (2), 501–516.
- GULA, J., BLACIC, T. M. & TODD, R. E. 2019 Submesoscale coherent vortices in the Gulf Stream. *Geophys. Res. Lett.* **46**.
- GULA, J., MOLEMAKER, M.J. & MCWILLIAMS, JAMES C. 2014 Submesoscale cold filaments in the Gulf Stream. *J. Phys. Oceanogr.* **44** (10), 2617–2643.
- GULA, J., MOLEMAKER, M.J. & MCWILLIAMS, JAMES C. 2015a Gulf Stream dynamics along the Southeastern U.S. Seaboard. *J. Phys. Oceanogr.* **45** (3), 690–715.
- GULA, J., MOLEMAKER, M.J. & MCWILLIAMS, JAMES C. 2015b Topographic vorticity generation, submesoscale instability and vortex street formation in the Gulf Stream. *Geophys. Res. Lett.* **42**, 4054–4062.
- GULA, J., MOLEMAKER, M.J. & MCWILLIAMS, JAMES C. 2016a Submesoscale dynamics of a Gulf Stream frontal eddy in the South Atlantic Bight. *J. Phys. Oceanogr.* **46**, 305–325.
- GULA, J., MOLEMAKER, M.J. & MCWILLIAMS, JAMES C. 2016b Topographic generation of submesoscale centrifugal instability and energy dissipation. *Nat. Commu.* **7**, 12811.
- GULA, J. & PELTIER, W.R. 2012 Dynamical downscaling over the Great Lakes Basin of North America using the WRF regional climate model: The impact of the Great Lakes system on regional greenhouse warming. *Journal of Climate* **25**, 7723–7742.
- GULA, J., PLOUGONVEN, R. & ZEITLIN, V. 2009a Ageostrophic instabilities of fronts in a channel in the stratified rotating fluid. *J. Fluid Mech.* **627**, 485–507.
- GULA, J. & ZEITLIN, V. 2010 Instabilities of buoyancy driven coastal currents and their nonlinear evolution in the two-layer rotating shallow water model. Part I. Passive lower layer. *J. Fluid Mech.* **659**, 69–93.
- GULA, J. & ZEITLIN, V. 2014 Instabilities of shallow-water flows with vertical shear in the rotating annulus. In *Modelling Atmospheric and Oceanic Flows: Insights from Laboratory Experiments and Numerical Simulations* (ed. T. von Larcher & P.D. Williams). AGU, Washington, D. C., ISBN: 978-1-118-85593-5.
- GULA, J., ZEITLIN, V. & BOUCHUT, F. 2010 Instabilities of buoyancy driven coastal currents and their nonlinear evolution in the two-layer rotating shallow water model. Part II. Active lower layer. *J. Fluid Mech.* **665**, 209–237.
- GULA, J., ZEITLIN, V. & PLOUGONVEN, R. 2009b Instabilities of two-layer shallow-water flows with vertical shear in the rotating annulus. *J. Fluid Mech.* **638**, 27–47.
- HAINES, T.W.N. & MARSHALL, J. 1999 Gravitational, symmetric, and baroclinic instability of the ocean mixed layer. *J. Phys. Oceanogr.* **28**, 634–658.
- HANEY, J.C. 1987 Ocean internal waves as sources of small-scale patchiness in seabird distribution on the Blake Plateau. *The Auk* **104**, 129–133.
- VAN HAREN, HANS 2016 Do deep-ocean kinetic energy spectra represent deterministic or stochastic signals? *Journal of Geophysical Research: Oceans* **121** (1), 240–251.

- HIDE, R. & TITMAN, C.W. 1967 Detached shear layers in a rotating fluid. *J. Fluid Mech.* **29**, 39–60.
- HOLLOWAY, GREG 1987 Systematic forcing of large-scale geophysical flows by eddy-topography interaction. *Journal of Fluid Mechanics* **184**, 463–476.
- HOLLOWAY, G. 1992 Representing topographic stress for large-scale ocean models. *J. Phys. Oceanogr.* **22**, 1033–1047.
- HOSKINS, B.J., MCINTYRE, M.E. & ROBERTSON, A.W. 1985 On the use and significance of isentropic potential vorticity maps. *Q.J.R. Meteorol. Soc.* **111** (470), 877–946.
- HOSKINS, B. J. 1974 The role of potential vorticity in symmetric stability and instability. *Q.J.R. Meteorol. Soc.* **100**, 480–482.
- HOSKINS, B. J. 1982 The mathematical theory of frontogenesis. *Ann. Rev. Fluid Mech.* **14**, 131–151.
- HUGHES, C.W. 2000 A theoretical reason to expect inviscid western boundary currents in realistic oceans. *Ocean Modelling* **2**, 73–83.
- HUGHES, C.W. & DE CUEVAS, B.A. 2001 Why western boundary currents in realistic oceans are inviscid: A link between form stress and bottom pressure torques. *J. Phys. Oceanogr.* **31**, 2871–2886.
- JACKSON, L., HUGHES, C.W. & WILLIAMS, R.G. 2006 Topographic control of basin and channel flows: The role of bottom pressure torques and friction. *J. Phys. Oceanogr.* **36**, 1786–1805.
- JOCHUM, MARKUS, BRIEGLB, BRUCE P., DANABASOGLU, GOKHAN, LARGE, WILLIAM G., NORTON, NANCY J., JAYNE, STEVEN R., ALFORD, MATTHEW H. & BRYAN, FRANK O. 2013 The impact of oceanic near-inertial waves on climate. *Journal of Climate* **26** (9), 2833–2844.
- KLYMAK, J., SHEARMAN, R.K., GULA, J., LEE, C.M., D'ASARO, E.A., THOMAS, L., HARCOURT, R., SHCHERBINA, A., SUNDERMEYER, M.A., MOLEMAKER, M.J. & MCWILLIAMS, JAMES C. 2016 Submesoscale streamers exchange water on the North Wall of the Gulf Stream. *Geophys. Res. Lett.* **43**, 1226–1233.
- KOSTIANOV, A.G. & BELKIN, I.M. 1989 A survey of observations on intrathermocline eddies in the world ocean. In *Mesoscale/Synoptic Coherent structures in Geophysical Turbulence* (ed. J.C.J. Nihoul & B.M. Jamart), *Elsevier Oceanography Series*, vol. 50, pp. 821 – 841. Elsevier.
- KOSTIANOV, A.G. & RODIONOV, V.B. 1986a *Intrathermocline Eddies in the Ocean*, chap. Coastal upwelling zones - a source of intrathermocline eddy formation, pp. 50–52. P.P. Shirshov Inst. of Oceanology, Moscow (in Russian).
- KOSTIANOV, A.G. & RODIONOV, V.B. 1986b On the formation of intrathermocline eddies in the Canary upwelling region. *Okeanologiya (in Russian)* **26**, 892–895.
- KRUG, M.J., SWART, S. & GULA, J. 2017 Submesoscale cyclones in the Agulhas Current. *Geophys. Res. Lett.* **44**.
- KUO, H.L. 1949 Dynamic instability of two-dimensional non-divergent flow in a barotropic atmosphere. *J. Met.* **6**, 105–122.
- LAHAYE, NOÉ, GULA, JONATHAN & ROULLET, GUILLAUME 2019a Sea surface signature of internal tides. *Geophysical Research Letters* **46** (7), 3880–3890.
- LAHAYE, NOÉ, GULA, JONATHAN & ROULLET, GUILLAUME 2020 Internal tide cycle and topographic scattering over the North Mid-Atlantic Ridge. *to be submitted to J. Phys. Oceanogr.* .

- LAHAYE, NOÉ, GULA, JONATHAN, THURNHERR, ANDREAS M., REVERDIN, GILLES, BOURUET-AUBERTOT, PASCALE & ROULLET, GUILLAUME 2019b Deep currents in the rift valley of the north mid-atlantic ridge. *Frontiers in Marine Science* **6**, 597.
- LARGE, W.G., MCWILLIAMS, JAMES C. & DONEY, S. 1994 Oceanic vertical mixing: A review and a model with a nonlocal boundary layer parameterization. *Rev. Geophys.* **32**, 363–403.
- LE CORRE, M., GULA, J., SMILENOVA, A. & HOUPERT, L. 2019a On the dynamics of a deep quasi-permanent anticyclonic eddy in the rockall trough. *to be submitted to Deep Sea Res.* .
- LE CORRE, M., GULA, J., SMILENOVA, A. & HOUPERT, L. 2019b On the dynamics of a deep quasi-permanent anticyclonic eddy in the rockall trough. *Proceedings of the 24th Congrès Français de Mécanique* .
- LE CORRE, M., GULA, J. & TRÉGUIER, A.-M. 2019c Barotropic vorticity balance of the north-atlantic subpolar gyre in an eddy-resolving model. *Ocean Sci. Discuss.* .
- LECUN, YANN, BENGIO, YOSHUA & HINTON, GEOFFREY 2015 Deep learning. *Nature* **521**, 436 EP –.
- LEHAHN, Y., d'OIDIO, F., LÉVY, M. & HEIFETZ, E. 2007 Stirring of the northeast atlantic spring bloom: A lagrangian analysis based on multisatellite data. *Journal of Geophysical Research: Oceans* **112** (C8).
- LEMARIÉ, F., KURIAN, J., SHCHEPETKIN, A.F., MOLEMAKER, M.J., COLAS, F. & MCWILLIAMS, JAMES C. 2012 Are there inescapable issues prohibiting the use of terrain-following coordinates in climate models? *Ocean Modelling* **42**, 57–79.
- LEONARD, A. 1975 Energy cascade in large-eddy simulations of turbulent fluid flows. In *Turbulent Diffusion in Environmental Pollution* (ed. F.N. Frenkel & R.E. Munn), *Advances in Geophysics*, vol. 18, pp. 237 – 248. Elsevier.
- LILLY, JONATHAN M. & RHINES, PETER B. 2002 Coherent eddies in the Labrador Sea observed from a mooring. *J. Phys. Oceanogr.* **32** (2), 585–598.
- LING, JULIA, KURZAWSKI, ANDREW & TEMPLETON, JEREMY 2016 Reynolds averaged turbulence modelling using deep neural networks with embedded invariance. *Journal of Fluid Mechanics* **807**, 155–166.
- LOCARNINI, R. A., MISHONOV, A.V., ANTONOV, J.I., BOYER, T.P., GARCIA, H.E., BARANOVA, O.K., ZWENG, M.M., PAVER, C.R., REAGAN, J.R., JOHNSON, D.R., HAMILTON, M. & SEIDOV, D. 2013 *World Ocean Atlas 2013, Volume 1: Temperature..* S. Levitus, Ed., A. Mishonov technical editor, NOAA Atlas NESDIS 73.
- LUKAS, ROGER & SANTIAGO-MANDUJANO, FERNANDO 2001 Extreme water mass anomaly observed in the Hawaii ocean time-series. *Geophys. Res. Lett.* **28** (15), 2931–2934.
- LUYTEN, JAMES, STOMMEL, HENRY & WUNSCH, CAU 1985 A diagnostic study of the northern atlantic subpolar gyre. *Journal of Physical Oceanography* **15** (10), 1344–1348.
- MACKINNON, JENNIFER A., ZHAO, ZHONGXIANG, WHALEN, CAITLIN B., WATERHOUSE, AMY F., TROSSMAN, DAVID S., SUN, OLIVER M., ST. LAURENT, LOUIS C., SIMMONS, HARPER L., POLZIN, KURT, PINKEL, ROBERT, PICKERING, ANDREW, NORTON, NANCY J., NASH, JONATHAN D., MUSGRAVE, RUTH, MERCHANT, LYNNE M., MELET, ANGELIQUE V., MATER, BENJAMIN, LEGG, SONYA, LARGE, WILLIAM G., KUNZE, ERIC, KLYMAK, JODY M., JOCHUM, MARKUS, JAYNE, STEVEN R., HALLBERG, ROBERT W., GRIFFIES, STEPHEN M., DIGGS, STEVE, DANABASOGLU, GOKHAN, CHASSIGNET, ERIC P., BUIJSMAN, MAARTEN C., BRYAN, FRANK O.,

- BRIEGLB, BRUCE P., BARNA, ANDREW, ARBIC, BRIAN K., ANSONG, JOSEPH K. & ALFORD, MATTHEW H. 2017 Climate process team on internal wave–driven ocean mixing. *Bulletin of the American Meteorological Society* **98** (11), 2429–2454.
- MAHADEVAN, AMALA 2016 The impact of submesoscale physics on primary productivity of plankton. *Annual review of marine science* **8**, 161–84.
- MALLARD, M., BULLOCK, R., NOLTE, C., ALAPATY, K., OTTE, T. & GULA, J. 2014 Using a coupled lake model with WRF for dynamical downscaling. *J. Geophys. Res.* **119**, 7193–7208.
- MALLARD, M. S., NOLTE, C. G., SPERO, T. L., BULLOCK, O. R., ALAPATY, K., HERWEHE, J. A., GULA, J. & BOWDEN, J. H. 2015 Technical challenges and solutions in representing lakes when using WRF in downscaling applications. *Geosci. Model Dev.* p. in press.
- MANLEY, T. O. & HUNKINS, KENNETH 1985 Mesoscale eddies of the Arctic Ocean. *J. Geophys. Res. Oceans* **90** (C3), 4911–4930.
- MARCHESIELLO, P., MCWILLIAMS, JAMES C. & SHCHEPETKIN, A. 2001 Open boundary conditions for long-term integration of regional oceanic models. *Ocean Modelling* **2**, 1–20.
- MARZOCCHI, ALICE, HIRSCHI, JOËL J.-M., HOLLIDAY, N. PENNY, CUNNINGHAM, STUART A., BLAKER, ADAM T. & COWARD, ANDREW C. 2015 The north atlantic subpolar circulation in an eddy-resolving global ocean model. *Journal of Marine Systems* **142**, 126 – 143.
- MASON, E., MOLEMAKER, M.J., SHCHEPETKIN, A.F., COLAS, F., MCWILLIAMS, JAMES C. & SANGRA, P. 2010 Procedures for offline grid nesting in regional ocean models. *Ocean Modelling* **35**, 1–15.
- McDOWELL, S.E. & ROSSBY, H.T. 1978 Mediterranean water: An intense mesoscale eddy off the bahamas. *Science* **202**, 1085–1087.
- MCWILLIAMS, J.C., COLAS, F. & MOLEMAKER, M.J. 2009 Cold filamentary intensification and oceanic surface convergence lines. *Geophys. Res. Lett.* **36**, L18602.
- MCWILLIAMS, JAMES C. 1984 The emergence of isolated, coherent vortices in turbulent flow. *AIP Conference Proceedings* **106** (1), 205–221.
- MCWILLIAMS, JAMES C. 1985 Submesoscale, coherent vortices in the ocean. *Rev. of Geophys.* **23**, 165–182.
- MCWILLIAMS, JAMES C. 2016 Submesoscale currents in the ocean. *Proc. R. Soc. A* **472** (2189).
- MCWILLIAMS, JAMES C., GULA, J., MOLEMAKER, M.J., RENAULT, L. & SHCHEPETKIN, A. 2015 Filament frontogenesis by boundary layer turbulence. *J. Phys. Oceanogr.* **45**, 1988–2005.
- MCWILLIAMS, JAMES C., GULA, JONATHAN & MOLEMAKER, M. JEROEN 2019 The gulf stream north wall: Ageostrophic circulation and frontogenesis. *Journal of Physical Oceanography* **49** (4), 893–916.
- MCWILLIAMS, JAMES C. & MOLEMAKER, M.J. 2011 Baroclinic frontal arrest: A sequel to unstable frontogenesis. *J. Phys. Oceanogr.* **41**, 601–619.
- MENSA, J.A., GARRAFFO, Z., GRIFFA, A., OZGOKMEN, T.M., HAZA, A. & VENEZIANI, M. 2013 Seasonality of the submesoscale dynamics in the Gulf Stream region. *Ocean Dynamics* pp. 53–85.
- MOLEMAKER, M.J., MCWILLIAMS, JAMES C. & CAPET, X. 2010 Balanced and unbalanced routes to dissipation in an equilibrated Eady flow. *J. Fluid Mech.* **654**, 35–63.

- MOLEMAKER, M.J., MCWILLIAMS, JAMES C. & DEWAR, W.K. 2015 Submesoscale instability and generation of mesoscale anticyclones near a separation of the California Undercurrent. *J. Phys. Oceanogr.* **45**, 613–629.
- MOLEMAKER, M.J., MCWILLIAMS, JAMES C. & YAVNEH, I. 2005 Baroclinic instability and loss of balance. *J. Phys. Oceanogr.* **35**, 1505–1517.
- MOREL, YVES, GULA, JONATHAN & PONTE, AURÉLIEN 2019 Potential vorticity diagnostics based on balances between volume integral and boundary conditions. *Ocean Modelling* **138**, 23 – 35.
- MORVAN, M., L'HÉGARET, P., CARTON, X., GULA, J., VIC, C., SOKOLOVSKIY, M. & KOSHEL, K. 2019 The life cycle of submesoscale eddies generated by topographic interactions. *Ocean Science Discussions* **2019**, 1–20.
- MÜLLER, P., MCWILLIAMS, JAMES C. & MOLEMAKER, M.J. 2005 Routes to dissipation in the ocean: The 2d/3d turbulence conundrum. In *Marine Turbulence: Theories, Observations and Models*, (ed. H. Baumert, J. Simpson & J. Sundermann). Cambridge Press.
- MUNK, W. 1981 Internal waves and small-scale processes. In *Evolution of Physical Oceanography* (ed. B. Warren & C. Wunsch). The MIT Press.
- MUNK, WALTER H. 1950 On the wind-driven ocean circulation. *Journal of Meteorology* **7** (2), 80–93.
- NAGAI, T., TANDON, A., KUNZE, E. & MAHADEVAN, A. 2015 Spontaneous generation of near-inertial waves by the Kuroshio front. *J. Phys. Oceanogr.* **45**, 2381–2406.
- NAVEIRA GARABATO, ALBERTO C., FRAJKA-WILLIAMS, ELEANOR E., SPINGYS, CARL P., LEGG, SONYA, POLZIN, KURT L., FORRYAN, ALEXANDER, ABRAHAMSEN, E. POVL, BUCKINGHAM, CHRISTIAN E., GRIFFIES, STEPHEN M., MCPHAIL, STEPHEN D., NICHOLLS, KEITH W., THOMAS, LEIF N. & MEREDITH, MICHAEL P. 2019 Rapid mixing and exchange of deep-ocean waters in an abyssal boundary current. *Proceedings of the National Academy of Sciences* **116** (27), 13233–13238.
- NIKURASHIN, M., VALLIS, G.K. & ADCROFT, A. 2013 Routes to energy dissipation for geostrophic flows in the Southern Ocean. *Nature Geosci.* **6**, 58–51.
- ORR, W.M.F. 1907 The stability or instability of the steady motions of a perfect liquid and of a viscous liquid. *Proc. R. Irish Acad.* **27**, 69–138.
- PENNELL, R., STEGNER, A. & BERANGER, K. 2012 Shelf impact on buoyant coastal current instabilities. *J. Phys. Oceanogr.* **42**, 39–61.
- PENVEN, P., DEBREU, L., MARCHESEILLO, P. & MCWILLIAMS, JAMES C. 2006 Application of the ROMS embedding procedure for the Central California Upwelling System. *Ocean Modelling* **12**, 157–187.
- PLougoven, Riwal & Zhang, Fuqing 2014 Internal gravity waves from atmospheric jets and fronts. *Reviews of Geophysics* **52** (1), 33–76.
- POULIN, F.J., STEGNER, A., HERNANDEZ-ARENCEIBIA, M., MARRERO-DIAZ, A. & SANGRA, P. 2014 Steep shelf stabilisation of the Bransfield coastal current: Linear stability analysis. *J. Phys. Oceanogr.* **44**, 714—732.
- QIU, BO, CHEN, SHUIMING, KLEIN, PATRICE, WANG, JINBO, TORRES, HECTOR, FU, LEE-LUENG & MENEMENLIS, DIMITRIS 2018 Seasonality in transition scale from balanced to unbalanced motions in the World Ocean. *Journal of Physical Oceanography* **48** (3), 591–605.

- QIU, BO, NAKANO, TOSHIYA, CHEN, SHUIMING & KLEIN, PATRICE 2017 Submesoscale transition from geostrophic flows to internal waves in the northwestern Pacific upper ocean. *Nature Communications* p. 14055.
- RAMANANTSOA, J.D., KRUG, M., PENVEN, P., ROUAULT, M. & GULA, J. 2017 Coastal upwelling south of madagascar : temporal and spatial variability. *J. Mar. Syst.* **178**, 29–37.
- RAMANANTSOA, J.D., PENVEN, P., KRUG, M., GULA, J. & ROUAULT, M. 2018 Uncovering a new current : the South-west MADagascar Coastal Current (SMACC). *Geophys. Res. Lett.* **178**, 29–37.
- RAYLEIGH, LORD 1880 On the stability, or instability of certain fluid motions. *Proc. R. Soc. Lond.* **9**, 57–70.
- RENAULT, LIONEL, MCWILLIAMS, JAMES C. & GULA, JONATHAN 2018 Dampening of submesoscale currents by air-sea stress coupling in the californian upwelling system. *Scientific Reports* **8** (1), 13388.
- RENAULT, L., MOLEMAKER, M.J., GULA, J., MASSON, S. & MCWILLIAMS, JAMES C. 2016a Control and stabilization of the Gulf Stream by oceanic current interaction with the atmosphere. *J. Phys. Oceanogr.* .
- RENAULT, LIONEL, MOLEMAKER, M. JEROEN, MCWILLIAMS, JAMES C., SHCHEPETKIN, ALEXANDER F., LEMARIÉ, FLORIAN, CHELTON, DUDLEY, ILLIG, SERENA & HALL, ALEX 2016b Modulation of wind work by oceanic current interaction with the atmosphere. *Journal of Physical Oceanography* **46** (6), 1685–1704.
- RIBSTEIN, B., GULA, J. & ZEITLIN, V. 2010 (a)geostrophic adjustment of dipolar perturbations, formation of coherent structures and their properties, as follows from high-resolution numerical simulations with rotating shallow water model. *Phys. Fluids* **22**, 116603.
- ROCHA, CESAR B., CHERESKIN, TERESA K., GILLE, SARAH T. & MENEMENLIS, DIMITRIS 2016a Mesoscale to submesoscale wavenumber spectra in drake passage. *Journal of Physical Oceanography* **46** (2), 601–620.
- ROCHA, CESAR B., GILLE, SARAH T., CHERESKIN, TERESA K. & MENEMENLIS, DIMITRIS 2016b Seasonality of submesoscale dynamics in the kuroshio extension. *Geophysical Research Letters* **43** (21), 11,304–11,311, 2016GL071349.
- ROULLET, G., CAPET, X. & MAZE, G. 2014 Global interior eddy available potential energy diagnosed from Argo floats. *Geophys. Res. Lett.* **41**, 1651–1656.
- ROULLET, G., MOLEMAKER, M.J., DUCOUSSO, N. & DUBOS, T. 2017 Compact symmetric poisson equation discretization for non-hydrostatic sigma coordinates ocean model. *Ocean Modelling* **118** (Supplement C), 107 – 117.
- RUAN, XIAOZHOU, THOMPSON, ANDREW F., FLEXAS, MAR M. & SPRINTALL, JANET 2017 Contribution of topographically generated submesoscale turbulence to southern ocean overturning. *Nature Geoscience* **10**, 840.
- SAKAI, S. 1989 Rossby-Kelvin instability: a new type of ageostrophic instability caused by a resonance between Rossby waves and gravity waves. *J. Fluid Mech.* **202**, 149–176.
- SALMON, R. 1980 Baroclinic instability and geostrophic turbulence. *Geophys. Astrophys. Fluid Dyn.* **10**, 25–52.
- SAMELSON, R.M. & PEDLOSKY, J. 1990 Local baroclinic instability of flow over variable topography. *J. Fluid Mech.* **221**, 411–436.

- SASAKI, HIDEHARU, KLEIN, PATRICE, QIU, Bo & SASA, YOSHIKAZU 2014 Impact of oceanic-scale interactions on the seasonal modulation of ocean dynamics by the atmosphere. *Nature Communications* **5**, 5636.
- SCHAEFFER, AMANDINE, GRAMOULLE, A., ROUGHAN, M. & MANTOVANELLI, A. 2017 Characterizing frontal eddies along the east australian current from hf radar observations. *Journal of Geophysical Research: Oceans* **122** (5), 3964–3980.
- SCHOONOVER, J., DEWAR, W., WIENDERS, N., GULA, J., MCWILLIAMS, JAMES C., MOLEMAKER, M.J., BATES, S., DANABASOGLU, G. & YEAGER, S. 2016 North atlantic barotropic vorticity balances in numerical models. *J. Phys. Oceanogr.* **46**, 289–303.
- SCHUBERT, R., GULA, J., GREATBATCH, R.J., RATH, W. & BIASTOCH, A. 2019a Submesoscale kinetic energy cascade in the Agulhas region. *submitted to J. Phys. Oceanogr.* .
- SCHUBERT, R., SCHWARZKOPF, F. U., BASCHEK, B. & BIASTOCH, A. 2019b Submesoscale impacts on mesoscale agulhas dynamics. *Journal of Advances in Modeling Earth Systems* **0** (ja).
- SCHWARZKOPF, F. U., BIASTOCH, A., BÖNING, C. W., CHANUT, J., DURGADOO, J. V., GETZLAFF, K., HARLASS, J., RIECK, J. K., ROTH, C., SCHEINERT, M. M. & SCHUBERT, R. 2019 The inalt family – a set of high-resolution nests for the agulhas current system within global nemo ocean/sea-ice configurations. *Geoscientific Model Development* **12** (7), 3329–3355.
- SEN, A., SCOTT, R.B. & ARBIC, B.K. 2008 Global energy dissipation rate of deep-ocean low-frequency flows by quadratic bottom boundary layer drag: comparisons from current-meter data. *Geophys. Res. Lett.* **35**, L09606.
- SHAKESPEARE, C.J. & TAYLOR, J.R. 2014 The spontaneous generation of inertia-gravity waves during frontogenesis forced by large strain: theory. *J. Fluid Mech.* **757**, 817–853.
- SHCHEPETKIN, A.F. & MCWILLIAMS, JAMES C. 2005 The Regional Oceanic Modeling System (ROMS): A split-explicit, free-surface, topography-following- coordinate ocean model. *Ocean Modelling* **9**, 347–404.
- SHCHEPETKIN, A.F. & MCWILLIAMS, JAMES C. 2008 Computational kernel algorithms for finescale, multi-process, long-time oceanic simulations. *Handb. Numer. Anal.* **14**, 121–183.
- SHCHEPETKIN, A.F. & MCWILLIAMS, JAMES C. 2011 Accurate Boussinesq modeling with a practical, "stiffened" equation of state. *Ocean Modelling* **34**, 41–70.
- SHCHERBINA, A.Y., D'ASARO, E.A., LEE, C.M., KLYMAK, J.M., MOLEMAKER, M.J. & MCWILLIAMS, J.C. 2013 Statistics of vertical vorticity, divergence, and strain in a developed submesoscale turbulence field. *Geophys. Res. Lett.* **40**.
- SILVER, DAVID, HUANG, AJA, MADDISON, CHRIS J., GUEZ, ARTHUR, SIFRE, LAURENT, VAN DEN DRIESSCHE, GEORGE, SCHRITTWIESER, JULIAN, ANTONOGLOU, IOANNIS, PANNEERSHELVAM, VEDA, LANCTOT, MARC, DIELEMAN, SANDER, GREWE, DOMINIK, NHAM, JOHN, KALCHBRENNER, NAL, SUTSKEVER, ILYA, LILLICRAP, TIMOTHY, LEACH, MADELEINE, KAVUKCUOGLU, KORAY, GRAEPEL, THORE & HASSABIS, DEMIS 2016 Mastering the game of go with deep neural networks and tree search. *Nature* **529**, 484 EP –.
- SMILENOVA, A., GULA, J., LE CORRE, M. & HOUPERT, L. 2019 A persistent deep anticyclonic vortex in the Rockall Trough sustained by anticyclonic vortices shed from the slope current. *submitted to J. Geophys. Res. Ocean* .
- SMITH, W.H.F. & SANDWELL, D.T. 1997 Global seafloor topography from satellite altimetry and ship depth soundings. *Science* **277**, 1957–1962.

- SONNEWALD, MAIKE, WUNSCH, CARL & HEIMBACH, PATRICK 2019 Unsupervised Learning Reveals Geography of Global Ocean Dynamical Regions. *Earth and Space Science* p. 2018EA000519.
- SPENCE, PAUL, SAENKO, OLEG A., SIJP, WILLEM & ENGLAND, MATTHEW 2012 The Role of Bottom Pressure Torques on the Interior Pathways of North Atlantic Deep Water. *J. Phys. Oceanogr.* **42** (1), 110–125.
- SRINIVASAN, K., McWILLIAMS, J. C., MOLEMAKER, M. J. & BARKAN, R. 2019 Submesoscale vortex generation in the lee of a seamount. *J. Phys. Oceanogr.* .
- ST. LAURENT, L. C., TOOLE, J. M. & SCHMITT, R. W. 2001 Buoyancy forcing by turbulence above rough topography in the abyssal Brazil Basin. *J. Phys. Oceanogr.* **31**, 3476–3495.
- STEGNER, ALEXANDRE 2014 *Oceanic Island Wake Flows in the Laboratory*, chap. 14, pp. 265–276. American Geophysical Union (AGU).
- STOMMEL, H. 1948 The westward intensification of wind-driven ocean currents. *Eos, Transactions American Geophysical Union* **29** (2), 202–206.
- SULLIVAN, PETER P. & MCWILLIAMS, JAMES C. 2018 Frontogenesis and frontal arrest of a dense filament in the oceanic surface boundary layer. *Journal of Fluid Mechanics* **837**, 341–380.
- TAYLOR, J. & FERRARI, R. 2009 The role of secondary shear instabilities in the equilibration of symmetric instability. *J. Fluid Mech.* **622**, 103.
- TEDESCO, P., GULA, J., MENESGUEN, C., PENVEN, P. & KRUG, M. 2019 Generation of submesoscale frontal eddies in the Agulhas Current. *J. Geophys. Res. Oceans* **124**.
- TESTOR, P. & GASCARD, J-C. 2003 Large-scale spreading of deep waters in the western Mediterranean Sea by submesoscale coherent eddies. *J. Phys. Oceanogr.* **33** (1), 75–87.
- THOMAS, LEIF 2019 Enhanced radiation of near-inertial energy by frontal vertical circulations. *Journal of Physical Oceanography* **0** (0), null.
- THOMAS, L., TAYLOR, J.R., FERRARI, R. & JOYCE, T.M. 2013 Symmetric instability in the Gulf Stream. *Deep-Sea Res.* **91**, 96–110.
- THOMAS, L. N. & TAYLOR, J. R. 2010 Reduction of the usable wind-work on the general circulation by forced symmetric instability. *Geophysical Research Letters* **37** (18), n/a–n/a, l18606.
- THURNHERR, A. M., ST. LAURENT, L. C., SPEER, K. G., TOOLE, J. M. & LEDWELL, J. R. 2005 Mixing associated with sills in a canyon on the Mid-Ocean Ridge flank. *J. Phys. Oceanogr.* **35**, 1370–1381.
- TORRES, H. S., KLEIN, P., MENEMENLIS, D., QIU, B., SU, Z., WANG, J., CHEN, S. & FU, L. 2018 Partitioning ocean motions into balanced motions and internal gravity waves: A modeling study in anticipation of future space missions. *Journal of Geophysical Research: Oceans* .
- TREGUIER, A.M., THEETEN, S., CHASSIGNET, E.P., PENDUFF, T., SMITH, R., TALLEY, L., BEISMANN, J.O. & BONING, C. 2005 The North Atlantic Subpolar Gyre in four high-resolution models. *J. Phys. Oceanogr.* **35**, 757–773.
- UMLAUF, L. & BURCHARD, H. 2003 A generic length-scale equation for geophysical turbulence models. *Journal of Marine Research* **61** (2), 235–265.
- VANNESTE, J. 2013 Balance and spontaneous wave generation in geophysical flows. *Annual Review of Fluid Mechanics* **45** (1), 147–172.

- VIC, CLÉMENT, GULA, JONATHAN, ROULLET, GUILLAUME & PRADILLON, FLORENCE 2018 Dispersion of deep-sea hydrothermal vent effluents and larvae by submesoscale and tidal currents. *Deep Sea Res. Pt. I* **133**, 1 – 18.
- VIC, C., ROULLET, G., CARTON, X., CAPET, X., MOLEMAKER, M.J. & GULA, J. 2015 Eddy-topography interactions and the fate of the Persian Gulf Outflow. *J. Geophys. Res. Oceans* **120**, 6700–6717.
- VOLLANT, A., BALARAC, G. & CORRE, C. 2017 Subgrid-scale scalar flux modelling based on optimal estimation theory and machine-learning procedures. *Journal of Turbulence* **18** (9), 854–878.
- WAGNER, G. L. & YOUNG, W. R. 2016 A three-component model for the coupled evolution of near-inertial waves, quasi-geostrophic flow and the near-inertial second harmonic. *Journal of Fluid Mechanics* **802**, 806–837.
- WANG, YUAN, CLAUS, MARTIN, GREATBATCH, RICHARD J. & SHENG, JINYU 2017 Decomposition of the mean barotropic transport in a high resolution model of the North Atlantic Ocean. *Geophysical Research Letters* **44** (22), 11,537–11,546.
- WATERHOUSE, A.F., MACKINNON, J.A., NASH, J.D., ALFORD, M.H., KUNZE, E., SIMMONS, H.L., POLZIN, K.L., ST. LAURENT, L.C., SUN, O.M., PINKEL, R., TALLEY, L.D., WHALEN, C.B., HUUSSEN, T.N., CARTER, G.S., FER, I., WATERMAN, S., NAVIERA GARABATO, A.C., SANFORD, T.B., & LEE, C.M. 2014 Global patterns of diapycnal mixing from measurements of the turbulent dissipation rate. *J. Phys. Oceanogr.* **44**, 1854–1872.
- WENEGRAT, JACOB O., CALLIES, JÖRN & THOMAS, LEIF N. 2018a Submesoscale baroclinic instability in the bottom boundary layer. *Journal of Physical Oceanography* **48** (11), 2571–2592.
- WENEGRAT, JACOB O., THOMAS, LEIF N., GULA, JONATHAN & MCWILLIAMS, JAMES C. 2018b Effects of the submesoscale on the potential vorticity budget of ocean mode waters. *Journal of Physical Oceanography* **48** (9), 2141–2165.
- WHITT, DANIEL B. & THOMAS, LEIF N. 2013 Near-inertial waves in strongly baroclinic currents. *Journal of Physical Oceanography* **43** (4), 706–725.
- WILLIAMS, P.D., HAINE, T.W.N. & READ, P.L. 2008 Inertia-gravity waves emitted from balanced flows: Observations, properties, and consequences. *J. Atmos. Sci.* **65**, 3543–3556.
- WILLIAMS, R.G., WILSON, C. & HUGHES, C.W. 2007 Ocean and atmosphere storm tracks: The role of eddy vorticity forcing. *J. Phys. Oceanogr.* **37**, 2267–2289.
- WUNSCH, C. & ROEMMICH, D. 1985 Is the North Atlantic in Sverdrup balance? *J. Phys. Oceanogr.* **15**, 1876–1880.
- XIE, J.-H. & VANNESTE, J. 2015 A generalised-lagrangian-mean model of the interactions between near-inertial waves and mean flow. *Journal of Fluid Mechanics* **774**, 143–169.
- YEAGER, STEPHEN 2015 Topographic Coupling of the Atlantic Overturning and Gyre Circulations. *J. Phys. Oceanogr.* **45**, 27.
- ZHANG, R. & VALLIS, G.K. 2007 The role of bottom vortex stretching on the path of the North Atlantic western boundary current and on the northern recirculation gyre. *J. Phys. Oceanogr.* **37**, 2053–2080.

Curriculum Vitae

Curriculum vitae

Jonathan Gula

<http://mespages.univ-brest.fr/~gula>
ORCID: 0000-0002-0876-9557

Laboratoire d'Océanographie Physique et Spatiale,
LOPS/IUEM bâtiment D, rue Dumont d'Urville,
Tel.: +33 (0)2 90 91 55 39
jonathan.gula@univ-brest.fr

Born January 23rd, 1982. French Nationality. Married, 3 children.

Work Experience

since Sep. 2015 - Assistant Professor. Laboratoire d'Océanographie Physique et Spatiale (LOPS), Univ. Brest, IUEM, Brest, France.

2011-15 - Assistant Researcher - University of California, Los Angeles
Contact: James C. McWilliams. **Topic:** Submesoscale flows in the ocean

2009-11 - Postdoctoral fellow - University of Toronto - *Contact:* W.R. Peltier. **Topic:** Regional climate modeling and downscaling of global warming experiments.

Education

2020 - HDR (Habilitation à diriger des recherches) to be defended Jan. 16th, 2020 at Univ. Brest.
Title: Mesoscale and submesoscale turbulence in the presence of topography.
Link: <http://mespages.univ-brest.fr/~gula/hdr.pdf>

2006-09 - PhD - Laboratoire de Météorologie Dynamique, ENS, Paris
Supervisors: V. Zeitlin and R. Plougonven
Title: Ageostrophic instabilities of baroclinic flows in the atmosphere and ocean.

2005-06 - Master's degree in Ocean, Atmosphere and Climate - Université Paris VI
Master's speciality: Dynamics of the ocean and atmosphere.
Research assistant: Study of the Rossby-Kelvin instability
(V. Zeitlin et R. Plougonven, LMD, ENS, Paris)

2004-05 - Agrégation externe de Sciences Physiques - ENS Cachan
Superior diploma for teaching Physics and Chemistry in high school.

2003-04 - Maitrise in fundamental physics, ENS Cachan.
equivalent of first year of master in fundamental physics
Research assistant: Periodic Forcing of Baroclinic Basin-Scale Waves in a Rotating Stratified Basin. (*G. Ivey, University of Western Australia - Geophysical Fluid Dynamics group*)

2002-03 - Licence in fundamental Physics - ENS Cachan
equivalent of bachelor's degree in physics.
Research assistant: Experimental study of the electro-sismic response in a grès de Fontainebleau. (*J.-P. Vilotte, Institut de Physique du Globe de Paris - Mécanique des roches*)

Research

Research interests: Ocean dynamics, Turbulence, Mesoscale eddies, Submesoscale processes, Flow-topography interactions, Internal waves, Air-sea interactions, Western boundary currents, Lagrangian dispersion.

Publications

36 peer-reviewed publications in international journals (IF>1)
11 as first author, 8 as second author

1 book chapter, **5** conference proceedings

h-index = **18** (google scholar), **16** (Web of Science)

Communications

10 invited contributions [seminars (7), lectures (2), and poster (1)]
9 talks and 5 posters at international conferences as first author and presenter
≈ 70 accepted oral or poster contributions as co-author.

Other research activities

Member of section 19 (*The Earth System: superficial envelopes*) of the National Committee for Scientific Research (CoNRS) since 2017. [*Sections help define the scientific policy of the CNRS, analyze the current situation and outlook, recruit researchers and promote their careers, as well as monitor research unit activity.*]

Member of HCERES committee for LEGOS, 27-28 Nov 2019, Toulouse, France.

Organizer of laboratory meetings "Do While LOPS" for discussions related to programming, since 2018.

Co-Organizer of the Workshop on Non-Hydrostatic Ocean Modeling, 15-17 Oct 2018, Brest, France.

Editor of a special issue of the journal **Fluids** on *Submesoscale Processes in the Ocean*

Reviewer: Journal of Physical Oceanography, Geophysical Research Letters, Ocean Modeling, Journal of Fluid Mechanics, Ocean Dynamics, Nature Communications, Global Biogeochemical Cycles, Journal of Climate, Geophysical & Astrophysical Fluid Dynamics, AGU books, Nonlinear Processes in Geophysics, Remote Sensing of Environment, Journal of Advances in Modeling Earth Systems, Journal of Geophysical Research - Oceans, Journal of Geophysical Research - Atmospheres.

Evaluations: NSF, AO INSU-LEFE, PRACE.

Supervision

Master 1 A. Fadonougbo, 2017, Energy dissipation at western boundaries.

P. Tedesco, 2016, Submesoscale turbulence in the Sargasso Sea.

(co-direction) B. Tian, 2011, Regional climate change scenario for Western Canada.

Master 2 Yan Fei Er, 2019, Deep Learning for Ocean Models

N. Brice, 2019, Why are there more submesoscale anticyclones than cyclones in the interior ocean?

C. De Marez, 2018, Lee waves in the Gulf Stream

P. Tedesco, 2017, Submesoscale instabilities of the Agulhas Current.

E. Duyck, 2017, Drivers of the Subpolar Mode Water Formation in the North Atlantic subpolar gyre.

(co-direction) B. Ribstein, 2009, Formation et évolution de structures tourbillonnaires cohérentes.

PhD Ashwita Chouksey, 2019 - 2022 (with X. Carton):

Submesoscale coherent vortices in the Atlantic and their impact on the large scale circulation

L. Wang, 2019 - 2022 (co-direction 40%, with L. Memery):

Impact of the meso and submesoscale dynamics on the fate of exported particles in the deep ocean

P. Tedesco, 2017 - 2020 (co-direction 50%, with P. Penven and C. Menesguen):

Mesoscale eddy energy dissipation

M. Le Corre, 2016 - 2019 (with A.-M. Tréguier):

Dynamical processes driving turbulent mixing over the Reykjanes Ridge.

R. Juliano Dani, 2014 - 2018 (co-direction 20%, with M. Krug, M. Rouault and P. Penven):

Dynamics of the coastal upwelling south of Madagascar.

Postdoc C. Buckingham, 2019 - 2021: Centrifugal Instability in the Orkney Passage.

C. Vic, 2019 - 2021 (with B. Ferron): Investigating deep-ocean turbulence over the Reykjanes Ridge.

N. Lahaye, 2017 - 2019 (with G. Roullet): Submesoscale turbulence on the Mid-Atlantic Ridge.

C. Vic, 2016 (with G. Roullet): Dispersion of deep-sea hydrothermal vent effluents and larvae by submesoscale and tidal currents.

Thesis committee : J. Collin (2013-2016), T. Petit (2015-2018), M. Morvan (2016-2019), L. Siegelman-Charbit (2016-2019), C. De Marez (2018-2021)

Thesis jury : N. Malan (UCT, 2017), T. Capuano (LOPS, 2017), L. Siegelman-Charbit (LOPS, 2019), A. Ajayi (IGE, 2020)

Funded Projects

Principal Investigator

DEEPER - *Impacts of DEep submEsoscale Processes on the oceAn ciRculation*

ANR JCJC, 256 k€, 2020 - 2024

PRACE allocation, 20M cpu hours, 2019 - 2020

TADOMA - *Abyssal Turbulence on the Mid-Atlantic Ridge*
 SAD Région Bretagne / CG29 / Prestige, 130 k€, 2017 - 2019

Supervisor

SCALES - *Submesoscale Coherent vortices in the Atlantic and their impact on the Large scale circulation*
 ARED Région Bretagne / CNRS, PhD grant , 2019 - 2022

CIOP - *Centrifugal Instability in the Orkney Passage*
 C. Buckingham's Marie Curie fellowship, 173 k€, 2019 - 2021

TurbOR - *Turbulence Over Reykjanes*
 C. Vic's LabexMer fellowship, 150 k€, 2019 - 2021

EDDISSIP - *Mesoscale eddy energy dissipation*
 ARED Labex, PhD grant for P. Tedesco, 2017 - 2020

MEDDLE - *Dynamical processes driving turbulent mixing over the Reykjanes Ridge*
 ARED Labex, PhD grant for M. Le Corre, 2016 - 2019

Others

iAtlantic - *Integrated Assessment of Atlantic Marine Ecosystems in Space and Time*
 H2020 European project, participant, 10 M€, 2019 - 2023

TAWEPO - *Simulating Turbulent Mixing in the Abyssal Waters of the Equatorial Pacific Ocean*
 France-Stanford Collaborative project, french coordinator, 15 k€, 2018 - 2019

DELEOM - *DEep LEarning for Ocean Models*
 LabexMer, Co-I, 5 k€, 2018 - 2019

RADII - *Roads towArd DIssIpation*
 LEFE/IMAGO, participant, 12 k€, 2017 - 2019

LuckyScales - *Magma chamber to micro-habitats: dynamics of deep sea hydrothermal ecosystems*
 ANR, participant, 500 k€, 2014 - 2018

Teaching

2019-20 - Univ. Brest - Assistant Professor - (230h/yr):

- Jury Master 2: Ocean and Climate Physics
- Scientific writing (PhD students - 15h/yr)
- Scientific English (M2 - 24h/yr)
- Numerical Modelling (M2 - 35h/yr)
- Ocean Waves (M2 - 22h/yr)
- Ocean Turbulence (M2 - 21h/yr)
- Fluid Mechanics (M1 - 30h/yr)
- Data Analysis (M1 - 26h/yr)
- Applied Mathematics (M1 - 10h/yr)
- Computational Physics (L3 - 24h/yr)

Oct. 20, 2018 Master Class: "Realistic Modelling of the ocean" (2h).
Workshop on "Non-hydrostatic Ocean Modeling", Brest, France.

2015-20 - Univ. Brest - Assistant Professor - (\approx 200h/yr):

- Scientific writing (PhD students - 15h/yr)
- Scientific English (M2 - 24h/yr)
- Numerical Modelling (M2 - 35h/yr)

- Ocean Waves (M2 - 22h/yr)
- Ocean Turbulence (M2 - 21h/yr)
- Coastal Dynamics (M2 - 12h/yr)
- Fluid Mechanics (M1 - 30h/yr)
- Data Analysis (M1 - 26h/yr)
- Applied Mathematics (M1 - 10h/yr)
- Computational Physics (L3 - 24h/yr)
- Statistics and Physics (L1 - 34h/yr)

2006-09 - Université Paris VI - Teaching assistant. *Leading groups of 20 to 30 students in exercices, laboratory experiments and making exams.*

- Introduction to physics, BS (192h)
- Mathematics for physicists, BS (12h)

2005-06 - Lycée Janson de Sailly - Teaching assistant.

- *Oral exams for undergraduate students in Physics and chemistry (80h)*

Softwares

WRF-FLake : The Weather Research and Forecasting (WRF) model has been coupled with the Freshwater Lake (FLake) model.

Pyticles : Pyticles is a Python/Fortran hybrid parallelized code for Lagrangian particles 3D advection from high-resolution ocean models data. <https://github.com/Mesharou/Pyticles>

Skills

Languages: French (mother tongue) - English

Computer: Operating systems: Linux, MacOs, Windows.

Programing: Python, Fortran, C, C++, Perl, Shell, Html, Php, L^AT_EX.

Software: Matlab, Mathematica, Mapple, LabVIEW, ...etc..

Other: Driving licence - Motorbike licence - Scuba diver CMAS***

Publications

In journals:

[Supervised postdocs, PhD, or masters students are indicated in colors]

in revision/submitted. □

- Schubert, R., **J. Gula**, R.J. Greatbatch, W. Rath & A. Biastoch: The Submesoscale Kinetic Energy Cascade in the Simulated Agulhas Region, submitted to *J. Phys. Oceanogr.*
- Smilenova, A., **J. Gula**, **M. Le Corre** & L. Houpert: A persistent deep anticyclonic vortex in the Rockall Trough, submitted to *J. Geophys. Res. Ocean.*

- Buckingham, C., X. Carton, **J. Gula** & C. De Marez: The role of curvature in modifying frontal instabilities, submitted to *J. Phys. Oceanogr.*
- **De Marez, C., N. Lahaye & J. Gula:** Interaction of the Gulf Stream with small scale topography: a focus on lee waves, submitted to *Scientific Reports*
- **Le Corre, M., J. Gula & A.-M. Tréguier:** Barotropic vorticity balance of the North-Atlantic subpolar gyre in an eddy-resolving model, *Ocean Sci. Discuss.*, <https://doi.org/10.5194/os-2019-114>, in review, 2019.
- A. Solodoch, J.C. McWilliams, A. Stewart, **Gula, J.** & L. Renault: Why does the Deep Western Boundary Current “leak” around Flemish Cap?, submitted to *J. Phys. Oceanogr.*

2019

- Morvan M., P. L'Hégaret, X. Carton, **J. Gula**, C. Vic, M.A. Sokolovskiy & K.V. Koshel: The life cycle of submesoscale eddies generated by topographic interactions, *Ocean Science*. <https://doi.org/10.5194/os-2019-3>
- **Tedesco, P., J. Gula**, C. Menesguen, P. Penven & M. Krug, **2019**: Generation of submesoscale frontal eddies in the Agulhas Current, *J. Geophys. Res. Ocean*. <https://doi.org/10.1029/2019JC015229>
- **Lahaye, N.J., J. Gula**, A. Thurnherr, G. Reverdin, P.A. Bouruet-Aubertot & G. Roullet, **2019**: Deep currents in the rift valley of the North Mid-Atlantic Ridge, *Frontiers in Marine Science*.
- Morel, Y., **J. Gula** & A. Ponte, **2019**: Potential Vorticity diagnostics based on balances between volume integral and boundary conditions, *Ocean Model.*. <https://doi.org/10.1016/j.ocemod.2019.04.004>
- **Lahaye, N.J., J. Gula** & G. Roullet, **2019**: Sea-surface signature of internal tides, *Geophys. Res. Lett.*, 46, 3880-3890. <https://doi.org/10.1029/2018GL081848>
- **Gula, J.**, T. Blacic, & R.E. Todd, **2019**: Submesoscale coherent vortices in the Gulf Stream, *Geophys. Res. Lett.*, 46, 2704-2714. <https://doi.org/10.1029/2019GL081919>
- McWilliams, J.C., **J. Gula** & M.J. Molemaker, **2019**: The Gulf Stream North Wall: Ageostrophic Circulation and Frontogenesis, *J. Phys. Oceanogr.*, 49, 893–916. <https://doi.org/10.1175/JPO-D-18-0203.1>
- Chelton, D.B., M.G. Schlax, R.M. Samelson, J.T. Farrar, M.J. Molemaker, J.C. McWilliams & **J. Gula**, **2018**: Prospects for Future Satellite Estimation of Small-Scale Variability of Ocean Surface Velocity and Vorticity, *Prog. Oceanogr.*, 173, 256-350. doi:10.1016/j.pocean.2018.10.012.

2018

- Renault, L., J.C. McWilliams & **J. Gula**, **2018**: Dampening of Submesoscale Currents by Air-Sea Stress Coupling in the Californian Upwelling System, *Scientific Reports*, 8, 13388.
- Wenegrat, J.O., L.N. Thomas, **J. Gula** & J.C. McWilliams, **2018**: Effects of the submesoscale on the potential vorticity budget of ocean mode waters, *J. Phys. Oceanogr.*, 48, 2141–2165.
- **Ramanantsoa, J.D.**, P. Penven, M. Krug, **J. Gula** & M. Rouault, **2018**: Uncovering a new current: the Southwest Madagascar Coastal Current (SMACC), *Geophys. Res. Lett.*, 45, 1930-1938, doi:10.1002/2017GL075900.
- **Vic, C., J. Gula**, G. Roullet & F. Pradillon, **2018**: Dispersion of deep-sea hydrothermal vent effluents and larvae by submesoscale and tidal currents, *Deep Sea Res.*, 133, 1-18.
- **Ramanantsoa, J.D.**, M. Krug, P. Penven, M. Rouault & **J. Gula**, **2018**: Coastal upwelling south of Madagascar: temporal and spatial variability, *Journal of Marine System*, 178, 29-37.

2017

- Ardhuin, F., S.T. Gille, D. Menemenlis, C.B. Rocha, N. Raschle, B. Chapron, **J. Gula** & M.J. Molemaker, **2017**: Small-scale open-ocean currents have large effects on wind-wave heights, *J. Geophys. Res. Ocean.*, 122, doi:10.1002/2016JC012413.
- Krug, M., S. Swart & **J. Gula**, **2017**: Submesoscale cyclones in the Agulhas Current, *Geophys. Res. Lett.*, 44, 346–354.

2016

- **Gula, J.**, M.J. Molemaker & J.C. McWilliams, **2016**: Topographic generation of submesoscale centrifugal instability and energy dissipation, *Nat. Commun.*, 7, 12811.
- Renault, L., M.J. Molemaker, **J. Gula**, S. Masson & J.C. McWilliams, **2016**: Control and Stabilization of the Gulf Stream by Oceanic Current Interaction with the Atmosphere, *J. Phys. Oceanogr.*, 46, 3439–3453.
- Klymak, J.M., R.K. Shearman, **J. Gula**, C.M. Lee, E.A. D'Asaro, L. Thomas, R. Harcourt, A. Shcherbina, M.A. Sundermeyer, M.J. Molemaker & J.C. McWilliams, **2016**: Submesoscale streamers exchange water on the North Wall of the Gulf Stream, *Geophys. Res. Lett.*, 43, 1226–1233.
- **Gula, J.**, M.J. Molemaker & J.C. McWilliams, **2016**: Submesoscale dynamics of a Gulf Stream frontal eddy in the South Atlantic Bight, *J. Phys. Oceanogr.*, 46, 305-325.
- Schoonover, J., W. Dewar, N. Wienders, **J. Gula**, J.C. McWilliams, M.J. Molemaker , S. Bates & G. Danabasoglu, **2016**: North Atlantic vorticity balances in high resolution numerical models, *J. Phys. Oceanogr.*, 46, 289-303.

2015

- Vic, C., G. Roullet, X. Carton, X. Capet, M.J. Molemaker & **J. Gula**, **2015**: Eddy-topography interactions and the fate of the Persian Gulf Outflow, *J. Geophys. Res. Ocean.*, 120, doi:10.1002/2015JC011033.
- McWilliams, J.C., **J. Gula**, M.J. Molemaker, L. Renault & A. Shchepetkin, **2015**: Filament frontogenesis by boundary layer turbulence, *J. Phys. Oceanogr.*, 45, 1988-2005.
- **Gula, J.**, M.J. Molemaker & J.C. McWilliams, **2015**: Topographic vorticity generation, submesoscale instability and vortex street formation in the Gulf Stream, *Geophys. Res. Lett.*, 42, 4054-4062.
- Callies, J., R. Ferrari, J. M. Klymak & **J. Gula**, **2015**: Seasonality in submesoscale turbulence, *Nat. Commun.*, 6, 6862.
- Mallard, M.S., C.G. Nolte, T.L. Spero, O.R. Bullock, K. Alapaty, J. Herwehe, **J. Gula** & J. Bowden, **2015**: Challenges and Solutions in Representing Lakes when Using WRF in a Downscaling Application, *Geosci. Model Dev.*, 8, 1085-1096.
- **Gula, J.**, M.J. Molemaker & J.C. McWilliams, **2015**: Gulf Stream dynamics along the Southeastern U.S. Seaboard, *J. Phys. Oceanogr.*, 45, 690-715.

2014

- **Gula, J.**, M.J. Molemaker & J.C. McWilliams, **2014**: Submesoscale cold filaments in the Gulf Stream, *J. Phys. Oceanogr.*, 44, 2617-2643.
- d'Orgeville, M., W.R. Peltier, A. Erler & **J. Gula**, **2014**: Global Warming Impacts on Great Lakes Basin Precipitation Extremes, *J. Geophys. Res. Atmos.*, 119, 10799-10812.
- Mallard, M.S., C.G. Nolte, O.R. Bullock, T.L. Spero & **J. Gula**, **2014**: Using a Coupled Lake Model with WRF for Dynamical Downscaling, *J. Geophys. Res. Atmos.*, 119, 7193-7208.

2012

- **Gula, J.** & W.R. Peltier **2012**: Dynamical Downscaling over the Great Lakes Basin of North America using the WRF Regional Climate Model: The impact of the Great Lakes system on regional greenhouse warming, *Journal of Climate*, 25, 7723-7742.

2011

- Flór, J.-B., H. Scolan & **J. Gula**, **2011**: Frontal instabilities and waves in a differentially rotating fluid, *J. Fluid Mech.*, 685, 532-542.

2010

- **Ribstein, B., J. Gula & V. Zeitlin, 2010:** (A)geostrophic adjustment of dipolar perturbations, formation of coherent structures and their properties, as follows from high-resolution numerical simulations with rotating shallow water model, *Physics of Fluids*, 22, doi:10.1063/1.3514200.
- **Gula, J., V. Zeitlin & F. Bouchut, 2010:** Instabilities of buoyancy driven coastal currents and their nonlinear evolution in the two-layer rotating shallow water model. Part II. Active lower layer, *J. Fluid Mech.*, 665, 209-237.
- **Gula, J. & V. Zeitlin, 2010:** Instabilities of buoyancy driven coastal currents and their nonlinear evolution in the two-layer rotating shallow water model. Part I. Passive lower layer., *J. Fluid Mech.*, 659, 69-93.

2009

- **Gula, J., V. Zeitlin & R. Plougonven, 2009:** Instabilities of two-layer shallow-water flows with vertical shear in the rotating annulus, *J. Fluid Mech.*, 638, 27-47.
 - **Gula, J., R. Plougonven & V. Zeitlin, 2009:** Ageostrophic instabilities of fronts in a channel in the stratified rotating fluid., *J. Fluid Mech.*, 627, 485-507.
-

Book chapter:

- **Gula, J. & V. Zeitlin, 2014:** Instabilities of shallow-water flows with vertical shear in the rotating annulus,"Modelling Atmospheric and Oceanic flows: insights from laboratory experiments and numerical simulations", edited by T. von Larcher and P. Williams, AGU, Washington, D. C.
-

Proceedings:

- Dagallier, A., S. Cheinet, D. Juve, A. Ponte, & **Gula, J., 2019:** Travel times in complex environments, Proceedings of the 23rd International Congress on Acoustics, 9-13 september 2019, Aachen, Germany.
 - **Le Corre, M., J. Gula, A. Smilenova, & L. Houpert, 2019:** On the dynamics of a deep quasi-permanent anticyclonic eddy in the Rockall Trough., 24ème Congrès Français de Mécanique, 26-30 août 2019, Brest, France.
 - **Gula, J. & V. Zeitlin, 2011:** Instabilities of buoyancy driven coastal currents and their nonlinear evolution in the two layer rotating shallow water model, In Mathematical Theory and Modelling in Atmosphere-Ocean-Science. Eds. A. J. Majda, B. Stevens and R. Klein. Mathematisches Forschungsinstitut Oberwolfach, Report No. 34/2010.
 - **Gula, J., R. Plougonven & V. Zeitlin, 2007:** Ageostrophic instabilities of a front in a stratified rotating fluid., 18ème Congrès Français de Mécanique, 27-31 août 2007, Grenoble, France, (CD-ROM proceedings).
 - Wake, G. W., J. **Gula & G.N. Ivey, 2004:** Periodic Forcing of Baroclinic Basin-Scale Waves in a Rotating Stratified Basin, 15th Australasian Fluid Mechanics Conference, The University of Sydney, 13-17 December 2004, CD Rom: AFMC00097
-

Reports and Thesis:

- **Gula, J. & W.R. Peltier, 2011:** The impact of the Great Lakes system on regional greenhouse warming, Report for the Ontario Ministry of Environment.

- **Gula, J., 2009:** Ageostrophic instabilities of baroclinic flows in the atmosphere and ocean and their non-linear evolution, Thèse de Doctorat de l'Université Pierre et Marie Curie, Paris, France.

Communications (as presenter)

- Feb. 19, 2020** The impact of meso and submesoscale frontal eddies on cross-shelf transport in the Gulf Stream and Agulhas Current.
Poster (invited), Ocean Sciences Meeting, San Diego, CA, USA.
- Feb. 17, 2020** Generation of lee waves and submesoscale vortices in the wake of the Charleston Bump.
Oral, Ocean Sciences Meeting, San Diego, CA, USA.
- May 26, 2019** Dispersion of larvae in the deep ocean by submesoscale and tidal currents.
Oral (invited), "Advances in ocean biological observations – sustained system for deep-ocean meroplankton", Aveiro, Portugal.
- Oct. 20, 2018** When the Stream meets the Bump.
Oral (invited), Workshop on "Non-hydrostatic Ocean Modeling", Brest, France.
- Feb. 13, 2018** Dispersion of larvae by submesoscale and tidal currents.
Oral, Ocean Sciences Meeting, Portland, Oregon, USA.
- Feb. 11, 2018** Energy spectra in high-resolution realistic regional simulations.
Oral, Workshop on "Interactions between internal gravity waves and meso/submesoscale currents in the ocean", Portland, Oregon, USA.
- Oct. 15, 2017** Surface kinetic energy and balances in realistic high resolution simulations.
Oral, Workshop IGAFD : Interdisciplinary Geo-Astro Fluid Dynamic, Paris, France.
- May. 27, 2016** Topographic Generation of Submesoscale Centrifugal Instability and Energy Dissipation.
Oral, Colloquium Submesoscale Processes: Mechanisms, Implications and new Frontiers, Liège, Belgique.
- Mar. 22, 2016** Topographic Generation of Submesoscale.
Workshop on "Ocean Submesoscale Processes in the World Ocean", Brest, France.
- Jun. 19, 2015** Submesoscale Phenomena and Consequences around the Gulf Stream.
Séminaire, Laboratoire de Physique des Océans, Brest, France.
- Apr. 30, 2015** Submesoscale Phenomena and Consequences around the Gulf Stream.
Séminaire, Laboratoire de Glaciologie et Géophysique de l'environnement (LGGE), Grenoble, France.
- Dec. 17, 2014** Gulf Stream frontal eddies and their submesoscale interior.
Poster, American Geosciences Union Fall Meeting, San Francisco, California, USA.
- Feb. 28, 2014** Submesoscale instabilities and mixing on the Gulf Stream North Wall.
Oral, Ocean Sciences Meeting, Honolulu, Hawaii, USA.
- Jan. 8, 2013** Gulf Stream North Wall submesoscale fronts and instabilities.
Workshop on "Scalable lateral mixing and coherent turbulence", Stanford University, CA, USA.
- Dec. 10, 2012** Dynamics of the Gulf Stream: From gyre-scale balance to submesoscale generation.
Séminaire, Laboratoire de Physique des Océans, Brest, France.
- Jun. 20, 2012** Submesoscale dynamics in the Gulf Stream region.
Workshop on "Scalable lateral mixing and coherent turbulence", Woods Hole Oceanographic Institution, USA.
- Jan. 11, 2012** Small scale features in the Gulf Stream region.
Workshop on "Scalable lateral mixing and coherent turbulence", Portland, OR, USA.
- Dec. 5, 2011** Dynamical Downscaling over the Great Lakes Basin of North America: The impact of the Great Lakes system on regional greenhouse warming.
Poster, American Geosciences Union Fall Meeting, San Francisco, California, USA.

- May 18, 2011** Dynamical Downscaling over the Great Lakes Basin of North America: The impact of the Great Lakes system on regional greenhouse warming.
Séminaire, Department of Atmospheric and Oceanic Sciences, UCLA, Los Angeles, USA.
- Apr. 03, 2011** Dynamical Downscaling over the Great Lakes Basin of North America using the WRF Regional Climate Model. *Oral, EGU General Assembly, Vienna, Austria.*
- Fev. 05, 2010** Regional Climate Modelling at the UoFT: Physics and SciNet.
Climate Science Workshop: Regional Climate Modelling Capacity in Ontario. Toronto and Region Conservation Authority, Toronto, Canada.
- Sep. 02, 2009** Instabilities of coastal currents, NL evolution and vortex formation.
Oral, International Conf. on High-Reynolds Number Vortex Interactions, Brest, France.
- Aug. 31, 2009** Existence, propagation and collisions of localized dipolar vortices on the f-plane.
Poster, International Conf. on High-Reynolds Number Vortex Interactions, Brest, France.
- Apr. 24, 2009** Instabilities of two-layer shallow-water flows with vertical shear in the rotating annulus. *Oral, European Geosciences Union General Assembly, Vienna, Austria.*
- Jan. 9, 2009** Instabilities of two-layer shallow-water flows with vertical shear in the rotating annulus.
Oral, The Dynamics of Rotating Fluids Meeting, University College London.
- Dec. 9, 2008** Instabilities of 2-layer shallow-water flows with vertical shear in the rotating annulus.
Séminaire, Laboratoire des Ecoulements Géophysiques et Industriels (LEGI), Grenoble, France.
- Dec. 02, 2008** Instabilities of 2-layer shallow-water flows with vertical shear in the rotating annulus.
Séminaire, The Mathematical Institute, University of Oxford, UK.
- Nov. 5, 2007** Ageostrophic instabilities of a front in a stratified rotating fluid.
Séminaire, The School of Mathematics, University of Edinburgh, UK.
- Aug. 31, 2007** Ageostrophic instabilities of a front in a stratified rotating fluid.
Oral, Congrès Français de Mécanique, Grenoble, France.
- Apr. 18, 2007** Ageostrophic instabilities of balanced flows and their NL evolution.
Poster, European Geosciences Union General Assembly, Vienna, Austria.